MASS TRANSPORT PHENOMENA AT HOT MICROELECTRODES

A thesis submitted to the
College of Graduate Studies and Research
in partial fulfillment of the requirements
for the degree of Doctor of Philosophy
in the Department of Chemistry
University of Saskatchewan, Saskatoon

ALIAKSEI BOIKA

PERMISSION TO USE

In presenting this thesis in partial fulfilment of the requirements for a Doctor of Philosophy degree from the University of Saskatchewan, I agree that the Libraries of this University may make it freely available for inspection. I further agree that permission for copying of this thesis in any manner, in whole or in part, for scholarly purposes may be granted by the professor who supervised my thesis work or, in his absence, by the Head of the Department or the Dean of the College in which my thesis work was done. It is understood that any copying or publication or use of this thesis or parts thereof for financial gain shall not be allowed without my written permission. It is also understood that due recognition shall be given to me and to the University of Saskatchewan in any scholarly use which may be made of any material in my thesis.

Requests for permission to copy or to make other use of material in this thesis in whole or part should be addressed to:

Head of the Department of Chemistry
Department of Chemistry, University of Saskatchewan
110 Science Place
Saskatoon, SK S7N 5C9
Canada
Tel: (306) 966-4655 Fax: (306) 966-4730

ABSTRACT

Hot microelectrodes are very small electrodes (usually 1 – 100 μm in diameter), which have a surface temperature much higher than the temperature in the bulk solution. In this work, the heating is achieved by applying an alternating potential of very high frequency (100 MHz – 2 GHz) and of high amplitude (up to 2.8 V_{rms}) to the microelectrode. As a result, very fast (on the order of milliseconds) changes in the temperature of the electrolyte solution surrounding the electrode can be achieved. Due to the size of the heated microelectrodes, the hot zone in solution is small. Therefore, the solution can be easily overheated and temperatures above the boiling point can be reached.

The purpose of this research was to investigate and understand the phenomena occurring at ac polarized microelectrodes and to propose new applications of these electrodes. Using both steady-state and fast-scan (10 V s^{-1}) cyclic voltammetry measurements, mass transport of redox species has been studied at ac heated microelectrodes. It has been established that the convection at hot-disk microelectrodes is driven primarily by the electrothermal flow of an electrolyte solution. In addition, other effects such as ac dielectrophoresis and Soret (nonisothermal) diffusion are also observed. Numerical simulations have been employed to predict the distribution of temperature in the hot zone, the direction and magnitude of the electrothermal force and the solution flow rate, as well as the voltammetric response of hot-disk microelectrodes. The results of the simulations agree well with the experimental observations.

Theoretical findings of this PhD work are very important for the understanding of the fundamentals of high temperature electrochemistry, particularly mass transport. The proposed explanation of the convection mechanism is most likely applicable not only to ac polarized microelectrodes, but also to the microwave heated microelectrodes, since the only difference between these two heating methods is in the way of delivering electrical energy (wired vs. wireless). The results of the studies of Soret diffusion indicate that it contributes significantly to mass transfer of redox species at hot microelectrodes. Taking into account that the magnitude of the Soret effect has been considered negligible by other electrochemists, the results obtained in this work prove the opposite and show that Soret diffusion affects both the faradaic current and the half-

wave potential of the redox reaction. Therefore, the Soret effect can not be ignored if working with hot microelectrodes.

Hot microelectrodes can have a number of interesting applications. The results of the initial investigations indicate that these electrodes can be successfully used in the arrangement for Scanning Electrochemical Microscopy (such a novel technique is termed Hot-Tip SECM). In addition, the observed dielectrophoretic and electrothermal convection effects can enhance the performance of the electrochemical sensors based on hot microelectrodes. This can lead to the improvement of the detection limits of many biologically important analytes, such as proteins, bacteria and viruses.

ACKNOWLEDGMENTS

I would like to express my gratitude to my supervisor, Dr. Andrzej S. Baranski, for his help with the project, encouragement, understanding and support over all these years. The experience gained in his laboratory is greatly appreciated and valued.

I would also like to thank my advisory committee members: Drs. Ian Burgess (Chemistry), Stephen Reid (Chemistry) and David Dodds (Electrical and Computer Engineering) for the valuable discussions during the committee meetings.

Special thanks go to Lana Gutwin, a former member of Baranski's group, for proofreading my papers and for supporting me even after leaving the lab. And to Drs. Grzegorz Orlowski and Izabella Niewczas for their interest in my project and much appreciated encouragement during my studies at U of S.

I would like to thank Dr. Shatha Qaqish for taking AFM images for me.

The financial assistance from the University of Saskatchewan and Natural Sciences and Engineering Research Council of Canada is also greatly acknowledged.

DEDICATION

I would like to dedicate this thesis to my parents, Vasil and Liudmila Boika, my brother Aliaksandr and to Marcelina Łabaj for their enormous support throughout these school years. Thank you very much for believing in me!

TABLE OF CONTENTS

LIST OF TABLES

LIST OF FIGURES

LIST OF VIDEOS

LIST OF ABBREVIATIONS

ac	alternating current
ACV	alternating current voltammetry, alternating current voltammogram
AFM	Atomic Force Microscopy
CV	cyclic voltammetry
DEP	dielectrophoresis, dielectrophoretic
DNA	deoxyribonucleic acid
EDAS	Electrochemical Data Acquisition System
EDL	electric double layer
emf	electromotive force
FIDAP	Fluid Dynamics Analysis Package
HT-SECM	Hot-tip Scanning Electrochemical Microscopy
IHP	inner Helmholtz plane
IR	infrared
MV	methyl viologen
OHP	outer Helmholtz plane
RDE	rotating disk electrode
SAM	self-assembled monolayer
SECM	Scanning Electrochemical Microscopy
SS-CV	steady-state cyclic voltammetry, steady-state cyclic voltammogram
UME	ultramicroelectrode
ZTC	zero thermal conductivity

PREFACE

Hot microelectrodes have found numerous applications in the areas of electroanalytical and physical chemistry. However, when this project was started, very little was reported in the literature about the mass transport at these electrodes. Firstly, it was not clear what causes convection at ac polarized microelectrodes. Secondly, other research groups working with hot microelectrodes completely neglected the effect of Soret diffusion on the rate of mass transport of redox species. Presented thesis addresses these important issues of mass transport in nonisothermal electrochemical systems. The material is organized as follows. Introduction includes necessary theoretical background needed to understand the material discussed further in the thesis. At first glance it may seem that the topics covered in the introduction are chosen arbitrary, however, all of them are related to this research. Important details about the experimental setups are discussed in Chapter 2. After that the results of the studies of convection at hot microelectrodes are presented and discussed (Chapter 3). These results indicate that the convection at ac heated microelectrodes is driven primarily by the electrothermal flow of an electrolyte solution. Much better understanding of the phenomena observed at hot microelectrodes was reached when numerical simulations were employed (Chapter 4). The results of the simulations agree well with the experimental data. In addition, it is shown in Chapter 5 that Soret diffusion affects the response of hot microelectrodes (in particular, the faradaic current and the half-wave potential). Finally, Chapter 6 includes preliminary results of the studies in which hot microelectrodes were used in the arrangement for the Scanning Electrochemical Microscopy. To conclude, it should be stressed that the knowledge of the mass transport at hot microelectrodes is important not only for the area of fundamental electrochemistry, but also for the development of new applications of these electrodes. More details about this are provided in Chapter 7 (suggestions for further research).

CHAPTER 1: INTRODUCTION

1.1 WHAT ARE HOT MICROELECTRODES?

1.1.1 Methods for heating of electrodes

Hot (or heated) microelectrodes are microelectrodes which have the electrode surface temperature much higher than the temperature in the bulk solution. The term microelectrode (or ultramicroelectrode, UME) is used to describe an electrode which has at least one dimension very small, usually in the micrometer range.[1,2] The most popular UME geometries are those for which a voltammetric steady-state can be reached and which are small in all dimensions. Such geometries include disks, rings, ring-disks, hemispherical, spherical and finite conical electrodes (see Figure 1.1). Microcylindrical and microband electrodes were popular in the 1980's, because they provided relatively large currents compared to microdisk electrodes. Currently, they are much less popular than other UME geometries, because they do not reach a steady state and are not useful in eliminating ohmic (*iR*) drops.

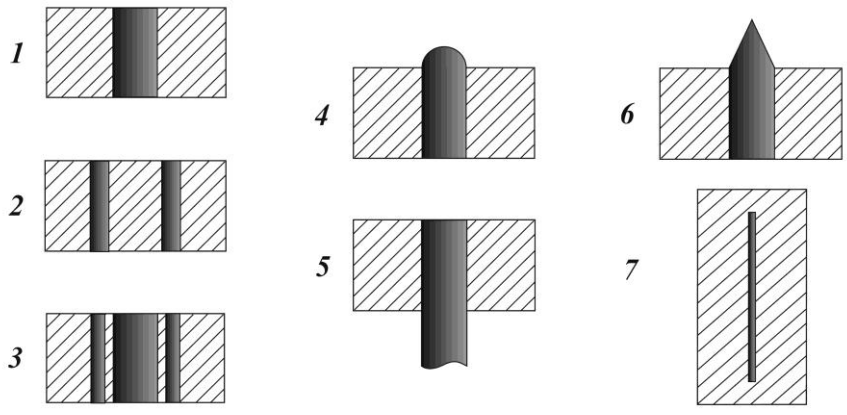

Figure 1.1 Types of microelectrodes: 1 – disk, 2 – ring, 3 – ring-disk, 4 – hemispherical; 5 – cylindrical; 6 – finite conical and 7 – microband (adapted from References 1 and 2).

Five major methods of heating an electrode have been reported: by using a laser beam,[3] by passing an alternating current through the body of the electrode,[4] by employing microwave[5] or rf[6] radiation or by modulating the electrode potential with high frequency and high amplitude alternating voltage.[7] All of these methods can be divided into two main groups: (1) methods based on direct heating of the electrode material (laser, ac current and rf radiation) and (2) methods based on indirect heating (microwave radiation, high frequency ac waveform). These methods will now be discussed in greater detail.

1.1.1.1 Direct heating of electrodes

1.1.1.1.1 Heating using a light beam

In his pioneering work, Miller proposes the use of a laser beam to illuminate an electrode disk and thus heat the solution in the vicinity of the electrode surface. In this design, a very thin layer of gold (approximately 10 μm thickness) serves as an electrode disk, backed by a somewhat thicker copper layer with the surface converted to a black, absorptive oxide film. Heat is supplied through an argon ion laser beam, which is incident on the back of the electrode. In this particular example, the electrode is rotated and the laser light is chopped at a frequency 5 – 10 Hz frequency. This results in the heating of the solution that is periodic and pulsed in nature. Standard voltammetric measurements can be carried out in such an experimental arrangement, and the method is termed Thermal Modulation Voltammetry (TMV).[3]

1.1.1.1.2 Heating by an alternating current

The body of an electrode can be heated by passing an electric current through it. In this case, Joule heating of the electrode material leads to heating of the solution. Direct current can not be used for this purpose because of the *iR* drop generated along the length of the electrode. This *iR* drop causes distortion of the electrochemical data and therefore should be eliminated. It has been proposed that ac currents (ca. 100 kHz frequency) could be used for heating instead of dc. The ac current also generates an undesired *iR* drop, however, by using specially designed electrodes the problem can be eliminated.[8,9] This is achieved by making the contact between the electrode and the potentiostat in the centre of the cylindrical microwire. As a result of the symmetrical

arrangement, the voltage developed at one side of the electrode is compensated by a corresponding voltage of the opposite sign which develops at the other side of the electrode. Provided that the two sections of the microwire have the same length, the ac voltage drop is eliminated. It was possible to maintain the surface temperature of a hot-wire electrode below the boiling point of the solution for an indefinite time, or well above the boiling point for a short time (in aqueous solutions, a surface temperature of 523 K was maintained for ~5 ms without boiling).[10] However, to provide a large temperature change, high currents (up to 6 A_{rms}) had to be used.[11]

1.1.1.1.3 Inductive heating of electrodes

A radio frequency electromagnetic field can also be used for thermal activation of electrochemical processes.[6] In this case, radiation from an 8 MHz generator causes the appearance of eddy currents in a thin foil Pt electrode. As a result, the electrode body heats up together with the solution around it. Reference and counter electrodes are placed outside the heated region.

1.1.1.2 Indirect heating of electrodes

1.1.1.2.1 Heating by microwave radiation

The use of microwave heating in electrochemistry was first demonstrated by Compton *et al*.[5] To conduct electrochemical measurements in a microwave field, a conventional potentiostat system and a microwave applicator are needed. Usually, microwave radiation at the commercially available frequency of 2.45 GHz is used. In the electrochemical cell, only the working electrode is placed in the microwave field. The heating is observed due to the absorption of the microwave energy in the region of the solution near the metal electrode. As a result of a self-focusing effect (the metal wire acts as an ‘antenna’), the strength of the electric field at the tip of the electrode is very high. Therefore, the solution close to the electrode surface (where the solution resistance develops) heats up. To minimize heating of the bulk solution, a slow flow of the electrolyte solution is maintained. During high temperature experiments, a vacuum degassing step is used to avoid gas bubble formation in the vicinity of the working electrode. Microwave heating in ionic liquids can cause a tremendous increase in

temperature in the region near the electrode. In this case, values of 600 K and even higher have been reported.[12]

1.1.1.2.2 Heating by high frequency ac waveform

An alternative approach to the heating of microelectrodes has been developed by Baranski.[7] In this case, a high frequency (100 MHz to 2 GHz) and high amplitude (up to 2.8 V_{rms}) sinusoidal waveform is superimposed on the potential waveform normally used in electrochemical measurements. As a result, a relatively large alternating current flows through the electrode. Since the resistance of the microwire is much smaller than the solution resistance, the heat is produced in the solution adjacent to the electrode, but not in the electrode material itself. For disk microelectrodes, a significant solution resistance develops only in the close proximity of the electrode, roughly at a distance comparable to the radius of the electrode. Therefore, the size of the hot zone is also comparable to the radius of the electrode. This heating method can be easily used in various electrochemical measurements using microelectrodes in different geometrical arrangements. In addition, easy control of the electrode temperature and very rapid change of temperature can be achieved.

1.1.2 Methods for determination of the electrode temperature

In electrochemical studies involving heated microelectrodes, it is important that the electrode temperature is known. A number of methods of electrode temperature determination have been proposed over the years. They can be divided into two main groups: direct and indirect, based on the method the temperature value is obtained.

1.1.2.1 Indirect methods of temperature determination

The methods of temperature determination discussed below are termed indirect because they rely on the measurement of parameters which are affected by temperature, such as potential, current or electrode resistance. Therefore, in order to determine the actual temperature value, a set of calculations needs to be performed and usually additional (calibration) experiments are required.

1.1.2.1.1 Resistance measurements

This method, suggested by Gruendler, is applicable only to heated cylindrical (microwire) electrodes. It is based on the fact that the resistance of a material depends on

temperature.[13,14] For a metallic resistor, such as a microwire electrode, the temperature dependence is given by the following equation:

$$R(T) = R_0[1+\alpha(T-T_0)] \tag{1.1}$$

where $R(T)$ is the resistance at the temperature T, R_0 is the so-called "cold" resistance (at room temperature T_0) and α is a constant, which has a value of $3.9083 \cdot 10^{-3}$ K^{-1} in the case of a Pt conductor.

During the experiments, the heating current is obtained from the voltage drop across a temperature independent series resistor. Therefore, it is possible to determine the resistance of the heated microwire (electrode), from which the temperature of the wire can be calculated according to the equation:

$$T_i = \left(\frac{R_i - R_0}{R_0 \cdot \alpha} \right) + T_0 \tag{1.2}$$

where R_i and T_i are the instantaneous values of the resistance and temperature of the electrode.

This method of temperature determination neglects the contribution of the solution to the overall conductivity of the microwire electrode. In addition, it gives an average value of temperature.

1.1.2.1.2 Potentiometric method of determination of electrode temperature

This method requires the knowledge of the temperature coefficient of the electrode reaction standard potential $\left(dE^0/dT\right)$, which has to be determined in a separate experiment.[15,16] During the calibration experiment, an open-circuit potential difference is measured between two identical microelectrodes immersed in two electrochemical cells connected with a salt bridge. Each cell contains equal concentrations of both forms of a redox species (for example, $Fe(CN)_6^{3-}/Fe(CN)_6^{4-}$) and the supporting electrolyte. The temperature of one of the cells is kept constant (i.e., by using ice), while the temperature of the other is varied with the use of a water bath. As a result, the temperature coefficient of the electrode reaction standard potential can be determined from the linear slope of the graph of open-circuit potential difference vs. temperature difference between the cells. The change of the temperature during the actual electrochemical experiments can

then be calculated from the shift in the half-wave potential determined from the voltammograms.

1.1.2.1.3 Logarithmic analysis of steady-state voltammograms

This method is based on the fundamental relation between the potential of the reversible electrode reaction and the current:[7,17]

$$E = E_{1/2} + \frac{RT}{nF} \ln\left(\frac{i}{i_{\text{lim}} - i} \right) \tag{1.3}$$

where E is the electrode potential, $E_{1/2}$ is the half-wave potential, R is the gas constant, F is the Faraday constant, n is the stoichiometric number of electrons involved in an electrode reaction, i is the current, i_{lim} is the limiting current and T is the electrode temperature.

According to this equation, the temperature of the solution at the electrode surface can be determined from the slope of the graph E vs. $\ln\left(\frac{i}{i_{\text{lim}} - i} \right)$.

1.1.2.2 Direct methods of temperature determination

Direct determination of the temperature of a hot microelectrode is challenging due to the dimensions of the studied systems; it is physically impossible to position a temperature measuring device close enough to the surface of the microelectrode without affecting the properties of the system (i.e., diffusion layer, temperature distribution). The only possibility of the direct measurement of the electrode temperature seems to be if the electrode acts as a temperature sensing device in itself. Such electrodes, termed thermocouple microelectrodes, have been developed during the course of this work. Their construction and operation is discussed in Chapter 2 of the thesis. Here, a brief discussion of the principles of temperature sensing by thermocouples is given.

1.1.2.2.1 Temperature determination using thermocouples

Temperature measurements with thermocouples are feasible due to the potential difference developed at the junction of two different metals.[18] This potential difference, called the thermoelectric electromotive force (e.m.f.), is a function of temperature according to the following general equation:

$$e = a_1 T + a_2 T^2 + a_3 T^3 + ... + a_n T^n \quad (1.4)$$

where e is the generated e.m.f. and T is the absolute temperature of the junction.
For some pairs of the materials, the terms in the above equation, which involve higher powers of T (a_2T^2, a_3T^3, etc.), are approximately zero and the e.m.f. – temperature relationship is approximately linear.

Thermocouples can be constructed from a variety of the base metals, such as copper and iron, the base-metal alloys of alumel (Ni/Mn/Al/Si), chromel (Ni/Cr), constantan (Cu/Ni), nicrosil (Ni/Cr/Si) and nisil (Ni/Si/Mn), the noble metals platinum and tungsten, and the noble-metal alloys of Pt/Rh and W/Re. Each standard combination of these materials used in thermocouple production is assigned an internationally recognized type letter (E, J, K, N, T, etc.).

1.1.2.3 Other methods of temperature measurement

IR imaging (thermography) is a popular method of non-contact temperature measurement. The temperature profile along a heated cylindrical microelectrode has been estimated using IR photography.[19] However, the absolute values of the temperature of the electrode and the aqueous solution around it can not be determined directly, because water absorbs in the IR region of the spectrum.

One can envision the applicability of temperature measurements utilizing color indicators or involving the change of state of materials.[18] Color indicators consisting of special paints or crayons could be applied to the surfaces of interest (glass, for example). Once a heated microelectrode is positioned close to such a surface, a chemical reaction should occur in the paint or crayon and a permanent color change should form. Similarly, a very thin film (several microns) of a temperature sensitive material such as paraffin wax could be deposited on a surface (glass slide). When a hot microelectrode is brought near such a surface, the melting of the film could be observed, which indicates that the temperature in solution has reached (or exceeded) the melting temperature of the paraffin. One of the disadvantages of these approaches is that, depending on the electrode size, the color change (or the change of the state of a temperature sensing material) might not be easily detected, even under the microscope. Another disadvantage is that changes in these materials take time to develop, so these methods can not be used

to monitor instantaneous temperature changes. It should also be realized that the precision of the temperature determination by these methods is rather low (the temperature of the solution near the surface can actually be higher than the temperature at which the changes in the material occur). However, these approaches can still be useful in some cases and can be considered semi-quantitative methods of temperature measurement.

1.1.3 Temperature distribution at heated electrodes

Unlike the case where the whole solution is heated, temperature gradients exist when dealing with microelectrodes heated *in situ*. The method of electrode heating (direct or indirect), as well as the geometry of the electrode (cylindrical, disk, etc.) affect the way the heat is produced and distributed in each of the systems. However, it should be realized that in any of these cases, the temperature of the solution near a hot microelectrode will be higher than in the bulk solution. This introduces a major difficulty in the study of hot electrodes: even though the temperature of the solution at the electrode surface can be evaluated, the distribution of temperature further away from electrode can not be measured experimentally.

Beckmann *et al.* have applied digital simulation in order to calculate the temperature distribution in solution around a heated cylindrical microelectrode.[20] Simulations of the hot wire electrochemical cell were done using the fluid dynamics program FIDAP. For the purposes of the simulation, the microwire (25 μm in diameter) was assumed to lie horizontally in the centre of a 4-mm wide vertical channel. The simulated chemical system contained 1 mM $Ru(NH_3)_6Cl_3$ in aqueous solution. The temperature dependent values of the viscosity, density, specific heat and thermal conductivity of water were inputted to the FIDAP program as data tables taken from the literature. The diffusion coefficient for $Ru(NH_3)_6^{3+}$ was determined from fast scan cyclic voltammetric experiments and, similarly, entered as a data table. The results of the simulations indicate that the temperature profile expands much further into the solution than any concentration profile that could be generated by the electrode process. This means that the electrode reaction and mass transport processes occur at a nearly uniform temperature.

Heat dissipation, convection and thermal gradients in a microwave activated electrochemical system were also modeled by Marken *et al*. using FIDAP finite element simulation.[21] The model consisted of a glass rod (0.1 cm length, 0.1 cm radius), which had a 100 μm in diameter platinum wire at its centre. A flat face of this rod was in contact with a cylindrical volume of solution (0.1 cm radius and 0.15 cm length). The thermal conductivity of the glass, water and platinum, as well as the density and viscosity data for the aqueous 0.1 M KCl solution were used as input parameters. To include convective flow, volume expansion data for water were entered and the boundary conditions of zero velocity gradient (for the lower and circumferential surfaces of solution volume), zero velocity (on the glass and platinum surfaces) and zero radial velocity (on the axis) were applied. The results of the simulations indicate that the thermal effect is most pronounced close to the electrode surface, where the current density is high (microwave focusing). However, due to the high heat conductivity of Pt compared to water, a thermal gradient adjacent to the electrode surface is formed. This leads to the development of a so-called 'hot spot' – a zone of solution at some distance from the electrode – where the values of solution temperature are much higher than those at the surface of the electrode.

The distribution of temperature around a hot spherical microelectrode under steady-state conditions has been investigated by Baranski.[7] The heat is produced in a zone of solution near the electrode and heat transfer is considered from that zone into the bulk of the solution. The equation obtained for the temperature as a function of the distance from the centre of the electrode sphere is relatively simple:

$$T(r) = T_b + \frac{\rho(T) I^2}{32 k \pi^2 r r_0}\left(2 - \frac{r_0}{r}\right) \qquad (1.5)$$

where $T(r)$ is the solution temperature at distance r, T_b is the temperature of the bulk solution, $\rho(T)$ is the specific solution resistance at a given temperature, k is the thermal conductivity coefficient of the solution, I is the heating current, and r_0 is the radius of the electrode.

The thermal conductivity coefficient in the above equation depends somewhat on temperature; however, this dependence was not accounted for. The temperature

dependence of the specific solution resistance can be reasonably well approximated using an Arrhenius-type equation:

$$\rho(T) = \rho_{298} \exp\left[-A\left(\frac{1}{298K} - \frac{1}{T} \right) \right] \tag{1.6}$$

where ρ_{298} is the specific resistance of the solution at 298 K and A is the constant, which can be estimated as 1876 K^{-1} based on the temperature dependence of the viscosity of water.

Replacing the heating current I with the excitation voltage ΔV and the solution resistance, equation 1.5 can be rewritten as:

$$T(r) = T_b + \frac{\Delta V^2}{2\rho k}\left(\frac{r_0}{r} \right)\left(2 - \frac{r_0}{r} \right) \tag{1.7}$$

According to this equation, the solution temperature is highest at the surface of the electrode ($r = r_0$) and decreases farther into the bulk of solution.

1.2 PHENOMENA DUE TO PRESENCE OF TEMPERATURE AND POTENTIAL GRADIENTS IN SOLUTION

In general in electrochemical experiments, the faradaic current, measured as a function of applied potential, is determined by the rates of processes such as:

A. mass transfer of the reactant of the electrochemical reaction to the electrode surface,
B. electron transfer occurring at the electrode surface,
C. chemical reactions that might precede or follow the electron transfer, and
D. other surface reactions, such as adsorption, desorption, or electrodeposition.[17]

Therefore, if the mass transfer is the rate limiting step of the overall electrode process, the current will be determined by the rate of transfer of the redox species to the electrode. This leads to a very important equation describing the mass transfer, the Nernst-Planck equation. For an isothermal system, this equation (given here for one-dimensional mass transfer along the x-axis) is as follows:

$$J_i(x) = -D_i \frac{\partial C_i(x)}{\partial x} - \frac{z_i F}{RT} D_i C_i \frac{\partial \varphi(x)}{\partial x} + C_i \upsilon(x) \tag{1.8}$$

where $J_i(x)$ is the flux of species i (mol s^{-1} cm^{-2}) at distance x from the electrode surface, D_i is the diffusion coefficient (cm^2 s^{-1}), $\partial C_i(x)/\partial x$ is the concentration gradient at distance x, $\partial\varphi(x)/\partial x$ is the potential gradient due to ionic migration, z_i and C_i are the charge and concentration (mol cm^{-3}) of species i, respectively, and $\upsilon(x)$ is the velocity (cm s^{-1}) with which a volume element in solution moves along the axis. The three terms on the right-hand side of the equation represent the contributions of diffusion, migration and convection, respectively.

In classical electrochemical experiments, which are done at constant temperature, the effect of ion migration on mass transfer is minimized by use of a large excess of supporting electrolyte (usually, 100 times the concentration of the redox species). In addition, the effect of natural convection, caused by density gradients, is minimal in quiescent solutions. Therefore, the flux of redox species is largely determined by diffusion.

The situation changes dramatically when a temperature gradient is created in solution due to the use of heated electrodes. An increase in solution temperature not only leads to an increase in the diffusion coefficient of the species, but also to the appearance of a new mode of mass transfer: nonisothermal or Soret diffusion, also known simply as thermodiffusion. For this reason, in the next Section (Section 1.2.1) the theory of Soret diffusion will be provided.

While doing research with microelectrodes heated by a high frequency ac waveform, it was realized that some other very important effects are present, due to both the strong ac electric potential and temperature gradients in solution around the hot electrode. These are dielectrophoresis and electrothermal fluid flow, which belong to a large group of electrokinetic phenomena. Therefore, in the following several Sections of this Chapter, the theoretical background to these effects will also be provided.

1.2.1 Nonisothermal diffusion (thermodiffusion, Soret diffusion)

1.2.1.1 Early studies

The presence of temperature gradients in solution leads to the redistribution of neutral molecules or ions of dissolved species resulting in the appearance of concentration

gradients. This phenomenon was first discovered by C. Ludwig in 1856 and later rediscovered by C. Soret in 1879.[22,23]

In his experiments, Soret measured the concentration of a salt (NaCl, KCl, LiCl, KNO_3, $NaNO_3$, $Cu(NO_3)_2$, Na_2SO_4, $CuSO_4$, KI, KBr, $K_2Cr_2O_4$) in aqueous solutions contained in straight and U-shaped tubes.[22] One end of the tube was kept at 78 °C, and the other at 15 to 18 °C. By cutting the extremities of the tubes and collecting the solution in three parts (the lower, the middle and the upper parts), he demonstrated that the salt concentrated at the colder end of the tube. Some of his findings were that the difference in concentration of the salt between the cold and hot ends of the tube increased with time and the initial concentration. The dependence of the concentration difference on time was justified by the fact that a steady state had not been reached at the moment that sampling of the solution occurred. Therefore, to investigate the second point, Soret used only data obtained after 50-56 days for tubes with a length 30 cm. Based on the results of the study of different salts, Soret concluded that for the same initial concentration, the difference of concentration between the cold and hot ends was an increasing function of the molar mass of the salt. Soret also realized the role of the convection (he stopped using U-shaped tubes due to the irregular temperature distribution in them), the necessity of heating from top and having the temperature gradient aligned with the gravity gradient.

1.2.1.2 Theory of thermodiffusion

Once a temperature gradient is created in solution, an additional term needs to be included in equation 1.8 (discussed previously), so the flux can now be written as

$$J_i(x) = -D_i \frac{\partial C_i(x)}{\partial x} - D_i^T C_i \left(\frac{\partial T}{\partial x} \right) - \frac{z_i F}{RT} D_i C_i \frac{\partial \varphi(x)}{\partial x} + C_i \upsilon(x) \qquad (1.9)$$

The second term in this equation represents the contribution from thermodiffusion. The magnitude of the thermodiffusion term is proportional to the concentration of the diffusing species and the temperature gradient. The negative sign (assuming a positive value of D_i^T) indicates that the flux due to thermodiffusion occurs down the temperature gradient; that is, towards the cold portion of the solution. This agrees well with the findings of Soret. The coefficient of proportionality, D_i^T ($cm^2\ s^{-1}\ K^{-1}$), is called the

thermal diffusion coefficient. Theoretically, it can be positive, negative or zero. Negative values of D_i^T imply that the species *i* diffuses towards the hot zone in the solution.

If for a moment the contributions to the flux from the migration and convection are neglected, then equation 1.9 can be written as

$$J_i(x) = -D_i \frac{\partial C_i(x)}{\partial x} - D_i^T C_i \left(\frac{\partial T}{\partial x} \right) \tag{1.10}$$

For a steady state ($J_i(x) = 0$) this can be rearranged to give:

$$-\frac{1}{C_i}\left(\frac{dC_i}{dT} \right) = \frac{D_i^T}{D_i} \tag{1.11}.$$

The ratio of the thermal diffusion coefficient to the ordinary diffusion coefficient is termed the Soret coefficient (σ) of the species *i*:

$$\sigma_i = \frac{D_i^T}{D_i} = -\frac{\ln(C_2/C_1)}{T_2 - T_1} \tag{1.12}$$

where σ_i has units of K^{-1}; C_2 is the concentration of the species at the temperature T_2 and C_1 – at the temperature T_1.

It should also be mentioned here that when a temperature gradient is created in solution, the concentration expressed in volume units (molarity) changes at the heated portion of solution because of the change in density, even though no transport of matter yet occurred. Therefore, it is preferable that concentration is expressed on the basis of weight units (molality).

The Soret coefficient defined by equation 1.12 may be considered a "pure" coefficient, since the effects of ionic migration and convection have been neglected in the derivation of the equation. However, for solutions of electrolytes, thermodiffusion of ions can result in the formation of a thermoelectric potential gradient.[23] In this case, ionic migration caused by the thermoelectric potential gradient will be present and will affect the flux of ions under consideration. The magnitude of the thermoelectric potential may be difficult to determine in the case of complex electrolyte solutions. However, it should be proportional to the temperature gradient. As a result, the contribution from the thermoelectric migration to the flux of ion *i* can be considered together with the "pure"

Soret effect using a complex thermal diffusion coefficient D_i'. This coefficient accounts for contributions from both thermal diffusion and thermoelectric migration. Provided that the effect of convection on flux is negligible, equations 1.10 – 1.12 still hold and they can be used in the determination of Soret coefficients.

1.2.1.3 Methods of determination of Soret coefficients

Here, a brief overview of the major methods available for the determination of Soret coefficients is given. Once again, it should be realized that in order to study thermodiffusion experimentally, convective mixing needs to be eliminated or minimized. This is because the concentration changes due to thermodiffusion can easily be masked by remixing processes due to convection and mechanical vibrations. As a result, the use of specially designed experimental cells is required. In such cells the only two important processes that need to take place are the heat conduction and the de-mixing of the solution. Therefore, in most of the cells reported in the literature, the studied solution is enclosed between two planar horizontal surfaces maintained at two different temperatures (the upper one being the hotter). The distance between the two horizontal surfaces must be constant, and the vertical walls need to be disposed in such a way that they disturb the stability of the solution layer as little as possible. It must be recognized that the presence of temperature differences between the walls and the liquid in contact with them is inevitable due to heat losses and the difference in the thermal properties of the two media. Consequently, local convection currents are likely to be established near them.

To monitor the change in concentration of the components of a solution, an analytical method needs to be employed which will not disturb the transport processes taking place in the system. For non-electrolyte solutions and sufficiently concentrated electrolyte solutions an optical method is convenient; for diluted electrolyte solutions a conductimetric method is generally appropriate.

1.2.1.3.1 Optical method

This method, originally developed by Tanner,[24] relies on the measurement of the refractive index gradient across the volume of the cell. In the proposed setup, light from a lamp is focused by means of a condensing lens and supplied to the collimator of a

spectroscope permanently fixed in a horizontal position. In this way parallel light is obtained, which is then passed through a slit to the cell. From the cell the light is received by a fixed focus camera, with which images can be taken. The solution in the cell is bounded from the top and bottom by the silver-plated surfaces of two hollow copper blocks and on the sides by four glass strips. The glass strips in the pass of the light beam are optically plane. The copper blocks are kept at constant temperature by the circulation of water from two electrically heated thermostats.

In an isothermal cell, the image due to the light from the slit is, initially, a horizontal line. Once the temperature gradient is applied to a cell filled with pure liquid (a one-component system), a displaced line image can be seen as soon as a steady-state temperature gradient is established. The line is not in general horizontal, because the temperature coefficient of the refractive index for the liquid in the cell usually varies slightly with temperature. When a mixture of components is present in the cell, the initial displacement may be followed by another, rapid at the ends of the image but much slower in the centre. Eventually, once the steady-state concentration gradient is established, an approximately linear image is reobtained. The displacement of a particular point on the image from its original position is related to the refractive index gradient dn/dz according to the equation:

$$Z = lf \frac{dn}{dz} \tag{1.13}$$

where Z is the measured displacement of a point, l is the length of the light path in the cell, f is the focal length of the lens, and z is the height of the plane above the base of the cell.

In order to calculate the concentration gradient in the steady state, one needs to measure the displacement of the centre of the steady state image from the centre of the image present a few minutes after the temperature gradient has been established in solution. This is done to separate the effect of the temperature gradient on the refractive index from the effect of the concentration gradient which results from diffusion. In the cell used in experiments, the establishment of the temperature gradient is practically complete in five minutes. Therefore, only the change in refractive index after the five minute interval is used in calculations. The concentration gradient can be determined

using the following equation identical to equation 1.13, except that differentials are substituted with finite differences:

$$\Delta n = \frac{h}{lf} Z_0 \qquad (1.14)$$

where h is the vertical height of the cell and Z_0 is the limiting diffusion displacement obtained by extrapolation of the displacement Z of the curve to time $t = \infty$.

The expression h/lf can be obtained by a calibration experiment with pure water. In this case, the change in the refractive index of water (Δn) is calculated using the temperature coefficient of water (at the mean temperature) and the temperature difference between the plates. In order to convert Δn to ΔC (concentration change), a value of the rate of change of the refractive index with the concentration of solute, dn/dC, is required for the particular concentration of the solution. This rate of change varies somewhat with temperature, however, the value for the mean temperature of the cell can be used without introducing much error. The relation between refractive index and concentration of the solution can be taken as follows:

$$n = n_0 + \beta C + \gamma C^2 \qquad (1.15)$$

where n_0 is the refractive index of the solvent (water) and the coefficients β and γ can be calculated by measuring the refractive index of two solutions of known concentration. Hence dn/dC, which is equal to $\beta + 2\gamma C$, can be determined for any value of the concentration C. As a result, the change in concentration of the solute due to formation of the temperature gradient can be calculated and used to obtain the Soret coefficient.

The disadvantage of the optical method is that the image produced is not sharp if the diagonal slit is narrow. It is also difficult to identify accurately a point on the image with a particular plane in the cell.

1.2.1.3.2 Conductimetric method

The optical method is not satisfactory for the study of the Soret diffusion in dilute solutions. However, in case of electrolytes, the use of conductimetric measurements is well justified, since electrical conductivity is directly proportional to the concentration of the solution.

One setup that can be used for conductimetric measurements of Soret coefficients is proposed by Agar and Turner.[25] There, two of the bounding surfaces (top and bottom) are used as conductivity electrodes. The third electrode is placed in the cavity connecting with the centre of the cell through a small hole. As a result, concentration changes can be followed by measuring the ratio of conductivities between the upper and middle electrodes, and the middle and lower electrodes. Soret coefficients can be evaluated quite easily based on the initial rate of change of the conductivity ratio with time, or from the difference between the initial and final conductivity ratios. Coefficients obtained from the initial rate of change of the conductivity ratio are considered to be more reliable because in the latter case convective remixing is taking place.

A similar setup has been used by Snowdon and Turner in their conductimetric experiments.[26] The cell is incorporated in an audio-frequency bridge so that the upper and lower portions of the solution form two arms of the network. The potential of the "centre-tap" is compared with that of an adjustable tapping of a transformer bridge using a tuned amplifier and oscilloscope. The transformer bridge is very convenient to use, because it is considerably less sensitive to stray capacitances than the bridge network described by Agar and Turner.[25]

The bridge reading falls with time – initially, in a straight line, but later exponentially, tending to a steady-state value. It has been shown previously[25] that the function Y_t, given by equation 1.16, varies with time according to the expression defined by equation 1.17:

$$Y_t = \frac{R_{lh} - R_{uh}}{R_{lh} + R_{uh}} \tag{1.16}$$

where R_{lh} is the resistance of the lower half of the cell and R_{uh} is the resistance of the upper half of the cell.

$$Y_t - Y_0 = \frac{8 b_{01} \sigma \Delta T}{\pi^3} F \tag{1.17}$$

In this equation 1.17 Y_0 is the value of Y for the uniform solution with a temperature difference ΔT applied across it, σ is the Soret coefficient and m is the molality of the solution.

The parameter b_{01} is given by the following expression:

$$b_{01} = -\left[1 + \left(\partial \ln \Lambda / \partial \ln C\right)_T\right] \tag{1.18}$$

where Λ is the equivalent conductivity at concentration C.

The function F is defined by the equation:

$$F = \frac{\pi^3}{32} - \sum_{n=1}^{\infty} \frac{1}{n^3} \sin \frac{n\pi}{2} \exp\left(-\frac{n^2 t}{\theta}\right) \tag{1.19}$$

where θ is the characteristic time and t is the time from the beginning of the experiment.

Characteristic time θ in equation 1.19 is given by:

$$\theta = \frac{a^2}{\pi^2 D} \tag{1.20}$$

where a is the height of the cell and D is the diffusion coefficient at the mean temperature.

Therefore, if Y_t (equation 1.17) is plotted against F, then the Soret coefficient σ can be obtained from the slope of this graph.

1.2.1.3.3 Methods based on separation of cold and hot parts of solution

These methods of determination of Soret coefficients do not require complex experimental setups or sophisticated methods of analysis of the solution composition. The change in the concentration due to thermodiffusion can be evaluated by means of the percentage-density data for the solutions under study.

Riehl was the first to propose a simple apparatus where hot and cold parts of solution were separated by a cellophane membrane (10 – 40 μm thick).[27] It was assumed that thermodiffusion occurred within the pores of the membrane with a steady-state concentration gradient being established very rapidly. Concentration changes then occurred in the reservoirs by a combination of diffusion and convective stirring.

A cell very similar to this has also been described by Morin *et al*.[28] Some possible errors of such setups are loss of solvent due to evaporation and, in certain cases, a transfer of solvent across the membrane by thermo-osmosis. The magnitude of the latter effect depends on the membrane material and the mean temperature: thus, it can be eliminated by suitable choice of these variables.

A more serious problem is the measurement of the effective temperature difference (ΔT_{eff}) across the membrane, since it is less than the temperature difference measured between the body of solutions in the two compartments (ΔT). The ratio ΔT_{eff} / ΔT depends on the thickness of the membrane and the rate of stirring of the solutions. As a result, the accuracy of the determination of Soret coefficients is impaired. In addition, the measured Soret coefficients in 0.1 M solutions of simple chlorides and sulfates decreased as the pore size of the membrane increased. These difficulties are largely overcome if sintered glass disks are used instead of organic membranes.[29]

If the studied systems have very low diffusion constants, then the time required to establish the steady state becomes very large. To overcome this difficulty, Thomaes developed a cell where the hot and cold plates are separated by a distance of only 0.1 mm.[30]

1.2.2 Electrokinetics

Electrokinetics studies the movement of a liquid or particles under the action of an electric field (dc or ac). Electrokinetic phenomena include electroosmosis, electrothermal fluid flow, dielectrophoresis, electrophoresis and electrowetting.[31,32] In this work, the first three phenomena are of particular importance, since they determine the solution flow (and, therefore, the convection) at ac heated electrodes. The theoretical background of these effects will be discussed in the next several Sections.

1.2.2.1 Electroosmosis

Electroosmosis can be defined as the flow of electrolyte solution relative to a stationary charged surface (e.g. microchannel or electrode). It can be classified in two groups: classic (dc) electroosmosis and field-induced electroosmosis (usually ac).[31] In both instances, the central point is the formation of the electrical double layer. However, in classic electroosmosis, double layer formation occurs due to the permanent charge resulting from surface functional groups. This is in contrast to field-induced electroosmosis, where the surface charge is primarily induced by the applied external electric field. This case is particularly important to electrochemists, since the charge-inducing surface is the electrode itself. Before more information is provided on this topic, the behavior of ions and dipoles in alternating electric fields and the structure of

the double layer will be considered. This knowledge is required for a better understanding of the phenomena of ac electroosmosis and the electrothermal fluid flow.

1.2.2.1.1 Behaviour of ions and dipoles in electric fields

The application of an electric field E to an electrolyte solution results in a flow of current.[17,32] The current can be carried by different types of ions, each of them having different ion mobility. The current density, J, for each type of ions i is given by the following expression (Ohm's law):

$$\bar{J}_i = \sigma_i \bar{E} \tag{1.21}$$

where σ_i is the electrical conductivity of the ionic species *i*.

The total current density is the sum of the contributions from each individual type of ions, and the overall electrical conductivity of an electrolyte solution can then be expressed as:

$$\sigma = \sum_i \lambda_i C_i \tag{1.22}$$

where C_i is the concentration of ions of type i and λ_i is the ionic conductivity (S m^2 mol^{-1}).

The ionic conductivity is defined by the following equation:

$$\lambda_i = z_i F u_i \tag{1.23}$$

where z_i is the valence of ion i and u_i is the mobility (m^2 V^{-1} s^{-1}), and F is the Faraday constant.

The mobility of ions characterizes their motion in solution; it is related to the diffusion coefficient D_i according to the equation:

$$u_i = D_i \frac{q}{k_B T} = D_i \frac{F}{RT} \tag{1.24}$$

where q is the charge of the ions, k_B is the Boltzmann constant and R is the gas constant.

For a symmetrical electrolyte (an electrolyte for which the absolute value of z_i is equal for all ions), such as potassium chloride, the conductivity (equation 1.25) is given by:

$$\sigma = (\lambda_+ + \lambda_-)C = \Lambda C \qquad (1.25)$$

where Λ is the molar conductivity (S m^2 mol^{-1}), λ_+ and λ_- are the ionic conductivities of the cations and anions, respectively.

This equation shows clearly that the conductivity of an electrolyte solution is proportional to the concentration of ions in it. The molar conductivity Λ is constant for concentrations up to approximately 10^{-3} M. At concentrations higher than this, the ions start to interact with each other, and molar conductivity is influenced by higher order effects.

At the molecular level, when ions are placed in a solvent, they generally interact with the solvent molecules. This process is called solvation or, if the solvent is water, hydration. The nature of this phenomenon can be explained by the fact that water molecules have a permanent dipole moment and are highly polarizable. Therefore, those molecules of water which are in the immediate vicinity of an ion are polarized by its local electrical field. The result of this is the formation of a hydration atmosphere: that is, a region of oriented water dipoles which screen the ion from other ions in the solution. The local electrical potential falls off exponentially with the distance from the ion. The length scale of this decay is given by the Debye length (usually written as κ^{-1}), which is the distance at which the potential decreases to 1/*e* of its maximum value. For a monovalent ion, the Debye length is given by the equation:

$$\kappa^{-1} = \left(\frac{q^2 n_0}{\varepsilon k_B T} \right)^{-\frac{1}{2}} \equiv \left(D \frac{\varepsilon}{\sigma} \right)^{\frac{1}{2}} \qquad (1.26)$$

where ε is the dielectric permittivity of the medium and n_0 is the number density of ions in the bulk solution (m^{-3}) and other terms have their usual meanings.

The polarization of water molecules leads to the formation of a region around an ion that has very different properties from the bulk liquid. First of all, this applies to dielectric permittivity: the polarized molecules are prevented from responding to an

applied electrical field, therefore, the local permittivity is reduced. This decrease has been found to vary linearly with the concentration of ions:

$$\varepsilon = \varepsilon_s + \delta C \tag{1.27}$$

where ε_s is the static dielectric permittivity of water, C is the molar concentration of ions and δ is the dielectric decrement. The dielectric decrement is a coefficient that determines the magnitude of the decrease in permittivity in an electrolyte solution compared to a pure solvent.

The second effect of polarization is that water molecules become structured around the ions. As a result, when an ion moves, its "atmosphere" moves along with it, making the structure bigger than the ion itself. The radius of such a hydrated ion is called the hydration radius and it is used in calculations of the viscous drag force and the diffusion coefficient of ions.

Another important characteristic of an electrolyte is the charge relaxation time. This is the time that it takes for an ion to move a distance on the order of the Debye length, κ^{-1}. From equation 1.26, the charge relaxation time can be determined as:

$$\tau_q = \frac{1}{D\kappa^2} = \frac{\varepsilon}{\sigma} \tag{1.28}$$

The inverse of this time is the charge relaxation frequency. Both of these parameters are important in understanding the effect of frequency of the electric field on the electrothermal flow of solution (Chapter 1.2.2.2).

The strength of the applied electric field can affect the structure of the hydrated ions and also lead to an increase in conductivity of the electrolyte solution. These are so-called non-linear effects, which are observed either for high-strength or high-frequency electric fields (known as the Wien effect and the Debye-Falkenhagen effect, respectively).

The Wien effect is observed at very high values of the electric field, when the ions in the electrolyte move so fast that there is not enough time for the ionic atmosphere to restore itself around them. This condition is observed when the ion velocity is larger than $1/\kappa\tau_q$. As a result, the conductivity of the electrolyte increases considerably. The

value of the electric field at which this effect is observed depends on the concentration of the ions in solution. This is about 10^7 V m^{-1} for a 0.01 M electrolyte solution and increases for more concentrated solutions.

The Debye-Falkenhagen effect is observed when the frequency of the applied field is very high. In this case, the ionic cloud cannot polarize in response to the change in the direction of ion movement. For this effect to be observed, the frequency of the applied electric field must be larger than the charge relaxation frequency of the electrolyte.

1.2.2.1.2 Electrical Double Layer

The current understanding of double layer structure can be described in terms of the Gouy-Chapman-Stern model.[17,32] According to this model, a charged surface (such as a polarized metal electrode) in contact with an electrolyte solution will attract ions of the opposite polarity (counterions) and repel ions with like charge (co-ions). As a result, an electrical double layer is formed. This electrical double layer, considered in a greater detail, can be viewed as being comprised of several layers (Figure 1.2).

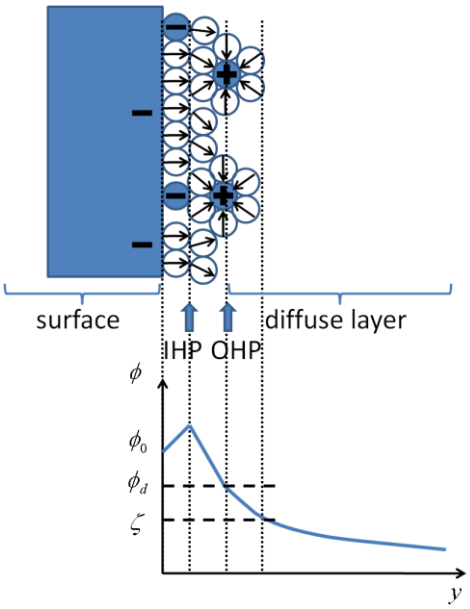

Figure 1.2 Schematic diagram of the electrical double layer (*top*). Also shown (*bottom*) is the variation in electrostatic potential with distance y from the surface, highlighting the diffuse layer potential ϕ_d and the zeta potential ζ, which is the potential at the hydrodynamic slip plane (more details in the text). ϕ_0 is the surface potential. The circles with arrows inside represent water dipoles (the arrow indicates the direction of the dipole moment), while circles with positive or negative signs represent cations or anions, respectively (adapted from Reference 32).

In solution, the double layer consists of a compact and a diffuse layer. The compact layer includes solvent molecules and specifically adsorbed non-solvated ions or molecules, and is bounded by the inner Helmholtz plane (IHP). The nearest solvated ions are bounded by the outer Helmholtz plane (OHP). The diffuse layer extends from the OHP into the bulk of the solution and includes all nonspecifically adsorbed solvated ions required to maintain the overall electrical neutrality of the double layer, according to the equation 1.29.

$$q^S = q^i + q^d = -q^M \tag{1.29}$$

In this equation, q^S is the total charge density (μC cm^{-2}) of the solution portion of the double layer, q^i is the charge density due to specifically adsorbed ions, q^d is the charge density in the diffuse layer and q^M is the total charge density on the metal electrode.

The thickness of the diffuse layer (at constant temperature) depends on the total ionic concentration of the electrolyte solutions: for concentrated solutions (>10^{-2} *M*) it is less than ~ 100 Å.

The structure of the double layer described above indicates that the system of an electrode in an electrolyte solution can be considered to be a capacitor with a nonuniform charge density: when a constant potential is applied to the electrode, the charge distribution will change in a way analogous to the charging of a capacitor. As a result of this, most of the applied potential drops across the double layer, and the potential in the bulk solution may only be a fraction of that applied to the electrode. When an alternating potential is applied to the electrode, the double-layer capacitance can be thought of as a reactance of value $-j/(\omega C)$ (where j is an imaginary unit, ω is the angular frequency and *C* is the double layer capacitance, assuming ideal capacitor behavior) in series with the impedance of the suspending medium. Therefore, at low frequencies ($\omega \rightarrow 0$), the value of this reactance will approach infinity and the voltage drop across the solution will be negligible. These considerations lead to the following electrical circuit diagram describing the behavior of an electrode-electrolyte system in the absence of any electrode reactions (Figure 1.3).

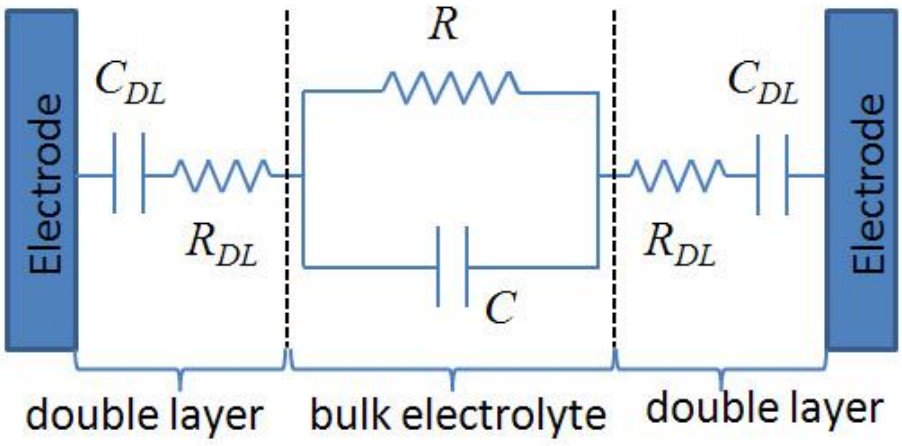

Figure 1.3 Approximate circuit diagram for a system consisting of two metal electrodes immersed in an electrolyte solution. *R* is the solution resistance and *C* is the solution capacitance. The model assumes that no electrochemical reactions occur at the electrodes (adapted from Reference 32).

According to this circuit, in the high frequency limit (no double layer effect) the total capacitance will tend to a constant value proportional to the permittivity of the bulk electrolyte and the total resistance will be inversely proportional to the conductivity of the solution. At low frequencies, both the capacitance and resistance will be affected by the double layer. In general, the double layer impedance is represented by the impedance of the constant phase element (CPE) written in the form:

$$Z_{DL} = \frac{A}{(j\omega)^{\beta}} = \frac{A}{\omega^{\beta}}\left[\cos\left(\frac{\pi}{2}\beta\right) - j\sin\left(\frac{\pi}{2}\beta\right)\right] \qquad (1.30)$$

Here, A and β are constants. β is equal to 1 for an ideal capacitor and 0 for a perfect resistor. For solid electrodes β is typically between 0.7 and 0.9.

1.2.2.1.3 Theory of electroosmosis

Electroosmosis occurs when an electric field is applied tangential to a surface immersed in an electrolyte solution. Consequently, the charges in the double layer experience a force and move, pulling the fluid along. The velocity of the electroosmotic flow is zero at the surface and increases to its maximum value at the slip plane (see Figure 1.2).

The numerical value of the velocity (u_x) of the electroosmotic flow in an infinitely wide planar channel can be determined from the balance of the Coulomb force acting on

the liquid and the frictional force opposing the flow. As a result, the following equation is obtained:[32]

$$u_x = \frac{E_x q}{\kappa \eta} \tag{1.31}$$

where E_x is the electric field strength in the *x*-direction (parallel to the surface), q is the charge density in the diffuse part of the EDL and η is the fluid viscosity.

As can be seen in this equation, the flow velocity is directly proportional to the electric field strength and the charge density. One should also realize that the fluid displacement will be non-zero only in a dc field: for an ac field and the geometry considered, the fluid will move in an oscillatory matter.

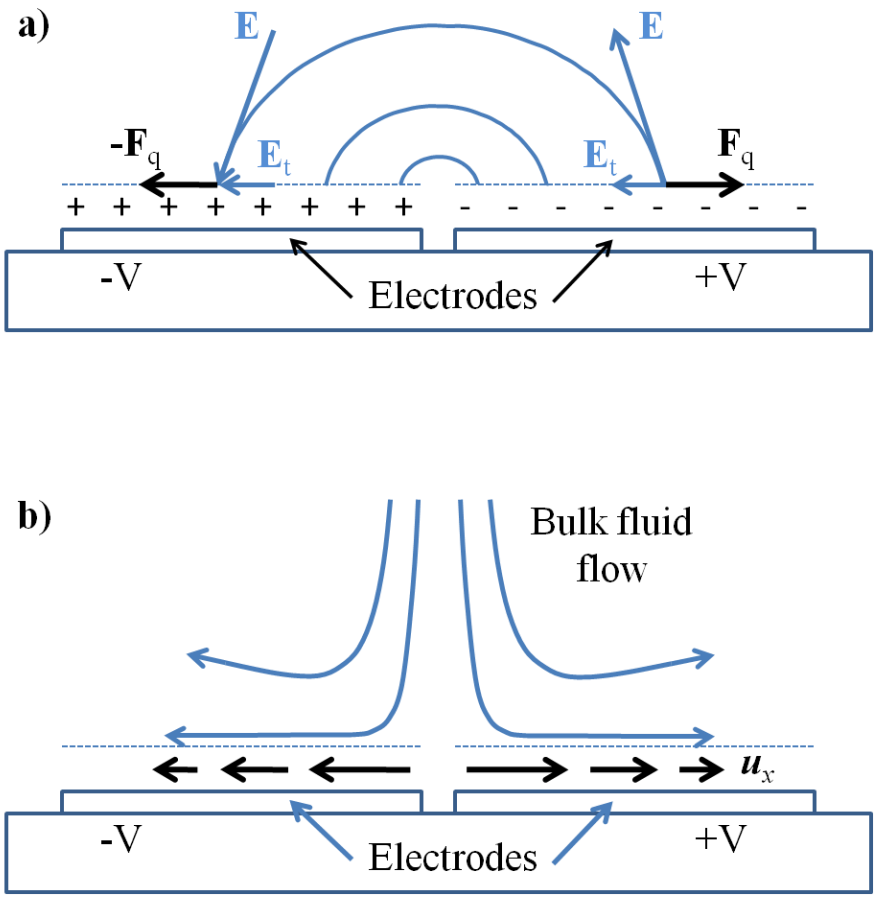

Figure 1.4 **a)** A diagram outlining the mechanism of ac electroosmosis. **b)** As a result of the interaction of the tangential field E_t with the charge in the double layer, a surface fluid flow appears (velocity u_x), which leads to the bulk flow of electrolyte solution (adapted from Reference 32).

A number of experiments have shown that a non-zero time-averaged flow of electrolyte solution can be observed at ac polarized microelectrodes. This can be explained by the nonuniformity of the electric field at the microelectrode surface. For clarification, let us consider two planar electrodes positioned close to each other (Figure 1.4). These electrodes are polarized by voltages $\pm V$, so that the electric field E exists between them. As a result, the force F (due to the tangential components E_t of the electric field) acts on an induced charge in the double layer, which leads to the flow of the solution.

Figure 1.4a shows the system for one half-cycle of the ac perturbation. During the other half-cycle, the signs of the applied potentials, induced charges and the direction of the tangential field are opposite. Therefore, the direction of the force vector remains the same and a steady-state flow of the solution occurs.

From equation 1.31, it is known that the flow velocity depends on the magnitude of the tangential component of the electric field and the charge. The charge in the diffuse double layer can be represented as the sum of a constant term and a time-dependent excess charge, which varies with the field. Consequently, one can expect that the magnitude of the electroosmotic flow will also depend on the frequency of the ac perturbation. At low frequencies, the potential drop across the suspending medium (and therefore E_t) is zero and no flow of solution occurs. At high frequencies, the potential across the double layer and the induced charge are both zero and, again, there is no electroosmosis. For this reason, ac electroosmotic flow is observed only at frequencies between 10 and 100 kHz. Since the magnitude of the tangential electric field is larger closer to the edges of the polarized microelectrodes, the flow velocity will decrease with distance from the electrode edge.

1.2.2.2 Electrothermal fluid flow

As the frequency of the applied ac field increases, the velocity of the electroosmotic flow decreases. However, the flow of solution does not cease, since there is a second type of fluid flow that occurs at all frequencies, but generally has a lower magnitude than ac electroosmosis. This is the electrothermal fluid flow.

The theoretical description of the electrothermal flow is based on a general expression for the electrical force acting on a liquid subjected to the electric field[32,33]:

$$\bar{f}_E = \rho_q \bar{E} - \frac{1}{2}\left|\bar{E}\right|^2 \nabla\varepsilon + \frac{1}{2}\nabla\left(\rho_m \frac{\partial\varepsilon}{\partial\rho_m}\left|\bar{E}\right|^2\right) \tag{1.32}$$

where ρ_q is the volume charge density, ε is the permittivity of the medium, ρ_{m} represents the density of the matter and $\bar{E}$ is the electric field.

The first term in this equation represents the Coulomb force, the second is the dielectric force and the last is the electrostriction pressure. For an incompressible fluid the electrostriction pressure has no effect on the dynamics of the system and therefore can be ignored.

Evaluation of the first two terms in the above equation shows that, for an isothermal fluid, there is no free charge in the system (i.e., the local concentration of cations is equal to the local concentration of anions everywhere in the solution). Therefore, the Coulomb force is equal to zero. In addition, the permittivity gradient is also zero. Thus, there is no force on the dielectric. As a result, the total body force on the fluid under isothermal conditions is zero. These considerations indicate that the electrothermal flow is present only when both electric potential and temperature gradients are present in solution. When this is the case, gradients of permittivity and conductivity result and give rise to an electrical force, causing solution motion.

Equation 1.32 can be rewritten for time-averaged force per unit volume in the following form:

$$\left\langle \bar{f}_E \right\rangle = -\frac{1}{2}\left[\left(\frac{\nabla\sigma}{\sigma} - \frac{\nabla\varepsilon}{\varepsilon}\right)\cdot\bar{E}\,\frac{\varepsilon\bar{E}}{1+(\omega\tau)^2} + \frac{1}{2}\left|\bar{E}\right|^2\nabla\varepsilon\right] \tag{1.33}$$

where $\tau = \varepsilon/\sigma$ is the charge relaxation time. The first term in this equation represents the Coulomb force and the second term represents the force on a dielectric. $\nabla\varepsilon$ and $\nabla\sigma$ are the gradients of permittivity and conductivity, respectively.

If the temperature gradient is known, the force on the liquid can be computed using equation 1.33. Taking into account that $\nabla\sigma = (\partial\sigma/\partial T)\ \nabla T$ and $\nabla\varepsilon = (\partial\varepsilon/\partial T)\ \nabla T$, then

$$\left\langle \bar{f}_E \right\rangle = -\frac{\varepsilon}{2}M(\omega)\nabla T\left(\bar{E}\right)^2 \tag{1.34}$$

where $M(\omega) = \dfrac{\frac{1}{\sigma}\frac{\partial\sigma}{\partial T} - \frac{1}{\varepsilon}\frac{\partial\varepsilon}{\partial T}}{1+(\omega\tau)^2} + \dfrac{1}{2\varepsilon}\dfrac{\partial\varepsilon}{\partial T}$ gives the variation of force as a function of the frequency ω.

Frequency dependence of the electrical force has two distinct limits: at low frequencies the Coulomb force dominates, and at high frequencies the dielectric force dominates. Typically, these forces act in opposite directions: over a certain range of frequencies this results in the change of the flow pattern.

Since the flow direction is determined by the balance of the two forces, one can determine the frequency, at which the magnitude of the Coulomb force is equal to the magnitude of the dielectric force. This frequency is called the cross-over frequency, f_c:

$$f_c \approx \frac{1}{2\pi\tau}\left(2\frac{\left|\frac{\partial\sigma}{\sigma\partial T}\right|}{\left|\frac{\partial\varepsilon}{\varepsilon\partial T}\right|}\right)^{\frac{1}{2}} \qquad (1.35)$$

For aqueous electrolytes, typical values are: $(1/\sigma)\cdot(\partial\sigma/\partial T)$ = +2% per degree and $(1/\varepsilon)\cdot(\partial\varepsilon/\partial T)$ = –0.4 % per degree. Therefore, it can be seen that the value of f_c is on the order of the inverse of the charge relaxation time, τ .

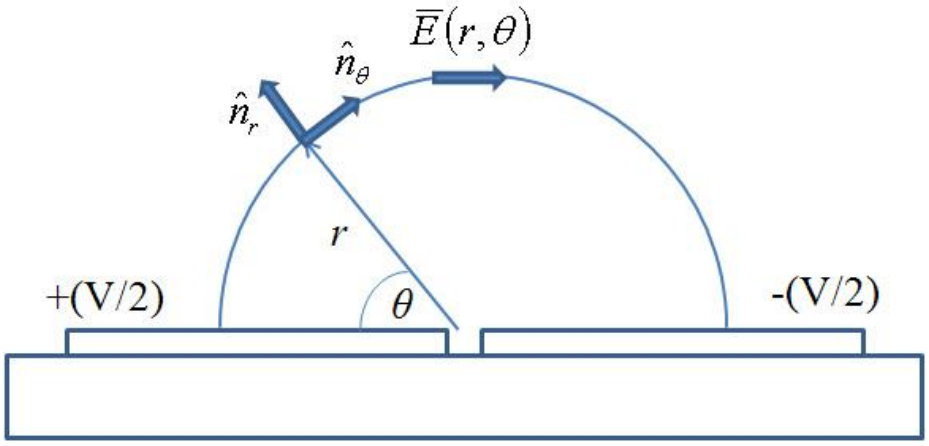

Figure 1.5 Schematic diagram showing the electrode arrangement used as a model in calculations of the electrothermal force on an electrolyte solution (adapted from Reference 33).

Calculations of the electrothermal force have been done by Ramos *et al*. for an electrode system consisting of the two thin parallel metal plates with a very small interelectrode gap mounted on an insulator with an electrolyte solution above the plates (Figure 1.5).[33] In this case, the following expression was obtained for the electrothermal force:

$$\left\langle \bar{f}_E \right\rangle = -M(\omega)\frac{2}{\pi^3 k}\frac{\varepsilon\sigma V^4}{r^3}\left(1-\frac{2\theta}{\pi}\right)\hat{n}_\theta \qquad (1.36)$$

where k is the thermal conductivity of the solution and V is the amplitude of the applied ac waveform.

Equation 1.36 indicates that the electrothermal force has a dependence both on angular frequency and on distance. It increases to a maximum value at the electrode surface, since r tends to zero and θ tends to zero and π. The force also depends on the conductivity of the solution and the applied voltage to the power of four. At frequencies below the charge relaxation time, solution flow is directed down into the inter-electrode gap and out across the electrode. At high frequencies (above the charge relaxation time), the direction of the flow is reversed. This flow pattern agrees well with the effect of the frequency on the electrothermal force discussed previously.

An estimate of the order of magnitude of typical solution flow rate can be made using the following relation:

$$|\bar{u}| \sim |\bar{f}_E| \frac{l^2}{\eta} \qquad (1.37)$$

where l is a distance characteristic of the microelectrode structure (e.g. 10 – 100 μm) and η is the solution viscosity. According to this equation, the flow velocity is on the order of 10 μm s^{-1} for typical electrothermal forces acting in the electrode geometry discussed.

1.2.2.3 Dielectrophoresis

1.2.2.3.1 Theoretical aspects

Dielectrophoresis is defined as the translational motion of neutral matter caused by polarization effects in a nonuniform electric field.[34] The physical origin of

dielectrophoresis is relatively simple. However, it should be realized that although any electric field (whether uniform or nonuniform) exerts a force upon a charged body, only nonuniform electric fields exert a force upon neutral bodies. This becomes clearer if the responses of both charged and neutral particles are considered in uniform and nonuniform electric fields (Figure 1.6).

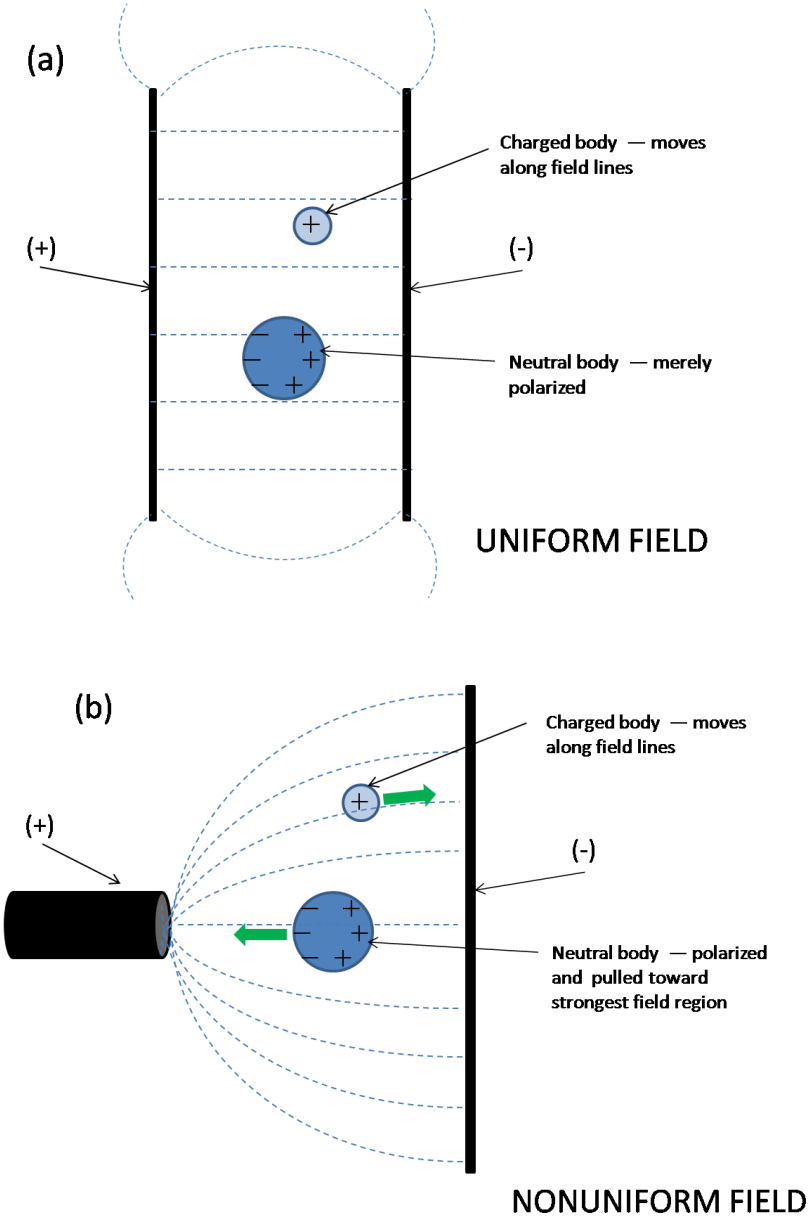

Figure 1.6 Behaviour of neutral and charged bodies in (**a**) a uniform electric field and (**b**) a nonuniform electric field (adapted from Reference 34).

In a uniform electric field, a charged particle is pulled along the field lines towards the electrode with the charge opposite to that of the particle. In the same field, a neutral particle will only be polarized but will not move towards either of the electrodes. This is because the forces acting on each of the sides of the polarized particle are equal. If the particle is elongated or anisotropic in its polarizability, a torque may be produced but not a net translational force.

In a nonuniform field, the behaviour of the charged and neutral particles is different from that in the uniform field. The charged particle behaves essentially the same way as before: it is attracted towards the electrode of the opposite polarity and pulled along the field lines in that direction. The neutral particle will also have a translational force upon it, because the fields operating on the positive and negative regions of the polarized particle are not equal. This gives rise to a net force (termed the dielectrophoretic force) and the particle moves towards the electrode with the stronger electric field. It should also be realized that this dielectrophoretic force exerted on a neutral polarizable body is normally in the same direction, regardless of which electrode is charged positive or negative. Therefore, the applied field could be that due to an alternating potential.

An expression for the dielectrophoretic force can be derived in the following way.[32] Consider the case of an ac electric field with a spatially varying field magnitude and constant phase. The harmonic potential can be represented using tensor notation as:

$$\phi(\bar{x},t)=\mathrm{Re}[\tilde{\phi}(\bar{x})e^{j\omega t}] \tag{1.38}$$

where j is the imaginary unit ($j^2 = -1$), $\bar{x}$ is the position [the tilde indicates the complex phasor ($\phi=\phi_R + j\phi_I$)] and Re[…] indicates the real part of.

The electric field (vector $\bar{E}$) is then given by:

$$\bar{E}(\bar{x},t)=\mathrm{Re}[\tilde{\bar{E}}(\bar{x})e^{j\omega t}] \tag{1.39}$$

where $\tilde{\bar{E}}=-\nabla\tilde{\phi}$ is the corresponding phasor. The field phasor can be assumed to be real since the phase is constant throughout the system (i.e., $\tilde{\bar{E}}=\bar{E}=-\nabla\phi_R$).

The force on an induced dipole in the electric field ($\bar{F}_{DEP}$) can be written as:

$$\bar{F}_{DEP}=(\tilde{p}\cdot\nabla)\bar{E}\,e^{j\omega t} \tag{1.40}$$

where $\tilde{p}$ is the dipole moment phasor and ∇ is the del vector.

The dipole moment of a spherical particle ($\tilde{p}$) is defined as:

$$\tilde{p} = \upsilon \tilde{\alpha} \overline{E} e^{j\omega t} \tag{1.41}$$

where υ is the volume of the sphere and $\tilde{\alpha}$ is a complex effective polarizability.

Therefore, the time-averaged force on the particle can be written as:

$$\left\langle \overline{F}_{DEP} \right\rangle = \frac{1}{2} \upsilon \mathrm{Re}[\tilde{\alpha}] \left(\overline{E} \cdot \nabla\right) \overline{E} \tag{1.42}$$

Using a vector identity for the irrotational field that $\nabla\left(A \cdot B\right) = \left(A \cdot \nabla\right)B + \left(B \cdot \nabla\right)A$, the dielectrophoretic force is given by:

$$\left\langle \overline{F}_{DEP} \right\rangle = \frac{1}{4} \upsilon \mathrm{Re}[\tilde{\alpha}] \nabla \left(\overline{E} \cdot \overline{E}\right) \quad or \quad \left\langle \overline{F}_{DEP} \right\rangle = \frac{1}{4} \upsilon \mathrm{Re}[\tilde{\alpha}] \nabla \left|\overline{E}\right|^2 \tag{1.43}$$

where $\overline{E}$ is the amplitude of the electric field.

If the field is described using root-mean-square (rms) values, the above equation becomes:

$$\left\langle \overline{F}_{DEP} \right\rangle = \frac{1}{2} \upsilon \mathrm{Re}[\tilde{\alpha}] \nabla \left|\overline{E}_{rms}\right|^2 \tag{1.44}$$

This is also the expression for the dielectrophoretic force in a dc field.

Analysis of the above equation reveals that the dielectrophoretic force depends on the volume of the particle, the square of the gradient of the field magnitude and the real part of the effective polarizability. Polarizability is determined by the permittivity and conductivity of both the particle and the suspending medium, as well as the frequency of the electric field. By substituting for the effective polarizability, the full expression for the time-averaged dielectrophoretic force is obtained:

$$\left\langle \overline{F}_{DEP} \right\rangle = \pi \varepsilon_m a^3 \mathrm{Re}\left[\frac{\tilde{\varepsilon}_p - \tilde{\varepsilon}_m}{\tilde{\varepsilon}_p + 2\tilde{\varepsilon}_m}\right] \nabla \left|\overline{E}\right|^2 \tag{1.45}$$

where ε_m is the permittivity of the medium and *a* is the radius of the spherical particle. The term in the square brackets represents the real part of the Clausius-Mossotti factor,

which describes the frequency dependence of the force. Here, $\tilde{\varepsilon}_p$ is the complex permittivity of the particle and $\tilde{\varepsilon}_m$ is the complex permittivity of the medium.

According to the above equation 1.45, positive dielectrophoresis occurs if the polarizability of the particle is greater than the suspending medium: in this case, the particle moves towards the region of high electric field strength. Negative dielectrophoresis occurs if the polarizability of the particle is less than that of the suspending medium. As a result, the particles would move away from the region of high field strength.

1.2.2.3.2 Dielectrophoresis in different field geometries

The term $\nabla\left|\overline{E}\right|^2$, which has been used in the discussed above equations, is the (geometric) gradient of the square of the field intensity. This quantity is otherwise known as the field factor. It signifies the effect that the applied electric field has on the dielectrophoretic force.

The field factor is controlled by the electrode geometry. In an early monograph by Pohl, three typical geometries were considered: spherical, cylindrical and 'isomotive'.[34] However, with advances in micro and nanofabrication, new electrode geometries became available, which could generate very strong electric fields capable of manipulating submicrometer particles with relative ease. In this Chapter, the three most widely used electrode geometries will be discussed (in addition to the typical geometries): namely, polynomial, castellated and interdigitated electrode arrays. Most practical electrode designs can be approximated by considering one of these field geometries. It should also be realized that other than for the simplest electrode geometries, calculation of the electric field distribution is a laborious process. A number of methods, both analytical and numerical, have been proposed in the literature and several commercially available software programs exist for this purpose. However, these will not be discussed in great detail here.

1.2.2.3.2.1 Spherical electrode geometry

An example of an electrode configuration which can be approximated to a spherical geometry is a rounded wire tip extending into a hollow formed by an outer electrode. It can be described mathematically by a spherical capacitor with a central sphere of radius

r_1 and an outer concentric shell of radius r_2. The potential at any point between these spherical shells (with the inner shell at potential ϕ_1 and the outer shell grounded) is given by:

$$\phi_{spher} = \frac{\phi_1 r_1}{r}\left(\frac{r_2 - r}{r_2 - r_1}\right) \tag{1.46}$$

and the filed, $\overline{E}_{spher}$, is given by:

$$\overline{E}_{spher} = -\nabla\phi = \frac{\hat{r}_0 r_1 r_2 \phi_1}{r^2(r_2 - r_1)} \tag{1.47}$$

where $\hat{r}_0$ is the unit radial vector.

In this case, the field factor is expressed by the following formula:

$$\nabla\left|\overline{E}_{spher}\right|^2 = \frac{-\hat{r}_0\left(2r_1^2 r_2^2 \phi_1^2\right)}{r^5(r_2 - r_1)^2} \tag{1.48}$$

1.2.2.3.2.2 Cylindrical electrode geometry

Practical electrode arrangements, which can be approximated by cylindrical symmetry are (a) a central wire held coaxially within an outer cylindrical electrode, (b) a wire-plate combination with two components held parallel to each other, and (c) a wire-wire electrode pair consisting of parallel wires. In the latter two arrangements, the cylindrical symmetry is only roughly approximated, even close to the surface of the wire electrode.

For ideal cylindrical symmetry, with the inner electrode having radius r_1 at potential ϕ_1 concentric to a grounded outer electrode of radius r_2, the potential at some distance r ($r_1 \le r \le r_2$) from the central axis is:

$$\phi_{cyl} = \phi_1\left[\frac{\ln\left(\frac{r}{r_2}\right)}{\ln\left(\frac{r_1}{r_2}\right)}\right] \tag{1.49}$$

The field, $\overline{E}_{cyl}$, is given by:

$$\overline{E}_{cyl} = \frac{-\hat{r}_0 \phi_1}{r \ln\left(\frac{r_1}{r_2}\right)} \tag{1.50}$$

The corresponding field factor can then be represented as follows:

$$\nabla\left|\overline{E}_{cyl}\right|^2 = \frac{-2\hat{r}_0 \phi_1^{\ 2}}{r^3\left[\ln\left(\frac{r_1}{r_2}\right)\right]^2} \tag{1.51}$$

From the equations 1.48 and 1.51 it can be noted that the spherical and cylindrical field geometries are quite inhomogeneous, in the sense that the dielectrophoretic force produced by them varies substantially with position, *r*, in the vicinity of the electrodes. In the case of spherically symmetric electrodes, this force varies inversely with the fifth power of *r*, and with the third power in the cylindrical case. If we consider two particles with the same size and dielectric properties carried by the fluid past an electrode of either spherical or cylindrical geometry, then the dielectrophoretic force on each of the particles would differ considerably, even if their position with respect to the electrodes was only slightly different. This can lead to a decrease in the efficiency of analytical separations of particles that differ somewhat in dielectric properties.

1.2.2.3.2.3 Isomotive geometry

A field that provides a constant or reasonably constant force on a particle, wherever it might be in the field space, is referred to as an 'isomotive' field. The need for isomotive electrodes arises because of the inefficiency of separations by spherical or cylindrical electrodes discussed above – the difference in the force due to the placement of the particles in the field may mask the effect of the dissimilarity of their dielectric properties.

By solving the Laplace equation with the equation for the dielectrophoretic force on a spherical particle (equation 1.44), Pohl developed the following expression that describes surfaces of constant potential in an isomotive field:[34]

$$\phi = \left(\frac{2}{3}\right)\left(\frac{2F_{DEP}}{\upsilon\alpha}\right)^{1/2} r^{3/2} \sin\left(3\theta/2\right) \tag{1.52}$$

where α is the polarizability and υ is the volume of the sphere, F_{DEP} is the constant dielectrophoretic force, and θ accepts only the following values: $\frac{2}{3}\pi \le \theta \le \frac{4}{3}\pi$.

A graph of the lines of constant potential following this relationship (equation 1.52), including a practical design for the isomotive field electrode system, is shown in Figure 1.7.

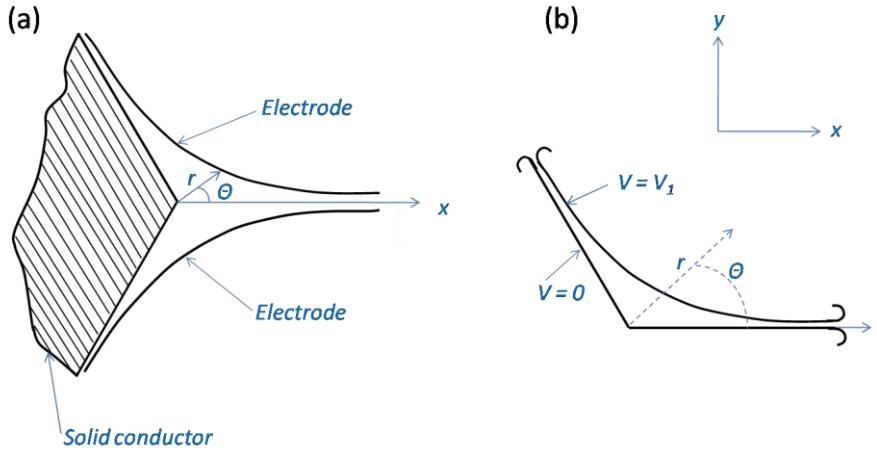

Figure 1.7 Isomotive electrode geometry. (**a**) Lines of constant potential in a field exerting a constant radial force. (**b**) A practical design for an isomotive field electrode system shown as a cut in the xy-plane. The curved electrode is at the ac or dc potential V_1 and the other one is grounded. The smoothed curving of the tips is used to avoid high field gradients (adapted from Reference 34).

1.2.2.3.2.4 Polynomial electrodes

Polynomial electrodes are electrodes, which have the shape of their ends in the form of a circle or hyperbolae.[32,35] The latter group is based on the isomotive electrode design described previously. Usually, polynomial electrodes consist of 2n electrodes; however, the simplest useful case is the four-electrode system referred to as a quadrupole (Figure 1.8). The dimensions of polynomial electrodes are largely determined by the capabilities of the manufacturing process. Typical electrode dimensions for manipulation of sub-micrometer particles are 5 – 10 μm across the centre (distance d in Figure 1.8), with a 2 – 3 μm gap between adjacent electrodes.

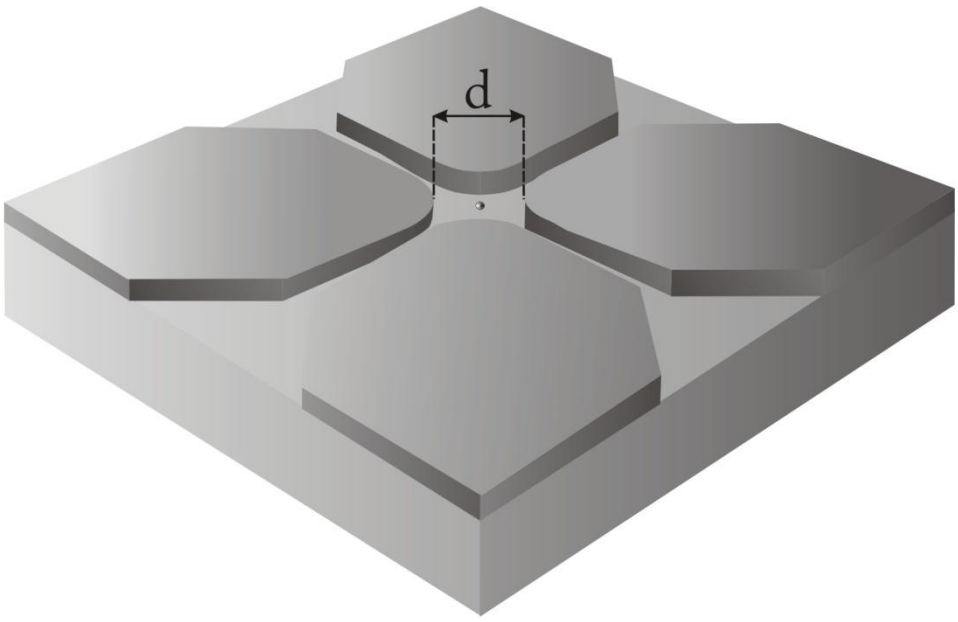

Figure 1.8 Schematic diagram of a polynomial (quadrupole) electrode design (adapted from Reference 35).

Simulation of the electric field indicates that the highest field strength regions are located along the electrode edges, while the region of the lowest field strength is in the centre of the four electrodes. As a result, positive dielectrophoresis leads to the accumulation of particles at the electrode edges. Negative dielectrophoresis of the particles results in them being trapped in the centre of the electrode assembly (indicated by a point in Figure 1.8). If the distance *d* is much larger than the particle size, these electrodes can be used to measure the velocity of particles over the central region for both positive and negative dielectrophoresis.

Calculations of the DEP force show that under positive dielectrophoresis conditions, a particle just above the electrode is pulled towards the edge by a force which increases rapidly in magnitude (by three decades) over a short distance. At heights well above the electrodes there is a vertical force directed downwards everywhere. Negative dielectrophoresis of particles indicates that there is a trap in the centre of the array. However, the trap is not closed, since there is no downward force in the centre apart from gravity. If a second pair of quadrupole electrodes is placed above the first, then the negative DEP becomes closed. This is known as an octopole field cage.

1.2.2.3.2.5 Castellated electrodes

A castellated electrode array consists of square features on parallel wires, as shown in Figure 1.9 below. The arrays are similar to the polynomial electrodes in that the high field regions are located along the electrode edges. However, the electric field has the highest strength at the tips of the castellations. This results in the formation of locally closed low field strength regions in each of the bays.

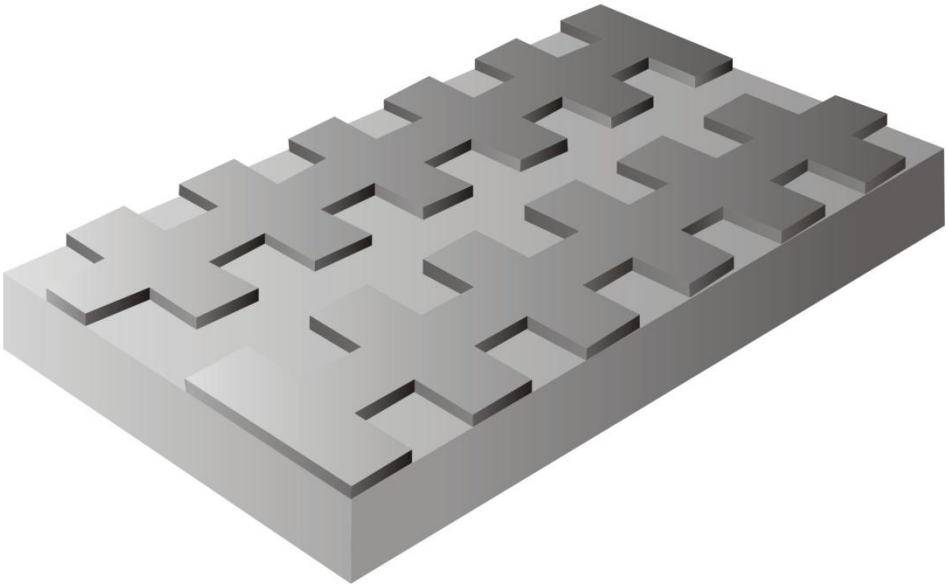

Figure 1.9 A diagram of a castellated electrode design, consisting of square features on parallel wires (adapted from Reference 35).

Far above the electrodes, the DEP force increases exponentially towards the surface. Close to the electrode surface, particles experiencing negative dielectrophoresis are pushed towards the traps in the bays between the castellations. Positive dielectrophoresis leads to the accumulation of particles at electrode edges and especially at the tips of the castellations.

The castellated structure is simple to fabricate over large areas. It has been used in the development of particle separation systems and as an electrode array for investigation of particle characteristics.

1.2.2.3.2.6 Interdigitated finger (or bar) electrode arrays

Interdigitated electrode arrays consist of a large number of successively addressed parallel bar electrodes (typically 10 – 40 μm wide), as shown in Figure 1.10. These arrays have found widespread use in the area of ac electrokinetics for DEP separation systems (field flow fractionation combined with DEP and gravitational forces) and for generating electric fields for travelling wave dielectrophoresis.

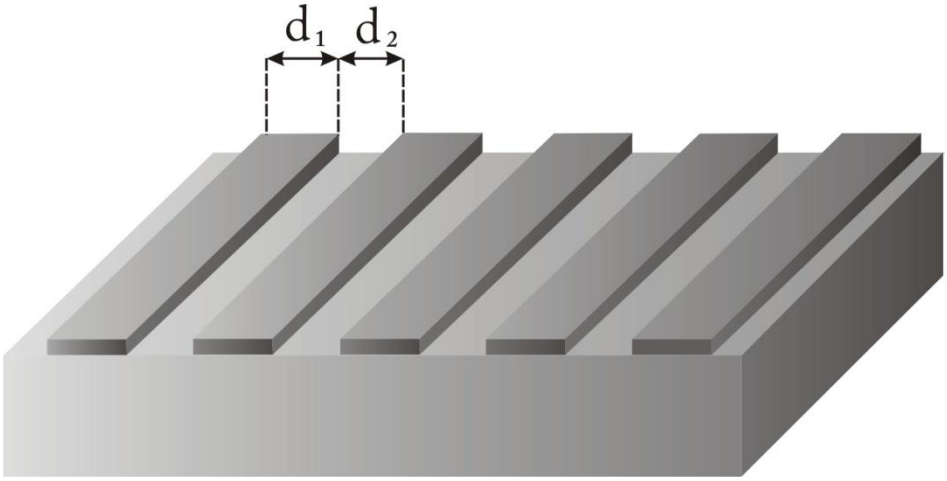

Figure 1.10 Schematic diagram of an interdigitated electrode array consisting of parallel finger (or bar) electrodes (adapted from Reference 32).

DEP force calculations indicate that at large distances from the electrode surface, the force direction is straight downwards with a constant magnitude for any given height. When particles approach a height comparable to the width of an individual bar electrode (d_1), the direction of the force is no longer vertical, but points towards the electrode edges. In addition, the magnitude of the force increases rapidly. Calculations also show that by increasing the electrode width (d_1) relative to the gap width (d_2), the DEP force can be increased by a factor of three for the same applied voltage.[32]

1.2.2.3.2.7 Other electrode designs

Other popular electrode geometries include parallel finger paired electrodes and microtip electrodes (Figure 1.11). Electrodes of the former design have a large trapping area and are widely used for fabrication of sensors and field-effect transistors. Microtip electrodes have rather low effective trapping area, but can generate a large DEP force. Therefore,

these electrodes have been used efficiently to capture single nanoparticles (11 nm in diameter).[36]

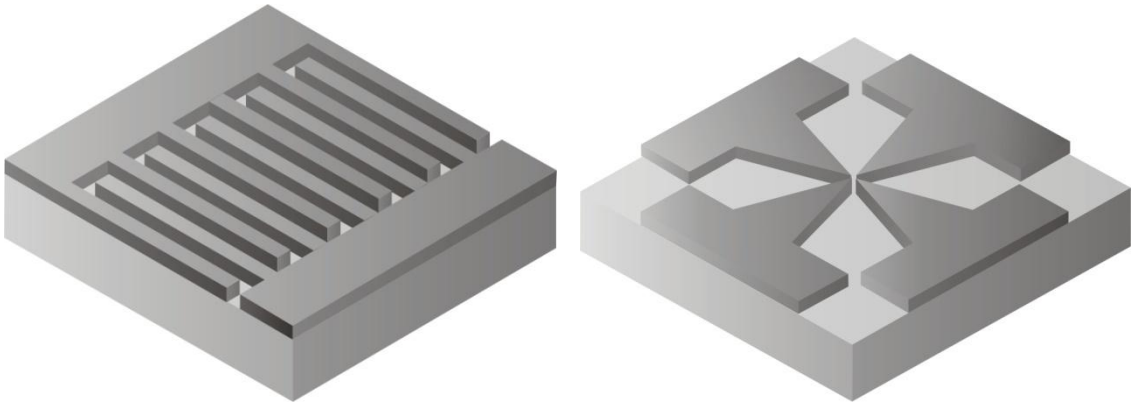

Figure 1.11 Designs of parallel finger paired electrodes (*left*) and microtip electrodes (*right*) (adapted from Reference 46).

A novel development in DEP electrode design is the fabrication of 3D electrodes. In this way DEP manipulation of particles is improved, since the electrode structure is extended into the solution volume. However, the fabrication procedure is more complicated. Simpler designs of this kind involve pairs of microelectrodes positioned on the top and bottom sides of microchannels.[37,38] If such electrode pairs are asymmetric, then the electric fields created have continuously varying magnitude along the transverse direction of the channel. As a result, the magnitude of the DEP force also varies, which leads to an increase in the sorting sensitivity of the separation.[39] The electrodes can be also positioned on the side walls of microchannels. In this case, the DEP forces are generated laterally, which has certain advantages for particle separation.[40]

Voldman *et al.* report the fabrication of a microdevice (cytometer), in which the electroplated 3D gold pillars (19 μm diameter, 50 μm height) are used as electrodes for dielectrophoretic manipulation of biological cells.[41] By using carbon microelectromechanical systems (C-MEMS) process, a carbon-based 3D post electrode array has been fabricated.[42] The advantage of using these electrode designs for dielectrophoretic manipulation of particles is not only due to the extension of the electric field further into solution as compared to 2D electrodes. Rather, it has been shown that

the shape and position of the electrode posts can be chosen so that the effect of solution velocity on the dielectrophoretic separation is minimized.[42]

A number of setups have been developed that allow the generation of a nonuniform electric field using arrays of insulating posts.[43-45] This method is referred to as insulator-based or electrodeless dielectrophoresis (iDEP). The advantages are that such devices are less expensive to fabricate, and the insulators retain their functionality despite the surface fouling. The usual setup consists of an array of insulating structures and two electrodes to create an electric field. Due to irregularities in the array construction, zones of high and low electric field intensity are formed. As a result, dielectrophoretic traps are created.

The electrode designs discussed above are the ones most widely used for dielectrophoresis studies. However, it is obvious that the process of development of the most suitable electrode geometry (for a particular purpose) is ongoing. One can envision that more electrode designs are going to appear in the future, which would allow the dielectrophoretic manipulation of single biomolecules and nanoparticles. Current progress in this area has been summarized in a number of excellent reviews.[46-48]

1.3 APPLICATIONS OF HEATED ELECTRODES

1.3.1 Analytical applications

Current research involving heated microelectrodes is largely directed towards finding applications to electroanalysis. This is dictated by the advantages which they introduce over conventional methods of electrochemical detection. These include:

A. enhanced mass transport due to heating, leading to a significant improvement of the signal-to-noise ratio,
B. acceleration of sluggish reaction kinetics,
C. ability to analyze volatile and thermally unstable analytes,
D. enhanced selectivity due to thermal discrimination of different analytes, and
E. removal of deposited substances from the electrode surface (electrode 'cleaning').

The formation of the hot zone in solution due to heating results in the increase of the diffusion coefficients of dissolved species and also in the appearance of convection.

Consequently, the mass transport of analytes is intensified in proportion to the temperature of the solution around the electrode. This effect of heating has been utilized extensively in the stripping analysis of zinc,[49] cadmium,[49-53] lead[49,53-55], arsenic[56,57], mercury,[57,58] copper[57] and palladium[59]. The main benefit of using heated microelectrodes for stripping is the enhancement of mass transport during the accumulation step. However, heating can also accelerate the kinetically sluggish processes of deposition and stripping.[54,59] As a result, typically 10 to 16-fold enhancement of sensitivity is achieved with heating, while the noise level is essentially unaffected. In some cases, even more dramatic (up to 34-fold) increase in the stripping signal has been observed.[60]

Since only the portion of solution that is the closest to the electrode surface is heated, the temperature of the bulk solution does not change markedly. This opens the possibility of analyzing volatile and thermally sensitive substances: for example, dissolved oxygen has been determined at a heated platinum microwire[16] and at a microwave heated generator-collector gold electrode system.[61]

It has been shown that by using heated electrodes the selectivity of amperometric glucose biosensors can be enhanced.[62-64] The selectivity improvement is achieved due to the fact that the change of the sensor temperature affects its response to the substrate (glucose) and the interfering compound (ascorbic acid or maltose) differently. Thus, by employing a mathematical model, it is possible to discriminate against the interfering signal and obtain the true concentration of the substrate in a sample. When Nafion is used as an enzyme protective layer, it is possible to operate the sensor at temperatures up to 67.5 °C without any thermal inactivation. As a result, a significant (24-fold) increase in the signal is achieved.[64]

DNA hybridization detection has been improved considerably by application of heated microelectrodes.[65-68] Temperature greatly influences the hybridization step: the response of the heated sensor is increased by up to 140-fold and the hybridization time is reduced considerably.[66] In contrast, convectional mass transport has smaller effect on the hybridization process.[67] Using heated biosensors, DNA melting curves can be evaluated in a very simple way.[68]

Heating has been shown to be very helpful for minimizing electrode fouling effects.[69] This is especially important for the performance of electrochemical sensors, because their response is strongly affected by the state of the electrode surface. For electrode cleaning, a combination of thermal and electrochemical conditioning steps has been proposed.[70] The heating is believed to accelerate degradation reactions occuring at the negative (reduction) potential. In addition, hydrogen evolution could also play a significant role in electrode cleaning.

1.3.2 Application of hot microelectrodes in fundamental studies

In addition to electroanalytical applications, heated electrodes have also been used to study various physicochemical phenomena. As was discussed in the beginning of Section 1.2, the faradaic current is affected by numerous processes, including mass transport and the kinetics of electron transfer. An increase in temperature due to heating will affect these processes and the faradaic current. In addition, temperature variation near the electrode surface will also influence processes in the electrical double layer, such as adsorption of ions and orientation of solvent molecules. Therefore, by employing hot electrodes, it is possible to examine the effect of temperature on both transport and double layer processes. Such applications of heated electrodes are of particular importance for the further development of fundamental electrochemistry.

A change of temperature at the electrode surface affects the double layer capacitance. This is because both the Helmholtz layer and diffuse layer capacitances are temperature sensitive. The temperature rise leads to an increase in the thickness of the diffuse layer and, as a result, a decrease of its capacitance. This effect can be explained by the more intensive thermal motion of ions and solvent molecules at the higher temperature. The temperature dependence of the Helmholtz layer capacitance is determined by temperature effects on the specific adsorption of ions (if present) and the orientation of adsorbed solvent molecules, such as water dipoles. The general rule is that the EDL capacitance decreases with temperature. This is supported by the Gouy-Chapman-Helmholtz equation for double layer capacitance:[17]

$$\frac{1}{C_d} = \frac{x_2}{\varepsilon\varepsilon_0} + \frac{1}{\left(2\varepsilon\varepsilon_0 z^2 e^2 n^0 / k_B T\right)^{1/2} \cosh\left(ze\phi_2 / 2k_B T\right)} \qquad (1.53)$$

where x_2 is the thickness of the Helmholtz layer, ε is the dielectric permittivity of the solvent, z is the magnitude of the charge on the ions, e is the charge on an electron, n^0 is the number concentration of each ion in the bulk solution, k_B is the Boltzmann constant, T is the temperature and ϕ_2 is the electrostatic potential at the IHP.

In this equation (1.53), the first term is the reciprocal of the Helmholtz layer capacitance and the second is the reciprocal of the diffuse layer capacitance. One can see that the decrease in the double layer capacitance is due both to the temperature terms and the temperature dependence of the dielectric permittivity of the solvent (the dielectric permittivity of water decreases with temperature). The above equation does not take into account the specific adsorption of ions, which affects the charge in the double layer and the double layer capacitance. At higher temperatures, the effect of specific adsorption of ions is expected to decrease, which should also result in the decrease of EDL capacitance.

Illumination of the electrode surface by laser pulses (temperature jump method) has been used for the determination of the potential of zero charge (pzc) of Au(111).[71] The method involves recording (by an oscilloscope) the transient currents obtained after the laser illumination of the Au(111) electrode in 0.01 M perchloric acid solution. In this experiment, the potential of the working electrode has been varied between 0.05 and 1.0 V vs. a Pd/H_2 reference electrode. It has been established that, in the lower potential region, the current transients are in a negative direction. However, when the potential is increased, the magnitude of the current decreases and eventually becomes positive. It has been determined that the potential at which the transient current changes sign is very close to the potential of zero charge for the Au(111) electrode in the studied system. The explanation of this effect is based on the fact that the heating of the electrode surface by a laser affects the double layer capacitance (equation 1.53). As a result, the current transient observed after the laser pulse is due to the recovery of the double layer charge, when the temperature of the electrode reaches the value in the bulk solution. The sign of the current transient is indicative of the sign of the double layer charge at the potential of the experiment. This makes the proposed method very attractive in determination of the zero charge potential.

The same approach has been applied to the determination of the potential of maximum entropy and a relative measurement of the entropy of double layer formation at Pt(111) and Au(111) single-crystal electrodes.[72-75] In these experiments, the induced temperature change is small. Therefore, the measured change in the open circuit potential can be approximated linearly as:

$$\Delta E = \left(\frac{\partial E}{\partial T} \right)_q \Delta T \tag{1.54}$$

where the term in the parentheses is the temperature coefficient of the open-circuit potential and *q* stands for the charge of the double layer.

After the laser pulse, the electrode temperature falls with time ($\Delta T \sim 1/\sqrt{t}$). Therefore, the temperature coefficient of the open-circuit potential is determined from the slope of a plot of ΔE vs. $1/\sqrt{t}$. The entropy of formation of the double layer, ΔS, is then evaluated based on the following relation:

$$\left(\frac{\partial E}{\partial T} \right)_q = -\left(\frac{\partial \Delta S}{\partial q} \right)_T \tag{1.55}$$

To obtain a plot of ΔS, one needs to integrate a plot of the slopes of ΔE vs. $1/\sqrt{t}$ as a function of *q*. When the curve ΔS vs. *q* passes through a maximum, $(\partial \Delta S / \partial q)_T$ will be zero, as will be the potential change due to electrode heating. Therefore, the potential of zero transient can identified with the potential of maximum entropy of double layer formation. It should also be noted that the values of entropy obtained this way are relative. The calculation of absolute values requires an independent calibration of the temperature change. Recently, the same method has been shown to be very useful in the study of the net orientation of interfacial water on Pt(111), Pt(100) and Pt(110) surfaces as a function of potential.[76,77]

Microwave-heated electrodes have been used for the determination of diffusion coefficients of redox species at elevated temperatures, activation energies of diffusion and standard rate constants of electrode reactions.[78-80] The variation of the diffusion coefficient with temperature is given by the following Arrhenius plot equation:

$$\ln D = \ln D_0 - \frac{E_A}{RT} \tag{1.56}$$

where D is the diffusion coefficient, E_A is the activation energy of diffusion, R is the molar gas constant, T is the temperature and D_0 is the pre-exponential factor, which in a first approximation can be considered temperature independent.

The above equation can be rewritten in a form similar to equation 1.6:[7]

$$D = D_{298} \frac{T}{298K} \exp\left[A\left(\frac{1}{298K} - \frac{1}{T} \right) \right] \tag{1.57}$$

where D_{298} is the diffusion coefficient at 298 K and A is 1876 K^{-1} for aqueous solutions.

The activation energy of diffusion, E_A, is the parameter signifying the energy barrier that the diffusing species needs to overcome, and is caused by the surrounding solvent molecules. It can be determined from the slope of the graph of $\ln D$ vs. $1/T$. The diffusion coefficient of the redox species can easily be obtained from the value of the limiting current, according to equation 1.58:

$$i_{ss} = nFAmC_b \tag{1.58}$$

where A is the surface area of the electrode, C_b is the bulk concentration of the species and m is the mass-transfer coefficient, which is directly proportional to the diffusion coefficient and depends on the microelectrode geometry.

According to this equation, in an isothermal solution (when the whole solution volume is heated), the value of the diffusion coefficient can be determined from the value of the limiting current. However, under non-isothermal solution heating, when temperature gradients are present, equation 1.58 cannot be used and more complex modeling of the system is required. For this purpose, a commercially available finite difference modeling package (FIDAP) has been used.[78,81] The simulated and experimentally determined values of the activation energy of diffusion agree very well for a number of systems. In addition, a different computer simulation package, called DigiSim, has been used to determine standard rate constants for the reduction/oxidation of potassium ferri-/ferrocyanide in aqueous KCl solution.[79] This was done by fitting simulated voltammograms to experimental steady state voltammograms.

Studies were also done to investigate the phenomenon of convection at heated electrodes. Initially, convection had been attributed exclusively to the formation of density gradients as a result of the presence of temperature gradients in solution.[16] Gruendler refers to this form of convection as "thermal stirring"; however, no extensive investigation of this phenomenon has been undertaken. Later, Ghanem *et al.* observed "jet-boiling" at microwave-heated microelectrodes, which was responsible for very high rates of mass transport at these electrodes.[82] A "steam bubble" model of convection has been proposed. According to this model, convection is increased due to the collapse of bubbles formed during solvent boiling.[79,83]

CHAPTER 2: EXPERIMENTAL

2.1 REAGENTS

All solutions were prepared using Millipore water and ACS grade chemicals. Methyl viologen (Sigma-Aldrich), as well as all other chemicals, were used without any further purification. Gold powder used in video experiments was purchased from Alfa Aesar; the average particle size was 0.5-0.8 μm.

2.2 ELECTROCHEMICAL CELL

In most experiments, a standard three electrode electrochemical cell was used. However, controlled temperature isothermal experiments were carried out with a cell equipped with a water jacket and a circulating water bath (Haake, Germany). Platinum or gold microelectrodes were used as the working electrode. The auxiliary and pseudo-reference electrodes were usually made of a platinum wire 0.3 mm in diameter (Alfa Aesar). In some cases, a standard Ag|AgCl|KCl(sat.) reference electrode was employed.

Electrochemical measurements were done without the removal of dissolved oxygen.

2.3 ELECTRODE FABRICATION

2.3.1 Working electrodes

2.3.1.1 Disk microelectrodes

Disk working electrodes (with a diameter 10 μm or larger) were prepared by sealing platinum or gold microwires (Goodfellow Metals Ltd.) into glass tubing (World Precision Instruments). A lead was made by connecting a copper wire with a microwire with the aid of a small piece of Pb-Sn solder. Then the electrode tip was cut and the electrode was polished with 3- and 0.3-μm finishing films on the Micropipette Beveller (WPI, model 48000) to achieve a mirror-like surface.

2.3.1.2 Electrochemically sharpened microelectrodes

Platinum disk microelectrodes with a diameter smaller than 10 μm were obtained by the electrochemical etching of a platinum wire based on a procedure described in the literature.[84] A 25 μm platinum wire was sharpened by periodical dipping (for 1-2 s) of one of its ends into a 14% calcium chloride solution. The ac signal applied between the microwire and a counter platinum electrode placed in the solution was 7 V_{rms}, 60 Hz. After sealing such a sharp microwire in glass it is very important to polish it well, so that only the very tip of the wire gets exposed. To simplify the polishing task, a method recently reported by Zhang *et al.*[85] was used. The method is based on the electronic monitoring of the electrode resistance. Using this approach electrodes as small as 1 μm in diameter were prepared. The exact value of the electrode radius was determined from the value of the limiting current.

2.3.1.3 Recessed electrodes

A recessed electrode can be fabricated quite easily by etching a corresponding disk microelectrode, so that a piece of the microwire is removed and a microchannel is formed. In the simplest case, the same procedure for etching can be used as discussed above (electrochemically sharpened microelectrodes). However, a new method for controlled etching of disk microelectrodes has been developed during this PhD work. By using this method, it is possible to fabricate recessed electrodes with a predetermined length of a channel (or the ratio of the channel length to the radius of a microelectrode disk). The principles are given below.

AC waveform used for etching is generated by the Electrochemical Data Acquisition System (EDAS), which is discussed in more detail in Section 2.4.3 (see Figure 2.6). Briefly, digital signal from the Microcontroller unit (PIC18F2558) is converted to the analog form by a 16-bit Digital to Analog Converter (LTC1655) and supplied through the Analog Conditioning Circuit to the Potentiostat (Auxiliary Electrode). However, the discussed EDAS is designed specifically to be used with microelectrodes and cannot handle currents larger than 2 mA, which may not be sufficient for electrode etching. Therefore, an additional electronic circuit is used to amplify the ac signal, as shown in Figure 2.1. In this Figure, the gain of the first amplifier (LM1458N) is given by the formula:

$$Gain = 1 + \frac{R_2}{R_1} \tag{2.1}$$

and has a value of 4.75 according to the values of the taken resistors. The second is the unity gain buffer amplifier (BUF634T) with a large output current limit of 250 mA.

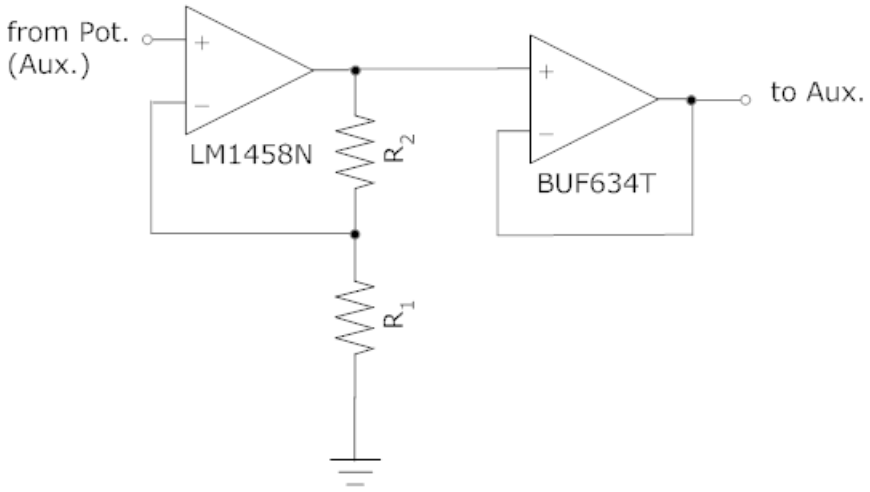

Figure 2.1 Electronic circuit used to amplify the EDAS output; R_1 = 2.65 kΩ, R_2 = 9.95 kΩ. Other explanations in the text.

As a result, by observing the value of the ac current flowing in solution (disk microelectrode is connected to the working input of the potentiostat), it is possible to fabricate recessed microelectrodes with a required length of the channel. This is so since as the length of a channel increases due to etching, the solution resistance increases and the ac current decreases. The current is monitored in real time with the discussed EDAS and a typical current-time curve looks as shown in Figure 2.2.

To fabricate a recessed electrode with a known length of a channel, etching should be stopped once the current reaches the value given by the formula:

$$I_2 = I_1 \frac{R_1}{R_2} \tag{2.2}$$

where I_1 is the initial value of the current before the onset of etching and R_1 is the solution resistance in the case of a disk microelectrode. I_2 is the value of the current at the end of etching when the solution resistance reaches the desired value R_2.

The value of resistance R_1 can be determined using the formula for the solution resistance for flow of current to a disk microelectrode (equation A1.4, Appendix A1). According to this formula, solution resistance for a 25 μm Pt disk microelectrode in 0.1 M $CaCl_2$ solution (specific solution resistance 48.823 Ω·cm) is 9.76 kΩ.

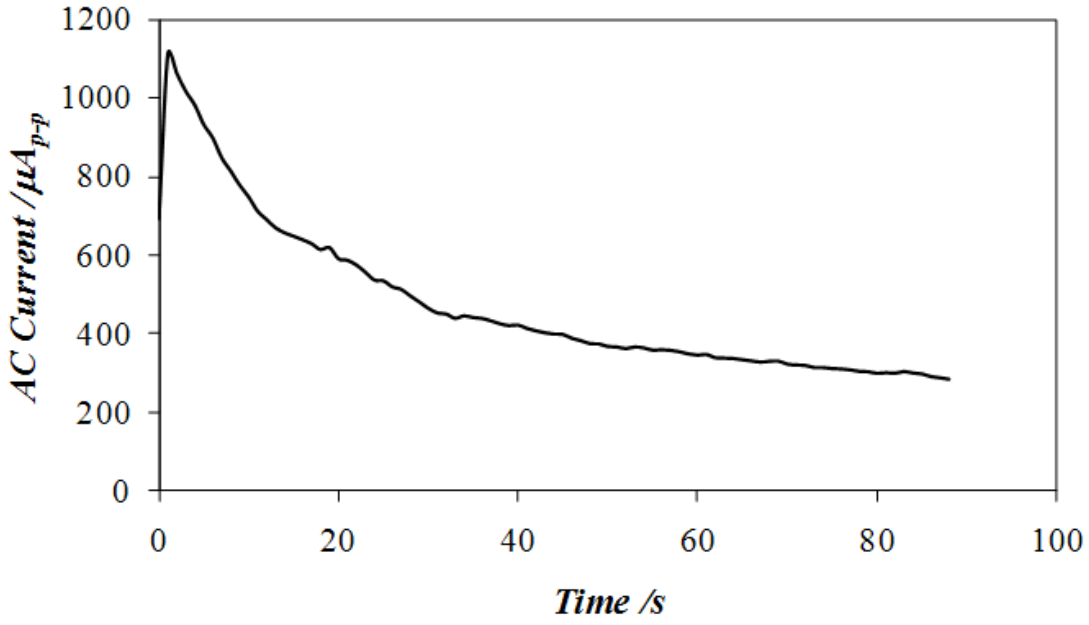

Figure 2.2 Alternating current – time curve recorded during etching of a 25 μm Pt disk electrode in 0.1 M $CaCl_2$ solution. AC waveform applied between an auxiliary Pt electrode and a Pt microelectrode was 19 $V_{p\text{-}p}$, 62.5 Hz.

The solution resistance in the case of a recessed microelectrode (R_2) can be obtained from the simulation results.[86] To confirm that the length of a channel in a recessed electrode has the desired value, steady-state voltammograms are recorded and the channel length is determined from the value of the limiting currents according to the formula:[87]

$$\frac{d}{a} = \left(\frac{i_{\lim}^{disk}}{i_{\lim}^{recessed}} - 1 \right) \frac{\pi}{4} \qquad (2.3)$$

where d/a is the ratio of the length of a channel in a recessed electrode to the radius of the electrode microwire (12.5 μm), $i_{\lim}^{disk}$ and $i_{\lim}^{recessed}$ are the limiting currents recorded with a disk and a recessed electrode, respectively. The limiting currents given in Table

2.1 corresponded to the oxidation of $Fe(CN)_6^{4-}$ in 0.010 M $K_4Fe(CN)_6$, 2.0 M KCl, 0.020 M KCN solution ($i_{\lim}^{disk}$ = 35.07 nA for a 25 μm Pt disk electrode). I_2' is the actual value of the ac current recorded after *t* seconds of etching.

Table 2.1 Summary of fabrication of recessed microelectrodes.

Elec-trode	I_1, mA (p-p)	I_2, mA (p-p)	I_2', mA (p-p)	*t*, s	R_2, kΩ	$i_{\lim}^{recessed}$, nA	*d*/*a* (expected)	*d*/*a* (from eq. 2.3)
1	1.11	0.32	0.28	88	33.6	8.71	2.00	2.38
2	1.07	0.18	0.17	304	58.4	5.88	4.00	3.90
3	1.18	0.54	0.50	28	21.3	18.24	1.00	0.72
4	1.02	0.22	0.20	187	46.0	7.31	3.00	2.98

2.3.1.4 Thermocouple microelectrodes

Thermocouple microelectrodes used in the experiments were fabricated as follows.[88] A piece of the ordinary microscope glass slide (4 mm by 15 mm) was used as a support of the whole assembly. A thermocouple (Pt/13% Rh-Pt, OMEGA part number P13R-001) was placed on the glass surface and the joint of the two microwires was carefully positioned very close to one of the edges. In order to isolate microwires from one another and to secure their position on the glass slide, UV curable adhesive was used (Norland Products, NOA 81). To make a contact between each of the microwires and a copper wire, a piece of tin solder was carefully melted using a butane torch. After that, the adhesive was used once again to isolate wires and joints and to provide enough rigidity to the electrode. As a final step, the side of the glass-polymer electrode body was polished to expose the disk of the thermocouple joint. This step was very crucial in the whole fabrication process as it is quite easy to polish off the joint of the two microwires and thus destroy the electrode. A side view of one of the thermocouple electrodes is shown in Figure 2.3.

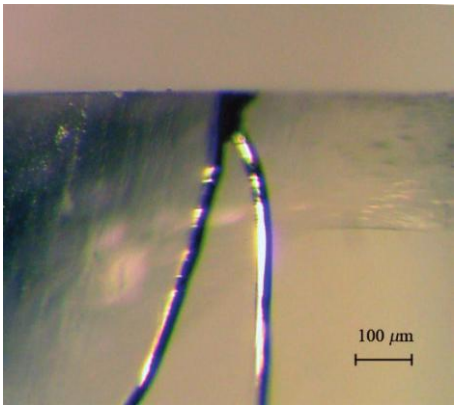

Figure 2.3 Side view of the tip of a thermocouple microelectrode. Reproduced with permission from Reference 88. Copyright 2008 American Chemical Society.

2.3.2 Reference and auxiliary electrodes

A laboratory-made Ag|AgCl|KCl(sat.) electrode was used as a reference electrode in those experiments, where a precise control of the working electrode potential was required, or in order to calibrate pseudo-reference electrodes. Platinum and tungsten wires ~0.3 mm in diameter were used as pseudo-reference electrodes in the experiments, where it was not convenient to use a standard Ag|AgCl electrode (Scanning Electrochemical Microscopy experiments). The advantage of using a pseudo-reference electrode was also in that the contamination of the supporting electrolyte (due to the leakage of ions from the reference electrode solution) was minimized. Auxiliary electrodes were usually made of platinum wire ~0.3 mm in diameter.

2.4 ELECTRONIC SETUP AND DATA ACQUISITION

2.4.1 Electronic Circuit

The block diagram of the electronic setup used in this work is shown in Figure 2.4. The high-frequency sinusoidal waveform was produced by a Hewlett-Packard signal generator (model HP8648B). In typical experiments, frequencies ranging from 100 MHz to 2 GHz and voltage amplitudes ranging from 0 to 2.8 V_{rms} were used. The higher frequency signal was passed from the generator output through capacitor C_1 (1 nF), resistor R_1 (100 Ω), and capacitor C_4 (10 nF) to the generator ground. At frequencies larger than 100 MHz, capacitors C_1 and C_4 present negligible impedance; hence, resistor R_1 was polarized with an alternating voltage. Since the working electrode input of the

potentiostat is at a virtual ground potential, point B shown in Figure 2.4 was also at a ground potential, and the potential of the working electrode oscillated about the ground potential following the polarization changes of resistor R_1. The magnitude of these oscillations was measured at point A with a simple rectifying circuit, based on a high speed Schottky diode (Infineon BAT62-02LS), connected to a 12-bit analog-to-digital converter (ADC). Alternating polarization of the working electrode caused a flow of significant currents (up to about 3 mA_{rms}) through the solution resistance of the working electrode and produced Joule heating; these currents sank to ground through the auxiliary and reference electrodes and capacitor C_5. Low-pass LC filters were used on all three lines connecting the cell with the potentiostat (details of the filters are shown in Figure 2.4) to prevent high-frequency currents from entering the potentiostat. The low-pass filter on the working electrode line is absolutely essential (insufficient filtering can cause, for example, frequency dependent offset currents). Resistor R_2 (100 Ω) is needed to reduce the noise level for currents recorded with the potentiostat. It should be noted that the dc currents passing between the Aux. and W. terminals of the potentiostat were always very small (<1 μA), so resistors R_1 and R_2 produced a negligible ohmic drop (<0.2mV).

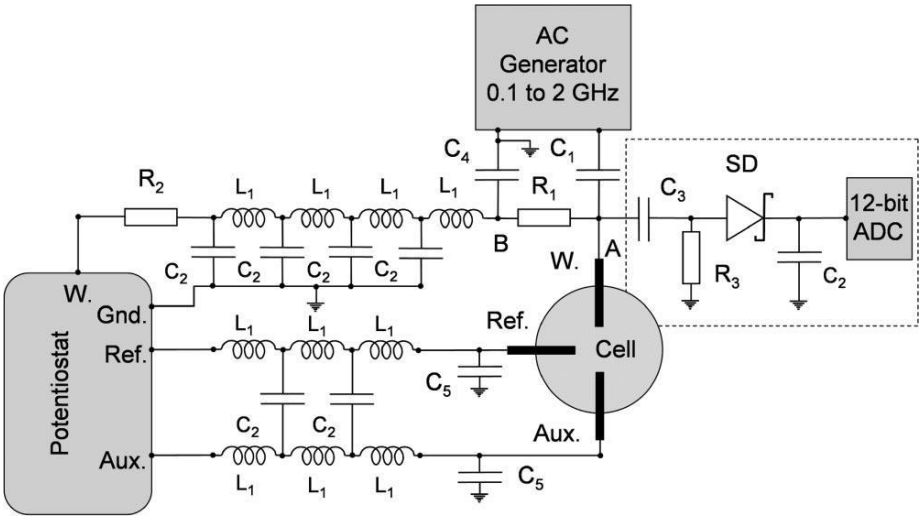

Figure 2.4 An interface between a potentiostat, an ac generator and an electrochemical cell (W. is the working, Aux. is the auxiliary, and Ref. is the reference electrode). C_1 and C_3 are 1 nF capacitors; C_2, C_4 and C_5 are 10 nF capacitors; R_2 and R_1 are 100 Ω resistors; R_3 is a 100 kΩ resistor; and L_1 is a 33 nH inductor. The area enclosed by a dotted line border indicates the ac amplitude monitoring circuit with a high speed Schottky diode (SD). Reproduced with permission from Reference 88. Copyright 2008 American Chemical Society.

There is no compelling evidence that the low-pass filters on the auxiliary and the reference electrode lines are necessary, but they were used anyway. The filters and the ac voltage monitoring circuit were made on a small printed circuit board using surface-mount elements suitable for high frequencies. The connection between the HP8648B and the filter board was made either with a short (~60 cm) coaxial cable or, in some experiments, the filter board was directly connected to the ac generator output. Electrodes with short leads (<3 cm) were connected directly to the filter board. Alternatively, it is possible to modulate the potential of the solution in the electrochemical cell by applying the high-frequency ac signal to the auxiliary and the reference electrodes (rather than to the working electrode). Such an arrangement shown in Figure 2.5 was used to perform measurements with a microthermocouple electrode.

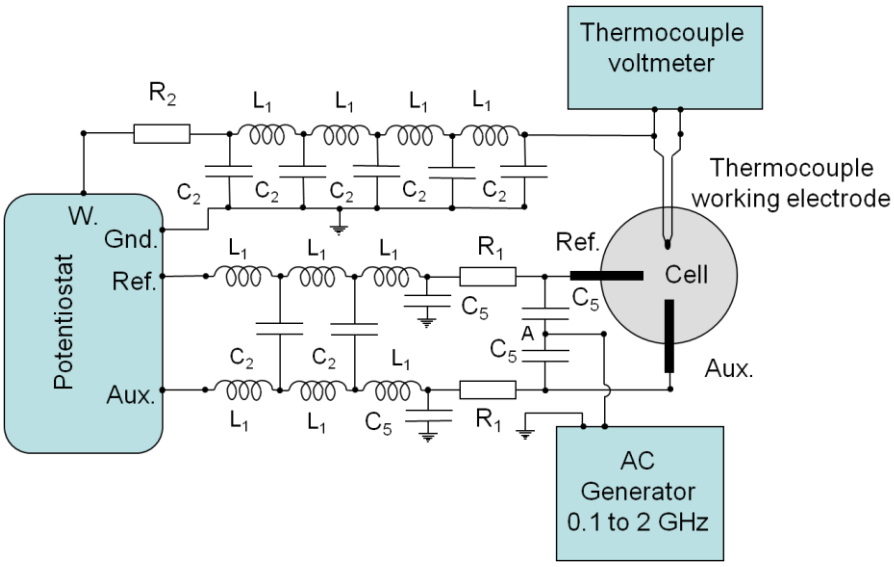

Figure 2.5 An interface between a potentiostat, an ac generator and an electrochemical cell used in measurements with a thermocouple microelectrode. C_2 and C_5 are 10 nF capacitors; R_2 and R_1 are 100 Ω resistors and L_1 is a 33 nH inductor. Reproduced with permission from Reference 88. Copyright 2008 American Chemical Society.

However, since the stray capacitance of the solution is much larger than the stray capacitance of the working electrode, the diagram shown in Figure 2.5 usually cannot be used at frequencies higher than about 500 MHz. The use of high frequency modulation in voltammetric experiments is somewhat complicated because inductance of connectors and stray capacitance of electrodes and cells have to be taken into account. Important

aspects of such measurements are discussed in Chapter 3. It should also be noted that the operation of a potentiostat (Figures 2.4 and 2.5) is controlled by means of a computer. Further details on the electrochemical data acquisition are provided in Section 2.4.3 (see Figure 2.6).

2.4.2 Temperature measurements with thermocouple microelectrodes

Temperature readings during the experiments with thermocouple microelectrodes were done with a digital thermometer (OMEGA HH501AR) incorporated into the electronic circuit (Figure 2.5). The accuracy of this thermometer, not including possible thermocouple error, is ±(0.0% reading +2 °C) on the 0-50 °C scale and ±(0.1% reading +1 °C) on the 50-1767 °C scale. The temperature resolution was 1 °C.

2.4.3 Data acquisition

Electrochemical measurements were carried out with a custom designed data acquisition system (Figure 2.6) based on a microcontroller (Microchip PIC18F46J50), which was linked with a computer via a USB interface. A three-electrode potentiostat was based on a classical design,[17] where the working electrode is at virtual ground potential and the dc potential is applied to the solution via the auxiliary and reference electrodes. The dc potential of the cell was controlled by a 16-bit digital-to-analog converter (DAC8560). Scanning of the dc potential range was performed in a staircase fashion. The potential steps in the scanning waveform were always less than 1 mV. The current was sampled with a 16- bit analog-to-digital converter (ADS8326) after passing through an antialiasing 4th order low-pass filter made of two operational amplifiers, four capacitors, and four digital potentiometers. The software for the microcontroller was written in assembly language (with an assembler provided by Microchip), and the PC software (for data acquisition and processing) was written using Microsoft Visual C++, version 6.0 and Visual Basic, version 6.0. The experimental data were further processed in Microsoft Excel.

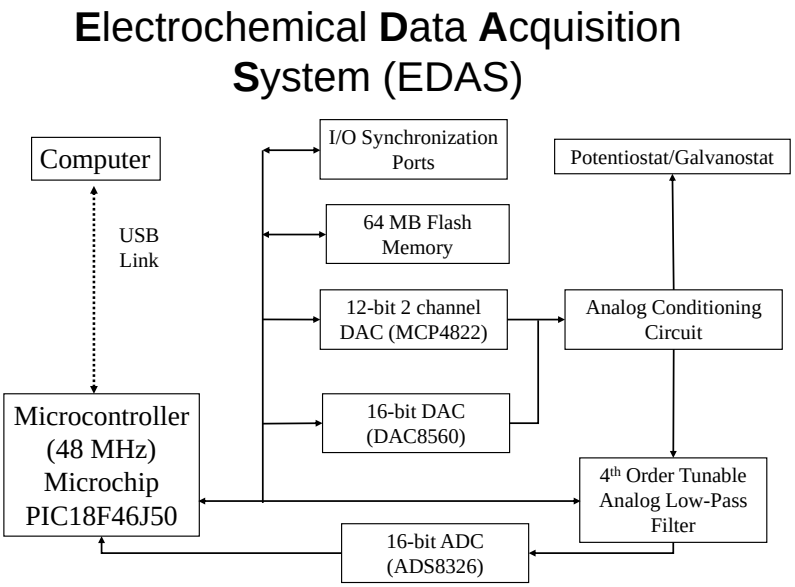

Figure 2.6 Diagram of the Electrochemical Data Acquisition System. Details in the text.

2.5 SCANNING ELECTROCHEMICAL MICROSCOPY SETUP

A setup which was used for the Scanning Electrochemical Microscopy (SECM) measurements is shown in Figure 2.7. Positioning of a microelectrode over a sample surface was achieved by using three high-resolution microtranslation stages (M-110.12S, Physik Instrumente) controlled by an Apollo 3-channel motion controller (C-630.32, Physik Instrumente). Each of the stages allows 0.05 μm minimal incremental motion, 5 mm travel range and motion velocity up to 1.5 mm/s. The controller, in conjunction with the custom-developed software, provided control of the electrode position in all three axes. Microtranslation stages were mounted onto a metal plate and positioned on a stage of the inverted metallurgical microscope (XJL-17 Series, 1000× maximum magnification). Thus, it was possible to observe the sample and the tip of a microelectrode under the microscope. For additional general information about operation of SECM interested readers are referred to the dissertation by Diakowski.[115]

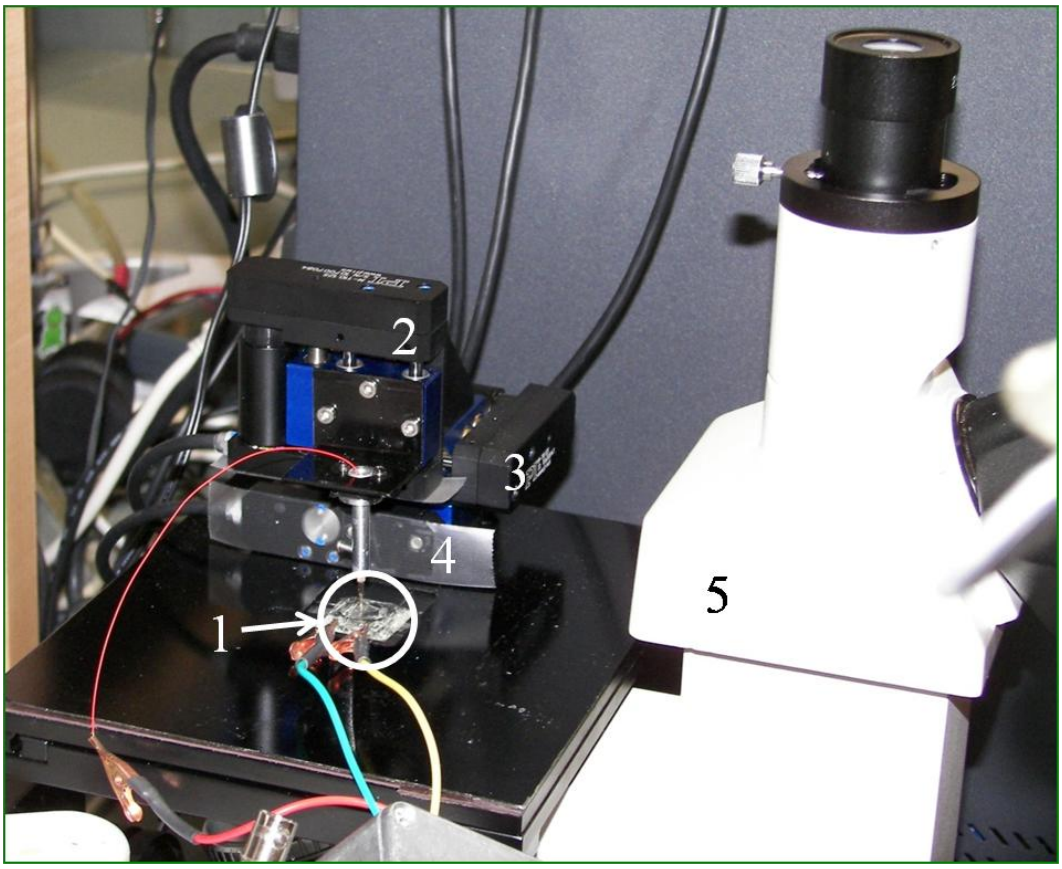

Figure 2.7 SECM setup. 1 – electrochemical cell; 2, 3, 4 – microtranslation stages; 5 – microscope.

2.6 VIDEO EXPERIMENTS

For video experiments, a setup similar to the one discussed in Section 2.5 was developed. It included the XJL-17 inverted metallurgical microscope and a miniaturized electrochemical cell made of a glass slide in order to allow microscopic observation of the electrode processes. Videos and pictures were taken with the 3.1 Megapixel Digital Microscope Camera (USBCAM-3M, World Precision Instruments) and, in some cases, edited with respect to their size. It should also be noted that in all of the recorded videos hot microelectrodes were oriented with their surface parallel to the gravitational field lines. The moment when the heating is applied is indicated by a characteristic clicking sound and by corresponding subtitles. In addition, representative frames of all videos can be found in Appendix E2 (full-length video files are enclosed on a CD).

CHAPTER 3: CONVECTION AT AC HEATED DISK MICROELECTRODES

In this Chapter, convection at ac heated disk microelectrodes is discussed. The material is organized in the following order. Firstly, a short foreword to the study of mass transport at hot microelectrodes is given. Secondly, the mechanism of the high frequency ac heating of an electrolyte solution is explained. Particularly, the equivalent circuit of a hot microelectrode and the parameters affecting the ac heating are discussed. After that, methods of temperature determination of a hot microelectrode are compared and discussed. The knowledge of the temperature is very important for the interpretation of the effect of the heating on mass transport at hot microelectrodes. Finally, the mechanism of convection is explained in a somewhat intuitive way, without the use of numerical simulations (this will be done in Chapter 4).

3.1 FOREWORD

When this PhD project was started, two important questions about the mass transport at hot microelectrodes were not answered in the literature. First of all, it was not clear what causes convection in such systems. Is it buoyancy force or, may be, some other force? In addition, other research groups working with heated microelectrodes (Compton and Marken, Gruendler) completely neglected the effect of Soret diffusion on the mass transfer. The results of the studies of the Soret effect undertaken during this PhD work will be provided in Chapter 5. In the current Chapter, convection at microelectrodes polarized by a high frequency ac waveform will be discussed.

The simplest way of studying mass transport at hot microelectrodes is by using steady-state voltammetric measurements. This method is very convenient, since the value of the limiting current, which can be readily obtained from the voltammogram, is directly proportional to the rate of mass transfer of redox species to the electrode. An

example of the two steady-state voltammograms is given in the Figure 3.1. One of the voltammograms was recorded at room temperature, and the other one – with a hot microelectrode.

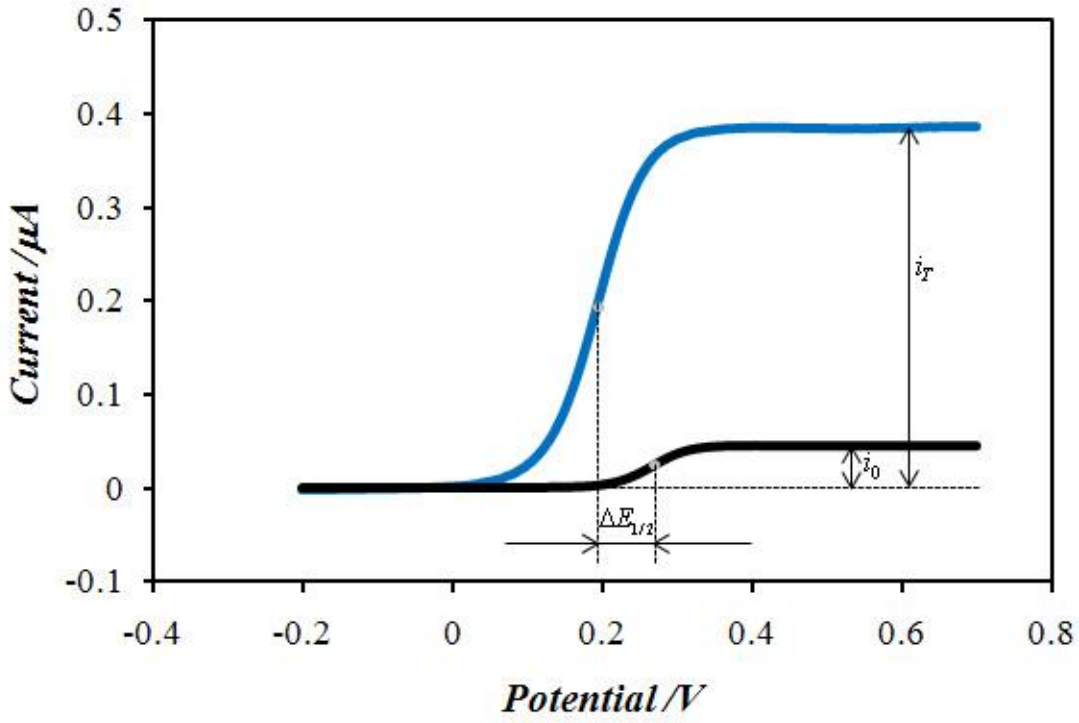

Figure 3.1 Steady-state voltammograms recorded at room temperature (black) and with a hot microelectrode (blue). Solution: 0.0125 M $K_4Fe(CN)_6$, 0.02 M KCN and 0.5 M KCl. Working electrode: 25 μm Pt disk; scan rate: 0.015 V/s; heating: 100 MHz, 2.8 V_{rms}

As can be seen in Figure 3.1, the magnitude of the limiting current increases substantially due to the heating by a high frequency ac waveform. This increase can be expressed as the limiting current enhancement factor, given by the formula:

$$\chi = \frac{i_T}{i_0} - 1 \qquad (3.1)$$

where i_T is the limiting current (due to oxidation of $Fe(CN)_6^{4-}$) measured after the ac excitation signal is applied and i_0 is the limiting current recorded at room temperature (without heating).

As a result, one can judge the rate of mass transfer by the value of the limiting current enhancement factor. It can also be noticed that ac heating leads to the shift in the value of the half-wave potential ($\Delta E_{1/2}$ in Figure 3.1). The magnitude of this shift is directly related to the change in the electrode temperature. However, more details will be provided later, when the temperature determination methods will be discussed. In the following Section, the mechanism of the high frequency ac heating will be explained.

3.2 MECHANISM OF HIGH FREQUENCY AC HEATING

3.2.1 Electronic circuit considerations

In order to understand how the heating of an electrolyte solution occurs when an ac waveform is applied to a microelectrode, an equivalent circuit of the electrochemical cell needs to be considered. In general, the cell can be represented as a circuit consisting of electronic components, such as resistors, capacitors and inductors. The behaviour of this electronic circuit with respect to the applied perturbation (ac waveform) should be the same as of the actual electrochemical cell. Figure 3.2 illustrates a proposed equivalent circuit of a hot microelectrode in electrolyte solution (point A in the Figure below corresponds to point A in Figure 2.4).

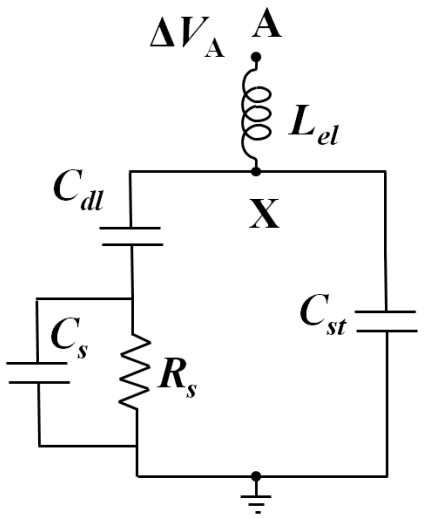

Figure 3.2 Equivalent circuit of a hot microelectrode. L_{el} – inductance of wires, C_{dl} – double layer capacitance, C_s – solution capacitance, C_{st} – stray capacitance, R_s – solution resistance, ΔV_A – output voltage of a signal generator.

The specific double layer capacitance of an electrode in an aqueous electrolyte solution is between 10 to 40 μF/cm^2.[17] Solution capacitance is equal to $4\varepsilon r_0$, where ε is the dielectric permittivity of the solution and r_0 is the radius of a disk microelectrode. Stray capacitance can be approximated by the capacitance of a cylindrical capacitor, since a metal microwire and an electrolyte solution (which are the conductors of the ac heating current) are separated by a layer of glass. The value of the solution resistance is given by the relation $R_s = \rho/4r_0$, where ρ is the specific resistance of the solution. Derivation of these expressions for the solution resistance, solution and stray capacitances is given in Appendix A.

In the case of ac heated disk microelectrodes, the heat is generated in solution due to a sufficiently large ac current flow through the solution resistance (Section 1.1.1.2.2). This is because the solution resistance is much larger than the resistance of a microwire. For example, a two centimeter Pt microwire (25 μm in diameter) has the resistance of only 4.3 Ohm. The value of the resistance of 2 M KCl aqueous solution is equal to 972 Ohm, which is about 226 times larger than in the case of a microwire. Therefore, the heat generation in the microwire can be neglected, and the microelectrode temperature is increasing due to heat transfer from the solution.

From Figure 3.2 it also follows that the ac heating current can be attenuated by the interfacial capacitance (C_{dl}) of the microelectrode. In addition, the presence of the inductor L_{el} in the circuit, as well as the capacitors C_s and C_{st}, affects the magnitude of the ac voltage drop on R_s, thus affecting the heating of the solution.

The impedance of a capacitor is given by the formula:

$$Z_C = -\frac{j}{\omega C} \tag{3.2}$$

where j is the imaginary unit, ω is the angular frequency and C is the capacitance.

Hence, the impedance of a capacitor decreases at higher frequencies of ac modulation. Impedance of an inductor, on the contrary, increases with frequency and, in addition, it has the opposite sign:

$$Z_L = j\omega L \tag{3.3}$$

where L is the inductance.

From equation 3.2 and the electronic diagram in Figure 3.2 it is clear that, in order to have an effective heating of the solution, the capacitive attenuation and, consequently, ac polarization of the electrode-solution interface need to be minimized. Therefore, the frequency of the ac excitation signal has to be large, typically larger than 100 MHz. On the other hand, at such high frequencies even short leads have significant impedance (equation 3.3). For example, a typical nonferromagnetic wire has an inductance of about 8 nH/cm, so a 3 cm lead exhibits an impedance of 150 Ω at 1 GHz frequency. A very small capacitance of 1 pF at 1 GHz exhibits an impedance of only 160 Ω. However, since impedances of inductors and capacitors have opposite signs, a small inductor (L) in series with a small capacitor (C) at a certain frequency provide a low impedance (theoretically, zero impedance) path for ac currents. This frequency is called the resonance frequency and it is given by the formula:

$$f_{res} = \frac{1}{2\pi\sqrt{LC}} \tag{3.4}$$

As a result, even without a rigorous analysis of the electronic circuit shown in Figure 3.2, one can expect that the effectiveness of the solution heating will depend on the frequency of ac waveform. This was illustrated by the following experiment (Figure 3.3), which was performed with a 25 μm Pt disk electrode in 0.5 M KCl containing 12.5 mM $K_4Fe(CN)_6$ and 5 mM KCN. In this experiment, the filter board (shown in Chapter 2, Figure 2.4) was connected directly to the ac generator, without a coaxial cable, and very short (~ 2 cm long) electrodes were plugged directly to the filter board without using any additional leads. With such an arrangement it was possible to obtain significant heating of the electrode even at frequencies larger than 1 GHz.

Effectiveness of the heating was monitored by calculating the limiting current enhancement factor (equation 3.1). Since the magnitude of the limiting current is determined by the rate of mass transfer of the redox species ($Fe(CN)_6^{4-}$), which is affected by the temperature of the electrode, higher values of the limiting current enhancement factor χ indicate more effective heating of the microelectrode (i.e., the electrode temperature is higher). The results obtained for frequencies ranging from 150 to 1950 MHz and for different amplitudes of the excitation signal are shown in Figure

3.3. In addition, the amplitude of the alternating potential applied to the working electrode at point A (ΔV_A, see Figure 3.2) was monitored during these measurements by the ac amplitude monitoring circuit (Chapter 2, Figure 2.4), and the results are presented in Figure 3.4.

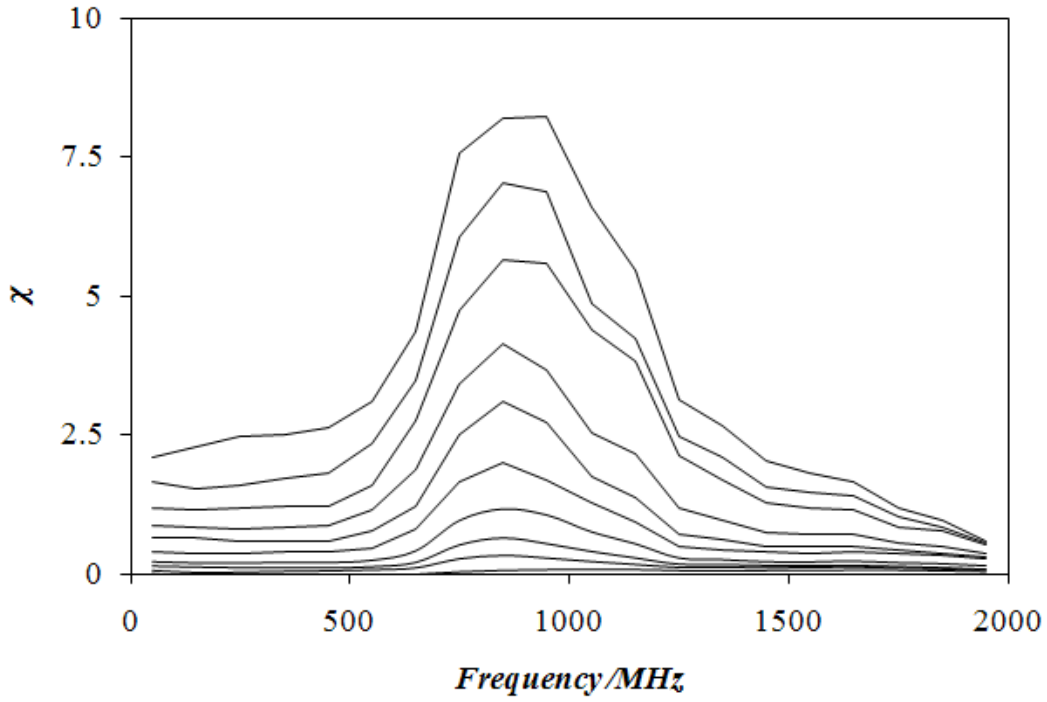

Figure 3.3 The limiting current enhancement factor plotted as a function of the excitation frequency. Amplitudes of alternating voltage applied to the electrode are shown in Figure 3.4. The experiments were performed with a Pt disk electrode (25 μm in diameter, 2 cm long) in 0.5 M KCl containing 12.5 mM $K_4Fe(CN)_6$. The dc potential of the working electrode was 500 mV, which corresponded to the oxidation of $Fe(CN)_6^{4-}$. Reproduced with permission from Reference 88. Copyright 2008 American Chemical Society.

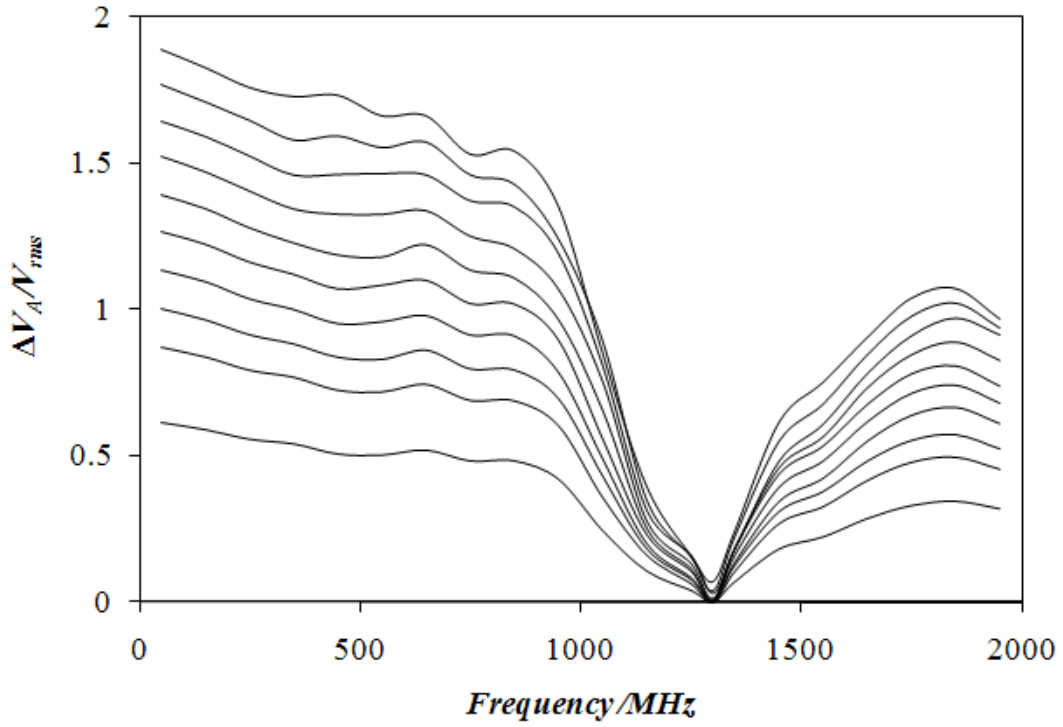

Figure 3.4 The magnitude of alternating potential applied to the working electrode lead during the measurements presented in Figure 3.3. Reproduced with permission from Reference 88. Copyright 2008 American Chemical Society.

As expected, the shape of the curves shown in Figures 3.3 and 3.4 is characteristic of an inductance-capacitance resonance (equation 3.4). In this case, the inductance can be attributed to the short lead of the electrode, and the series capacitance arises mainly from the stray capacitance of the electrode. At the resonance frequency, which is about 1.3 GHz, the impedance of L_{el} in series with C_{st} drops to almost zero and shunts the 50 Ω output of the ac generator. So, in this case, the electrode acts as a notch filter. This explains why the ac potential measured at point A drops to almost zero, but the ac current passing through the circuit is still large and the potential difference between points B and the ground is also quite large. Therefore, at this frequency a substantial current passes through the solution resistance and a quite substantial heating of the electrode is observed. In this particular experiment, the maximum heating, which can be attributed to the maximum of power dissipation on R_s, was observed at about 850 MHz.

In addition, the limiting current enhancement factor correlates very well with ΔV_A^4, as shown in Figure 3.5 for four different frequencies.

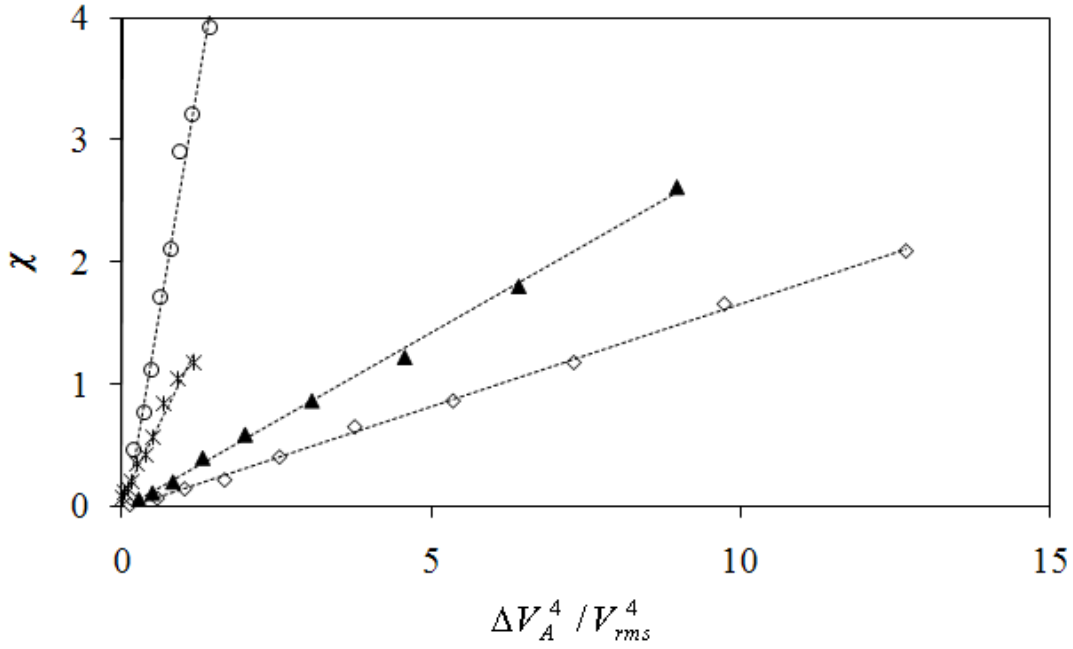

Figure 3.5 Correlation between the limiting current enhancement factor and ΔV_A^4 based on data presented in Figures 3.3 and 3.4. The plots were made for the following frequencies: (◇) 50, (▲) 450, (○) 950 and (∗) 1750 MHz. Reproduced with permission from Reference 88. Copyright 2008 American Chemical Society.

3.2.2 Parameters affecting high frequency ac heating of microelectrodes

As has been mentioned earlier, the frequency of the ac modulation is of major importance for the heating of an electrolyte solution. In this Section, other parameters affecting the ac heating will be discussed in greater detail in order to provide a better understanding of the subject.

If we refer again to the electronic diagram in Figure 3.2, it is obvious that the Joule heating of the solution is determined by all of the components of the circuit and the applied voltage ΔV_A. Therefore, a rigorous approach to evaluating the Joule heating of microelectrodes requires that the discussed electronic circuit is analyzed and an expression for the electrical power dissipated by the solution resistance is obtained.

The electrical power (P) dissipated by the solution resistance (R_s) is given by the following expression:

$$P = I_{R_s} \cdot \Delta V_{R_s} = \frac{\Delta V_{R_s}^2}{R_s} \tag{3.5}$$

where I_{R_s} is the ac current and ΔV_{R_s} is the ac voltage across the solution resistance (not to be mistaken for ΔV_A).

This simple formula clearly shows that the Joule heating is affected by the ac voltage drop and the value of the solution resistance. The solution resistance is proportional to the specific solution resistance (Appendix A1), which depends on the electrolyte concentration. For example, at 25 °C the specific resistance of $KCl_{(aq.)}$ solution decreases from $3.96 \cdot 10^{-1}$ Ohm·m to $4.86 \cdot 10^{-2}$ Ohm·m, when the concentration of KCl increases from 0.2 M to 2 M, respectively. Therefore, the solution resistance decreases with an increase in the electrolyte concentration, and, according to equation 3.5, the dissipated electrical power increases. As a result, concentrated electrolyte solutions are heated more effectively compared to dilute ones (i.e., higher electrode temperatures are reached for the same value of ΔV_{R_s}).

The same equation 3.5 shows that the effectiveness of the heating also depends on the amplitude of ac potential applied across the solution resistance (ΔV_{R_s}). However, it is not easy to tell how big ΔV_{R_s} really is, even if the potential ΔV_A is measured only 2 cm away from the electrode interface. Some approximate predictions of the ratio $\Delta V_{R_s} / \Delta V_A$ are shown in Figure 3.6. These results were obtained by analyzing the electronic circuit in Figure 3.2 as discussed in Appendix B. In the calculations, the following values were used: L_{el} = 16 nH was estimated based on the length of the electrode lead (2 cm) and the value of the specific inductance of a wire (8 nH/cm), C_{dl} = 147 pF was obtained from the value of the specific double layer capacitance (30 μF/cm^2), R_s = 3.36 kΩ was calculated from the electrode radius and the specific resistance of 0.5 M KCl using equation A1.4 in Appendix A1, C_s = 0.0347 pF (at 50 MHz) was calculated from the electrode radius and the dielectric properties of water (ε_s = 78.36, ε_∞ = 5.2 and $\tau = 8.27 \times 10^{-12}$ s) based on equations A2.6 and A2.7 in Appendix A2, and finally, C_{st} = 0.913 pF was calculated from L_{el} and the resonance frequency of the system (1.305 MHz) using equation 3.4 . In the same Figure 3.6 a normalized 4th root

of the function $S(\omega)=d\chi/d(\Delta V_A^4)$ is included, the calculation of which is based on the experimental data from Figures 3.3 and 3.4. These two sets of data correlate very well at low frequencies, which may suggest that, at least at frequencies below 1100 MHz, the limiting current enhancement factor is independent of frequency of ac modulation.

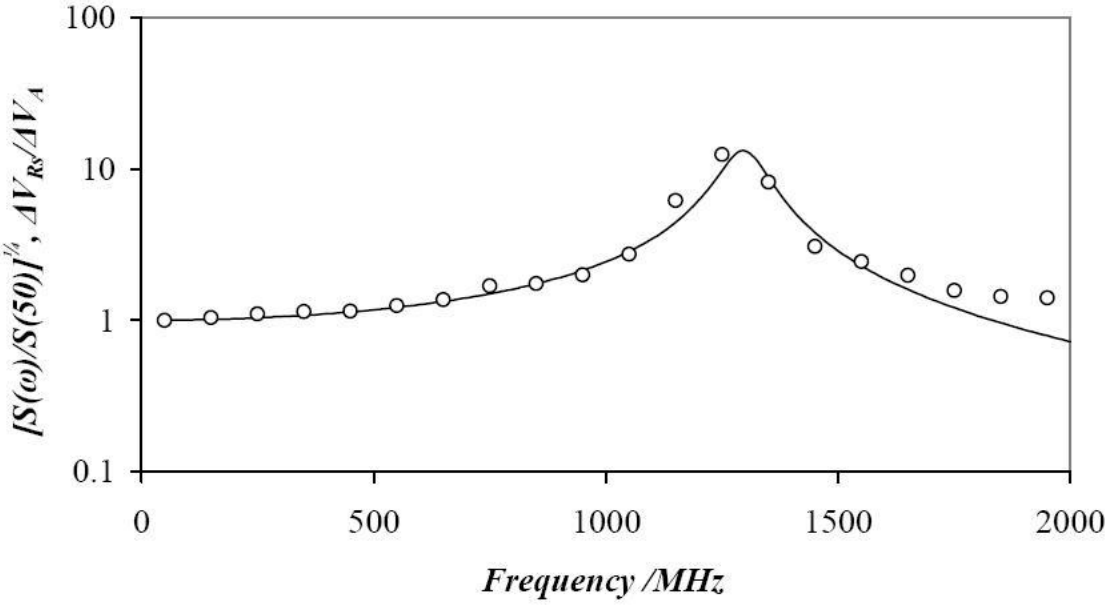

Figure 3.6 The ratio of $\Delta V_{Rs}/\Delta V_A$ based on the equivalent circuit in Figure 3.2 with the following values: L_{el} = 16 nH, C_{st} = 0.913 pF, C_{dl} = 147 pF, R_s = 3.36 kΩ, C_s = 0.0347 pF (the frequency dispersion of C_s was taken into account, but this effect is very small).The markers represent a normalized 4th root of $S(\omega)=d\chi/d(\Delta V_A^4)$ based on the experimental data in Figures 3.3 and 3.4. Reproduced with permission from Reference 88. Copyright 2008 American Chemical Society.

The results shown in Figure 3.6 are indicative of the already mentioned *LC* resonance, which determines the value of the maximum heating frequency (~850 MHz in Figure 3.3). In practice, this value is affected mainly by such parameters as the length of the electrode, the thickness of the insulator around the microwire and the depth of immersion of the electrode into the solution. The length of the electrode (and also of the coaxial cable, if it is connected between the signal generator and the working electrode) determines the value of the inductance L_{el}. The thickness of the insulator (glass) around

the electrode microwire and the depth of immersion of the electrode into an electrolyte solution affect the value of the stray capacitance C_{st}. This is explained in detail in Appendix A3.

a)

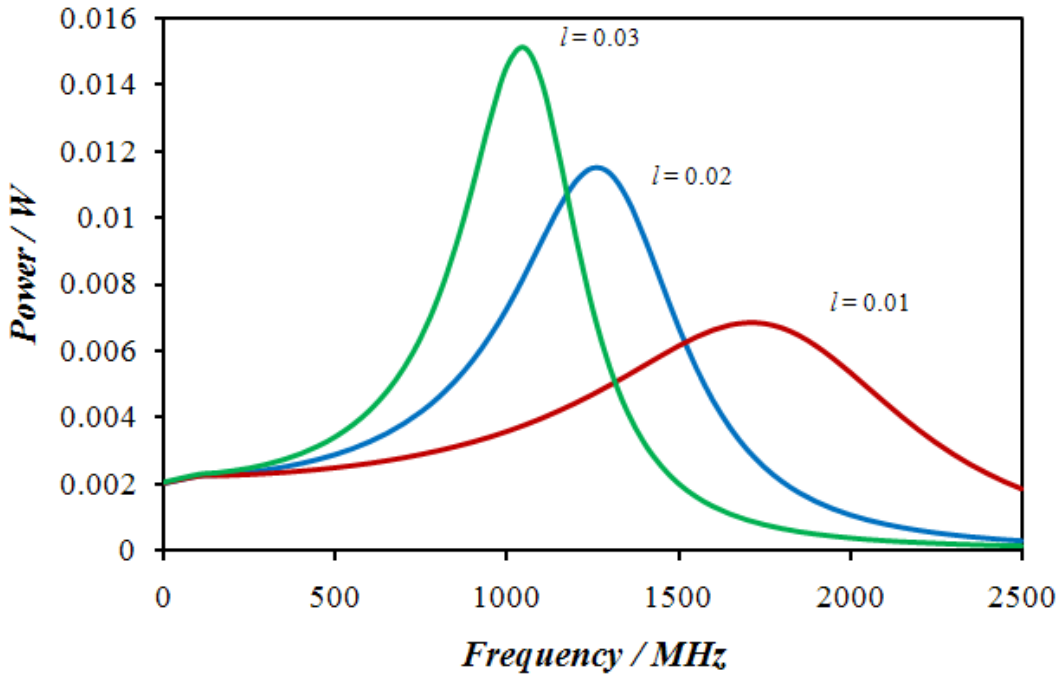

b)

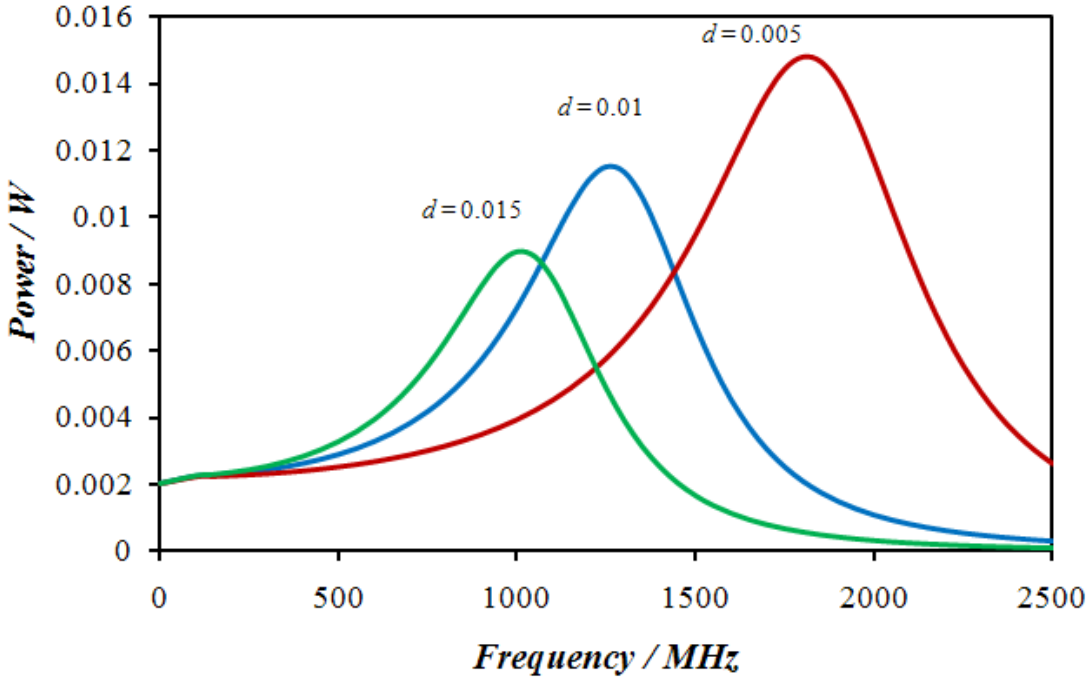

c)

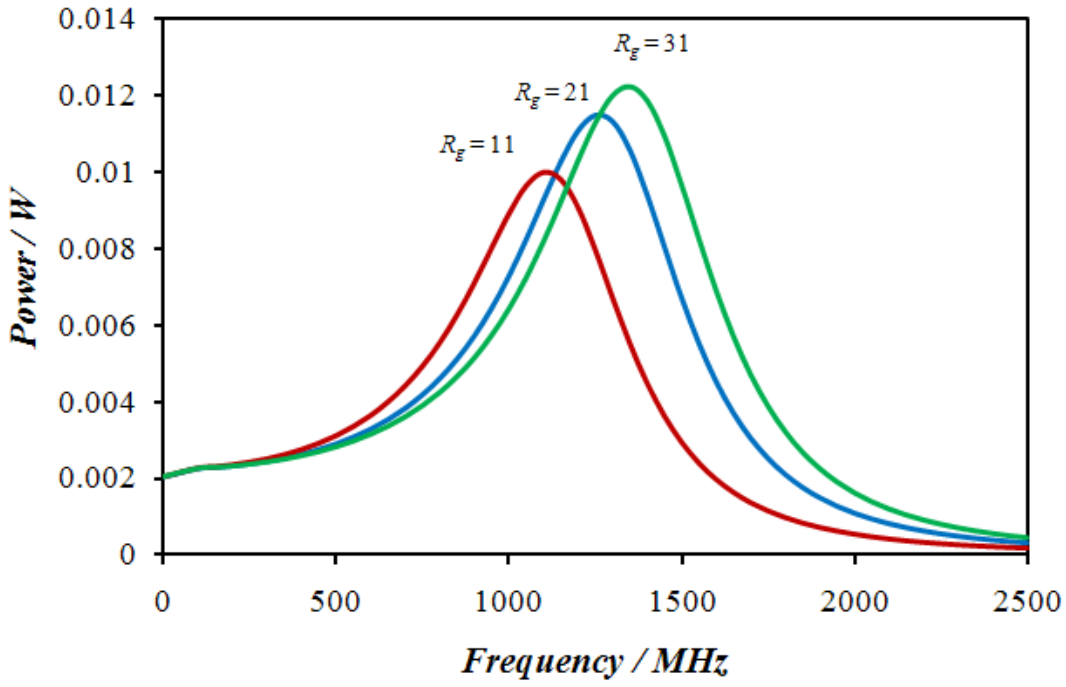

Figure 3.7 Effect of the electrode length *l* (in m) **(a)**, the depth of the electrode immersion into solution *d* (in m) **(b)** and the thickness of the glass insulator expressed by R_g factor **(c)** on the magnitude and frequency dependence of the power dissipated by the solution resistance. The results are based on the analysis of the circuit shown in Figure 3.2 with the values of the electronic components given in the legend to Figure 3.6 and above each of the curves. AC voltage applied to the electrode: 2.8 V_{rms}; output impedance of the ac generator: 50 Ohm.

The results in Figure 3.7 (a) – (c) show how the magnitude and frequency of the maximum power dissipated by the solution resistance are affected by L_{el} and C_{st}. An increase in the length of a microelectrode (or a coaxial cable) leads to the shift of the maximum power to lower frequencies and also to the increase of its magnitude (case a). The opposite effect is observed if a shorter electrode is used. Similar trend is obtained when the depth of the microelectrode immersion into solution is varied (case b). However, in this case, the magnitude of the maximum power is decreasing with an increase in the immersion depth, and increasing, if the depth of the electrode immersion is getting smaller. On the contrary, an increase in the thickness of the glass insulating layer (larger values of R_g factor) results in the shift of the maximum power towards higher frequencies and also in the increase of its magnitude, as shown in Figure 3.7, c.

R_g is a dimensionless parameter determined from the ratio of the total tip radius (i.e., electrode radius plus the thickness of the insulating sheath) to the electrode radius.

Frequency dependence of the maximum power shown in Figure 3.7 agrees very well with the equation for the resonance frequency (equation 3.4) and the expression for the stray capacitance (equation A3.1 in Appendix A3). Furthermore, under the conditions stated in Figure 3.7 it may be concluded that, in order to heat electrolyte solutions more effectively, one needs to use longer microelectrodes with larger R_g factor, which are barely dipped into the solution. This conclusion, however, should be treated carefully, since all of the components of the electronic circuit in Figure 3.2 affect the power dissipated by the solution resistance. Therefore, under different conditions, the above conclusion may not be valid.

To work with hot microelectrodes, one is not required to operate at the frequency of the maximum power. This is illustrated well by the results in Figure 3.3, where a substantial increase in the limiting current is observed in a wide range of frequencies. In fact, it is quite complicated to predict the optimal frequency, since most of the parameters affecting the heating cannot be conveniently controlled (R_g factor, length of the microelectrode and the coaxial cable, depth of the immersion into solution). However, if one wishes to perform the heating at the frequency of the maximum power, it can be determined from the experiment identical to the one described in the legend of Figure 3.3. In the following step, the steady-state voltammograms can be recorded and the mass transfer at hot microelectrodes can be studied.

3.2.3 Determination of electrode temperature

Knowledge of the temperature of a hot microelectrode is of major importance in the study of mass transfer. This is so since the temperature affects all modes of mass transfer of redox species towards and from the electrode (equation 1.9 in Section 1.2.1.2). Therefore, when this project was started, an effort was made to evaluate and compare available methods of temperature determination.

As has been discussed in Section 1.1.2, two indirect methods of temperature determination are described in the literature: potentiometric method and a method based on the logarithmic analysis of steady-state voltammograms. According to the potentiometric method, the temperature of a hot microelectrode is determined from the

shift of the half-wave potential (Figure 3.1) and the value of the temperature coefficient of the electrode reaction standard potential (see Appendix C1 for details). In the case of the $Fe(CN)_6^{4-}$ /$Fe(CN)_6^{3-}$ redox couple, the change of the standard potential with an increase of temperature is quite large (about –1.5 mV/°C). However, that shift of the standard potential is expected to depend on the supporting electrolyte concentration. In addition, Soret diffusion of the redox species and the supporting electrolyte ions may affect the accuracy of this method. Determination of the electrode temperature from the logarithmic analysis of steady-state curves appeared to be based on relatively simple and solid theoretical grounds. However, it has been noted that this method usually returns much higher values of temperature than the ones determined from the half-wave potential shift. Consequently, it had to be established which method is affected by systematic errors.

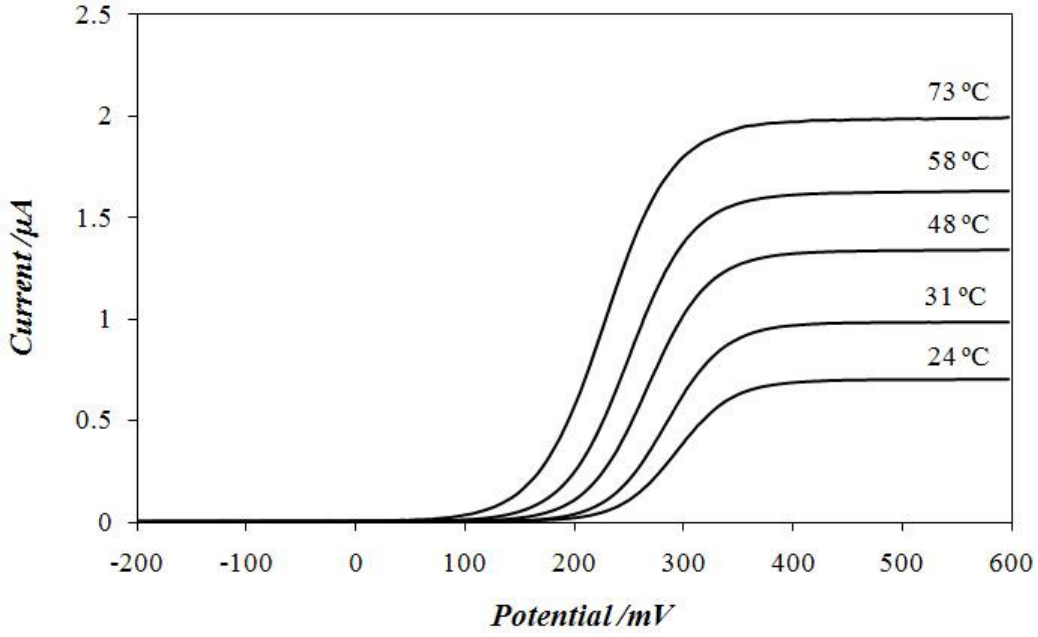

Figure 3.8 Changes in steady-state voltammograms caused by superimposed sinusoidal waveform at a frequency of 155 MHz. Alternating potential amplitudes in V_{rms}: 0, 0.6, 1.0, 1.3, and 1.6 for the curves from the lowest to the highest. Solution: 0.05 M $K_4Fe(CN)_6$, 2 M KCl. Working electrode: thermocouple microelectrode (~200 μm in diameter). Reference electrode: Ag|AgCl|KCl(sat.). Auxiliary electrode: 0.3 mm Pt wire. Sweep rate: 1 mV/s. Temperature reading from the thermocouple meter is shown above each curve. Reproduced with permission from Reference 88. Copyright 2008 American Chemical Society.

To assess the discussed methods of temperature determination, a first direct method for measuring the temperature of a hot microelectrode has been developed in the course of this PhD work. This method is based on the use of special thermocouple microelectrodes. By employing such electrodes it is possible to determine the value of the temperature by reading the thermoelectric potential with a thermocouple meter and, at the same time, do electrochemical measurements as with ordinary hot-disk microelectrodes. Figure 3.8 shows steady-state cyclic voltammograms obtained with a microthermocouple electrode heated to various temperatures by a high frequency ac current. The temperature readings are shown above each voltammogram.

Table 3.1 Temperature dependence of the standard potential of the $Fe(CN)_6^{4-}$ / $Fe(CN)_6^{3-}$ redox couple. Reproduced with permission from Reference 88. Copyright 2008 American Chemical Society.

Solution Composition	$\Delta E°/\Delta T$ [mV/K]	Standard deviation [mV/K]	R^2 (data points)
50 mM $K_3Fe(CN)_6$, 50 mM $K_4Fe(CN)_6$, 2 M KCl	–1.305	0.008	0.9997 (8)
25 mM $K_3Fe(CN)_6$, 25 mM $K_4Fe(CN)_6$, 1 M KCl	–1.355	0.012	0.9994 (8)
12.5 mM $K_3Fe(CN)_6$, 12.5 mM $K_4Fe(CN)_6$, 0.5 M KCl	–1.431	0.008	0.9998 (8)
5 mM $K_3Fe(CN)_6$, 5 mM $K_4Fe(CN)_6$, 0.2 M KCl	–1.485	0.004	0.9999 (8)
2.5 mM $K_3Fe(CN)_6$, 2.5 mM $K_4Fe(CN)_6$, 0.1 M KCl	–1.526	0.008	0.9998 (8)
1.25 mM $K_3Fe(CN)_6$, 1.25 mM $K_4Fe(CN)_6$, 0.05 M KCl	–1.559	0.003	0.9999 (8)

In order to determine the effect of the supporting electrolyte concentration on the temperature dependence of the standard potential of the $Fe(CN)_6^{4-}$ /$Fe(CN)_6^{3-}$ redox couple, potentiometric measurements were carried out of a cell Pt| $K_4Fe(CN)_6$, $K_3Fe(CN)_6$, KCl || $K_4Fe(CN)_6$, $K_3Fe(CN)_6$, KCl | Pt. Concentrations of all components in both half cells were exactly the same; however, the left-hand half cell was kept at 0 °C, whereas the temperature of the right-hand half cell was varied from 0 to 85 °C. The salt bridge contained 2 M KCl solution, the surface area of the Pt electrodes was about 0.25 cm^2, and the potential was measured with a high impedance ($>10^{12}\,\Omega$) digital voltmeter. The results of these measurements are summarized in Table 3.1.

The electrode temperature was calculated for the different curves shown in Figure 3.8 using two methods: (i) temperature designated as $T_{\Delta E}$ was calculated from observed changes in the half-wave potential and an appropriate $\Delta E°/\Delta T$ value listed in Table 3.1, (ii) temperature designated as T_{slope} was calculated from the slope of the logarithmic analysis of a voltammetric curve (see Section 1.1.2.1.3 and Appendix C2). Both $T_{\Delta E}$ and T_{slope} were proportional to the measured thermocouple temperature (T_{TC}). However, the proportionality coefficients were significantly different: $\Delta T_{\Delta E}/\Delta T_{\text{TC}} = 1.00 \pm 0.03$ ($R^2 = 0.994$) whereas $\Delta T_{\text{slope}}/\Delta T_{\text{TC}} = 1.18 \pm 0.04$ ($R^2 = 0.995$). Therefore, in the case of the temperature determined from the logarithmic analysis, a systematic error of +18% was detected. Moreover, in other experiments performed with ordinary disk microelectrodes, it was observed that the ratio $\Delta T_{\text{slope}}/\Delta T_{\Delta E}$ rapidly increases with a decrease of the electrode radius. For example, the ratio was about 2 for a 25 μm electrode and about 4.5 for a 3.3 μm electrode (in all these cases a relatively low frequency of 145-165 MHz was used). Some temperatures determined by logarithmic analysis in the heating experiments with very small electrodes were irrationally high (e.g., >500 °C).

It is known that the oxidation of $K_4Fe(CN)_6$ can be inhibited by the formation of a Prussian blue-like film on the electrode surface.[89] Therefore, it is possible that the formation of such a film can be accelerated by an elevated temperature causing systematic errors in the logarithmic analysis. However, the quasireversibility of the redox process has to be ruled out as a likely source of the observed discrepancies. In order to detect any contamination of the electrode surface, test voltammograms were always recorded at identical conditions (without heating) at the beginning and at the end

of each experimental series. In more than 95% of cases these voltammograms were identical, and only the experimental series with reproducible test voltammograms were used in analysis. The logarithmic analysis of the voltammograms recorded without heating always gave correct slopes expected for a fully reversible redox process. Moreover, many experiments were done with 0.05 M KCN added to the supporting electrolyte to prevent Prussian blue formation. The results obtained with and without KCN were statistically identical. It has also been noted that for the electrodes of the same size the ratio $\Delta T_{slope}/\Delta T_{\Delta E}$ depends on the heating frequency. In Figure 3.9 a plot of $\Delta T_{slope}/\Delta T_{\Delta E}$ versus the heating frequency observed at a 25 μm Pt disk electrode in 0.5 M KCl containing 12.5 mM $K_4Fe(CN)_6$ is shown. The ratio dropped from 2 to 1.1 with the change of frequency from 145 to 900 MHz; however, at higher frequencies the ratio increases again up to about 1.6 at 1850 MHz.

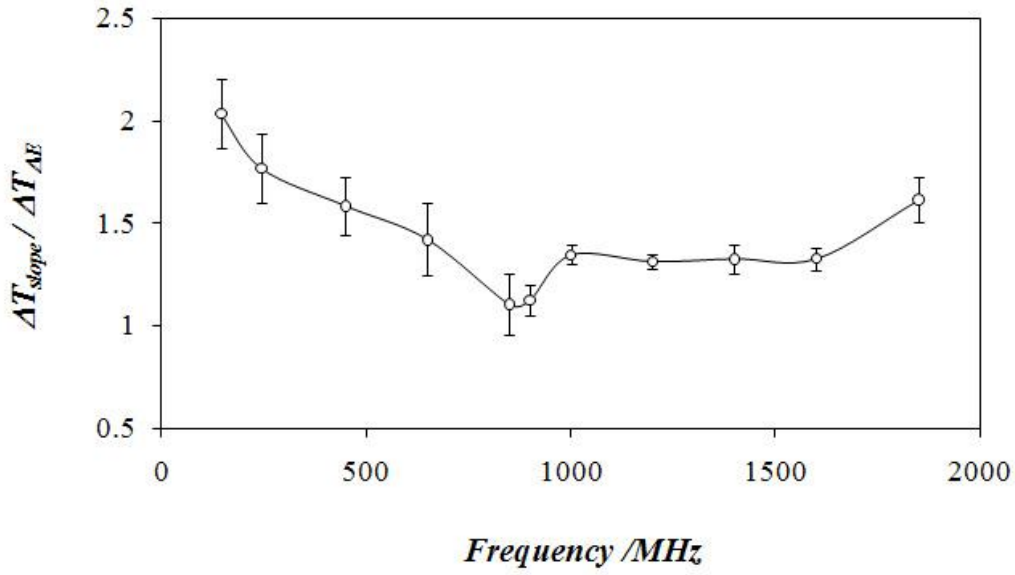

Figure 3.9 Frequency dependence of the $\Delta T_{slope}/\Delta T_{\Delta E}$ ratio observed at a Pt disk electrode (25 μm in diameter) in 0.5 M KCl containing 12.5 mM $K_4Fe(CN)_6$. Reproduced with permission from Reference 88. Copyright 2008 American Chemical Society.

The observed decrease in the magnitude of the systematic errors in ΔT_{slope} with an increase of the electrode diameter and an increase of frequency from 140 to 900 MHz

seems to correlate with the magnitude of the ac polarization of the electrode/solution interface, which could indicate that the errors are caused by faradaic rectification effects.[90] It is also absolutely clear that one of the two methods of temperature determination (half-wave potential shift or logarithmic analysis) must be inaccurate, and all experimental results indicate that the temperature determined from the logarithmic analysis is not reliable. On the other hand, measurements performed with the thermocouple microelectrode point out that determination of the electrode temperature from the half-wave potential shift is quite accurate. Therefore, this method of temperature determination was employed in all future work presented in this thesis. However, before we proceed to the results of the study of convection at hot microelectrodes, let us briefly discuss the effect of ac modulation on apparent reversibility of electrode processes.

3.2.4 Effect of ac modulation on apparent reversibility of electrode processes

As has been mentioned in the previous Section, determination of the temperature of a hot microelectrode from the logarithmic analysis of a steady-state voltammogram is not reliable and has an associated systematic error. Therefore, in the current Section an explanation is provided to the effect of ac modulation on apparent reversibility of electrode processes and, in particular, on the shape of steady-state voltammograms. The results which will be presented here are only a part of a new and very interesting research project. More details can be found in a recent publication by Baranski and Boika.[91]

In general, application of an alternating potential to a microelectrode (ΔV_A in Figure 3.2) leads to a potential drop across the solution resistance (ΔV_{R_s}) and a potential drop across the double layer ($\Delta V_{C_{dl}}$). For the heating of microelectrodes ΔV_{R_s} is of primary importance. However, particularly at lower frequencies of ac modulation, ac polarization of the double layer is substantial and it is responsible for faradaic rectification effects.

Faradaic rectification is a phenomenon which occurs due to a nonlinear relationship between the current flowing through the electrode and the potential across the electrode

interface. Current developments of the faradaic rectification technique for the study of electron-transfer kinetics have been summarized in a publication by Baranski and Diakowski.[90] For this project, however, it is important to realize that high frequency ac polarization of the electrode-solution interface affects the dc response (i.e., the current averaged over one ac cycle). This is especially noticeable in the case of irreversible redox processes, as shown in Figure 3.10 for a gold microelectrode in a sulfuric acid solution.

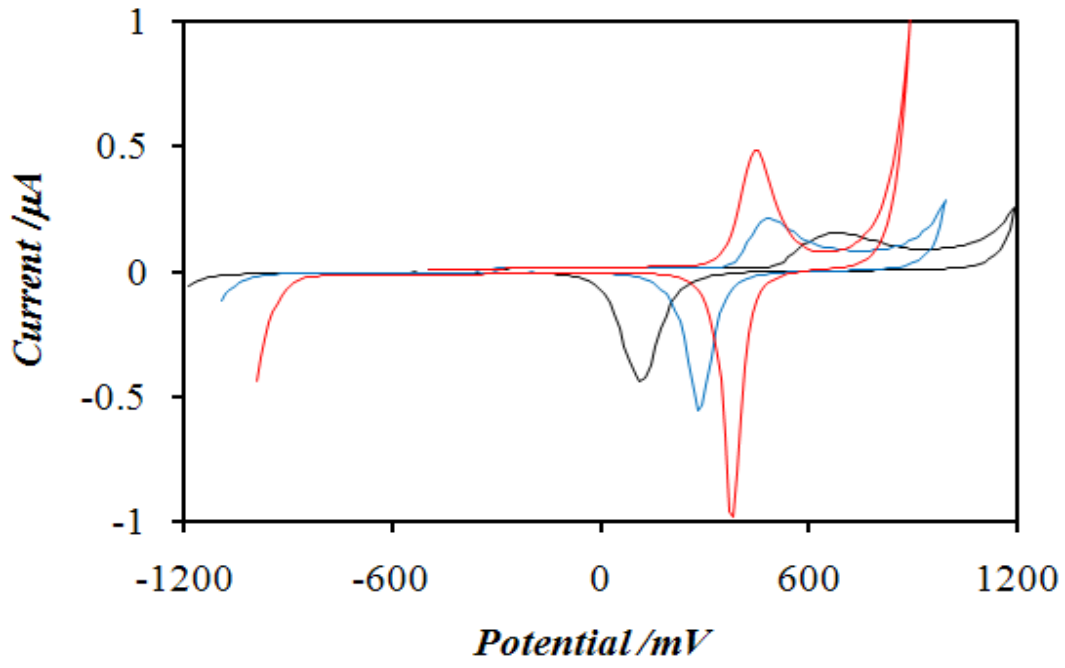

Figure 3.10 Cyclic voltammograms obtained with a 25 μm Au disk microelectrode in 0.3 M H_2SO_4 solution without superimposed ac modulation (black) and with ac modulation amplitudes 0.1 V_{rms} (blue) and 0.2 V_{rms} (red). The frequency of the ac modulation was 0.1 MHz, the scan rate was 20 V s^{-1}.

The redox processes shown by these voltammograms correspond to the formation of the gold oxide layer (anodic peak around 650 mV without ac modulation), gold oxide reduction (cathodic peak at 130 mV) and the formation of oxygen (most positive potentials) and hydrogen (most negative potentials). When the ac modulation is applied, all these processes are accelerated: the gold oxide formation/reduction process becomes more reversible (the peaks are sharper and the peak separation is smaller) and the

formation of oxygen and hydrogen occurs at less positive and less negative potentials, respectively. It should be noted here that the effects shown in Figure 3.10 are not caused by the heating of the sulfuric acid solution. This has been confirmed experimentally by adding 5 mM Fe(II) to the solution and measuring changes in the limiting current of Fe(II) oxidation during ac modulation. Detected change in the limiting current was negligible (less than 0.2 %), which means that the heating was insignificant, less than 0.1 K.

The effect of ac modulation on reversible or quasireversible processes (processes, which reach equilibrium during slow dc polarization, but not during an ac cycle) is the opposite to the case of completely irreversible processes. An increase of the amplitude of ac modulation leads to the decrease of the slope of steady-state voltammograms, so the voltammetric curves look like as if the process is less reversible. This is illustrated well in Figure 3.11 on the example of oxidation of potassium ferrocyanide.

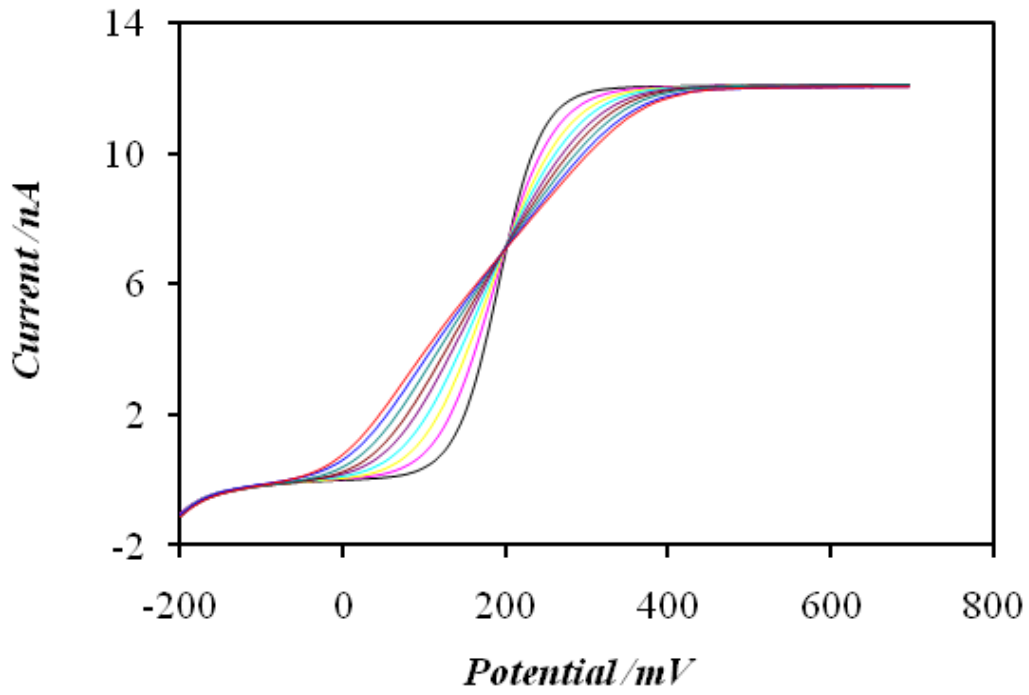

Figure 3.11 Steady-state voltammorgams corresponding to the oxidation of 20 mM $K_4Fe(CN)_6$ in 2 M KCl and 40 mM KCN at a 3.6 μm Pt disk microelectrode. The scan rate was 0.01 V/s and the ac modulation of 1 MHz with amplitudes (in V_{rms}): 0 (black), 0.053, 0.075, 0.092, 0.107, 0.12, 0.13, 0.14 and 0.15 (red).

Once again, the results in Figure 3.11 are not caused by the heating of the electrolyte solution, since the value of the limiting current does not change. However, such a change in slopes of the curves can be mistaken for heating. This is because the method of the temperature determination based on the logarithmic analysis is very sensitive to the shape of a steady-state voltammogram. Particularly, the value of the slope of the voltammogram at the half-wave potential is directly related to the temperature of a hot microelectrode according to the following equation:

$$\left(\frac{di}{dE}\right)_{i=\frac{i_{\lim}}{2}} = \frac{nF}{4RT_s} \cdot i_{\lim} \tag{3.6}$$

where T_s is the electrode surface temperature and $i_{\lim}$ is the value of the limiting current and other parameters have their usual meaning. Detailed derivation of this equation is given in Appendix C2.

Therefore, if the ac heating of the solution indeed occurs, then the presence of the effect shown in Figure 3.11 will result in the overestimation of the temperature of a hot microelectrode. The magnitude of the change in slope of the voltammogram (not caused by the temperature increase) is determined by the voltage drop across the double layer, which depends on the frequency of ac modulation. This is supported well by the results in Figure 3.12, where the ratio of the voltage drop across the double layer ($\Delta V_{C_{dl}}$) to the voltage applied to a microelectrode (ΔV_A) is plotted as a function of the frequency of ac modulation.

As can be seen in Figure 3.12, the ratio $\Delta V_{C_{dl}} / \Delta V_A$ is practically unity at low frequencies of ac modulation ($\leq$ 1 MHz). However, at higher frequencies this ratio is not equal to zero, which means that some polarization of the double layer still occurs. As a result, the slope of the voltammograms will be affected not only by temperature, but also by the faradaic rectification effect (as shown in Figure 3.11). Consequently, a systematic error in the value of temperature determined from the logarithmic analysis will be observed.

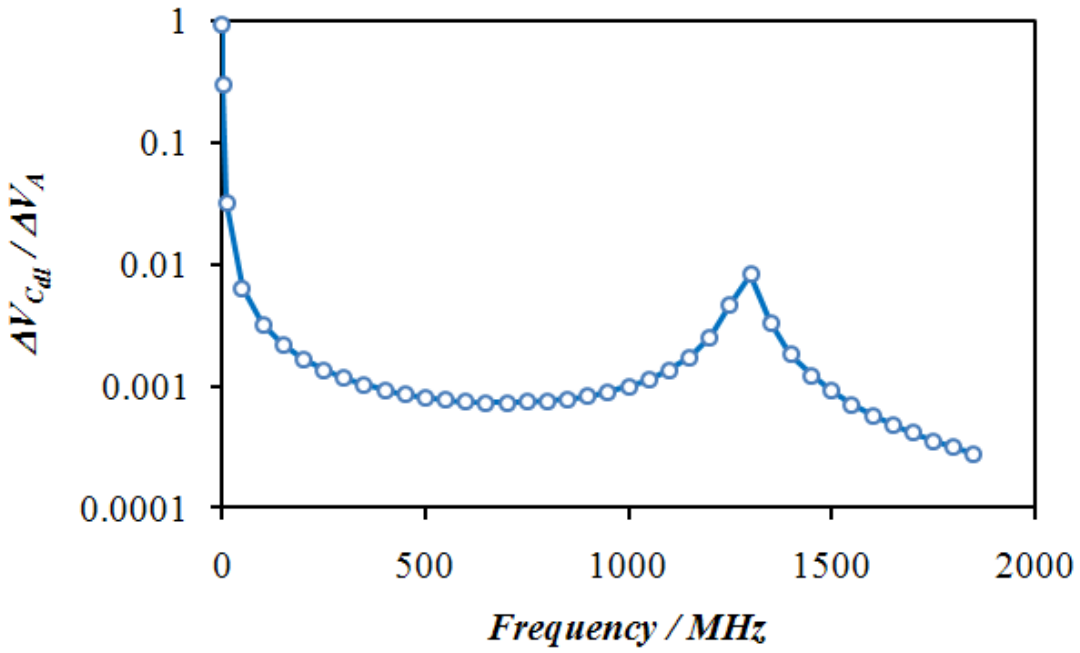

Figure 3.12 Frequency dependence (0.1 – 1850 MHz) of the ratio $\Delta V_{C_{dl}} / \Delta V_A$ based on the equivalent circuit in Figure 3.2 with the values of the electronic components as indicated in the legend of Figure 3.6.

It should also be noted here that the frequency dependence of the $\Delta V_{C_{dl}} / \Delta V_A$ ratio can explain the results shown in Figure 3.9: an increase in the $\Delta T_{\text{slope}}/\Delta T_{\Delta E}$ at frequencies above 900 MHz simply follows the change in $\Delta V_{C_{dl}} / \Delta V_A$. The match between these two sets of data is not quantitative, because the values of L_{el} and C_{st}, which determine the value of the resonance frequency, are not known precisely (the length of the electrode and the depth of its immersion into an electrolyte solution where not controlled when the experimental data in Figure 3.9 were collected).

3.3 CONVECTIONAL MASS TRANSPORT AT HOT MICROELECTRODES

The initial idea about convection at hot microelectrodes was that it is driven exclusively by buoyancy force. In general, buoyancy is the force acting on any object placed into liquid and it is given by the formula:

$$\bar{F}_b = -\rho V \bar{g} \qquad (3.7)$$

where ρ is the density of the liquid, V is the volume of the object and g is the gravitational acceleration. The negative sign in this equation indicates that buoyancy force is directed in the opposite direction to gravity.

The net force acting on the object is then equal to the sum of forces of gravity and buoyancy:

$$\overline{F}_{net} = (\rho_o - \rho) V \, \overline{g} \tag{3.8}$$

where ρ_o is the density of the object.

For a hot microelectrode, the above equation can be written in the following form:

$$\overline{F}_{net} = \frac{\partial \rho}{\partial T} \Delta T V \, \overline{g} \tag{3.9}$$

where the "object" is represented now by a hot zone in solution close to the electrode surface (volume *V*) and the term $\partial\rho/\partial T$ describes how the density of the liquid, such as water, changes with temperature.

Therefore, if convection in solution close to a hot microelectrode is driven by buoyancy, then the rate of convection should decrease with the size of the microelectrode. This is so since the size of the hot zone is proportional to the size of the microelectrode, and according to equation 3.9, the force should decrease for smaller electrodes. It is also expected that the rate of the convection driven by buoyancy depends on the orientation of the hot microelectrode with respect to the gravitational field. This can be explained by the interaction of the flowing solution with the electrode surface, which slows down the solution flow. When the surface of the electrode is perpendicular to the gravitational field (so-called horizontal orientation in Figure 3.13, a), then the rate of the convective flow of solution should be weaker compared to the vertical orientation of the electrode (Figure 3.13, b). As a result, it should be possible to observe corresponding changes in the magnitude of the limiting current enhancement factor when the size or orientation of the hot microelectrode is varied.

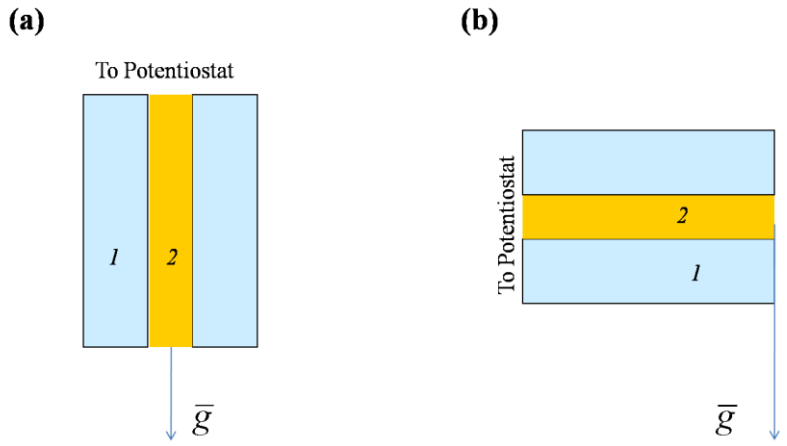

Figure 3.13 Orientation of microelectrodes used to investigate the effect of convection on mass transfer; **(a)** – horizontal orientation, **(b)** – vertical orientation. 1 – glass; 2 – metal wire.

To investigate these ideas, a set of experiments was done in which subsequent steady-state voltammograms corresponding to the oxidation of $Fe(CN)_6^{4-}$ were recorded at hot microelectrodes with a horizontal and a vertical orientation. It was expected that the vertical orientation would allow an easier flow of the solution and that would enhance the convectional mass transport. In addition, the experiments were carried out with Pt disk microelectrodes having different sizes (3.3, 10, 25, and 125 μm in diameter). The effect of convection was assessed by plotting the limiting current enhancement factor as a function of the electrode temperature determined from the shift of the half-wave potential (Figure 3.14).

The data in Figure 3.14 clearly indicate that the temperature dependence of the limiting current enhancement factor is independent of the electrode diameter. In the case of 10, 25, and 125 μm electrodes the vertical orientation produces significantly larger enhancement of the limiting current than the horizontal orientation. For a 3.3-μm electrode the changes caused by different orientations of the electrode were obscured by relatively large experimental errors and, because of this, only results obtained for the horizontal orientation are shown. In this case, the relatively large scatter of the data points can be attributed to a fast contamination of the electrode surface. In fact, during these measurements the electrode surface had to be cleaned a few times by wiping it with a soft paper tissue. In general, problems with the electrode contamination seem to increase with a decrease of the electrode radius. This is likely due to the fact that the rate

of diffusion of contaminants is inversely proportional to the electrode radius. In addition, an ac dielectrophoretic effect (which will be discussed at the end of this Chapter) may also contribute to the rapid contamination of very small electrodes.

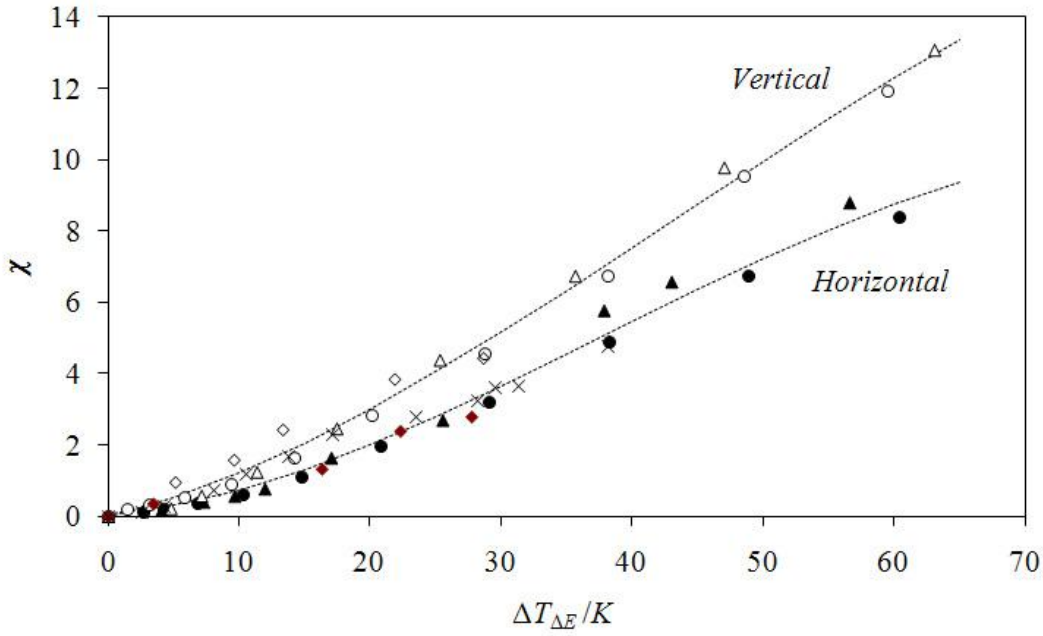

Figure 3.14 The limiting current enhancement factor plotted as a function of the electrode temperature for different electrode diameters and two different electrode orientations: electrode surface parallel to the gravitational field (◇ 125 μm, ○ 25 μm and △ 10 μm); electrode surface perpendicular to the gravitational field (◆125 μm, ● 25 μm ▲ 10 μm and × 3.3 μm) . These results are based on the steady-state oxidation of 10 mM $Fe(CN)_6^{4-}$ in 0.5 M KCl. Reproduced with permission from Reference 88. Copyright 2008 American Chemical Society.

In a different experimental series, the effect of the supporting electrolyte concentration on the limiting current enhancement factor was determined. In this case, steady-state voltammograms for the oxidation of $Fe(CN)_6^{4-}$ in KCl were recorded at a hot Pt disk electrode (25 μm in diameter). The concentration of KCl was varied from 0.2 to 2.0 M and the ratio of the supporting electrolyte concentration to the $K_4Fe(CN)_6$ concentration was kept constant and equal to 40. The plots of the limiting current enhancement factor as a function of the electrode temperature obtained in these experiments are shown in Figure 3.15.

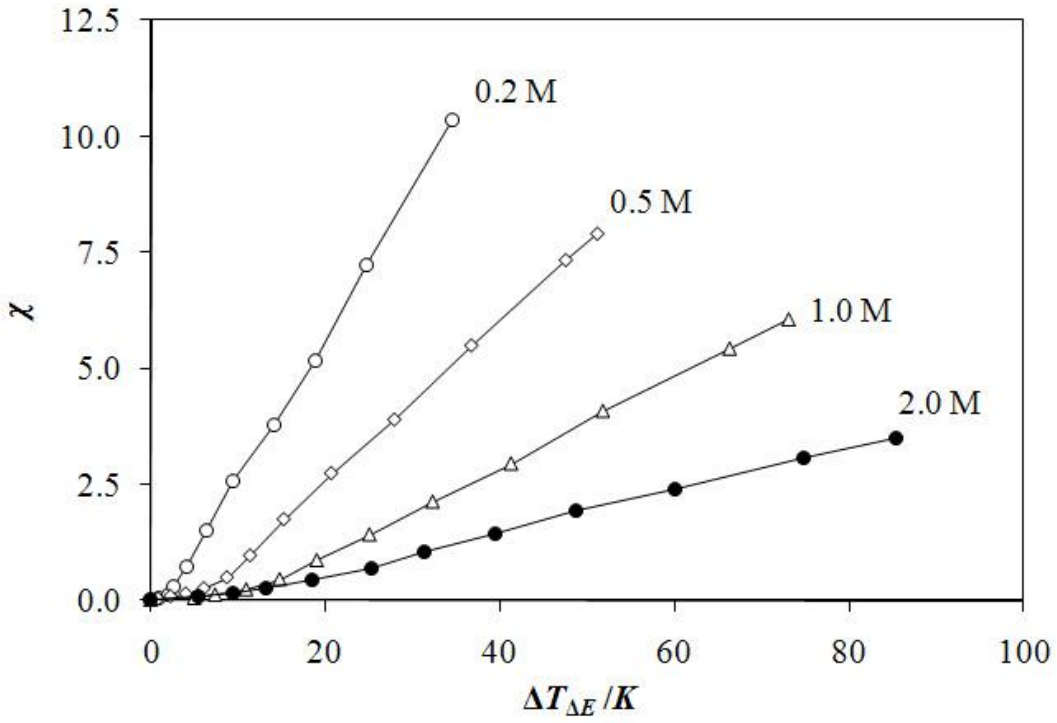

Figure 3.15 The limiting current enhancement factor plotted as a function of the change in the electrode temperature (determined from a shift of the half-wave potential) for different concentrations of the supporting electrolyte (KCl). Based on the steady-state oxidation $Fe(CN)_6^{4-}$ at a 25 μm Pt disk electrode. The ratio of concentrations of KCl to $Fe(CN)_6^{4-}$ was always 1:40, the solutions also contained 10 mM KCN. Reproduced with permission from Reference 88. Copyright 2008 American Chemical Society.

The results in Figure 3.15 show that the increase in the limiting current depends not only on the temperature difference (ΔT) between the bulk solution and the electrode, but also on the supporting electrolyte concentration (for the same value of ΔT). It should be emphasized that this conclusion is also valid if the electrode temperature is determined from the logarithmic analysis. This experimental series was repeated two times with statistically identical results.

In a control experiment conducted with a uniformly heated solution (using an electrochemical cell equipped with a water jacket, which was connected to a water circulation bath) the limiting current enhancement factors were determined for the oxidation of $Fe(CN)_6^{4-}$ as a function of the temperature and the supporting electrolyte concentration. It has been observed that the change of temperature by 30 K (from 25 to

55 °C) causes the enhancement factors of 1.03 ± 0.04, 0.89 ± 0.03, and 0.84 ± 0.03 in 0.2, 0.5 and 2.0 M KCl, respectively. Hence, the change of the viscosity of the solution with temperature most likely contributes to the limiting current enhancement observed at ac heated electrodes, but it cannot explain either the magnitude of the enhancement or the large effect of the supporting electrolyte concentrations shown in Figure 3.15 (here, for $\Delta T_{\Delta E}$ = 30 K, χ changes from about 9.8 to about 1.1 with a change of the concentration from 0.2 to 2.0 M). Furthermore, these large changes cannot be explained by very small (< 3%) changes in the thermal expansion coefficients of the studied solutions. Clearly, the major cause of the observed limiting current enhancements must be some kind of convection, which is not driven by buoyancy.

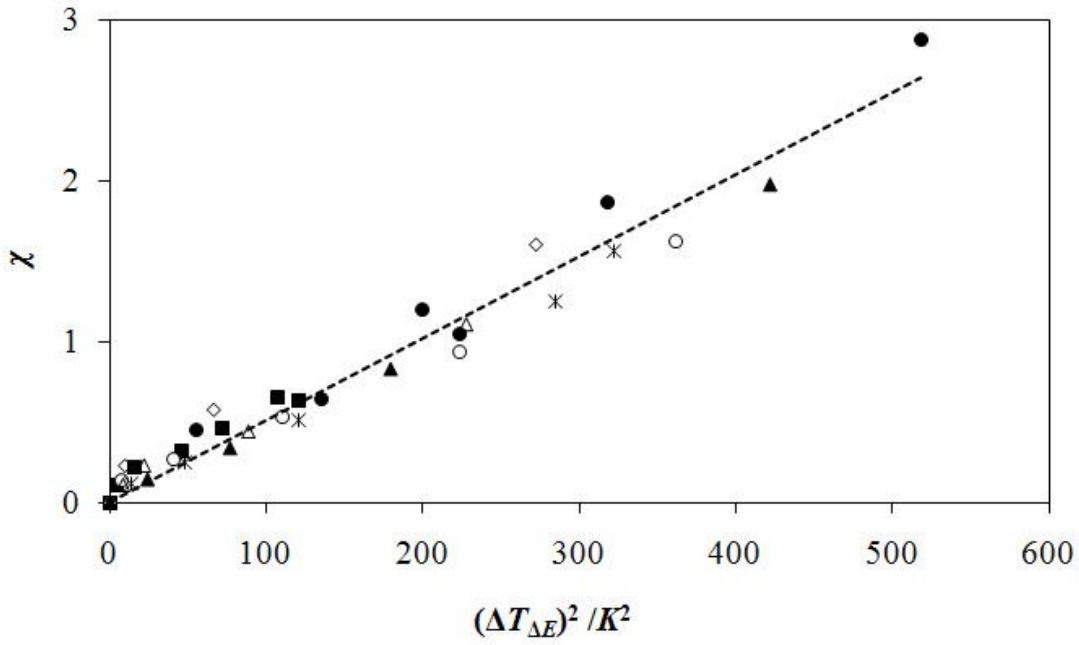

Figure 3.16 The limiting current enhancement factor plotted versus the square of the change in the electrode temperature. The results were obtained for the oxidation of 10 mM $Fe(CN)_6^{4-}$ in 0.5 M KCl at a 25 μm Pt disk electrode. The excitation waveform frequencies were: (●) 145, (◇) 800, (▲) 1000, (∗) 1200 and (△) 1400, (○) 1600 and (■) 1850 MHz. Reproduced with permission from Reference 88. Copyright 2008 American Chemical Society.

The effect of the excitation frequency on the convectional mass transport seems to be negligible. The limiting current enhancement factor was measured for the oxidation

of 10 mM $Fe(CN)_6^{4-}$ in 0.5 M KCl at a 25 μm Pt disk electrode. The electrode was heated with excitation waveforms of different frequencies ranging from 145 MHz to 1.85 GHz. The results shown in Figure 3.16 indicate that the limiting current enhancement factor depends only on the electrode temperature, but is independent of the excitation waveform frequency. In this case, the limiting current enhancement factor χ was plotted versus $(\Delta T_{\Delta E})^2$ and this relationship was determined to be linear provided that $\Delta T_{\Delta E} < 20$ K.

In addition, some experiments were done in very dilute solutions of the supporting electrolytes in order to check whether some enhancement in the limiting current can also be generated without heating, just by applying a high amplitude of ac polarization to the electrode. However, the result of this investigation was negative.

To obtain more information about the convection, hot-disk microelectrodes were observed under the metallurgical microscope. These observations were recorded and the obtained video files can be found on a CD disk enclosed with the printed copy of the thesis (representative frames are also included in Appendix E2). Two kinds of experiments were performed. In the first one (Video 3.1), gold microparticles (0.4-0.8 μm in diameter) were added to the solution.

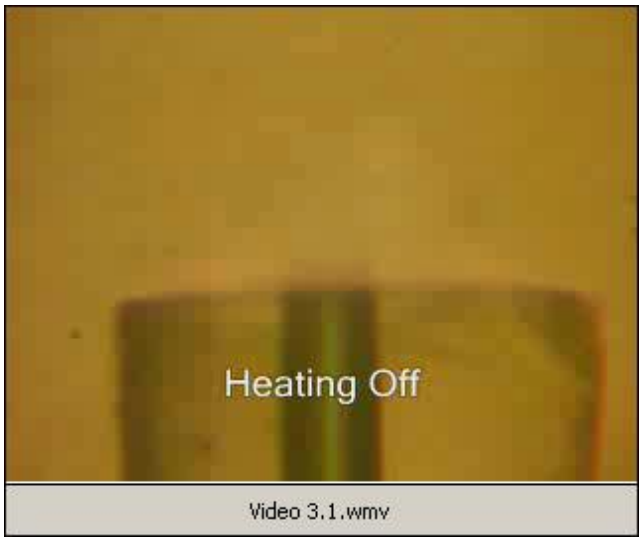

Video 3.1 Microscopic observations of convection at a 25 μm Pt disk electrode heated by an ac waveform of 2.0 V_{rms} at 160 MHz. The solution contained gold microparticles (0.4 to 0.8 μm in diameter) suspended in 0.6 M H_2SO_4 (see Appendix E2 for individual frames).

In this video one can clearly see the fast movement of the particles, which is caused by the heating of a 25 μm Pt electrode. The moment when the ac heating is turned on and off is indicated by a clicking sound and the appropriate subtitles.

Video 3.1 also shows interesting accumulation of gold microparticles at the circumference of the electrode. This accumulation is believed to be driven by the ac dielectrophoretic effect (Section 1.2.2.3). On the basis of Newman's works,[92,93] the potential gradient caused by the ohmic drop can be calculated in solution around a disk microelectrode polarized with an alternating voltage. At a frequency high enough to make the interfacial impedance negligible, the alternating electric field at the center of the electrode and near the electrode surface is given by the following equation:

$$\left(\frac{d\varphi}{dr}\right)_{r=r_0} = \frac{2\Delta V_{ac}}{\pi r_0} \qquad (3.10)$$

where ΔV_{ac} is the alternating voltage amplitude applied across the solution resistance and r_0 is the electrode radius.

So, for example, if r_0 = 12.5 μm and ΔV_{ac} = 2.8 V_{rms}, then the potential gradient reaches about $1.4 \cdot 10^5$ V m^{-1}. However, at the electrode circumference, the electric field is several times larger than at the electrode center, particularly when very high frequencies are used.[93] This is a so-called "edge" effect, which is responsible for the observed attachment of gold microparticles to the microelectrode surface at the disk circumference.

The dielectrophoretic force acting on gold microparticles is given by equation 1.45 (Section 1.2.2.3). For metal particles, the Clausius-Mossotti factor is equal to one. Therefore, they move towards the areas where the electric field is the strongest (i.e., the surface of a hot microelectrode). In addition, the field around a submicrometer metal particle attached to the electrode surface is even higher. For this reason, the particles are getting assembled into a wire.

In the second experiment (Video 3.2), the formation of the diffusion layer can be observed during the reduction of 50 mM methyl viologen in 0.5 M NaCl at a 25 μm Pt electrode. The first step of methyl viologen (MV^{2+}) reduction leads to the formation of a colored product ($MV^{+\cdot}$). Therefore, the behavior of the $MV^{+\cdot}$ diffusion layer with respect

to the applied ac heating can be easily monitored and it can provide information about the solution flow. The video shows the formation of a relatively wide spherical diffusion layer at the electrode without heating. This original diffusion layer is swept away momentarily when the heating is turned on. The new diffusion layer, which develops at the hot microelectrode, is significantly smaller due to a very strong convectional flow of the solution.

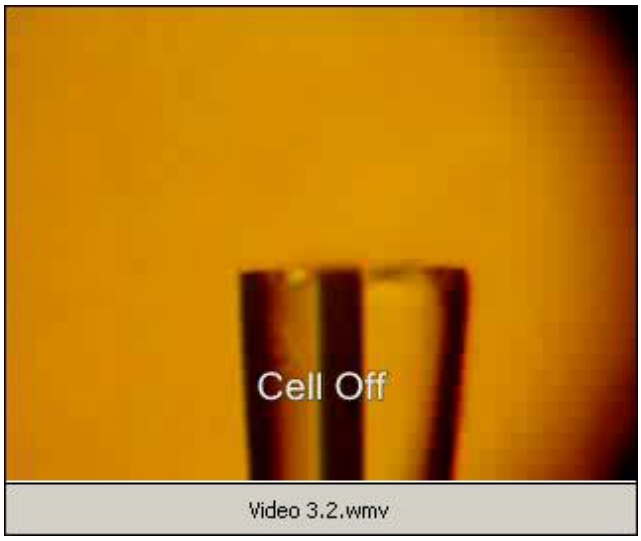

Video 3.2 Effect of ac heating on the diffusion layer formed during the reduction of 50 mM methyl viologen in 0.5 M NaCl at a 25 μm Pt electrode. The electrode was heated with an alternating voltage of 2.8 V_{rms} at 160 MHz; the dc potential of the working electrode was –0.5 V vs. Ag | AgCl(s) | 2 M KCl. The electrode axis was perpendicular to the gravitational field (see Appendix E2 for individual frames).

While working with very small hot microelectrodes, an interesting phenomenon has been observed. In the third video (Video 3.3), one can see that, due to the extreme heating of solution, vapour bubbles are formed at the surface of a hot microelectrode. These bubbles are immediately dislodged into the bulk solution. Interestingly, similar observations have been recently reported by Compton and co-workers[82] for microwave heated electrodes (they refer to this phenomenon "jet boiling").

Video 3.3 Jet boiling at an overheated 3.6 μm Pt electrode in 2.0 M KCl containing 50 mM methyl viologen. The electrode was heated with an alternating voltage of 2.8 V_{rms} at 165 MHz; the dc potential of the working electrode was –0.5 V vs. Ag | AgCl(s) | 2 M KCl. The electrode axis and the direction of the jet was perpendicular to the gravitational field (see Appendix E2 for individual frames).

Such a movement of the vapor bubbles can be explained by a strong negative dielectrophoretic effect: the bubbles have much lower permittivity than the surrounding solution, so they are pushed out of the high electric field.

3.4 MECHANISM OF CONVECTION AT ALTERNATING CURRENT HEATED MICROELECTRODES

A plausible mechanism of the convection observed at hot microelectrodes should explain why the limiting current enhancement factor is independent of the electrode radius and frequency (at least under the experimental conditions listed in Figures 3.14 and 3.16), but increases with a decrease of the supporting electrolyte concentration (Figure 3.15).

Strong effect of the supporting electrolyte concentration may suggest that this convection is linked to ac electrokinetic phenomena generated in the electrical double layer. The flow of solution induced by an ac polarization of the electrical double layer is known as the ac electroosmotic flow (Section 1.2.2.1). However, the electroosmotic flow depends very strongly on frequency and it is usually observed below 100 kHz. On the other hand, convection observed at ac polarized microelectrodes can be easily

explained by the electrothermal fluid flow, which may occur in an electrolytic solution if a large temperature gradient coincides with a large potential gradient (Section 1.2.2.2). The temperature gradient causes changes in the permittivity of the solution. This gives rise to the dielectric force, which pushes colder solution towards higher electric fields. The temperature gradient also causes changes in the electrical conductivity of the solution. This generates an unbalanced electrical charge in the solution, because a local concentration of ions, which move with the temperature gradient, tends to decrease, and a local concentration of ions, which move against the temperature gradient, tends to increase. This electrical charge interacts with the electric field giving rise to the Coulomb force. As a result, hotter solution is repelled from a high electric field. It should be noted that, in the case of a hot-disk microelectrode, both the dielectric and the Coulomb forces can drive the convection, but the direction of the solution flow in these two cases will be the opposite. A time-averaged electrothermal force per unit volume of an electrolyte solution is given by equation 1.34 (Section 1.2.2.2). In this equation, the effect of the frequency of ac modulation on the electrothermal force is expressed through the $M(\omega)$ frequency factor. When $\omega\tau$ << 1 (where τ is the charge relaxation time), the ac current flows through ohmic conductance and the force predicted by equation 1.34 is due to the Coulombic interactions. On the other hand, when $\omega\tau$ >> 1 the ac current flows through capacitance, and the force predicted by the same equation is the dielectric force.

In one-dimensional space with spherical symmetry equation 1.34 can be written as

$$F_E = -M(\omega)\frac{\varepsilon}{2}\frac{dT}{dr}\left(\frac{d\varphi}{dr}\right)^2 \qquad (3.11)$$

For a spherical electrode polarized with an alternating potential, $\frac{d\varphi}{dr} = \frac{\Delta V_{Rs}}{r_0}\cdot\left(\frac{r_0}{r}\right)^2$ and, based on the paper by Baranski,[7] (see equation 1.7) $\frac{dT}{dr} = \frac{\Delta V_{Rs}^2}{\rho k\, r_0}\left(\frac{r_0}{r}\right)^2\left(\frac{r_0}{r}-1\right)$ (where r_0 is the electrode radius, ΔV_{Rs} is the amplitude of the ac potential across the solution resistance and *k* is the thermal conductivity of the solution). Consequently, equation 3.11 can be written as

$$F_E = M(\omega)\frac{\varepsilon\sigma\Delta V_{Rs}^4}{2kr_0^3}\left(\frac{r_0}{r}\right)^6\left(1-\frac{r_0}{r}\right) = M(\omega)\frac{2\varepsilon k\Delta T^2}{\sigma r_0^3}\left(\frac{r_0}{r}\right)^6\left(1-\frac{r_0}{r}\right) \qquad (3.12)$$

where ΔT is the temperature difference between the electrode surface and bulk solution and other symbols have the same meanings as in equations 1.33 and 1.34.

The mass transfer and the current flow at a disk electrode are very similar to the ones observed at a spherical electrode. However, the heat transfer is quite different, because at a disk electrode the heat is generated only in the solution, but it dissipates in all directions (including the electrode body). In addition, the forces described by equation 1.34 point out of the center of the disk (if $\omega\tau$ <<1), but they are not evenly distributed around the electrode; the forces are the largest near the electrode edge and the weakest in the center, perpendicularly to the electrode surface.

The electrothermal force depends on both the electric field gradient and the temperature gradient. Therefore, ac modulation of the electrode potential without heating will not drive the convection, which is in agreement with the obtained results. According to equation 1.34, it can also be predicted that the rate of the convection should be proportional to ΔV_{Rs}^4, because $\nabla T \propto \sigma\Delta V_{Rs}^2$ and $\nabla\varphi \propto \Delta V_{Rs}$; the same can also be seen in equation 3.12. This prediction is in good agreement with the results presented in Figure 3.5, Section 3.1.1. However, this simple relationship is not strictly valid in the case of very intense heating and/or very intense convection, because the electrical conductivity of the solution changes with temperature and convection increases heat dissipation and alters the distribution of temperature around the electrode (although the effects listed here compensate each other to some extent). Consequently, for small ΔT the rate of convection should be proportional to ΔT^2; this relationship is observed in Figure 3.16, Section 3.3.

The electrode temperature depends on the Joule heating (equation 3.5). When the electrolyte solution is more dilute, R_s increases and, in order to keep the same temperature of the electrode, ΔV_{Rs}^2 has to be increased proportionally to R_s. If the temperature gradient is the same, then, according to equation 1.34, the force acting on solution should be proportional to ΔV_{Rs}^2. Therefore, if all other conditions are the same, the rate of the electrothermal convection should be proportional to the solution

resistance (or inversely proportional to the electrical conductivity of solution). This conclusion is in good agreement with the results presented in Figure 3.15.

To explain why the limiting current enhancement factor is independent of the electrode radius, let us consider the following. Firstly, it should be pointed out that at disk microelectrodes, the rate of diffusional mass transport is inversely proportional to the electrode radius, and it can be expressed in terms of the linear velocity of the depolarizer as $4D/\pi r_0$ (where D is the diffusion coefficient of the depolarizer and r_0 is the electrode radius).[17] Therefore, in order to have the limiting current enhancement factor independent of the electrode radius, the rate of convection expressed in terms of the linear velocity of solution must be inversely proportional to the radius. Secondly, let us take a look at two electrode systems, S and S', which differ only by the size of their electrode radii r_0 and r_0', respectively (Figure 3.17). These systems can be described using cylindrical coordinates normalized with respect to the electrode radii, so $\bar{r} = r/r_0 = r'/r_0'$ is the normalized distance from the axis of symmetry and $\bar{z} = z/r_0 = z'/r_0'$ is the normalized vertical distance from the electrode plane. The third coordinate, θ, which represents angular displacement about the axis of symmetry, is defined in the same way in both systems. Now, let us select in both systems two volume elements Δv and $\Delta v'$ enclosed by the same set of normalized coordinates ($\bar{r}, \bar{z}, \theta$ and $\bar{r} + \Delta\bar{r}, \bar{z} + \Delta\bar{z}, \theta + \Delta\theta$). These two volume elements will be called "analogous". It is obvious that, in this case, the ratio of the volumes is $\Delta v'/\Delta v = \left(r_0'/r_0\right)^3$. But, according to equation 1.34, the force acting on the two analogous volume elements must be the same, because ∇T and $\nabla\varphi$ are inversely proportional to the electrode radius.[7] However, the frictional force is proportional to the linear size and velocity of a moving object, so the velocities of these volume elements will be inversely proportional to the electrode radii. The same conclusion applies to any pair of analogous volume elements in these two systems. Hence, if all other conditions are the same, the linear velocity of solution driven by the electrothermal effect at a hot-disk electrode is, indeed, inversely proportional to the electrode radius.

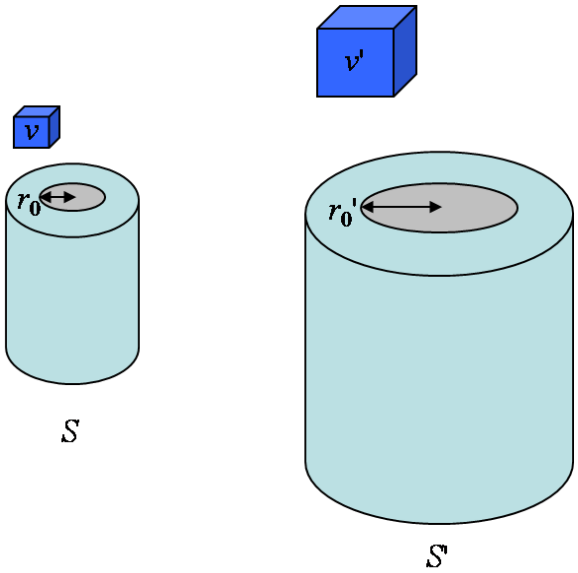

Figure 3.17 Electrode systems *S* and *S′* with defined "analogous" volume elements *v* and *v′*; r_0 and r_0' are the radii of the electrodes.

Following the same way of thinking, one could show that the rate of convection caused by buoyancy should be proportional to r_0^2 and it should have no observable effect on the mass transport at microelectrodes used in this work (calculations of the buoyancy force in microelectrode structures done by Ramos[33] also support this idea). This raises a question about how to explain the effect of the electrode orientation shown in Figure 3.14. It is believed that in the case of the vertical orientation, the symmetry of the hot zone becomes slightly distorted and the increased asymmetry of the temperature gradient intensifies the electrothermal convection.

Finally, let us discuss the effect of frequency. Equation 1.34 predicts that the electrothermal force strongly depends on frequency when $\omega \approx \tau^{-1}$. In addition, at a cross over frequency (f_c, equation 3.13) the force should drop to zero.

$$f_c = \frac{\varepsilon}{2\pi\sigma}\sqrt{1-2\frac{\partial\sigma/\partial T}{\partial\varepsilon/\partial T}} \qquad (3.13)$$

The results presented in Figure 3.16 show that the limiting current enhancement factor observed in 0.5 M KCl is independent of frequency between 0.145 and 1.85 GHz.

However, in this case, f_c = 4.3 GHz, so the frequency dependence may not be very strong in the discussed frequency range. Similar measurements were repeated with 0.1 M KCl. In this case, according to equation 3.13, f_c = 0.92 GHz and a clear frequency dependence was observed. In Figure 3.18 the experimental values of $\Delta\chi/\Delta T^2$ (i.e., the slopes of the graphs of the limiting current enhancement factors plotted versus $(\Delta T_{\Delta E})^2$) are compared with the theoretically predicted changes in the frequency factor $M(\omega)$. The match is not quantitative, but both relationships show very similar trends.

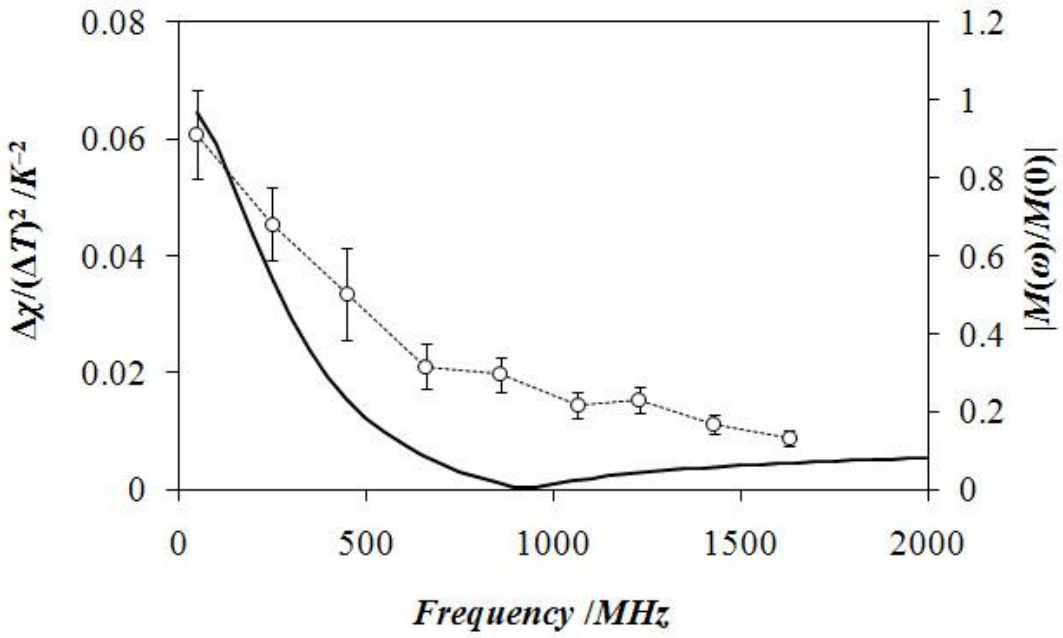

Figure 3.18 Markers show a frequency dependence of $\Delta\chi/(\Delta T)^2$ observed during the oxidation of 2.5 mM $Fe(CN)_6^{4-}$ in 0.1 M KCl and 5 mM KCN at a 25 μm Pt disk electrode. The solid line represents absolute values of *M(ω)* coefficient defined in equation 1.34 and normalized by *M(ω=0)*. Reproduced with permission from Reference 88. Copyright 2008 American Chemical Society.

A perfect match, in this case, cannot be expected, because values of the limiting current enhancement factor χ are only a very approximate measure of the rate of convection (χ is also affected by other parameters, such as the temperature dependence of the diffusion coefficient). Also, equation 1.34 is approximate, since a frequency dependence of dielectric permittivity and electrical conductivity of the solution was not

taken into account. Experimental data in Figure 3.18 are quite scattered, because heating in 0.1 M KCl is weak, the measurements have to be done with a relatively low concentration of the depolarizer (this increases the noise), and the curves are more distorted by the faradaic rectification, particularly at low frequencies. All this contributes to larger errors in the determination of $\Delta T_{\Delta E}$.

CHAPTER 4: SIMULATION OF ELECTROTHERMAL CONVECTION AT HOT MICROELECTRODES

In this Chapter, the results of numerical simulations of the effect of electrothermal convection on mass transfer at hot microelectrodes are presented. The material is arranged as follows. Firstly, a general introduction is given to the simulation model, including its simplifications and approximations. After that, more details are provided with respect to each simulation step, from the calculation of the ac potential distribution to the computation of the rate of mass transfer of redox species. At the end, the results of the simulations are analyzed and compared to the experimental data.

4.1 FOREWORD

There were a number of reasons for doing numerical simulations of the processes occurring at hot microelectrodes. First of all, from the results presented in previous Chapters, it is not clear what is the distribution of temperature in solution around a hot microelectrode. Experimentally it is possible to measure temperature only at the surface of the electrode. Yet, that value by itself is not sufficient to describe the temperature field in the hot zone. In Section 3.4 it was described that the presence of the temperature gradient together with the ac potential gradient leads to the appearance of the electrothermal convective flow of solution. To describe this convection (equation 3.12), an expression for the temperature gradient was used, which was developed for a hot spherical microelectrode. However, that model is not strictly applicable to disk microelectrodes, since it does not account for the heat transfer from solution into the electrode body. In addition, in a publication by Marken *et al.*,[21] who work with disk microelectrodes heated by microwave radiation, the authors report the formation of a 'hot spot' region in the diffusion layer of the electrode (Section 1.1.3). The temperature

of solution in that region, according to their simulation results, is much higher than the temperature at the electrode surface. Therefore, in order to address the phenomenon of electrothermal convection quantitatively, the distribution of temperature at hot-disk microelectrodes has to be determined. This information will be required in calculations of the electrothermal force and the rate, as well as the direction of solution flow.

The second reason for doing numerical simulations was to evaluate the effect of Soret diffusion on mass transfer of redox species at hot microelectrodes. According to the theory (Section 1.2.1.2, equation 1.9), the effect of thermodiffusion is complex, since thermoelectric migration can also affect the rate of mass transfer. In addition, strong convection can mask thermodiffusion. Therefore, the study of the Soret effect at hot microelectrodes is practically impossible without simulations. The details of these studies are presented in Chapter 5

Let us briefly discuss the simulation process. Numerical simulations involve the following steps:

a) calculation of the ac potential distribution and the potential gradient around a disk microelectrode,

b) calculation of the temperature distribution (initial and boundary conditions are stated on p. 105),

c) calculation of the electrical force acting on an electrolyte solution,

d) stream function calculation and determination of the linear flow rate of solution (initial and boundary conditions are stated on p. 112-113) and, finally,

e) calculation of the mass transfer rate and simulation of the voltammetric response of a hot microelectrode (initial and boundary conditions are stated on p. 116-117).

As one can see, in the first two steps (a, b) the temperature field is simulated. This data is used afterwards to determine the force acting on the solution and calculate the solution flow rate (c, d). In the final step (e), the rate of the redox species mass transfer is calculated and cyclic voltammograms are simulated. All these steps are explained further in this Chapter. Before the details are given, let us state the assumptions and approximations of the simulation algorithm.

In calculations of temperature distribution, it is assumed that the properties of the solution, such as its viscosity, electrical and thermal conductivities, are temperature

independent. Indeed, these parameters may be considered constant provided that the temperature change is low. Therefore, the simulations are done for what is called "low heating", when the electrode surface temperature does not exceed the temperature of the bulk solution by 10 – 15 K. In addition, the simulations do not account for the effect of convection on temperature distribution. However, the magnitude of this effect is not expected to be large in the case of weak ac heating.

A number of approximations are related to the definition of the boundary conditions (in calculations of the temperature distribution, electrothermal force and solution flow rate), the size of the simulation grid and the distance step Δh. The details about these approximations will be provided later in this Chapter. Here it should be noted that, theoretically, it is possible to account for the stated above simplifications and approximations. However, that would require much more time for the simulations to complete and, therefore, would not be effective considering currently available computing resources.

4.2 SIMULATION ALGORITHM

4.2.1 Coordinate system

Due to the symmetry of disk microelectrodes, the following cylindrical coordinate system has been used in simulations (Figure 4.1). In the top part of Figure 4.1 one can see what is called the simulation space – that part of the system including a disk electrode and an electrolyte solution in contact with it, for which the calculations are done. This space is divided into elements or cells forming the simulation grid (Figure 4.1, *Bottom*). Cells in the centre of the space (ρ = 0) have cylindrical shape, with the radius of their base equal to $\Delta h/2$ and the height Δh. All other elements can be represented as rings having the same thickness and height Δh. The value of the distance step (Δh) is determined by the electrode radius (r_0) and the number of rings (or elements) per electrode radius, n ($\Delta h = r_0/n$). Both of these parameters are entered into the simulation program (see Appendix E for details). The size (or volume) of the simulation space is controlled by the number of layers, into which the space is divided in z direction, and the number of rings in ρ direction. These parameters can also be selected in the simulation program.

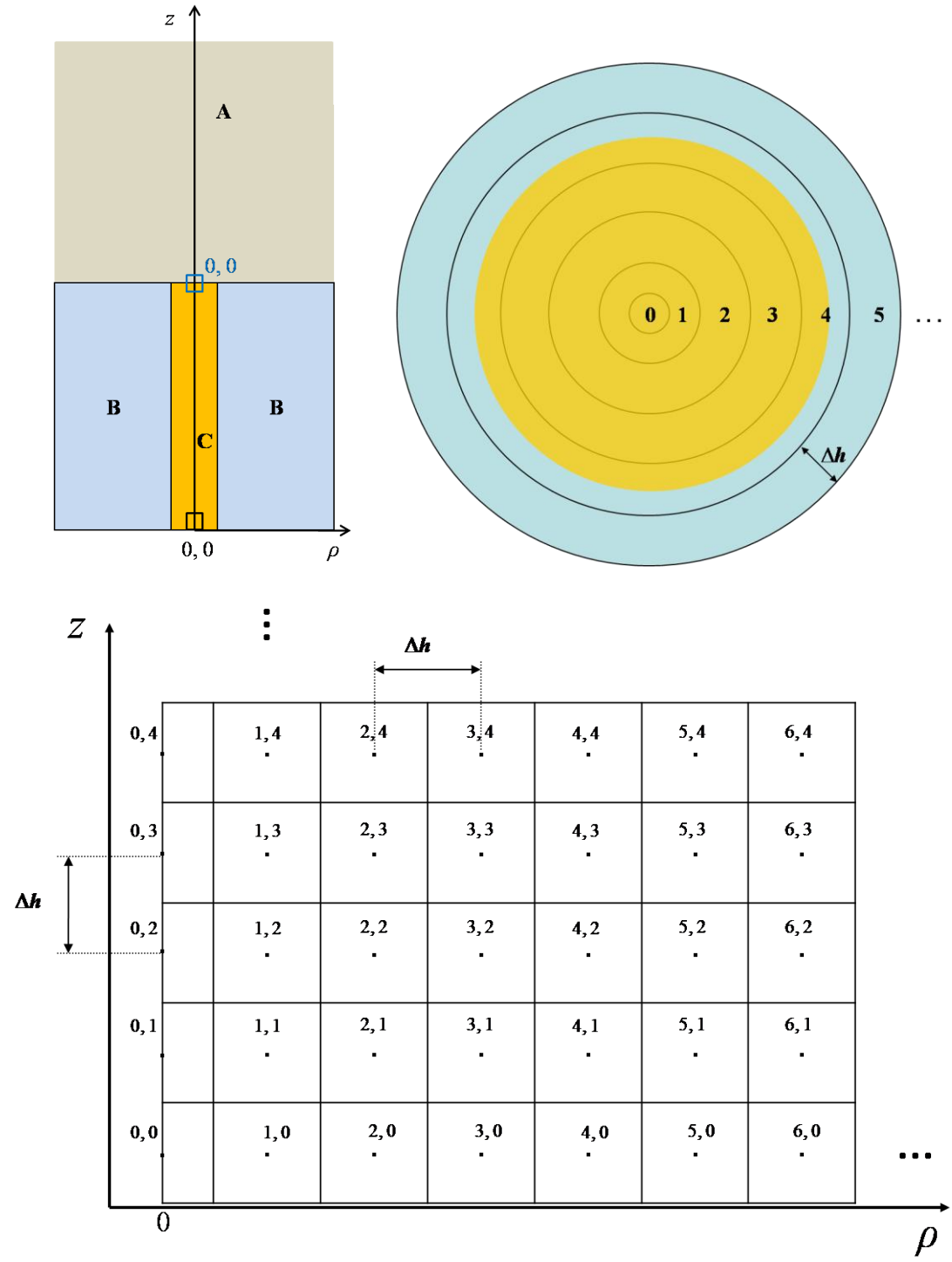

Figure 4.1 Description of the simulation space and the coordinate system used in numerical simulations in the case of a disk microelectrode. *Top* part shows the simulation space and how it is divided into elements (yellow circle represents the electrode disk). A – solution, B – insulation (glass), C – metal wire. *Bottom* part illustrates indexing of elements (simulation grid). Δh is the distance step.

The values of the variables of interest, such as ac potential, temperature, electrothermal force, stream function, solution flow rate and concentration of redox species are assigned or calculated for the centre of each element, which is represented by a dot (Figure 4.1, *Bottom*). The position of the elements in the simulation space is indicated by a pair of coordinates P and Z (P indicates the position along ρ-axis and Z – along z-axis). Thus, all the elements (or, alternatively, all the dots) form the simulation grid. In the simulation program it is possible to vary the number of layers, rings and rings per electrode radius, i.e. the simulation grid can be changed. Most of the simulation results, which will be shown and discussed in this thesis, have been obtained using a 128×128_8 grid (128 elements in ρ-direction (layers), 128 elements in z-direction (rings) and 8 elements per electrode radius). In some cases other grids have been used, such as 64×64_4, 256×256_16 and 512×512_32. It should also be clarified here that in the temperature distribution calculations the actual number of layers in the grid is twice the number indicated by the grid abbreviation (for example, 256 layers for a 128×128_8 grid). This is because the calculations of temperature distribution are done for the whole simulation space, which includes both the electrode body and the electrolyte solution. However, all other calculations are done only for the solution part, which constitutes one half of the overall simulation volume. Thus, the zeroth element (0, 0) in temperature calculations is located in the body of the electrode as shown by a black square in the top left part of Figure 4.1. However, for all other calculations the zeroth element is chosen to be at the interface between the electrode and the solution (blue square). In the following several Sections of this Chapter all equations used in numerical simulations will be discussed, including the appropriate initial and boundary conditions.

4.2.2 Calculation of the potential distribution

In general, potential distribution can be calculated by solving Laplace's equation. In the case of a disk electrode, this equation has been solved by Newman and the analytical solution is known:[92]

$$\frac{\Phi}{\Phi_0} = 1 - \left(\frac{2}{\pi}\right)\tan^{-1}\xi \qquad (4.1)$$

where Φ_0 is the potential on the surface of the electrode disk and ξ is the rotational elliptic coordinate.

ξ is related to cylindrical coordinates (Figure 4.1) by the following equations:

$$z = r_0 \xi \eta \tag{4.2}$$

and

$$\rho = r_0 \sqrt{\left(1+\xi^2\right)\left(1-\eta^2\right)} \tag{4.3}$$

In equations 4.2 and 4.3 r_0 is the radius of the electrode disk and η is the second elliptic coordinate.

Expressing ξ using cylindrical coordinates ρ and z one obtains that:

$$\xi = \sqrt{\frac{\left(\rho^2/{r_0}^2 + z^2/{r_0}^2 - 1\right) + \sqrt{\left(\rho^2/{r_0}^2 + z^2/{r_0}^2 - 1\right)^2 + 4z^2/{r_0}^2}}{2}} \tag{4.4}$$

As a result, equations 4.1 and 4.4 allow calculation of the ac heating potential distribution in an electrolyte solution. Therefore, in the next step, the temperature distribution can be determined.

4.2.3 Calculation of the temperature distribution

To determine the distribution of temperature in any system a heat conduction equation needs to be solved. This equation in Cartesian coordinates is written as follows:[94]

$$-\frac{\partial Q_x}{\partial x} - \frac{\partial Q_y}{\partial y} - \frac{\partial Q_z}{\partial z} + Q_g = d\,C\,\frac{\partial T}{\partial t} \tag{4.5}$$

where Q is the heat flux across a corresponding surface of an infinitesimally small control volume (rectangular parallelepiped dxdydz) in the direction indicated by the subscript x, y or z, Q_g is the rate of heat generation per unit volume, d is the density, C is the specific heat capacity of the material and t is time.

The heat fluxes can be expressed according to the Fourier's law of heat conduction and equation 4.5 can be rewritten as

$$\frac{\partial}{\partial x}\left(k\frac{\partial T}{\partial x}\right) + \frac{\partial}{\partial y}\left(k\frac{\partial T}{\partial y}\right) + \frac{\partial}{\partial z}\left(k\frac{\partial T}{\partial z}\right) + Q_g = d\,C\,\frac{\partial T}{\partial t} \tag{4.6}$$

where k is the thermal conductivity of the material.

Thus, the above equations 4.5 and 4.6 indicate that the temperature distribution in a body depends on its properties, such as the heat capacity and thermal conductivity. The exact solution of these equations depends also on the initial and boundary conditions imposed on the system. In some cases an analytical solution may be obtained. However, in most cases, numerical solutions are much easier to obtain considering the computing power of modern computers.

For the coordinate system shown in Figure 4.1 one can write the heat balance equation for each of the elements based on the energy conservation principle similar to equation 4.6:

$$CV\frac{\partial T}{\partial t} = Q_t + Q_b + Q_p + Q_s + Q_g \qquad (4.7)$$

where Q_t is the rate of heat transfer into a considered element from the above (top) element, Q_b is the rate of heat transfer from the bottom element, Q_p is the rate of heat transfer into a considered element from the preceding element, Q_s is the rate of heat transfer from the succeeding element and Q_g is the rate of generation of heat in the element due to ac heating. V is the volume of the element and C is its heat capacity expressed per unit volume.

After the rate of the heat transfer is expressed according to the Fourier's law, the equation for the temperature in the considered element can be written in the numerical form as follows:

$$T'_{\mathrm{P},Z} = T_{\mathrm{P},Z} + \frac{k\Delta t}{C(\Delta h)^2}\left[\begin{array}{l}\frac{S_v \Delta h}{V}\left(T_{\mathrm{P},Z+1} + T_{\mathrm{P},Z-1} - 2T_{\mathrm{P},Z}\right) + \\ + \frac{S_p \Delta h}{V}\left(T_{\mathrm{P}-1,Z} - T_{\mathrm{P},Z}\right) + \frac{S_s \Delta h}{V}\left(T_{\mathrm{P}+1,Z} - T_{\mathrm{P},Z}\right)\end{array}\right] + \frac{\Delta t}{CV}Q_g \qquad (4.8)$$

where S is the surface area between the neighbouring elements, T is the temperature in the particular element and T' – the temperature after the time period Δt passes. Other variables have the same meaning as described in equations 4.6 and 4.7.

In the above equation 4.8, the ratio of the surface area between the elements (S) to the volume of the considered element (V) multiplied by the distance step (Δh) is a dimensionless parameter A, which is calculated by one of the equations 4.9 – 4.11.

Subscript "*p*" indicates the surface area between the considered element and the proceeding one, "*s*" indicates the surface area between the considered and succeeding elements and "*v*" – between the considered element and the vertical element (either top or bottom).

$$A_p = \frac{S_p \Delta h}{V} = \frac{\pi (\Delta h)^2 (2\mathrm{P}-1)}{2\mathrm{P}\pi (\Delta h)^3} \Delta h = \frac{2\mathrm{P}-1}{2\mathrm{P}} \tag{4.9}$$

$$A_s = \frac{S_s \Delta h}{V} = \frac{\pi (\Delta h)^2 (2\mathrm{P}+1)}{2\mathrm{P}\pi (\Delta h)^3} \Delta h = \frac{2\mathrm{P}+1}{2\mathrm{P}} \tag{4.10}$$

$$A_v = \frac{S_v \Delta h}{V} = \frac{2\mathrm{P}\pi (\Delta h)^2}{2\mathrm{P}\pi (\Delta h)^3} \Delta h = 1 \tag{4.11}$$

where P is the index of the element.

The initial condition for equation 4.8 is that the temperature in all elements of the simulation volume is equal to the bulk temperature. The boundary conditions are that the temperature in the elements on the border of the simulation volume is always equal to the bulk temperature (for all time increments).

The value of the heat capacity in equation 4.8 corresponds, in general, to that of the electrode material, or the insulation material, or the solution depending on the position of the considered element. However, there is a set of elements for which the heat capacity is a combination of the capacities of the two or three phases. These are so called bordering elements (Figure 4.2) and the equations for the calculation of their heat capacities are discussed below.

Heat capacity of the elements 1 and 4 in Figure 4.2 is calculated most straightforwardly. Since a half of the element's volume, in each case, belongs to one phase and a half – to another, the combined heat capacity is then the average of the heat capacities of the corresponding phases:

$$C_{1(4)} = \frac{1}{2}\left[C_{C(B)} + C_A\right] \tag{4.12}$$

where $C_{1(4)}$ is the heat capacity of the element 1 or 4, $C_{C(B)}$ is the heat capacity of the electrode material (C) or the insulation (B) and C_A is the heat capacity of the solution (A).

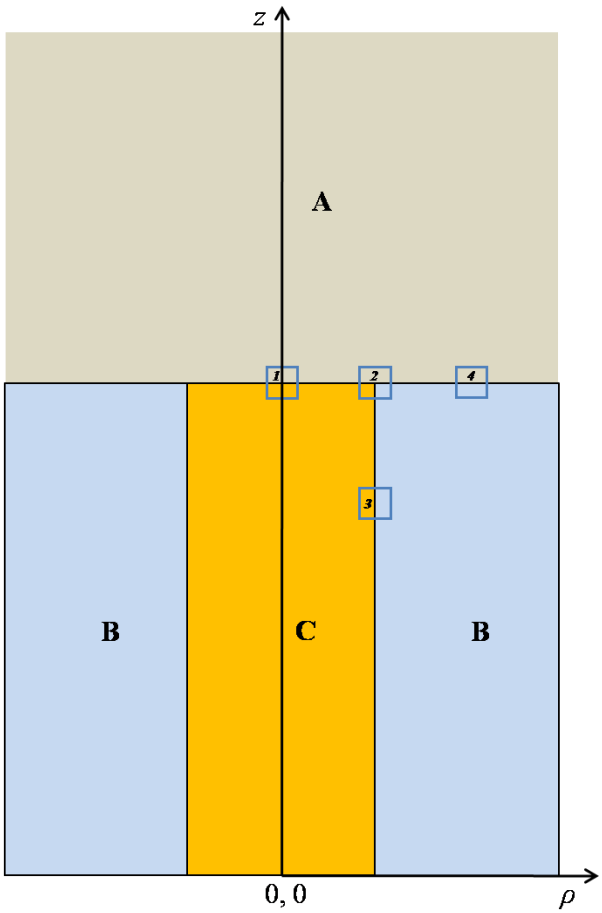

Figure 4.2 Selection of the elements that border phases with differing heat capacities. A – solution, B – insulation (glass), C – electrode material.

It may seem, from the first glance, that the heat capacity of the element 3 should also be calculated using equation 4.12. However, it should be realized that, due to the chosen coordinate system, the volume of the part of the element to the left from the phase boundary is smaller than that to the right from it. Therefore, the volume fractions of each of the phases are not equal to 0.5, but rather given by the following expressions:

$$\frac{V_C}{V} = \frac{\pi(\mathrm{P}\Delta h)^2 - \pi((\mathrm{P}-0.5)\Delta h)^2}{2\mathrm{P}\pi(\Delta h)^3}\Delta h = \frac{\mathrm{P}-0.25}{2\mathrm{P}} \tag{4.13}$$

$$\frac{V_B}{V} = \frac{\pi((\mathrm{P}+0.5)\Delta h)^2 - \pi(\mathrm{P}\Delta h)^2}{2\mathrm{P}\pi(\Delta h)^3}\Delta h = \frac{\mathrm{P}+0.25}{2\mathrm{P}} \tag{4.14}$$

where P is the index of the element and V is its volume.

Similarly, the heat capacity of the element 2 in Figure 4.2 is a combination of the heat capacities of the solution, the electrode material and insulation according to the equation:

$$C_2 = \frac{1}{2}\left(C_A + C_B \frac{\mathrm{P}-0.25}{2\mathrm{P}} + C_B \frac{\mathrm{P}+0.25}{2\mathrm{P}} \right) \tag{4.15}$$

It should also be realized that the value of the thermal conductivity coefficient used in equation 4.8 will depend on the particular element, to which the mentioned equation is applied. To illustrate this point, equation 4.8 for the element 2 in Figure 4.2 is as follows:

$$T'_{\mathrm{P},Z} = T_{\mathrm{P},Z} + \frac{\Delta t}{C(\Delta h)^2} \left\{ \begin{array}{l} k_A \left[A_v \left(T_{m,n+1} - T_{m,n} \right) \right] + \\ + \left(k_C \frac{\mathrm{P}-0.25}{2\mathrm{P}} + k_B \frac{\mathrm{P}+0.25}{2\mathrm{P}} \right) \left[A_v \left(T_{\mathrm{P},Z-1} - T_{\mathrm{P},Z} \right) \right] + \\ + \frac{1}{2}(k_A + k_C) \left[A_p \left(T_{\mathrm{P}-1,Z} - T_{\mathrm{P},Z} \right) \right] + \frac{1}{2}(k_A + k_B) \left[A_s \left(T_{\mathrm{P}+1,Z} - T_{\mathrm{P},Z} \right) \right] \end{array} \right\} + \frac{\Delta t}{CV} Q_g \tag{4.16}$$

where C is given by equation 4.15 and parameters A_p, A_s and A_v – by equations 4.9, 4.10 and 4.11, respectively.

Thus, in the above equation 4.16 the thermal conductivity coefficient used to calculate the rate of heat transfer from the top element into element 2 is that of the solution, while the thermal conductivity coefficient used to calculate the rate of heat transfer from the bottom element is a combination of the coefficients of the electrode material and the insulation material. Similarly, the coefficient used to calculate the rate of heat transfer from the preceding element is equal to the average of the thermal conductivity coefficients of the solution and the electrode material. And, finally, the thermal conductivity coefficient for the rate of heat conduction from the succeeding element into the considered element 2 is the average of the thermal conductivity coefficients of the solution and the insulation material.

In order to complete equation 4.8, the rate of the heat generation in each of the elements in the solution phase needs to be defined. It is calculated based on the formula for the heat dissipated on a resistor when the current passes through it:

$$Q_g = \frac{\Delta\Phi^2}{R} = \frac{\Delta\Phi^2\, S}{\rho l} \tag{4.17}$$

where $\Delta\Phi^2$ is the square of the voltage drop across the considered element, R is the resistance of the element, ρ is the specific solution resistance (not to be mistaken with the coordinate), l is the length of the element (Δh) and S is the area, through which the current passes between the elements.

4.2.4 Calculation of the electrothermal force and the rate of solution flow

To calculate the electrothermal force acting on an electrolyte solution, a numerical form of equation 1.33 (assuming $\omega << 1/\tau$) has been used. The general form of this equation for the ρ-component of the force is:

$$\left\langle \bar{f}_E \right\rangle_\rho = -\frac{\varepsilon_0}{2}\left[\left(\left(\frac{\sigma_{\mathrm{P},Z+1}-\sigma_{\mathrm{P},Z-1}}{\sigma_{\mathrm{P},Z}\cdot 2\Delta h}\varepsilon^r_{\mathrm{P},Z} - \frac{\varepsilon^r_{\mathrm{P},Z+1}-\varepsilon^r_{\mathrm{P},Z-1}}{2\Delta h}\right)\frac{\Phi_{\mathrm{P},Z+1}-\Phi_{\mathrm{P},Z-1}}{2\Delta h} + \left(\frac{\sigma_{\mathrm{P+1},Z}-\sigma_{\mathrm{P-1},Z}}{\sigma_{\mathrm{P},Z}\cdot 2\Delta h}\varepsilon^r_{\mathrm{P},Z} - \frac{\varepsilon^r_{\mathrm{P+1},Z}-\varepsilon^r_{\mathrm{P-1},Z}}{2\Delta h}\right)\frac{\Phi_{\mathrm{P+1},Z}-\Phi_{\mathrm{P-1},Z}}{2\Delta h}\right)\frac{\Phi_{\mathrm{P+1},Z}-\Phi_{\mathrm{P-1},Z}}{2\Delta h} + \frac{1}{2}\,\frac{\varepsilon^r_{\mathrm{P+1},Z}-\varepsilon^r_{\mathrm{P-1},Z}}{2\Delta h}E^2_{\mathrm{P},Z}\right] \tag{4.18}$$

and, for the z-component,

$$\left\langle \bar{f}_E \right\rangle_z = -\frac{\varepsilon_0}{2}\left[\left(\left(\frac{\sigma_{\mathrm{P},Z+1}-\sigma_{\mathrm{P},Z-1}}{\sigma_{\mathrm{P},Z}\cdot 2\Delta h}\varepsilon^r_{\mathrm{P},Z} - \frac{\varepsilon^r_{\mathrm{P},Z+1}-\varepsilon^r_{\mathrm{P},Z-1}}{2\Delta h}\right)\frac{\Phi_{\mathrm{P},Z+1}-\Phi_{\mathrm{P},Z-1}}{2\Delta h} + \left(\frac{\sigma_{\mathrm{P+1},Z}-\sigma_{\mathrm{P-1},Z}}{\sigma_{\mathrm{P},Z}\cdot 2\Delta h}\varepsilon^r_{\mathrm{P},Z} - \frac{\varepsilon^r_{\mathrm{P+1},Z}-\varepsilon^r_{\mathrm{P-1},Z}}{2\Delta h}\right)\frac{\Phi_{\mathrm{P+1},Z}-\Phi_{\mathrm{P-1},Z}}{2\Delta h}\right)\frac{\Phi_{\mathrm{P},Z+1}-\Phi_{\mathrm{P},Z-1}}{2\Delta h} + \frac{1}{2}\,\frac{\varepsilon^r_{\mathrm{P},Z+1}-\varepsilon^r_{\mathrm{P},Z-1}}{2\Delta h}E^2_{\mathrm{P},Z}\right] \tag{4.19}$$

where $\Phi_{\mathrm{P},Z}$ is the ac potential, $\varepsilon^r_{\mathrm{P},Z}$ is the relative dielectric constant and $\sigma_{\mathrm{P},Z}$ is the electrical conductivity in the solution element (P, Z). $E^2_{\mathrm{P},Z}$ is the square of the ac potential gradient, which is obtained from the ac potential field distribution (equation 4.1).

The values of the electrical conductivity of solution depend on temperature and, therefore, the index of the element. They are calculated according to the equation:

$$\sigma_{\mathrm{P},Z}(T) = \sigma(298K)\exp\left[A\left(\frac{1}{298K} - \frac{1}{T}\right)\right] \tag{4.20}$$

where A is a constant, which can be estimated as 1876 K^{-1} based on the temperature dependence of the viscosity of water; $\sigma(298K)$ is the electrical conductivity at the temperature of the bulk solution 298 K.

The change in the relative dielectric constant (ε^r) with temperature can be also estimated from the corresponding values for water.[95] In the temperature range 283 K – 363 K the dependence of the natural logarithm of ε^r of water on T is linear and follows the equation:

$$\ln\varepsilon^{\mathrm{r}} = -4.5986\cdot10^{-3}\,T + 5.7327 \tag{4.21}$$

After ρ- and z-components of the electrothermal force are determined, the magnitude of the force in each of the solution elements can be calculated:

$$\left\langle \bar{f}_E \right\rangle = \sqrt{\left\langle \bar{f}_E \right\rangle_\rho^2 + \left\langle \bar{f}_E \right\rangle_z^2} \tag{4.22}$$

where the electrothermal force f_E has units of newton per volume of the solution element.

The next step in simulations is the determination of the solution flow rate by solving the Navier-Stokes equation. For the incompressible Newtonian fluid such as water this equation has the following form:[32]

$$\rho_m \frac{\partial \bar{u}}{\partial t} + \rho_m(\bar{u}\cdot\nabla)\bar{u} = -\nabla p + \eta\nabla^2\bar{u} + \bar{f}_E \tag{4.23}$$

where ρ_m is the density of the fluid, $\bar{u}$ is its velocity, p and η are the pressure and viscosity, respectively; $\bar{f}_E$ is the body force, which, in this case, is the electrothermal force.

The second term on the left side of the above equation 4.23 is negligible in the case of the microsystems (systems with the length scale ~ 10^{-4} m); the fluid flow is said to be in the viscous fluid limit.[32] This means that if the deterministic force such as $\bar{f}_E$ is removed, the flow stops immediately. Therefore, assuming the steady-state flow, the Navier-Stokes equation can be simplified to:

$$-\nabla p + \eta\nabla^2\bar{u} + \bar{f}_E = 0 \tag{4.24}$$

Thus, to determine the rate of the solution flow, one needs to solve the above equation.

In order to reduce the number of unknowns in equation 4.24, a common approach is to take the curl of it:[33]

$$curl(-\nabla p)+curl(\eta\nabla^2\bar{u})+curl(\bar{f}_E)=0 \tag{4.25}$$

where curl is a vector operator that describes the rotation of a vector field.

For the cylindrical coordinate system curl of a vector field $\bar{F}$ is given by the following expression:

$$curl\,\bar{F}=\nabla\times\bar{F}=\begin{vmatrix}(1/\rho)\hat{\rho} & \hat{\varphi} & (1/\rho)\hat{z}\\ \frac{\partial}{\partial\rho} & \frac{\partial}{\partial\varphi} & \frac{\partial}{\partial z}\\ F_\rho & \rho F_\varphi & F_z\end{vmatrix}= \tag{4.26}$$
$$=\left(\frac{1}{\rho}\frac{\partial F_z}{\partial\varphi}-\frac{\partial F_\varphi}{\partial z}\right)\hat{\rho}+\left(\frac{\partial F_\rho}{\partial z}-\frac{\partial F_z}{\partial\rho}\right)\hat{\varphi}+\frac{1}{\rho}\left(\frac{\partial(\rho F_\varphi)}{\partial\rho}-\frac{\partial F_\rho}{\partial\varphi}\right)\hat{z}$$

where unit vectors $\hat{\rho}$, $\hat{\varphi}$, $\hat{z}$ form the basis of the coordinate system ($\hat{\varphi}$ is orthogonal to the plane $\rho 0z$) and F_ρ, F_φ, F_z are the projections of vector $\bar{F}$ on this basis.

Since the curl of the gradient of any scalar field is equal to zero, equation 4.25 can be rewritten as follows:

$$\eta\left(\nabla\times(\nabla^2\bar{u})\right)\cdot\hat{\varphi}+(\nabla\times\bar{f}_E)\cdot\hat{\varphi}=0 \tag{4.27}$$

Equation 4.27 directly relates the electrothermal force acting on solution to the rate of the solution flow. For two-dimensional flows it can be further simplified by introducing the stream function ψ. In this particular case the stream function is called the Stokes stream function ψ and it is defined as:[96]

$$-\frac{1}{\rho}\frac{\partial\psi}{\partial z}=u_\rho\,,\qquad \frac{1}{\rho}\frac{\partial\psi}{\partial\rho}=u_z \tag{4.28}$$

where u_ρ and u_z are the projections of the solution flow velocity vector $\bar{u}(\rho, z)$ on the coordinate axes ρ and z, respectively. Lines of constant ψ are called the stream lines, they are parallel to the direction of the solution flow everywhere in solution.

It should also be noted here that the chosen expression for the stream function (equation 4.28) adheres well to the continuity equation, which has the following form for a two-dimensional $(\rho,\ z)$ flow:

$$\frac{1}{\rho}\frac{\partial(\rho u_\rho)}{\partial\rho}+\frac{\partial u_z}{\partial z}=0 \tag{4.29}$$

By substituting equation 4.28 into equation 4.27 one obtains that:

$$\nabla^2\left(\frac{\partial^2\psi}{\partial\rho^2}+\frac{\partial^2\psi}{\partial z^2}-\frac{3}{\rho}\frac{\partial\psi}{\partial\rho}\right)=\frac{\rho}{\eta}\left(\nabla\times\bar{f}_E\right)\cdot\hat{\varphi} \tag{4.30}$$

Thus, the above equation relates the values of the electrothermal force in each of the solution elements (Figure 4.1) to the values of the stream function in those elements and, as a result, the rate of the solution flow. To solve equation 4.30 one, firstly, needs to calculate $\left(\nabla\times\bar{f}_E\right)\cdot\hat{\varphi}$, which is the dot product of the curl of $\bar{f}_E$ and $\hat{\varphi}$. Using equation 4.26 one can write that:

$$\left(\nabla\times\bar{f}_E\right)\cdot\hat{\varphi}=\frac{\partial f_{E,\rho}}{\partial z}-\frac{\partial f_{E,z}}{\partial\rho} \tag{4.31}$$

since $\hat{\rho}\cdot\hat{\varphi}=\hat{z}\cdot\hat{\varphi}=0$.

Consequently, the following expression must be solved numerically for every solution element $(\mathrm{P},\ Z)$:

$$\frac{\rho}{\eta}\left(\nabla\times\bar{f}_E\right)\cdot\hat{\varphi}=\frac{1}{2\eta}\left[\begin{array}{l}\mathrm{P}\cdot\left(f_{E,\rho}(\mathrm{P},Z+1)-f_{E,\rho}(\mathrm{P},Z-1)\right)-\left(\mathrm{P}+\frac{1}{2}\right)\cdot\left(f_{E,z}(\mathrm{P}+1,Z)-f_{E,z}(\mathrm{P},Z)\right)-\\ -\left(\mathrm{P}-\frac{1}{2}\right)\cdot\left(f_{E,z}(\mathrm{P},Z)-f_{E,z}(\mathrm{P}-1,Z)\right)\end{array}\right] \tag{4.32}$$

since $\rho=\mathrm{P}\Delta h$. The values of $\frac{\rho}{\eta}\left(\nabla\times\bar{f}_E\right)\cdot\hat{\varphi}$ obtained from the above equation 4.32 are further used to solve equation 4.30.

Close examination of equation 4.30 indicates that in order to obtain the values of the stream function, this equation needs to be integrated twice; after the first integration some function $\zeta(\rho,z)$ is determined such that:

$$\nabla^2\zeta = \frac{\rho}{\eta}\left(\nabla\times\bar{f}_E\right)\cdot\hat{\varphi}, \qquad \frac{\partial^2\psi}{\partial\rho^2}+\frac{\partial^2\psi}{\partial z^2}-\frac{3}{\rho}\frac{\partial\psi}{\partial\rho}=\zeta \tag{4.33}$$

Thus, in the second step, ζ function has to be integrated to give the values of the stream function ψ.

Numerical solution of equation 4.33, which leads to the values of ζ function, is obtained as follows. For the cylindrical coordinate system (Figure 4.1) the laplacian of some function $\phi(\rho,z)$ is given by the following expression:

$$\begin{aligned}\nabla^2\phi = &\frac{1}{(\Delta h)^2}\left[\phi(\mathrm{P}+1,Z)+\phi(\mathrm{P}-1,Z)+\phi(\mathrm{P},Z+1)+\phi(\mathrm{P},Z-1)-4\phi(\mathrm{P},Z)\right]+\\ &+\frac{1}{2(\Delta h)^2}\left[\frac{\phi(\mathrm{P}+1,Z)-\phi(\mathrm{P},Z)}{\mathrm{P}+0.5}+\frac{\phi(\mathrm{P},Z)-\phi(\mathrm{P}-1,Z)}{\mathrm{P}-0.5}\right]\end{aligned} \tag{4.34}$$

This equation is obtained based on the Taylor series expansion of the function $\phi(\rho,z)$ (Taylor's theorem).[97]

By rewriting the above equation for ζ one finds that:

$$\zeta(\mathrm{P},Z)=\frac{\frac{2\mathrm{P}+2}{2\mathrm{P}+1}\zeta(\mathrm{P}+1,Z)+\frac{2\mathrm{P}-2}{2\mathrm{P}-1}\zeta(\mathrm{P}-1,Z)+\zeta(\mathrm{P},Z+1)+\zeta(\mathrm{P},Z-1)-(\Delta h)^2\ f(\mathrm{P},Z)}{4+\frac{1}{2\mathrm{P}+1}-\frac{1}{2\mathrm{P}-1}} \tag{4.35}$$

where $f(\mathrm{P},Z)$ is the value of $\frac{\rho}{\eta}\left(\nabla\times\bar{f}_E\right)\cdot\hat{\varphi}$ in the element (P,Z) (see equation 4.33). Equation 4.35 indicates that the value of ζ function in each element (P,Z) is determined by the values of ζ function in the surrounding elements and by the value of $\frac{\rho}{\eta}\left(\nabla\times\bar{f}_E\right)\cdot\hat{\varphi}$ in the considered element (P,Z). In order to obtain $\zeta(\mathrm{P},Z)$ an iterative method is used. The idea behind this method is that the initial values of $\zeta(\mathrm{P},Z)$ are chosen to be zero and equation 4.35 is iterated until the values of $\zeta(\mathrm{P},Z)$ converge.

In the second integration step the following equation similar to equation 4.35 is applied:

$$\psi(\mathrm{P},Z)=\frac{\frac{2\mathrm{P}-2}{2\mathrm{P}+1}\psi(\mathrm{P}+1,Z)+\frac{2\mathrm{P}+2}{2\mathrm{P}-1}\psi(\mathrm{P}-1,Z)+\psi(\mathrm{P},Z+1)+\psi(\mathrm{P},Z-1)-(\Delta h)^2\ \zeta(\mathrm{P},Z)}{4-\frac{3}{2\mathrm{P}+1}+\frac{3}{2\mathrm{P}-1}} \tag{4.36}$$

However, in this case, the values of $\zeta(\mathrm{P},Z)$ are used instead of $\frac{\rho}{\eta}\left(\nabla\times\bar{f}_E\right)\cdot\hat{\varphi}$. Similarly to the first integration, equation 4.36 is iterated until the values of the stream function $\psi(\mathrm{P},Z)$ converge. The boundary conditions are defined so that the stream function is zero in the solution elements with Z = 1 and Z = 0 (electrode surface), in the elements on the border of the simulation volume and in the elements with P = 0 (symmetry axis). It should be noted that the same boundary conditions (but for ζ function) are also used in the first integration step.

The last step in the electrothermal convection simulation is the determination of the solution flow rate. This is done by differentiation of the stream function according to equation 4.28. In numerical form this equation can be written as:

$$u_\rho = -\frac{1}{2(\Delta h)^2\,\mathrm{P}}\left[\psi(\mathrm{P},Z+1)-\psi(\mathrm{P},Z-1)\right] \qquad u_z = \frac{1}{2(\Delta h)^2}\left[\frac{\psi(\mathrm{P},Z)-\psi(\mathrm{P}-1,Z)}{\mathrm{P}-0.5}+\frac{\psi(\mathrm{P}+1,Z)-\psi(\mathrm{P},Z)}{\mathrm{P}+0.5}\right] \quad (4.37)$$

After the ρ- and z-components of the solution flow rate are determined, the magnitude of the flow in each of the solution elements is calculated according to the equation similar to equation 4.22 for the electrothermal force.

4.3 CYCLIC VOLTAMMETRY SIMULATION

Faradaic current measured at the working electrode can be, in general, controlled either by the rate of mass transfer of redox species to the electrode, or by the rate of electron transfer. If the kinetics of the electron transfer between the electrode and the species is fast, then the rate of mass transfer controls the rate of the electrode reaction and the electrode process is called reversible. In this Section, cyclic voltammetry simulations will be considered only for the reversible electrode processes.

The rate of mass transfer is described by the Nernst-Planck equation, which, for an isothermal system, is the same as equation 1.8 (Section 1.2). The faradaic current is then given by the following equation (usually written for diffusion):

$$i = nFAD\left(\frac{\partial C}{\partial x}\right)_{x=0} \quad (4.38)$$

where n is a number of electrons transferred in the redox reaction, F is the Faraday constant, A is the surface area of the electrode, D is the diffusion coefficient of the species and $\left(\frac{\partial C}{\partial x}\right)_{x=0}$ is the concentration gradient at the electrode surface.

Thus, in order to simulate a cyclic voltammogram for a hot microelectrode, one must solve an appropriate mass transfer equation (equation 1.9, Section 1.2.1.2) and then determine the current based on the equation similar to equation 4.38.

If, for a moment, we restrict ourselves to the consideration of mass transfer of redox species only by diffusion and Soret diffusion, then the flux of the species is given by equation 4.39:

$$J = -D\left[\frac{\partial C(\rho,z)}{\partial \rho}+\frac{\partial C(\rho,z)}{\partial z}\right]-D^{T}C(\rho,z)\left[\frac{\partial T(\rho,z)}{\partial \rho}+\frac{\partial T(\rho,z)}{\partial z}\right] \qquad (4.39)$$

The derivatives in this equation are written according to the same coordinate system as the one used in the simulation of the electrothermal convection (Figure 4.1).

For any solution element in Figure 4.1 the flux can be expressed as a sum of fluxes from the neighboring cells:

$$J = J_s + J_p + J_t + J_b \qquad (4.40)$$

where the subscripts *s*, *p*, *t*, *b* have the same meaning as in equation 4.7.

Consequently, the number of moles of the redox species in the element can be calculated as follows:

$$C\,V = C_0\,V + \Delta t\left(J_s\,S_s + J_p\,S_p + J_t\,S_v + J_b\,S_v\right) \qquad (4.41)$$

where C_0 is the concentration of the species at the time t_0 (initial concentration), V is the volume of the solution element, S is the surface area between the corresponding element and the neighbouring element, from which the flux occurs (*s*, *p*, *t* or *b*), and Δt is the period of time, for which the flux takes place.

Substitution of equation 4.39 into the above equation 4.41 leads to the expression for the concentration of the redox species, given here in the numerical form:

$$C = C_0 + \frac{D\ \Delta t}{(\Delta h)^2}\left[\begin{array}{l} A_s\left(\Delta C_s + \sigma\ C_0\ \Delta T_s\ \right) + A_p\left(\Delta C_p + \sigma\ C_0\ \Delta T_p\ \right) + \\ + A_v\left(\Delta C_t + \sigma\ C_0\ \Delta T_t\ \right) + A_v\left(\Delta C_b + \sigma\ C_0\ \Delta T_b\ \right) \end{array}\right] \quad (4.42)$$

where A_p, A_s and A_v are given by equations 4.9– 4.11 and σ is the Soret coefficient of the redox species (equation 1.12); ΔC and ΔT are the concentration and temperature differences between the neighboring element and the considered one.

Diffusion coefficient D in the above equation depends on the temperature in the element. Therefore, its value will differ from one element to another and it can be calculated according to the formula:

$$D(T) = D(T_b)\frac{T}{T_b}\exp\left[-A\left(\frac{1}{T_b} - \frac{1}{T}\right)\right] \quad (4.43)$$

where $D(T_b)$ is the diffusion coefficient of the species in the bulk solution, where the temperature is equal to T_b (298 K). *A* is a constant, which can be estimated as 1876 K^{-1} based on the temperature dependence of the viscosity of water. *T* is the temperature of the solution in the considered element; its value is available from the results of the temperature distribution simulation discussed in Section 4.2.3.

One can notice that equation 4.39 is incomplete, because it does not include the convective contribution to the mass transfer. The convection results mainly from the action of the electrothermal force (given by equation 1.33, Section 1.2.2.2) on an electrolyte solution. Therefore, the convective term must be included into the mass transfer equation.

Variation of the concentration of the redox species with time due to convection ($\partial C_c/\partial t$) is given by:[17]

$$\frac{\partial C_c}{\partial t} = -\nabla\cdot\left(C\ \bar{u}\right) = -\nabla C\ \cdot\bar{u} \quad (4.44)$$

In numerical form this equation can be written as follows:

$$\Delta C_c = -\Delta t\left[\frac{C\ (\mathrm{P}+1, Z) - C\ (\mathrm{P}-1, Z)}{2\Delta h}u_\rho + \frac{C\ (\mathrm{P}, Z+1) - C\ (\mathrm{P}, Z-1)}{2\Delta h}u_z\right] \quad (4.45)$$

where u_ρ and u_z are the components of the solution velocity vector in ρ- and z-directions (equation 4.37).

As a result, equation 4.42 can be expanded to account for the effect of electrothermal convection:

$$C(\mathrm{P},Z) = C_0(\mathrm{P},Z) + \frac{D\ \Delta t}{(\Delta h)^2}\left[\begin{array}{l} A_s\left(\Delta C_s + \sigma\ C_0\ \Delta T_s\ \right) + A_p\left(\Delta C_p + \sigma\ C_0\ \Delta T_p\ \right) + \\ + A_v\left(\Delta C_t + \sigma\ C_0\ \Delta T_t\ \right) + A_v\left(\Delta C_b + \sigma\ C_0\ \Delta T_b\ \right) \end{array}\right] - \qquad (4.46)$$

$$- \frac{\Delta t}{2\Delta h}\left(\Delta C_\rho\, u_\rho + \Delta C_z\, u_z\right)$$

where $\Delta C_\rho = C\ (\mathrm{P}+1, Z) - C\ (\mathrm{P}-1, Z)$ and $\Delta C_z = C\ (\mathrm{P}, Z+1) - C\ (\mathrm{P}, Z-1)$.

In order to solve the above equation 4.46 for any moment of time one needs, firstly, to specify the initial and boundary conditions. The initial condition states the concentration of the redox species in every solution element at time $t = 0$. This 'zero' time can be chosen before the moment when the heating of the solution occurs. Therefore, the concentration in each element will be equal to the bulk concentration of the species. Alternatively, it can be chosen after the ac heating is applied and the Soret diffusion equilibrium is established. This means that the concentration in each solution element at $t = 0$ is determined by the formula (see also equation 1.12):

$$C = C_b \exp[-\sigma\ (T - T_b)] \qquad (4.47)$$

where C and T are the concentration and temperature in the element (P, Z) and C_b and T_b are the concentration and temperature in the bulk solution; σ is the Soret coefficient of the species.

The first boundary condition (for the electrode disk surface) is based on the assumption that the electrode redox reaction is controlled by an equilibrium condition (Nernstian system):[17]

$$C_R^s = C_t\ \frac{1}{1+\Theta} \qquad (4.48)$$

and

$$C_O^s = C_t - C_R^s \qquad (4.49)$$

where C_R^s and C_O^s are the surface concentrations of the reduced and oxidized species, respectively, and C_t is the total concentration of the species (both reduced and oxidized forms).

The second boundary condition for equation 4.46 is that the concentration of the redox species is equal to its bulk solution value in all elements on the border of the simulation volume. In addition, there is no flux of the species through the symmetry axis (P = 0) and through the electrode surface (all solution elements with Z = 0).

Coefficient Θ in equation 4.48 is given by the following relation:

$$\Theta = \exp\left[\frac{nF}{RT}\left(E - E^0\right)\right] \tag{4.50}$$

where E is the electrode dc potential, E^0 is the standard potential of the redox reaction and other symbols have their usual meanings.

The value of the standard potential E^0 in the above equation 4.50 is temperature dependent. Therefore, its value needs to be calculated for each of the elements on the electrode surface according to the formula:

$$E^0\left(T_s\right) = E^0\left(T_b\right) + \frac{dE^0}{dT}\left(T_s - T_b\right) \tag{4.51}$$

where $E^0\left(T_b\right)$ is the standard potential at room temperature (the temperature of the bulk solution) and dE^0/dT is the temperature coefficient of the electrode reaction standard potential (usually taken equal to –1.5 mV K^{-1}).

The change of the surface concentrations of the species from the values determined by the mass transport (equation 4.46) to the values controlled by the electrode potential (equations 4.48 and 4.49) is accompanied by the flow of the faradaic current. To calculate this current, the following equation is used:

$$I = J\ nF\ S_v = \frac{nF\ S_v\ D}{\Delta h}\left(\Delta C_v + \sigma\ C\ \Delta T_v\right) \tag{4.52}$$

where ΔC_v and ΔT_v are the differences in the concentration and temperature between the neighboring top cell and the considered cell on the surface of the electrode, S_v is the area between the cells and σ is the Soret coefficient of the redox species.

The value of *I* in the above equation 4.52 is the current flowing through one element on the surface of the electrode. Therefore, in order to obtain the total value of the faradaic current, the above equation must be applied to all electrode surface elements and the corresponding *I* values must be summed.

4.4 ELECTRODE HEATING AND TEMPERATURE DISTRIBUTION

In this Section, the results of the temperature distribution simulations at hot-disk microelectrodes are presented. These results indicate that there is a linear dependence between the temperature of the electrode and the square of the ac voltage drop across the solution resistance, $\Delta V_{R_s}^2$. This is explained well by the Joule heating of an electrolyte solution (equation 3.5, Section 3.2.2). The effect of the solution specific resistance on the temperature of a hot microelectrode also follows the expected trend: for the same value of $\Delta V_{R_s}^2$, the temperature decreases with an increase in the solution specific resistance. This, again, can be explained by the Joule heating considering the same equation 3.5.

Simulation results suggest that the temperature profile in solution near a hot microelectrode is strongly affected by the properties of the electrode body, in particular – the thermal conductivity of the metal wire. In Figure 4.3 the distribution of the temperature around heated microelectrodes is shown. In part (a) of the Figure the thermal conductivity coefficients of the metal and insulation material (glass) were taken equal to zero (such an electrode will be called a zero thermal conductivity (ZTC) electrode). Thus, no heat transfer into the body of the electrode has been taken into account. For other parts of Figure 4.3 (b, c, d) the values of the thermal conductivity coefficients corresponded to the thermal conductivity of borosilicate glass and bismuth (b), platinum (c) or gold (d).

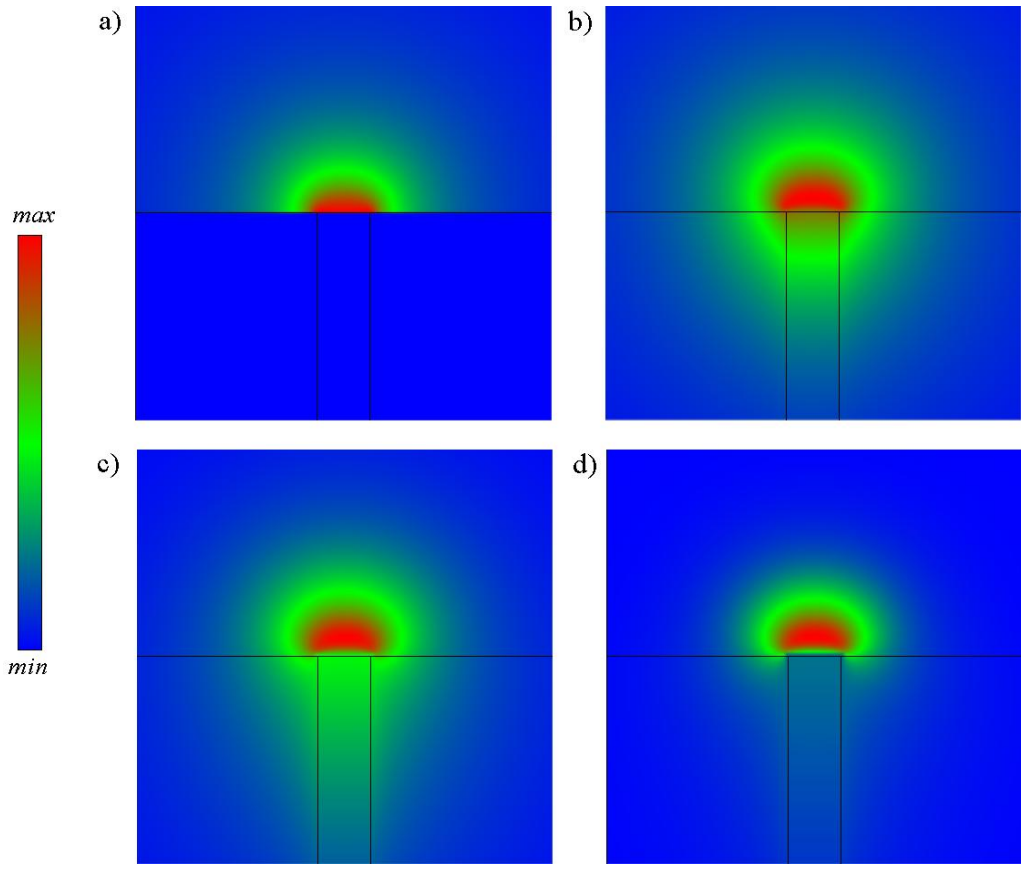

Figure 4.3 Temperature distribution around hot microelectrodes with differing thermal conductivities of the electrode body. a) Thermal conductivity of the metal and insulation are equal to 0 W cm^{-1} K^{-1} (ZTC electrode); b) thermal conductivity of metal wire is 0.0787 W cm^{-1} K^{-1} (Bi); c) thermal conductivity of metal wire is 0.716 W cm^{-1} K^{-1} (Pt); d) thermal conductivity of metal wire is 3.17 W cm^{-1} K^{-1} (Au). Thermal conductivity of insulation in b) – d) is 0.0092 W cm^{-1} K^{-1} (borosilicate glass). Thermal conductivity of solution in all cases is 0.00598 W cm^{-1} K^{-1} (water). *Scale: max* – maximum temperature; *min* – room temperature.

With no heat transfer into the body of the electrode, the temperature at the electrode surface is the highest (Figure 4.3, a). This agrees well with the previously developed model of a hot spherical microelectrode.[7] However, that early model is no longer applicable in the case of disk microelectrodes due to non-zero heat transfer into the electrode body. As a result, the temperature at the electrode surface is lower than the temperature in solution in close proximity to the electrode. This can be easily noticed once the temperature profiles corresponding to the results in Figure 4.3 are plotted, as shown below:

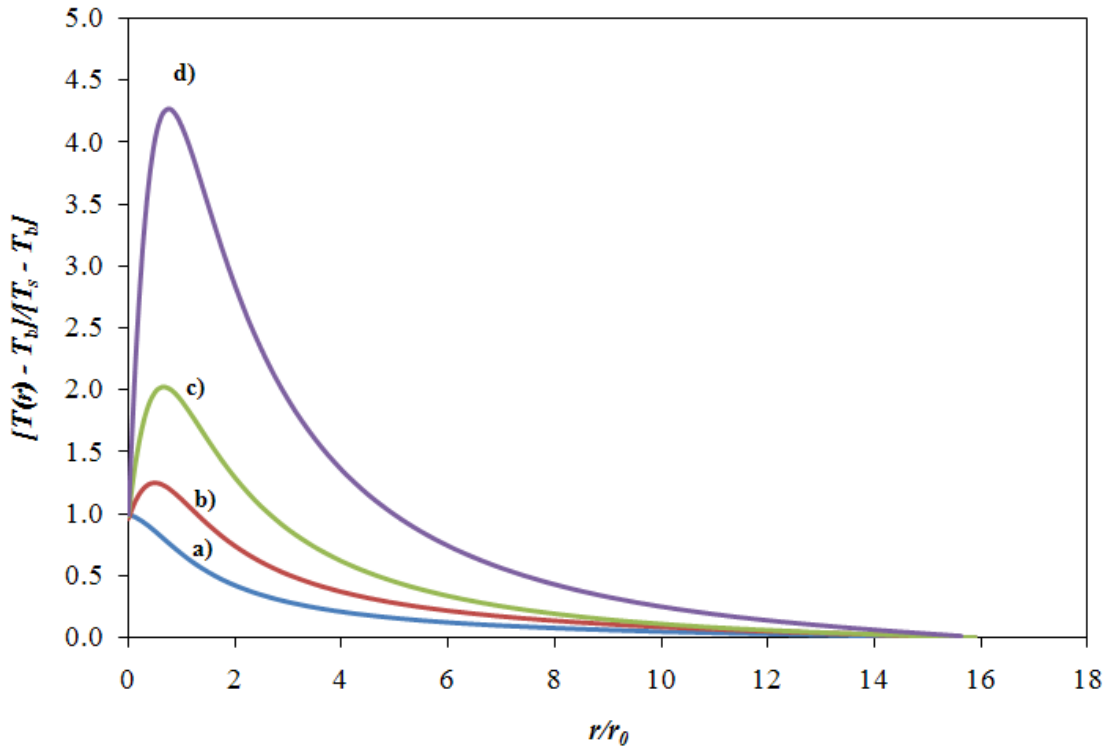

Figure 4.4 Normalized temperature change as the function of the normalized distance from the surface of ac heated disk microelectrodes. The curves are based on the results presented in Figure 4.3 (a – ZTC, b – Bi, c – Pt, d – Au). T_b – temperature in the bulk solution, T_s – temperature at the electrode surface; r – distance from the electrode surface, r_0 – electrode radius.

The results in Figure 4.4 (b) – (d) indicate that, due to the heat transfer into the electrode body, the maximum temperature is no longer located at the electrode surface; the higher the thermal conductivity of the metal, the further into the solution the point of the highest temperature value is located.

Based on the results of the temperature simulations a simple (empirical) expression for the temperature of a hot electrode could be proposed (equation 4.53). In this expression the characteristics of the electrode (geometry, radius, thermal conductivity) are related to the parameters of the ac heating (electrical power):

$$\Delta T = T_s - T_b = \frac{P}{r_0} k' \qquad (4.53)$$

where P is the ac electrical power supplied by the signal generator to the electrolyte solution, r_0 is the electrode radius and k' is the coefficient, which depends on the electrode geometry (spherical or disk) and the thermal conductivity of the electrode body and electrolyte solution (k' is inversely proportional to the thermal conductivity). T_s and T_b are the electrode surface and solution bulk temperatures, respectively.

In the case of a hot spherical microelectrode, the coefficient k' in equation 4.53 can be obtained using the expression for ΔT developed by Baranski:[7]

$$\Delta T = \frac{\Delta V_{R_s}{}^2}{2\rho k} \tag{4.54}$$

where $\Delta V_{R_s}{}^2$ is the square of the excitation voltage across the solution resistance, ρ is the specific solution resistance and k is the thermal conductivity of the solution.

Consequently, k' is equal to $1/8\pi k$ for a spherical microelectrode.

For disk microelectrodes, k' can be determined from the slope of the graph ΔT vs. $\frac{\Delta V_{R_s}{}^2}{\rho}$, since:

$$\Delta T = \frac{\Delta V_{R_s}{}^2}{R_s r_0} k' = \frac{4\Delta V_{R_s}{}^2}{\rho} k' \tag{4.55}$$

Thus, the slope of such a graph is equal to $4k'$.

As a result, the values of the temperature difference between the disk electrode surface and the bulk of the solution have been determined from the numerical simulations, and the coefficient k' for different metals is as follows: 6.07 (Bi), 2.45 (Pt) and 0.826 (Au). Obtained values of k' coefficient simply indicate that, for the same power P supplied to the solution, Bi microelectrodes will be heated to higher temperatures, than Pt or gold electrodes, provided that all the electrodes have the same radius (equation 4.53).

Equation 4.55 indicates that the radius of a hot-disk microelectrode does not affect the value of the electrode temperature reached during the ac heating. However, the rate of heating of microelectrodes depends on their radius. This is illustrated in Figure 4.5.

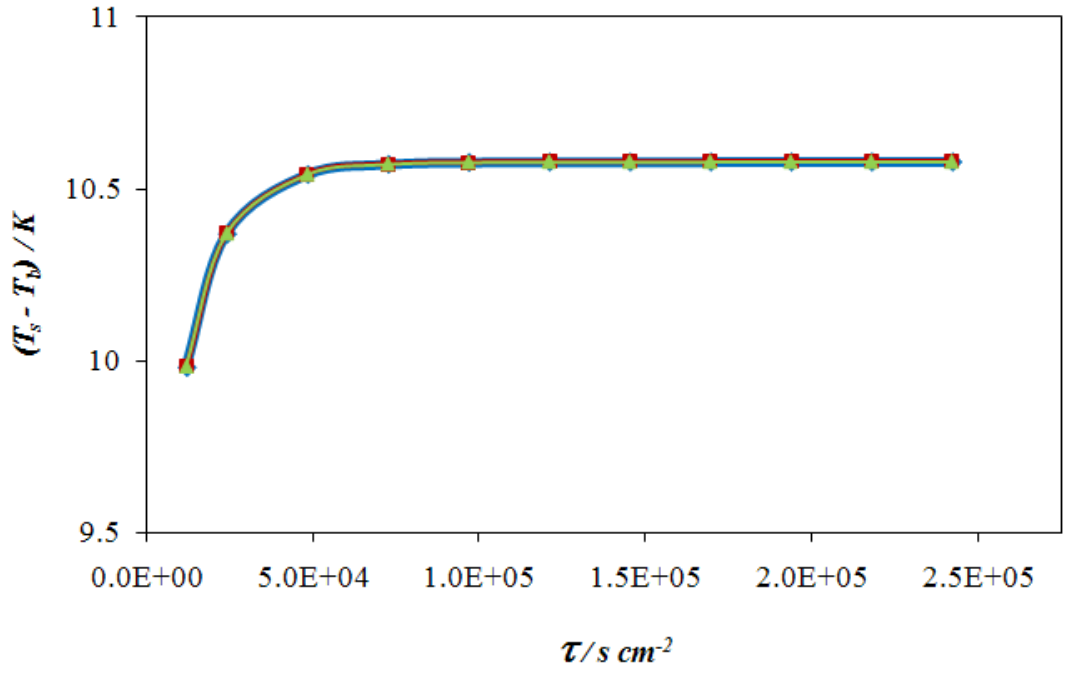

Figure 4.5 Change in the electrode surface temperature due to ac heating as a function of the time parameter τ ($\tau = t/r_0^2$). The results are based on temperature simulations for disk electrodes having the following radii: 1.25 μm (red), 12.5 μm (blue) and 125 μm (green).

The time parameter τ in Figure 4.5 is equal to the time of the heating (t) divided by the square of the electrode radius (r_0^2). The fact that the above curves overlap completely indicates that the rate of ac heating (as judged by the time required to reach a certain value of the electrode surface temperature T_s) is directly proportional to the electrode radius squared. Therefore, it can be written that:

$$\frac{t_2}{t_1} = \left(\frac{r_{02}}{r_{01}}\right)^2 \tag{4.56}$$

where r_{01} is the radius of the first electrode and r_{02} – the second electrode.

This equation can be obtained also from equation 4.16, which can be simplified to the following form:

$$\Delta T = T_s - T_b = t\left(\frac{Q_g}{CV} + \frac{a}{C r_0^2}\right) \tag{4.57}$$

where t is the heating time, r_0 is the electrode radius and a is the coefficient, which accounts for the heat transfer between the elements. Other symbols have the same meaning as discussed in equation 4.16.

Therefore, it can be written that:

$$\frac{t_2}{t_1} = \left(\frac{Q_{g1}}{V_1} + \frac{a}{r_{01}^2}\right) \cdot \left(\frac{Q_{g2}}{V_2} + \frac{a}{r_{02}^2}\right)^{-1} \tag{4.58}$$

since ΔT is the same for both electrode systems.

Taking into account that Q_g is proportional to r_0 (equation 4.17) and volume $V \sim r_0^3$, the above equation leads to equation 4.56.

4.5 RESULTS OF ELECTROTHERMAL CONVECTION SIMULATIONS

4.5.1 Comparison of simulation and experimental results

Here the results of the electrothermal convection simulations are discussed and compared with the experimental data. It should be realized that since simulations generally include some simplifications, exact correlation between the simulated and experimental results may not be possible. However, in this case even semiquantitative agreement can be useful in the explanation of the experimental results.

In Chapter 3 it has been shown experimentally that the electrothermally driven flow of an electrolyte solution is largely responsible for the enhancement of mass transport at ac heated disk microelectrodes. The results of the simulations presented here support those findings and provide much better understanding of the complex phenomena occurring at ac heated microelectrodes.

The rate of the solution flow depends linearly on $\Delta V_{R_s}^4$, the fourth power of the ac voltage applied across the solution resistance. This can be explained by the fact that the electrothermal force driving the flow of solution is proportional both to the temperature gradient and the square of the alternating potential gradient in solution. As a result, the

electrothermal force is proportional to $\Delta V_{R_s}^4$, as shown in equation 3.12 and Figure 3.5 (Chapter 3). Numerical simulations support this finding as shown in Figure 4.6.

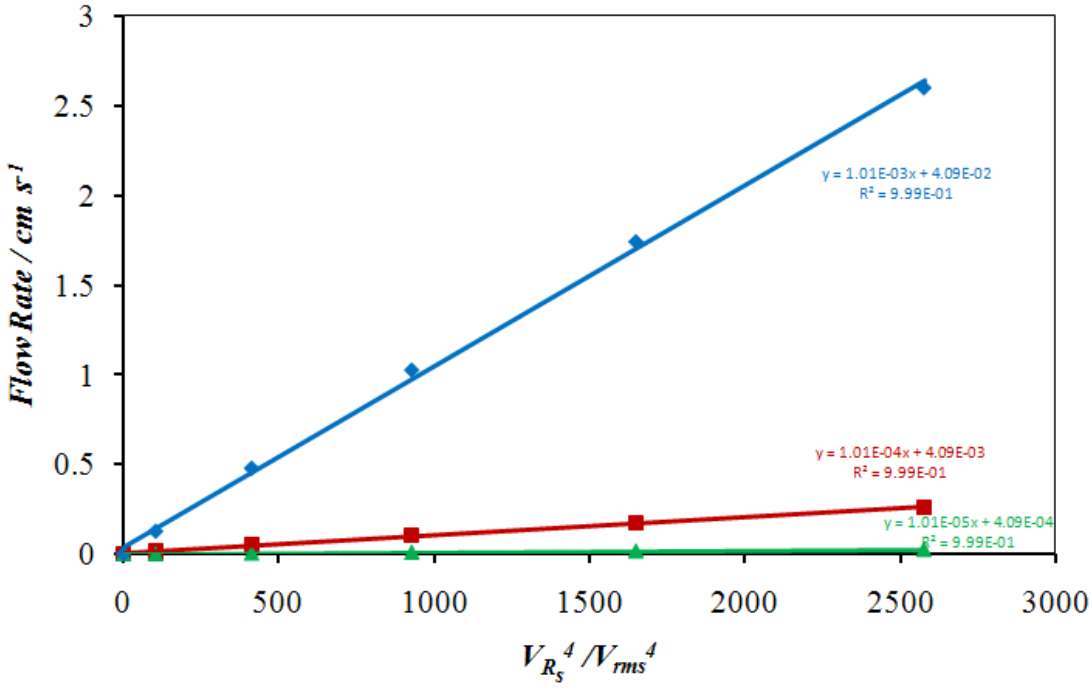

Figure 4.6 Dependence of the maximum solution flow rate on the fourth power of the ac voltage drop across the solution resistance. The results are based on numerical simulations of electrothermal convection observed in 0.2 M KCl solution at 2.5 μm (blue line), 25 μm (red line) and 250 μm (green line) Pt hot-disk microelectrodes.

Observed changes in slopes of the graphs in the above Figure 4.6 indicate that the rate of the solution flow is inversely proportional to the electrode radius. Therefore, the results of the simulations are in agreement with the theoretical findings about the electrothermal convection presented in Section 3.4.

Effect of the supporting electrolyte concentration on the temperature dependence of the simulated limiting current enhancement factor shows a very similar trend compared to the experimental data (Figure 4.7).

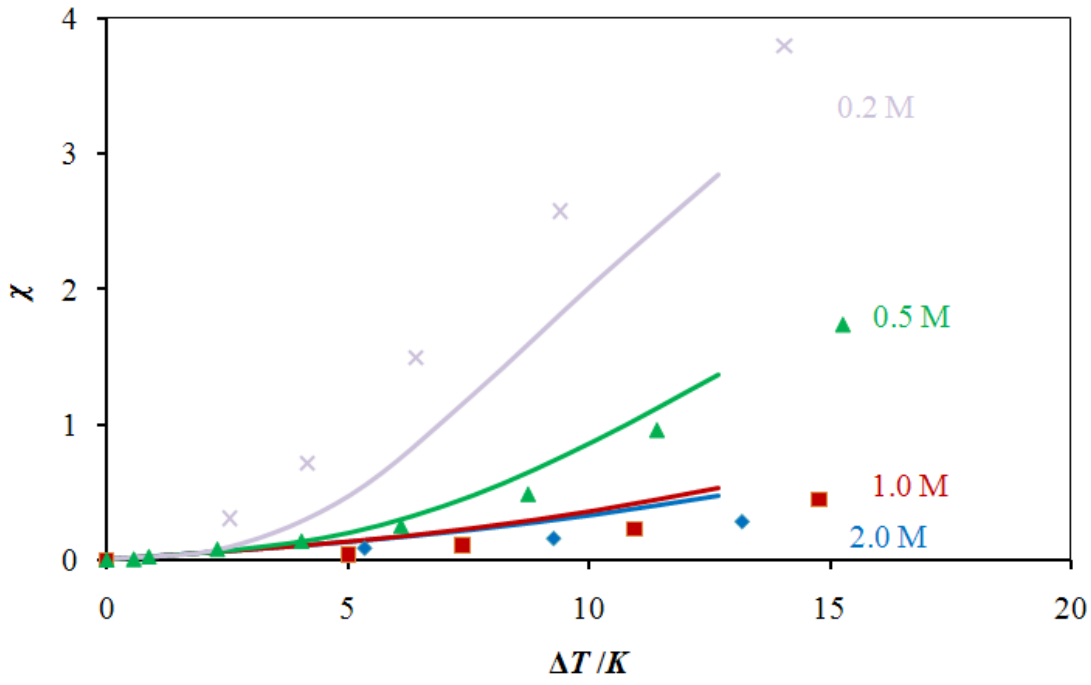

Figure 4.7 The limiting current enhancement factor plotted as a function of the change in the electrode temperature for different concentrations of the supporting electrolyte (KCl, concentrations are indicated beside each curve). Data points correspond to the experimental results for the steady-state oxidation of $Fe(CN)_6^{4-}$ at a 25 μm Pt disk electrode. Solid lines represent the results of the simulations obtained with a 128×128_8 grid.

The agreement between the experimental and the simulated data in the above Figure 4.7 is not quantitative. This may be caused by a number of factors, which are related to certain simplifications in the simulation algorithm. These simplifications influence the calculation of the temperature, the electrothermal force and also the solution flow rate. They are discussed below in more detail.

First of all, it should be realized that the simulated temperature field is approximate, since we do not account for the temperature dependence of the thermal conductivity coefficients of an electrode and solution, as well as the solution electrical conductivity (all these parameters are assumed constant). In addition, in simulations we neglect the effect of the electrothermal convection on the temperature distribution. Also, the simulated temperature distribution is not strictly at steady state, since it would require much more time or computer power to reach one. For example, in Figure 4.7 the values of the electrode surface temperature were obtained for the heating time equal to 37.8 ms.

Therefore, according to the results from Figure 4.5, these values of temperature are, probably, about 1-2 degrees lower than the steady-state values (in Figure 4.5, 37.8 ms heating time corresponds to the second left data point on the graph for a 12.5 μm electrode). However, in order to obtain a steady-state temperature distribution, it would take (depending on the grid size) anywhere from several days to several weeks of the computing time on a desktop computer with Intel® Core™2 Quad Processor Q9550 (2.83 GHz CPU speed).

The size of the distance step Δh has an important effect on the calculation of the electrothermal convection, solution flow rate and, therefore, the limiting current enhancement factor. The results in Figure 4.7 were obtained with a 128×128_8 grid. However, they are going to be somewhat different if another grid is used, such as 64×64_4 or 256×256_16, for example. This is illustrated well in Figure 4.8, where the same experimental data are plotted together with the simulation results obtained with a 64×64_4 grid. As one can see, the overlap between the two sets of data is worse than in Figure 4.7. One of the reasons for that is the finite thickness of the stagnant layer (this is the layer of solution adjacent to the electrode surface, in which no hydrodynamic flow occurs). In simulations the 'no flow' condition is fulfilled by the boundary condition of zero solution flow rate in all elements on the electrode surface (like elements 1, 2 and 4 in Figure 4.2). Therefore, the simulated stagnant layer has a thickness $\Delta h/2$, which is much larger than in reality (current thinking is that the stagnant layer is only few solvent molecules thick[32,98]). As a result, simulations of the limiting current enhancement factor have a large negative error associated with them, which is due to the overestimation of the stagnant layer thickness. The magnitude of this error decreases with the decrease of Δh, and a better match between the experimental and simulated data is achieved (Δh is equal to $1.5625 \cdot 10^{-4}$ cm for a 128×128_8 grid and $3.125 \cdot 10^{-4}$ cm for a 64×64_4 grid).

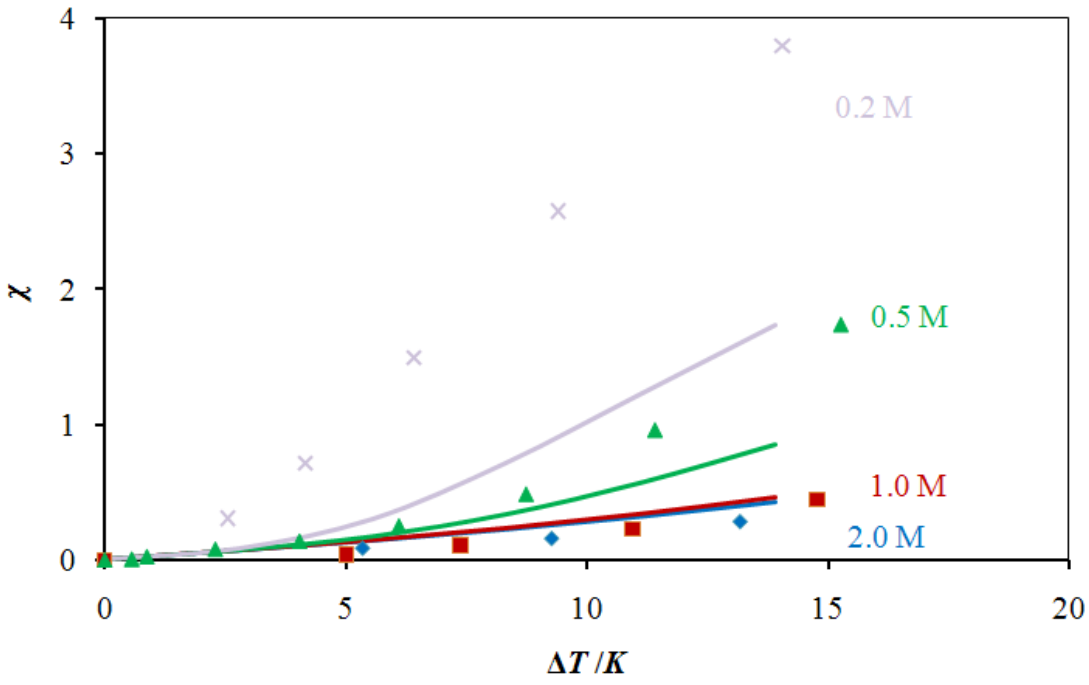

Figure 4.8 The limiting current enhancement factor plotted as a function of the change in the electrode temperature for different concentrations of the supporting electrolyte (KCl). Data points correspond to the experimental results for the steady-state oxidation of $Fe(CN)_6^{4-}$ at a 25 μm Pt disk electrode. Solid lines represent the results of the simulations obtained with a 64x64_4 grid.

There are a number of factors, which lead to positive errors in the limiting current simulations. The most important of them is related to the fact that, according to the works by Newman,[92,93] the electric potential (and, therefore, the potential gradient) goes to infinity at the electrode edge. The result of that is a large increase in the magnitude of the electrothermal force in solution elements at the edge of the electrode. Once Δh gets even smaller (when, for example, 256×256_16 or 512×512_32 grids are used instead of 128×128_8), a very large increase in the value of the solution flow rate in those elements is observed and the simulated limiting current enhancement ratio increases. In fact, the results of the simulations for a 256×256_16 grid (these data have been obtained only for some points on the curve, since it takes a very long time for the simulations to complete) are considerably larger than the experimental data in Figure 4.7. However, one has to realize that the theory of the edge effect developed by Newman strictly applies only to ideally smooth electrodes. On the atomic level no real electrode is ideally smooth, therefore, the assumption about the state of the electrode surface leads to the

overestimation of the simulated ac potential gradient and, subsequently, the solution flow rate and the limiting current values. In addition, it should be realized that, since glass is a harder material than platinum (glass is at level 6 to 7 and Pt is at level 4 to 4.5 on the Mohs scale of hardness), in real electrodes the disk of platinum sits somewhat below the surface of the glass insulation due to polishing (Figure 4.9). Thus, a disk electrode used in the experiments can be considered as a recessed electrode with a very short length of the channel (approaching zero). For this reason, the strength of the ac electric field at the electrode edge is not going to be as large as the one predicted by the simulations for an ideally smooth disk electrode. In fact, this may explain why the simulated values of the limiting current enhancement ratio obtained for a 128×128_8 grid fit the experimental data better than for a 256×256_16 or 512×512_32 grids.

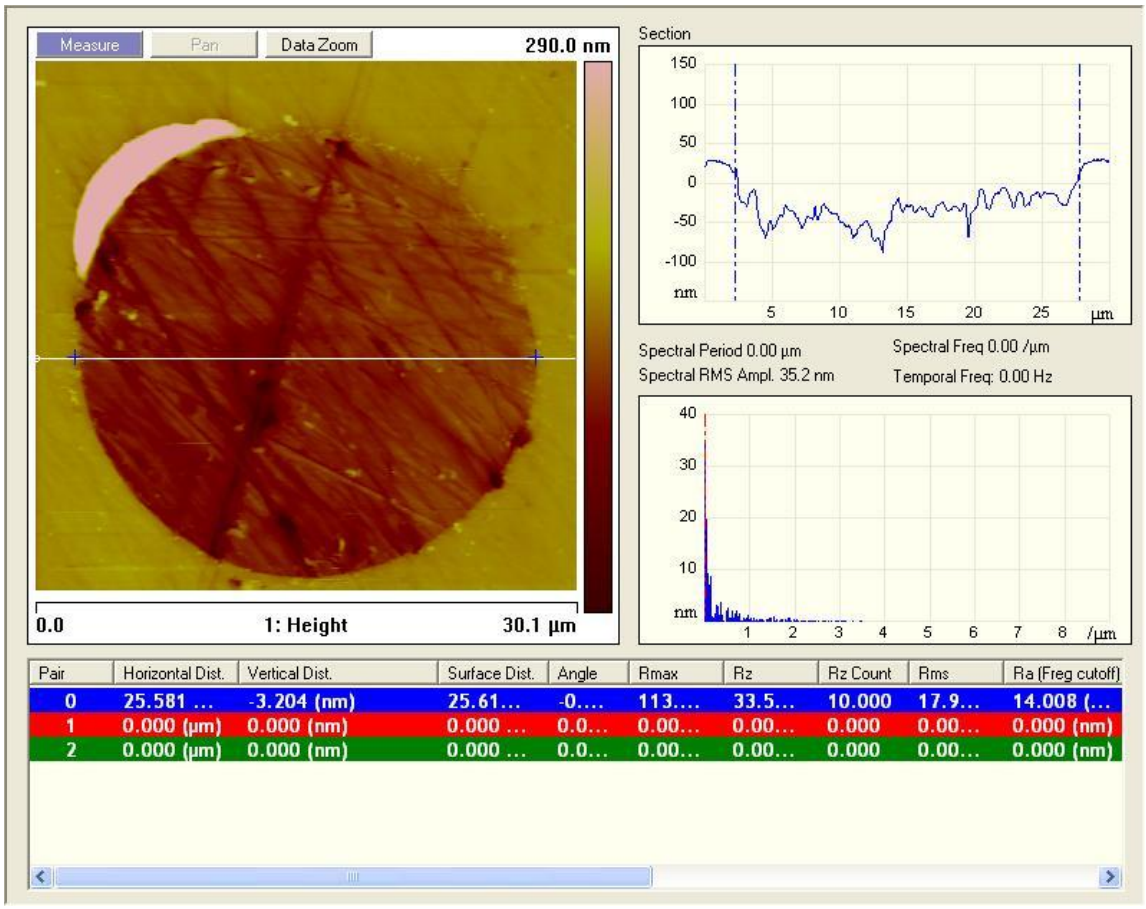

Figure 4.9 AFM image of the surface of a 25 μm Pt disk microelectrode. Top right graph suggests that the surface of the metal disk is lower than the surface of the glass by about 50 – 100 nm.

The assumption about the ideal state of the electrode surface (unity roughness) also leads to the positive error in the limiting current simulations due to the effect of the roughness of a surface on the rate of the solution flow near it. It is expected that the rate of the solution flow near a rough electrode surface will be lower than near an ideally smooth electrode due to the force of friction. As a result, the limiting current enhancement factor is expected to decrease when going from the ideally smooth electrode to the rough (real) electrode due to a decrease in the contribution of convection to the mass transfer.

Finally, one more effect can lead to a positive error in the simulations of the limiting current. It is called the Soret effect or nonisothermal diffusion (thermodiffusion). The details about how this phenomenon affects the mass transfer of the redox species at hot microelectrodes will be provided in the next Chapter. Here it should be mentioned that the results presented in Figure 4.7 were obtained for a zero value of the Soret coefficient of the redox species. However, if the Soret effect is taken into account, then for a positive value of the Soret coefficient (which means that redox species are diffusing towards a colder portion of the solution) the limiting current enhancement factor will decrease compared to the data in Figure 4.7.

As one can see, a number of factors result in both positive and negative errors in the limiting current simulations. Obviously, it is due to the compensation of these errors that the simulation and experimental data in Figure 4.7 correlate quite well. However, it should also be mentioned that the developed simulation program does not contain any adjustable (unjustified) parameters in its algorithm.

The results of the simulations of limiting current at hot microelectrodes support the experimental findings presented in Chapter 3 (Figure 3.14). As one can see in Figure 3.14, the size of a hot microelectrode does not have an effect on the limiting current enhancement factor. An explanation to these observations has been given in Section 3.4. The results of the simulations of the limiting current enhancement ratio shown in Figure 4.10 for three electrodes with different radii (1.25, 12.5 and 125 μm) fully agree with the proposed explanation that the convection at hot microelectrodes is largely due to the electrothermal flow of solution.

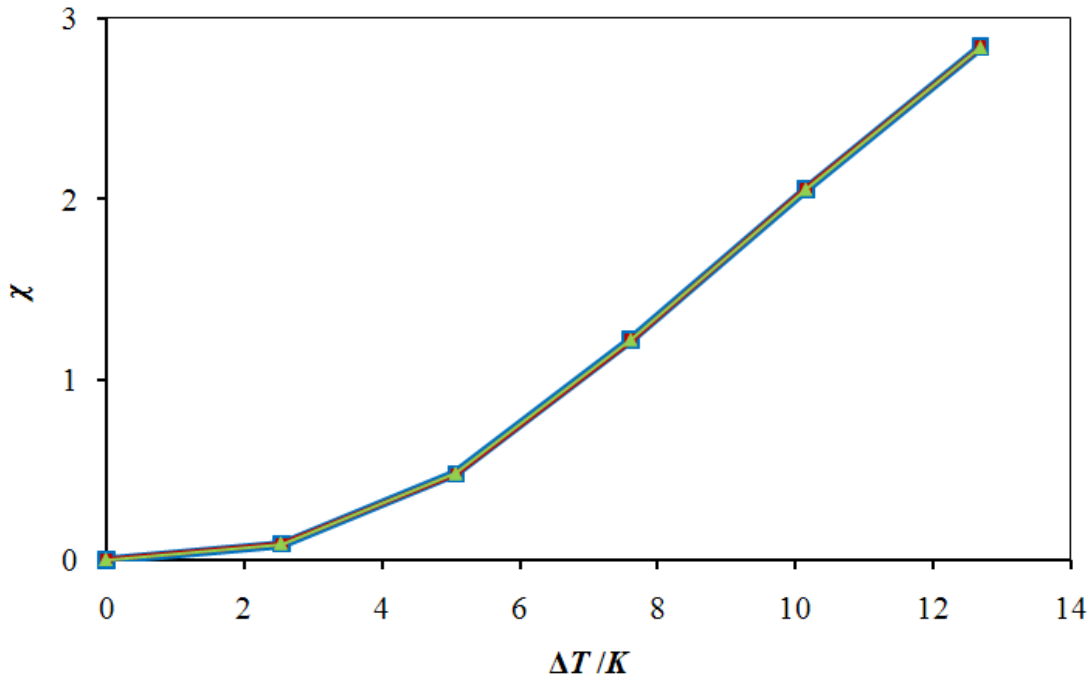

Figure 4.10 The limiting current enhancement factor plotted as a function of the change in the electrode temperature. The results are based on the simulations of the steady-state oxidation of $Fe(CN)_6^{4-}$ in 0.2 M KCl at hot-disk electrodes having the following radii: 1.25 μm (red), 12.5 μm (blue) and 125 μm (green). The size of the simulation grid was 128x128_8.

Using the simulation program it is also possible to determine the direction and magnitude of the solution flow due to the ac heating. A very interesting phenomenon has been predicted by the simulations and then observed experimentally: the direction of the solution flow has been found to depend on the properties of the electrode material, namely, its thermal conductivity. To fully comprehend this phenomenon, first of all, the nature of the electrothermal force needs to be understood well.

4.5.2 Mechanism of appearance of the electrothermal force

From equations 1.32 – 1.33 (Section 1.2.2.2) and discussion in Chapter 3 (Section 3.4) it is known that the electrothermal force is a sum of the Coulomb force acting on an unbalanced charge in solution and the dielectric force acting on water molecules. At frequencies of the ac signal below the cross-over frequency (given by equations 1.35 or 3.13), the Coulomb force is dominant and determines the magnitude and direction of the electrothermal force. Therefore, it is important to understand how the unbalanced charge

is formed in the ac heated electrolyte solution, since that determines the magnitude of the Coulomb force and, eventually, the flow of the solution.

Unbalanced charge is formed when both the temperature and electric potential gradients are present in solution (Figure 4.11). This condition is fulfilled for ac heated disk microelectrodes. For simplicity, let us initially consider the case when the thermal conductivity of the electrode material is zero (Figure 4.3, a). This means that the maximum temperature is reached at the electrode surface and the temperature gradient is directed towards the electrode disk everywhere in solution. Close to such an electrode one can choose an arbitrary volume element *v*. If, for a moment of time, the electric field strength vector is directed away from the electrode (Figure 4.11, a), then the local concentration of the negatively charged ions will decrease in the considered element *v*, while the concentration of the positively charged ions will increase in the same element. This is because the mobility of anions (given by equation 1.24, Section 1.2.2.1.1) will be higher than that of cations due to the direction of the temperature gradient. As a result, the considered volume element *v* will attain a net positive charge and the Coulomb force will be directed away from the electrode. The same conclusion is also reached for the other ac oscillation half-cycle (Figure 4.11, b), when the electric field strength vector is directed towards the surface of the electrode. The only difference is that the volume element will have a net negative unbalanced charge. However, the Coulomb force will still be directed away from the electrode.

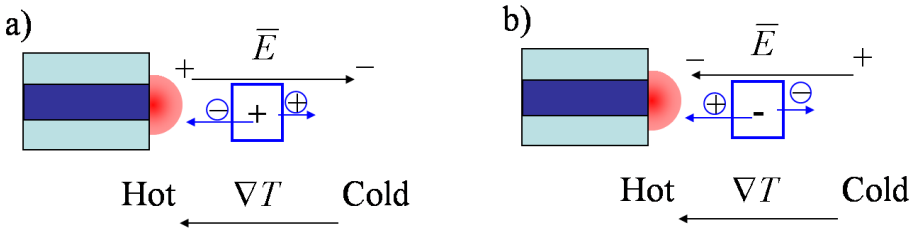

Figure 4.11 Mechanism of formation of an unbalanced charge in solution near an ac heated disk microelectrode. The electrode is shown from a side, with a hot zone represented by a red semicircle. An arbitrary solution volume element *v* is outlined by a blue square. Other explanations in the text.

As a second example, let us consider a hot Pt disk microelectrode. For this electrode the thermal conductivity of the metal wire is much higher than the thermal conductivity

of the solution. As a result, the heat transfer into the electrode body is substantial. Therefore, the maximum temperature due to the heating is located in solution, at a distance about 0.6 of an electrode radius away from the electrode disk (Figure 4.4, c). What this means is that in the vicinity of the electrode surface, where the ac electric field is the strongest, the temperature gradient is reversed, i.e. it is the opposite to the one discussed in the first case (Figure 4.11). Consequently, the Coulomb force close to the electrode surface will be directed towards the electrode disk.

To make the above considerations more clear, let us refer again to the equation for the electrothermal force, particularly, equation 1.33 (Section 1.2.2.2). In this equation, the term $\left(\frac{\nabla\sigma}{\sigma}-\frac{\nabla\varepsilon}{\varepsilon}\right)\cdot\varepsilon\overline{E}$ represents the unbalanced charge and has units of C cm^{-3}. The magnitude of this charge is proportional to the value of the dot product of the temperature gradient and the strength of the electric field $\overline{E}$, since $\nabla\sigma=(\partial\sigma/\partial T)\nabla T$ and $\nabla\varepsilon=(\partial\varepsilon/\partial T)\nabla T$. Thus, the expression for the Coulomb force could be written as $(\nabla T\cdot\overline{E})\overline{E}$, where the term in the parentheses describes the unbalanced charge. Therefore, the magnitude of the electrothermal force in each of the solution elements will depend both on the absolute values of the temperature gradient and the electric field strength vectors, and the cosine of the angle between them (this gives the value of the unbalanced charge). The direction of the Coulomb force vector, in general, will be determined by the direction of the field vector $\overline{E}$.The fact that the electric field is alternating does not mean that the Coulomb force is changing direction periodically. This has been explained in Figure 4.11 and, mathematically, can be written as $(\nabla T\cdot\overline{E})\overline{E}=(\nabla T\cdot(-\overline{E}))(-\overline{E})$. However, what makes the difference is how ∇T and $\overline{E}$ vectors are oriented with respect to each other in each of the solution elements, since that determines the sign and magnitude of the unbalanced charge. To explain this point, let us refer to Figure 4.12.

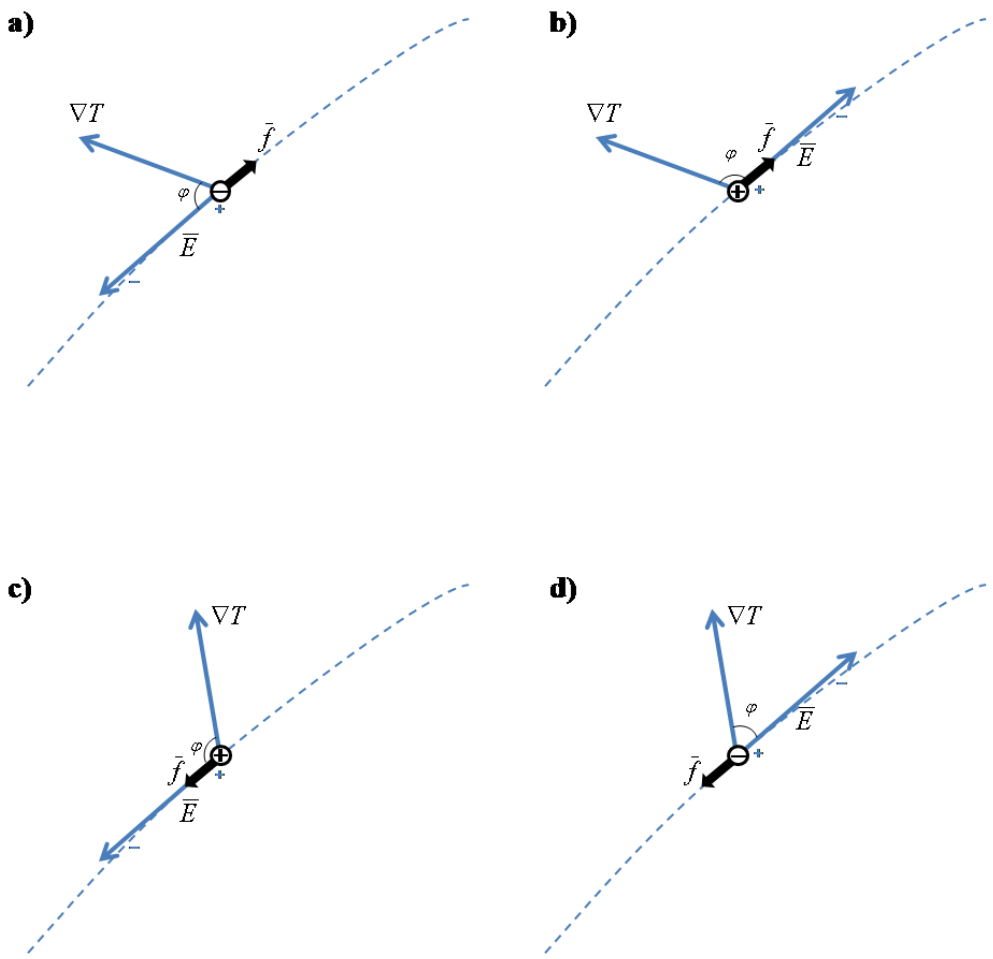

Figure 4.12 Effect of orientation of the electric field strength vector ($\bar{E}$) and the temperature gradient (∇T) on the direction of the Coulomb force ($\bar{f}$). Dashed line represents the line of the electric field and an open circle represents the centre of the element (grid point). The value of the unbalanced charge (either positive or negative) is indicated by the corresponding sign inside the open circle. φ is the angle between $\bar{E}$ and ∇T vectors.

First of all, what should be realized is that, in general, the temperature gradient ∇T and the electric field $\bar{E}$ are not parallel to each other as shown in Figure 4.11. Therefore, one can define an angle φ between these two vectors (Figure 4.12). Also, in Figure 4.12 let us assume that the bottom end of the electric field line (dash line) finishes on the surface of a hot microelectrode. Thus, in case (a) the ac electric field is directed towards the electrode and the angle φ between vectors $\bar{E}$ and ∇T is less than 90°. As a result, the projection of the temperature gradient on the electric field line will be oriented in the same direction as the electric field strength vector. This means that the considered

solution volume element will attain an unbalanced negative charge and the Coulomb force will be oriented in the direction opposite to $\overline{E}$ vector direction (which is also the opposite direction to the temperature gradient projection on the electric field line). The direction of the Coulomb force vector does not change for the other oscillation half cycle, when $\overline{E}$ vector is oriented away from the hot electrode (case b). In fact, the conclusions for these two cases (a) and (b) are identical to what has been discussed in Figure 4.11: the Coulomb force is directed away from the electrode. However, if the projection of the temperature gradient on the electric field line is oriented away from the electrode, as shown in cases (c) and (d), then the direction of the Coulomb force also changes to the opposite. Thus, from these considerations it may be concluded that the Coulomb force acting on an unbalanced charge is oriented in the direction opposite to the direction of the temperature gradient projection on the electric field line. In addition, since the ac electric field is the strongest at the edge of the microelectrode, the magnitude of the Coulomb force (and, therefore, the electrothermal force) is expected to be the largest at the disk circumference.

4.5.3 Results of simulations of the electrothermal force and solution flow

Discussed direction and magnitude of the Coulomb force have been confirmed by the results of the electrothermal force simulation (Figure 4.13) for a hypothetical case of a zero thermal conductivity microelectrode and for a Pt microelectrode. As expected, in the case of a zero thermal conductivity electrode the electrothermal force is directed away from the electrode surface everywhere in solution. This is so since the temperature gradient in each solution element is directed towards the electrode. However, for a Pt microelectrode the temperature gradient is reversed close to the electrode surface and the electrothermal force is directed towards the electrode. Also, in both cases the magnitude of the electrothermal force is the largest at the electrode disk circumference. This agrees well with the already mentioned findings of Newman that the electric field is the strongest at the electrode edge.

Simulations of the solution flow for these two systems revealed a very interesting phenomenon: for a zero thermal conductivity electrode the flow is directed towards the electrode surface, while it reverses the direction for a platinum electrode (Figure 4.14).

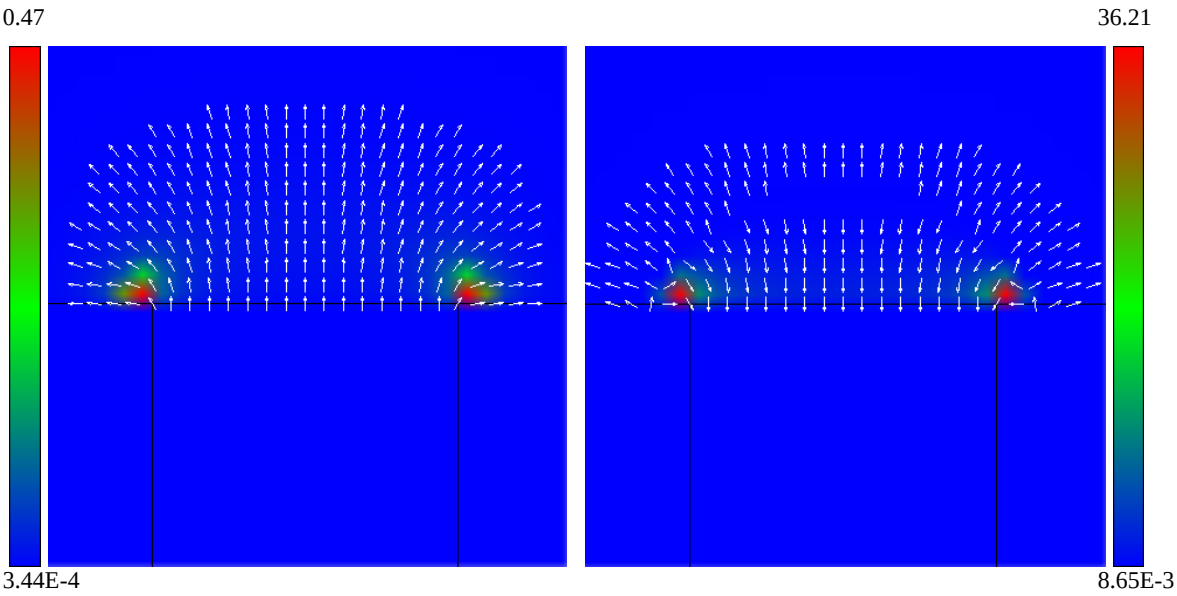

Figure 4.13 Results of the simulations of the electrothermal force (N cm^{-3}) for a 25 μm ZTC electrode (*left*) and a 25 μm Pt electrode (*right*). Simulation parameters: electrode temperature 308 K, concentration of the supporting electrolyte (KCl) 0.2 M. Magnitude of the force is indicated by the color on a corresponding color scale. Direction of the force is shown by arrows; however, the arrows are not displayed if the magnitude of the force is less than 0.5 % (ZTC electrode) or 0.2 % (Pt electrode) of its maximum value.

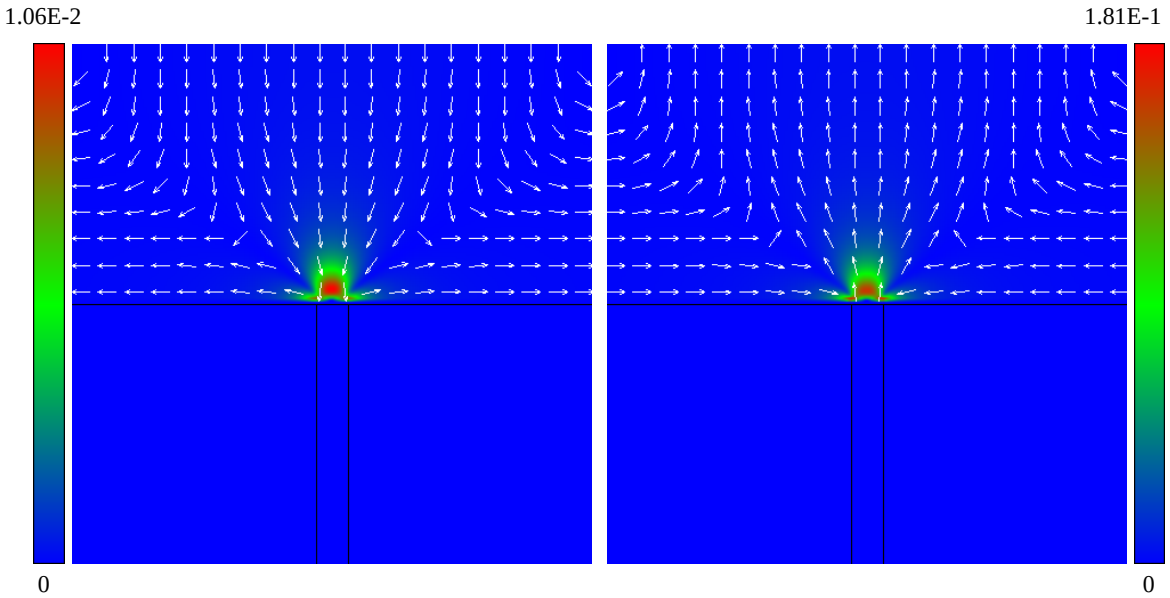

Figure 4.14 Results of the simulations of the linear flow rate of solution (cm s^{-1}) for a 25 μm ZTC electrode (*left*) and a 25 μm Pt electrode (*right*). Simulation parameters: electrode temperature 308 K, concentration of the supporting electrolyte (KCl) 0.2 M. Magnitude of the flow is indicated by the color on a corresponding color scale. Direction of the flow is shown by arrows.

Since the simulations for the two systems (ZTC electrode and Pt electrode) were done under similar conditions and the only difference was in the value of the thermal conductivity coefficients of electrode materials, it is clear that the observed variation in the direction of the solution flow is related to the difference in the temperature distribution around the discussed microelectrodes (Figure 4.4). However, the example of the electrode with a zero thermal conductivity of the body is rather hypothetical and has only theoretical value. Therefore, the same simulations were also done for a bismuth microelectrode, which has a very low thermal conductivity (0.0787 W cm^{-1} K^{-1} vs. 0.716 W cm^{-1} K^{-1} for Pt). The results obtained for the bismuth electrode were very similar to the results for the zero thermal conductivity electrode: namely, the flow of the solution was also found to be directed towards the electrode surface (Figure 4.15).

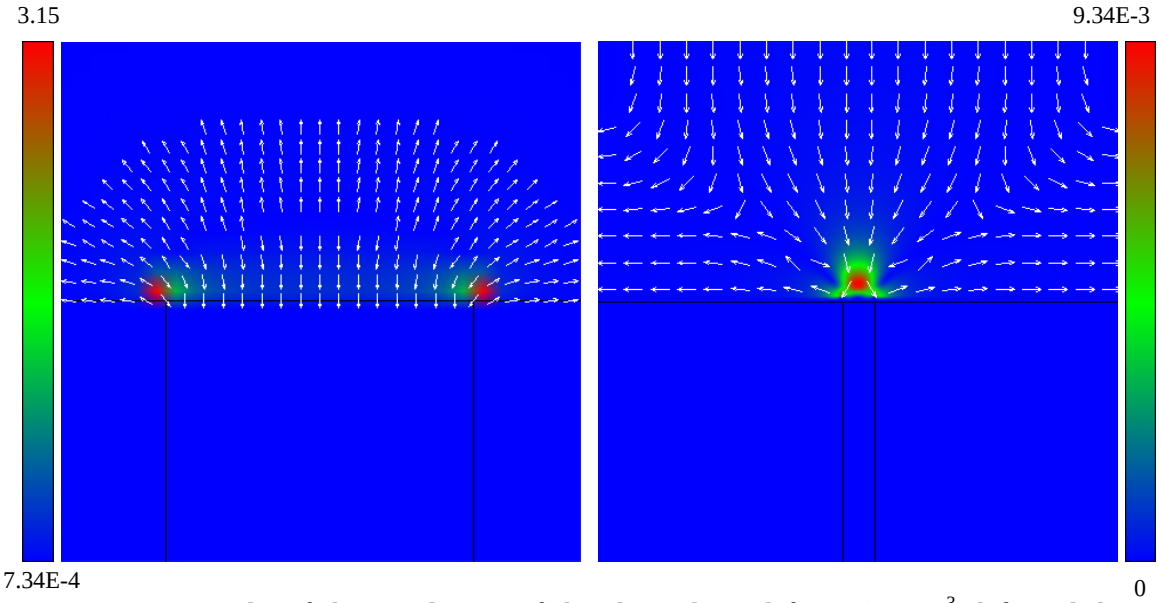

Figure 4.15 Results of the simulations of the electrothermal force (N cm^{-3}, *left*) and the linear flow rate of solution (cm s^{-1}, *right*) for a 25 μm Bi microelectrode. Other simulation parameters are the same as in Figures 4.13 and 4.14.

The biggest excitement occurred when the results of the solution flow simulations for platinum and bismuth hot-disk microelectrodes have been confirmed experimentally by recording real-time videos of methyl viologen reduction at these electrodes.

In the first movie (Video 4.1), one can see the formation of a wide colored diffusion layer due to MV^{2+} reduction on a Pt microelectrode. When the ac heating is turned on,

the initial diffusion layer is momentarily swept away from the electrode surface. This indicates that the solution flow is directed away from the electrode. This is in agreement with the simulation results in Figure 4.14.

Video 4.1 Solution flow around a hot Pt microelectrode during the reduction of 50 mM methyl viologen in 0.2 M KCl. The electrode was heated with an alternating voltage of 13.4V_{rms} at 20 MHz (see Appendix E2 for individual frames).

When a Bi microelectrode is used instead (Video 4.2), then the direction of the solution flow reverses. Once the ac heating is applied, the colored diffusion layer is getting shrunk with time due to the flow of the solution towards the electrode surface.

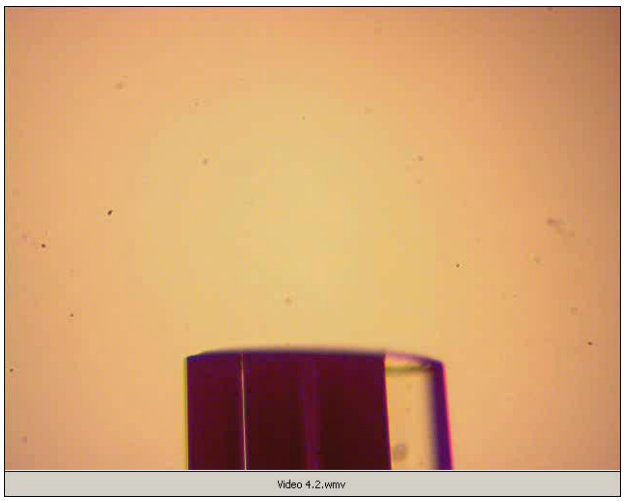

Video 4.2 Solution flow around a hot Bi microelectrode during the reduction of 50 mM methyl viologen in 0.2 M KCl. The electrode was heated with an alternating voltage of 13.4V_{rms} at 20 MHz (see Appendix E2 for individual frames).

These observations (Video 4.2) support the results shown in Figure 4.15.

The results of the solution flow simulations have been also supported by the simulations of the light transmittance (Figure 4.16). The idea behind these simulations was that if the simulated flow of solution is indeed correct, then the calculated light transmittance should also agree with the results of the video observations.

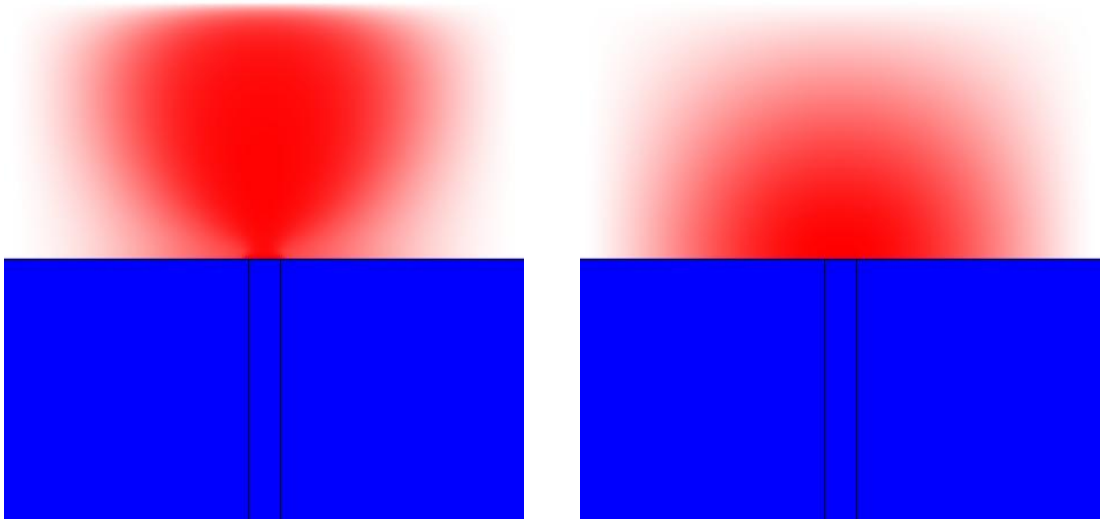

Figure 4.16 Results of the simulations of light transmission in solution around a 25 μm Pt (*left*) and a 25 μm Bi (*right*) hot microelectrodes. Simulation parameters: electrode temperature 308 K, concentration of the supporting electrolyte (KCl) 0.2 M, concentration of the absorbing species ($MV^{+\cdot}$) 10mM and the molar absorptivity $\varepsilon = 5 \cdot 10^4$ $M^{-1}cm^{-1}$.

Calculations of the transmittance (T) were based on the following equation:

$$T = \frac{I}{I_0} = 10^{-\varepsilon l C} \qquad (4.59)$$

where I is the intensity of light coming out of a sample, I_0 is the intensity of incident light, l is the path length of light, ε is the molar absorptivity and C is the concentration of the absorbing species ($MV^{+\cdot}$).

The values of the concentration of the absorbing $MV^{+\cdot}$ species in each solution element were determined by simulations as described in Section 4.3 (equation 4.46). The path length of light was calculated using the following formula for the length of a circle chord l (also, see Figure 4.17):

$$l = 2\sqrt{R^2 - h^2} \tag{4.60}$$

where R is the distance from the centre of the zeroth solution element (P = 0) to the outer boundary of the considered element and h is the perpendicular distance from the centre of the zeroth element to the centre of the considered element; h is equal to the product of P (index of the element) and Δh.

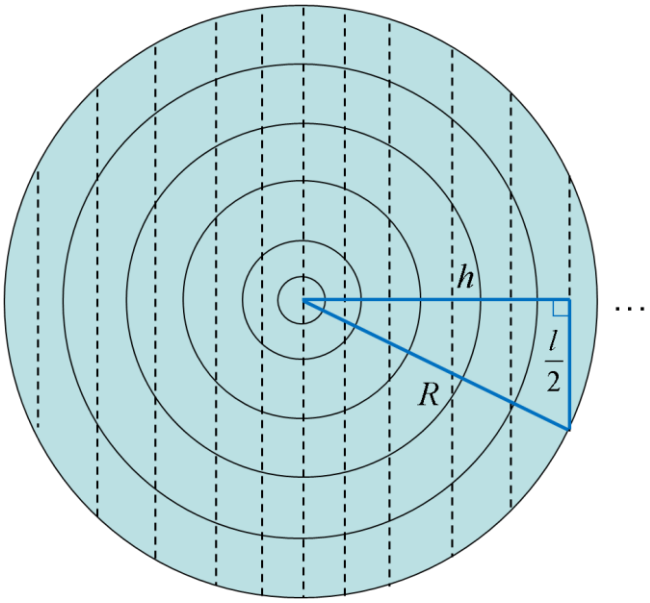

Figure 4.17 Calculation of the length of the light path represented by dashed lines passing through the centre of each solution element.

Thus, lower values of the solution transmittance in Figure 4.16 correspond to more intense red color and vice versa. It can be easily noticed that obtained transmittance simulation results are in a very good agreement with the results of the video observations (Videos 4.1 and 4.2). In particular, the shape of the red color zone (indicating low transmittance) in Figure 4.16 is elongated along z-axis in the case of a hot Pt microelectrode, and along ρ-axis for a Bi microelectrode. The same change in the shape of the $MV^{+\cdot}$ diffusion layer has been observed in the recorded videos. This means that the results of the numerical simulations discussed in this Chapter are reasonable and do not have any major mistake associated with them.

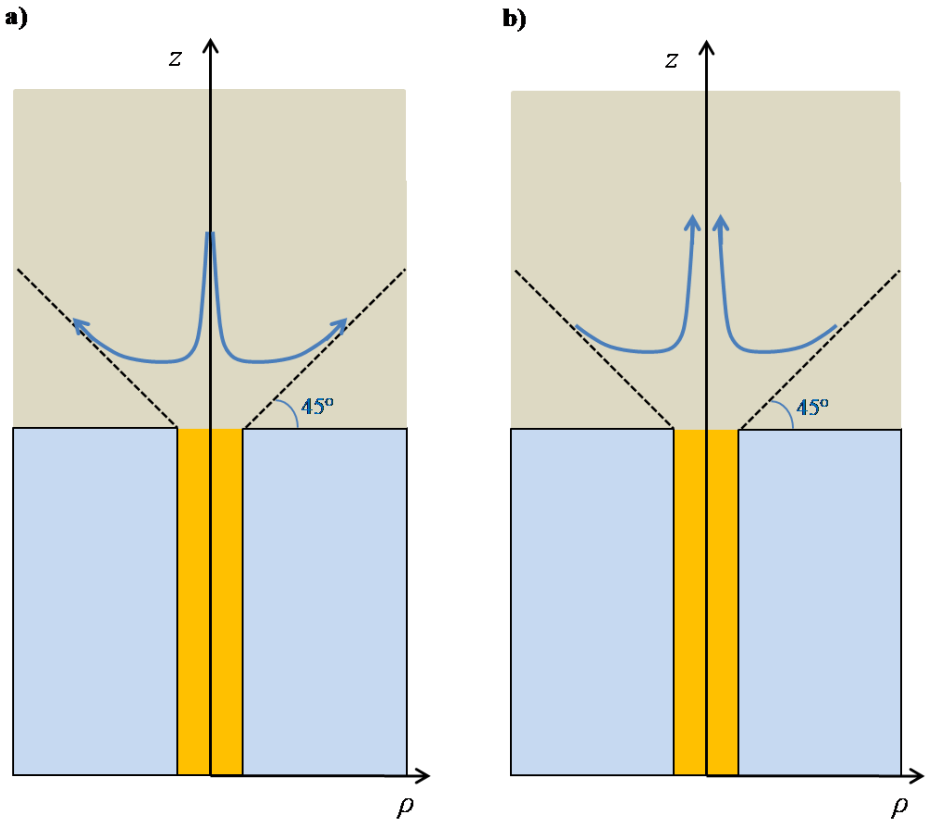

Figure 4.18 Qualitative explanation of the direction of solution flow indicated by blue arrows. In case (a) the electrothermal force in *z*-direction is weaker than along the 45° diagonal (represented by dashed lines); in case (b) the force in *z*-direction is stronger and the flow direction reverses.

The change of the direction of solution flow (as shown in Figures 4.14 and 4.15) can be qualitatively explained by evaluating the magnitude of the electrothermal force acting in two directions (Figure 4.18): along *z*-axis and along the diagonal, which is at 45° angle with respect to ρ-axis. The force along the diagonal is considered here since the ac electric field at the electrode disk circumference is the strongest and, in addition, diagonally polarized. The results of the electrothermal force simulations (Figures 4.13 and 4.15) indicate that, in general, the force is directed away from the electrode. This is because in most solution elements the temperature gradient is directed towards the electrode surface. As a result, the electrothermal force acting on an electrolyte solution along *z*-axis and along the diagonal will be directed away from the electrode. However, the magnitude of these forces will be different depending on the temperature distribution in solution near the electrode surface.

In the simplest case of the zero thermal conductivity electrode the electrothermal force along the 45° diagonal will be stronger then in *z*-direction, since the electric field is the strongest at the electrode edge and the temperature gradient everywhere in solution is directed towards the electrode surface. As a result, the flow of solution is directed towards the electrode, as shown in Figure 4.18, a.

However, if the maximum temperature is reached in solution and not at the electrode surface, then the force in *z*-direction can be larger than the force along the diagonal. This is so since in a number of solution elements along the 45° diagonal the temperature gradient can be orthogonal to the ac potential gradient (see Figure 4.12). Thus, the Coulomb force in such diagonal elements will be equal to zero, since the unbalanced charge is zero. As a result, the electrothermal force along *z*-axis will be larger than the force along the 45° diagonal and the flow of solution will be directed away from the electrode surface as shown in Figure 4.18, b.

CHAPTER 5: CONTRIBUTION OF SORET DIFFUSION TO MASS TRANSPORT AT HOT MICROELECTRODES

This Chapter contains the results of the studies of the Soret diffusion effect on mass transport of redox species at hot microelectrodes. The results presented here include both the experimental and simulated data. The details about the simulation algorithm used to account for the Soret effect can be found in Chapter 4 (Section 4.3). In general, the effect of Soret diffusion on mass transport is complex, since the presence of the supporting electrolyte ions in solution can also affect the behaviour of redox species (thermoelectric migration, Section 1.2.1.2). In addition, the Soret effect can be masked by strong convection. Therefore, its study would be practically impossible without the help from numerical simulations.

5.1 EXPERIMENTAL EVIDENCE FOR THE PRESENCE OF THE SORET EFFECT

Current literature on hot electrodes has a long history of neglecting the effect of Soret diffusion on mass transport of redox species. This could possibly be explained by the fact that electrochemists working in this field have drawn incorrect conclusions from the results of the early studies of thermodiffusion in nonisothermal electrochemical systems. As an example, let us refer to the work by Valdes and Miller,[99] in which the authors present the results of their studies of the effect of thermodiffusion on voltammetric response of thermally modulated rotating disk electrodes (RDE). Valdes and Miller conclude the publication by the statement that "thermodiffusion processes are not a contributory factor to limiting currents on a RDE". This is, probably, true under the conditions of their experiments (10 K difference in temperature between the electrode surface and the bulk solution, electrode rotation speeds on the order of 1000 rpm), since

the magnitude of the Soret effect is not particularly large in the systems with very intensive convection and low temperature perturbation. However, other research groups (see, for example, works by Gruendler and Marken[20]) have not realized this, and since the mentioned work of Valdes and Miller the magnitude of the Soret effect in nonisothermal electrochemical systems has been accepted to be negligible. Contrary to this, the results obtained during my PhD work indicate that Soret diffusion contributes significantly to mass transport at hot microelectrodes, especially when convection in the studied electrochemical systems is weak.

In order to decrease the rate of the electrothermal convection observed at hot microelectrodes it is beneficial to use recessed electrodes. It was expected that if recessed electrodes are employed, then the electrothermal flow of solution would be impeded by the channel walls and the Soret effect would be more visible. The experimental results indicating that Soret diffusion indeed affects the faradaic currents on hot microelectrodes are shown in Figure 5.1. As one can see, for the same amplitude of ac modulation an increase in the limiting current for the reduction of ferricyanide ions is much higher than for the oxidation of ferrocyanide ions. However, without ac heating (0 V_{rms}) the limiting currents in both cases are identical due to essentially the same diffusion coefficients of these redox species. Therefore, the only feasible explanation to the observed effect is that the Soret coefficients of ferri- and ferrocyanide ions are dissimilar.

In Figure 5.2 the absolute values of the limiting current enhancement factor for the reduction of $Fe(CN)_6^{3-}$ and for the oxidation of $Fe(CN)_6^{4-}$ are plotted as the function of the electrode temperature. These are the results of analyses of the steady-state voltammograms shown in Figure 5.1 with a few more data points. It is obvious that the Soret effect is indeed present under the experimental conditions stated in the legend to Figure 5.1.

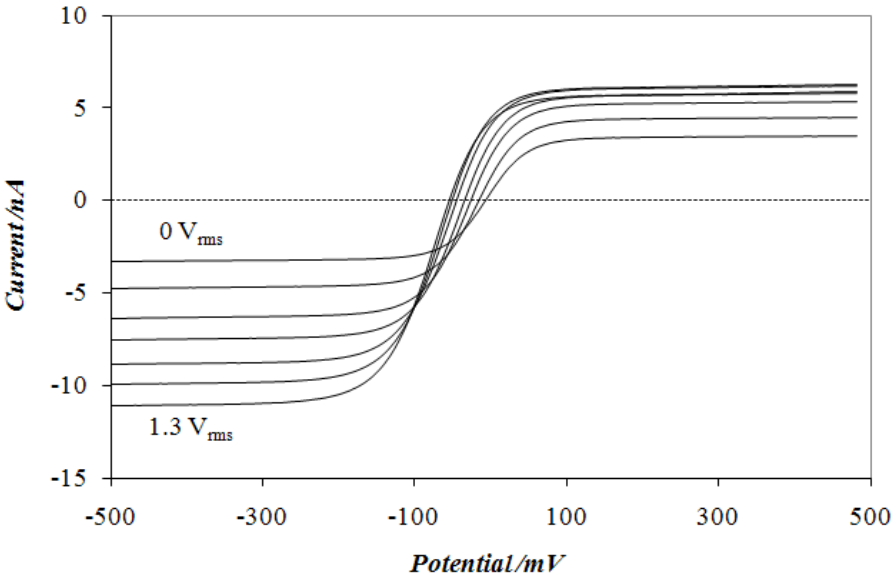

Figure 5.1 Steady-state voltammograms obtained at a 3.3 μm recessed Pt electrode (~8 μm length of the channel) heated to different temperatures by 1240 MHz sinusoidal waveforms with amplitudes ranging from 0 to 1.3 V_{rms}. The solution contained 50 mM $K_4Fe(CN)_6$, 50 mM $K_3Fe(CN)_6$ and 2 M KCl and the sweep rate was 50 mV s^{-1}.

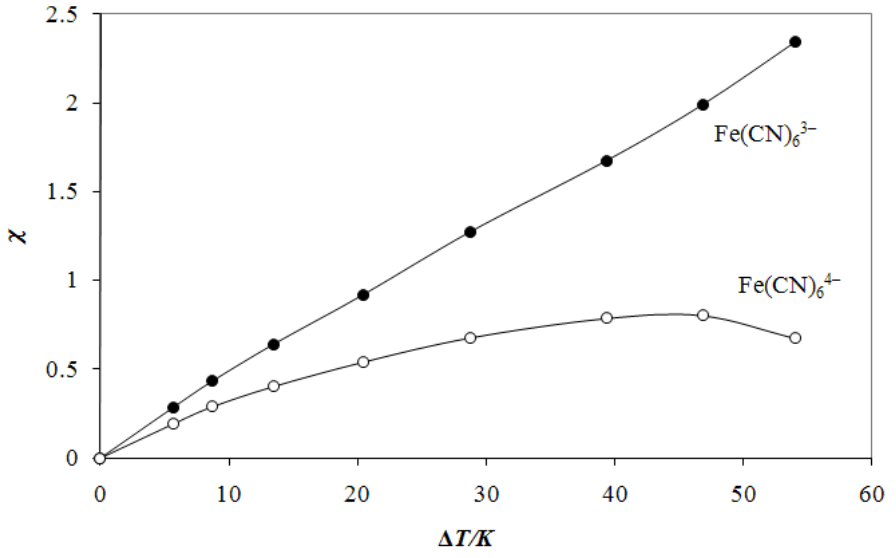

Figure 5.2 Temperature dependence of the limiting current enhancement factor for the reduction of $Fe(CN)_6^{3-}$ and for the oxidation of $Fe(CN)_6^{4-}$. All experimental conditions are the same as in Figure 5.1.

It should also be noted that the same effect, although smaller in magnitude, has been observed for a 25 μm Pt disk electrode in 2 M KCl under similar conditions: for ΔT = 60 K, $\chi_{reduction}$ = 2.27±.05 and $\chi_{oxidation}$ = 1.86 ±.04 (in 0.5 M KCl, $\chi_{reduction}$ = 9.30±.06 and $\chi_{oxidation}$ = 9.05±.05). These results indicate that the magnitude of the Soret effect is affected by the rate of the electrothermal convection (the rate of the electrothermal flow depends on the supporting electrolyte concentration).

Similar experiments were also performed with recessed Pt electrodes using cyclic voltammetry with the scan rate of 10 V/s. The previously described recessed electrode (Figure 5.1) had too large charging currents, therefore, another recessed Pt electrode was made, which had a 25 μm diameter and the length of the channel about 45 μm. The solution contained 50 mM $K_4Fe(CN)_6$ in 2 M KCl. Voltammograms recorded during a heating experiment are shown in Figure 5.3. In the actual experiment, CV curves have been recorded continuously in 0.5 s intervals. However, in Figure 5.3 only selected curves are shown.

Curve (a) was recorded at the beginning of the experiment without any heating. Then, as curve (b) has been recorded, the ac generator (set to the frequency of 165 MHz and the amplitude of 2.0 V_{rms}) was turned on. As a result, curve (b) overlaps with curve (a) up to the oxidation peak and, after that, shows a dramatic increase of current due to the heating. Curve (c) was recorded after continuous heating for about 10 s. At that time the electrode reached a steady state and preceding CV curves were identical with curve (c). The potential shift of curve (c) with respect to curve (a) allows determination of the hot electrode temperature, which was 78 °C higher than the initial temperature. At that temperature (~ 102 °C) the viscosity of the solution is much lower than at the room temperature, so the peak currents for curve (c) should be much higher than for curve (a), but they are not. This fact can be explained assuming that the hot zone inside the electrode channel was depleted from $Fe(CN)_6^{4-}$ due to the Soret effect. This assumption is also consistent with the magnitude of peak currents for curve (d) ,which was recorded immediately after turning the heating off. The solution in the hot zone cooled down very quickly (the standard potential determined from that curve indicates that the electrode temperature was only 18 °C higher than the initial temperature). Consequently, the viscosity of the solution increased, but the solution remained depleted from $Fe(CN)_6^{4-}$.

Therefore, the peaks were much smaller than for curve (a). However, after 10 s without heating, the solution inside the channel reached equilibrium and the recorded voltammogram, curve (e), overlapped with the initially recorded curve (a).

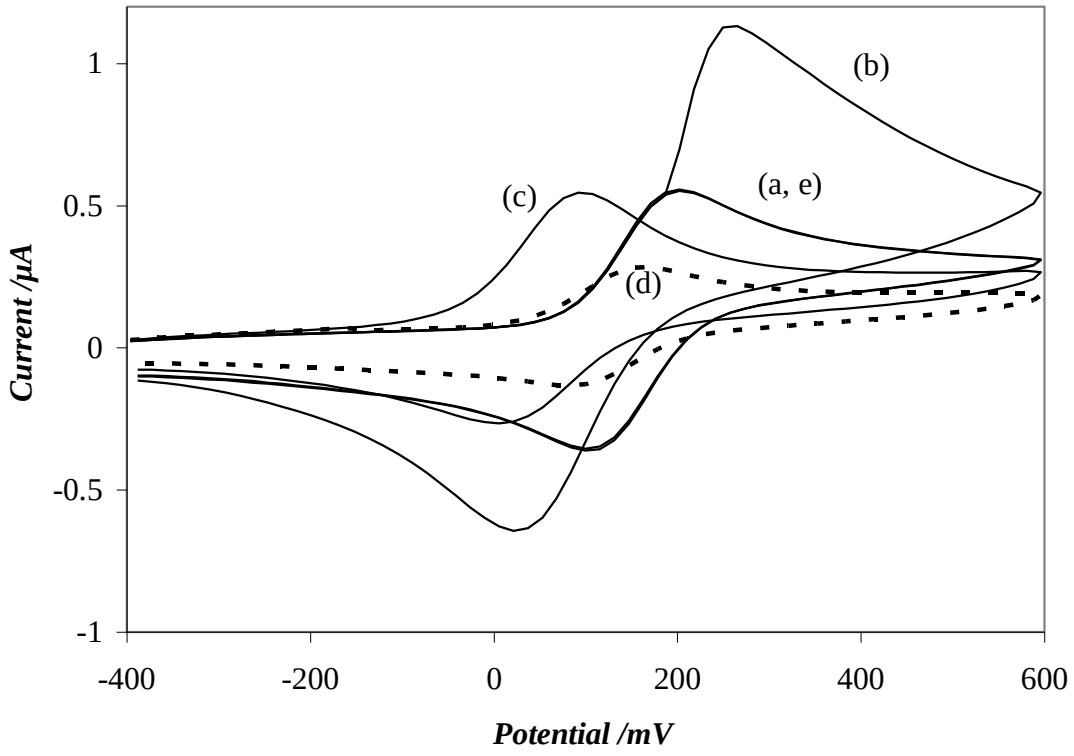

Figure 5.3 Cyclic voltammograms recorded in 50 mM $K_4Fe(CN)_6$ and 2 M KCl with a 25 μm recessed Pt electrode. The sweep rate was 10 V s^{-1}; the heating of the electrode by approximately 78 °C was caused by 165 MHz sinusoidal waveform with 2.0 V_{rms}. Two overlapping curves (a) and (e) were recorded at the beginning and at the end of the experiment with ac heating turned off. The heating was turned on during the recording of curve (b) and it was on for 10 s before (and during) recording of the curve (c). Curve (d) was recorded immediately after turning the heating off.

It should also be noted that similar changes in the voltammograms (as shown in Figure 5.3) were observed when a disk microelectrode was used instead of a recessed one under similar conditions. However, the magnitude of these changes was smaller, which suggests that the rate of the electrothermal convection indeed affects the magnitude of the Soret effect.

5.2 RESULTS OF THE SORET EFFECT SIMULATIONS

5.2.1 Effect of Soret diffusion on the faradaic current

The results of the numerical simulations of the effect of Soret diffusion on mass transport at hot microelectrodes support experimental observations: the limiting current enhancement factor is affected by the value of the Soret coefficients of the redox species. In Figure 5.4 one can see how the limiting current changes with variation of the Soret coefficient of the redox species both in magnitude and sign:

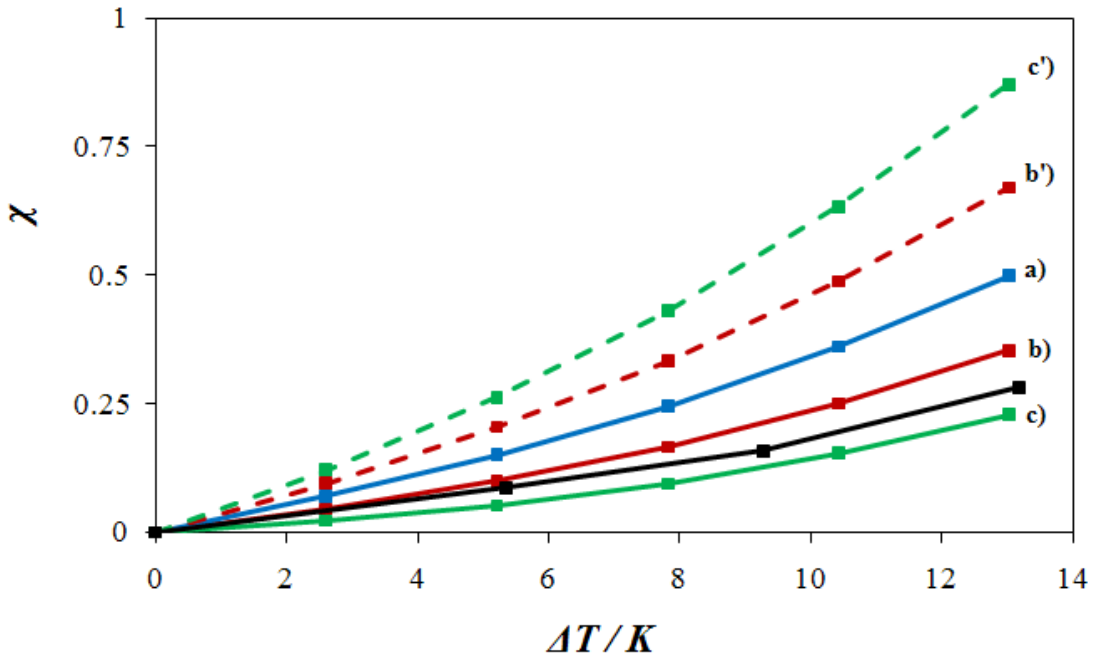

Figure 5.4 Effect of Soret diffusion on the limiting current enhancement factor. Simulations were done for the oxidation of the potassium ferrocyanide in 2 M KCl. Values of the Soret coefficients of ferrocyanide ions: a) σ_R = 0 K^{-1}; b) σ_R = $5 \cdot 10^{-3}$ K^{-1}; b') σ_R = $-5 \cdot 10^{-3}$ K^{-1}; c) σ_R = $1 \cdot 10^{-2}$ K^{-1}; c') σ_R = $-1 \cdot 10^{-2}$ K^{-1}; black curve represents experimental results.

Positive value of the Soret coefficient of the redox species indicates that the species (ferrocyanide ions, in this case) will be repelled from the hot zone. As a result, the decrease in the limiting current is observed for $\sigma_R > 0$ as shown by the curves (b) and (c). On the contrary, if the species has a negative Soret coefficient, its mass transfer rate towards the hot zone increases and the limiting current also increases as shown by

curves (b') and (c'). Clearly, the bigger the value of the Soret coefficient, the more pronounced the effect on the faradaic current is. For example, in the above Figure 5.4 the difference in the slopes between the linear parts of the curves (a) and (b) is negative 28%, while it increases to negative 52% for curves (a) and (c).

Obtained experimental results indicate that the effect of Soret diffusion on the limiting current decreases with the decrease in the supporting electrolyte concentration. The evidence for that is the already mentioned decrease in the difference between $\chi_{\text{reduction}}$ and $\chi_{\text{oxidation}}$ for a 25 μm Pt disk electrode in 2 M KCl and in 0.5 M KCl solutions. This fact means that the magnitude of the Soret effect decreases with an increase in the rate of the electrothermal convection in the system. The same results are also obtained from simulations. For example, the difference in slopes between curves (a) and (b) in Figure 5.4 decreases from negative 28% (2 M KCl solution) to negative 7.0% (0.2 M KCl). At the same time, the maximum linear flow rate of solution due to the electrothermal convection is about 8 times larger in 0.2 M KCl solution than in 2 M KCl. These findings support the idea that the effect of Soret diffusion on mass transfer of redox species is harder to notice in electrochemical systems with higher rate of convection.

5.2.2 Effect of Soret diffusion on the half-wave potential

Since Soret diffusion of redox species affects their concentration in the hot zone, it can also change the value of the half-wave potential. To understand this, let us firstly refer to the formula for the half-wave potential ($E_{1/2}$), which can be written as:[17]

$$E_{1/2} = E_{i=i_d/2} = E^0 + \frac{RT_s}{nF} \ln \frac{\left(C_{Ox}^s\right)_{i=i_d/2}}{\left(C_R^s\right)_{i=i_d/2}} \qquad (5.1)$$

where $E_{i=i_d/2}$ is the value of the potential on a steady-state voltammogram, for which the faradaic current (i) is equal to one half of the limiting current ($i_d/2$); $\left(C_R^s\right)_{i=i_d/2}$ and $\left(C_{Ox}^s\right)_{i=i_d/2}$ are the corresponding surface concentrations of the reduced and oxidized forms of the depolarizer, respectively. T_s is the temperature at the electrode surface and other symbols have their usual meanings.

If no temperature gradient exists near the electrode surface (isothermal conditions), the values of C_R^s and C_{Ox}^s in the above equation are equal (assuming identical diffusion coefficients of the species). Therefore, the value of the half-wave potential is equal to the standard potential (E^0) of the redox reaction. If the temperature gradient is present in solution near the electrode, then (according to equation 5.1) the value of the half-wave potential can be affected by the effect of temperature and by the Soret effect. The effect of temperature arises due to temperature dependence of the half-wave potential ($dE_{1/2}/dT = dE^0/dT$ if no Soret effect is present). However, under the nonisothermal conditions Soret diffusion will affect the shift in $E_{1/2}$ if the Soret coefficients of the reduced and oxidized forms of the depolarizer are dissimilar. The value of the Soret effect contribution to the half-wave potential can be expresses by the difference ($E_{1/2} - E^0$), which develops due to the fact that the surface concentrations of the redox species are not equal (equation 5.1).

It does not seem to be feasible to obtain an analytical expression that would include the contribution from the Soret effect to the half-wave potential. However, by using numerical simulations it is possible to model the effect of Soret diffusion on the surface concentrations of redox species and, therefore, the half-wave potential $E_{1/2}$.

As the simplest example, the results of the simulations of the Soret effect on $E_{1/2}$ for a hot spherical microelectrode will be discussed first (Figure 5.5). The complete discussion of the simulation algorithm used to obtain these data can be found in Appendix D. Here it should be noted that this algorithm is relatively simple; therefore, it was possible to do the simulations in Excel.

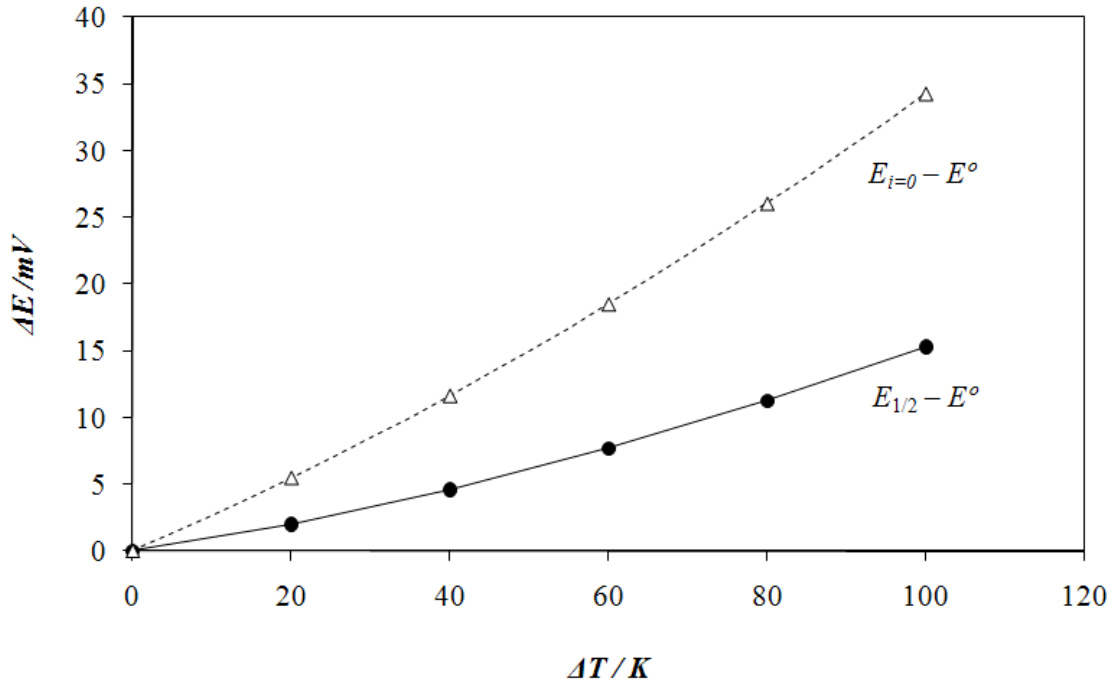

Figure 5.5 Temperature dependence of $E_{1/2} - E^0$ (●) and $E_{i=0} - E^0$ (△) obtained from numerical simulations of steady-state voltammograms at a hot spherical microelectrode. Value of the difference of Soret coefficients $(\sigma_R - \sigma_{Ox})$ = $1 \cdot 10^{-2}$ K^{-1}. Dashed line represents $E_{i=0} - E^0$ calculated using equation 5.2.

In Figure 5.5 one can see that the magnitude of the Soret diffusion effect on the half-wave potential (given by $E_{1/2} - E^0$) is not very large. These results indicate that, if the difference of the Soret coefficients of the redox species is $1 \cdot 10^{-2}$ K^{-1}, the contribution of Soret diffusion to the half-wave potential shift is about 10% (assuming the temperature coefficient of the standard potential equal to –1.5 mV K^{-1}). The temperature dependence of the difference between the zero current potential ($E_{i=0}$, expected in the case when bulk concentrations of both redox forms are identical) and the standard potential (E^0) is also plotted in Figure 5.5. This simulated relationship fully agrees with the results obtained using the following equation:

$$E_{i=0} = E^0 + \frac{RT_s}{nF}(\sigma_R - \sigma_{Ox})(T_s - T_b) \qquad (5.2)$$

where T_b is the temperature in the bulk of the solution (298 K).

The above equation 5.2 can be easily derived if one substitutes equation 1.12 (Section 1.2.1.2) for the ratio of the surface concentrations in equation 5.1. The fact that the simulated results and the analytical solution (equation 5.2) are identical means that the simulation algorithm used to obtain the data in Figure 5.5 is correct.

One would expect that the effect of Soret diffusion on the half-wave potential shift for a zero thermal conductivity disk electrode would be comparable to the one observed at a hot spherical electrode. This is so since, in both cases, the temperature distribution in solution is very similar (the maximum temperature value is reached at the electrode surface). In Figure 5.6 one can see the results of the simulations of the Soret effect on the half-wave potential shift for a zero thermal conductivity electrode. Blue data points (case a) were obtained for a zero difference of the Soret coefficients of the redox species (no Soret effect on $E_{1/2}$). Therefore, the slope of this graph is equal to –1.5 mV K^{-1}, since the same value of the temperature coefficient dE^0/dT is used in simulations (Section 4.3, equation 4.51). However, if the difference of the Soret coefficients is equal to $1 \cdot 10^{-2}$ K^{-1} (the Soret effect on $E_{1/2}$ is present), then the slope of the graph gets smaller (red data points, case b). This shift in $E_{1/2}$ could be rationalized if equation 5.1 is considered. When the Soret coefficient of the reduced form of the depolarizer is larger than that of the oxidized form ($\sigma_R - \sigma_{Ox} > 0$), the reduced form is expelled stronger from the hot zone. This results in the decrease of the surface concentration $\left(C_R^s\right)_{i=i_d/2}$ compared to $\left(C_{Ox}^s\right)_{i=i_d/2}$ and, therefore, the positive contribution of the Soret effect to the temperature dependence of the half-wave potential ($E_{1/2} - E^0 > 0$) is observed.

The dashed line in Figure 5.6 corresponds to the results obtained for the spherical microelectrode (Figure 5.5). The fact that it almost completely overlaps with the data for the zero thermal conductivity disk microelectrode (red data points, case b) suggests that the simulation algorithm developed for the hot-disk microelectrodes (Chapter 4) is correct and does not have any major mistakes.

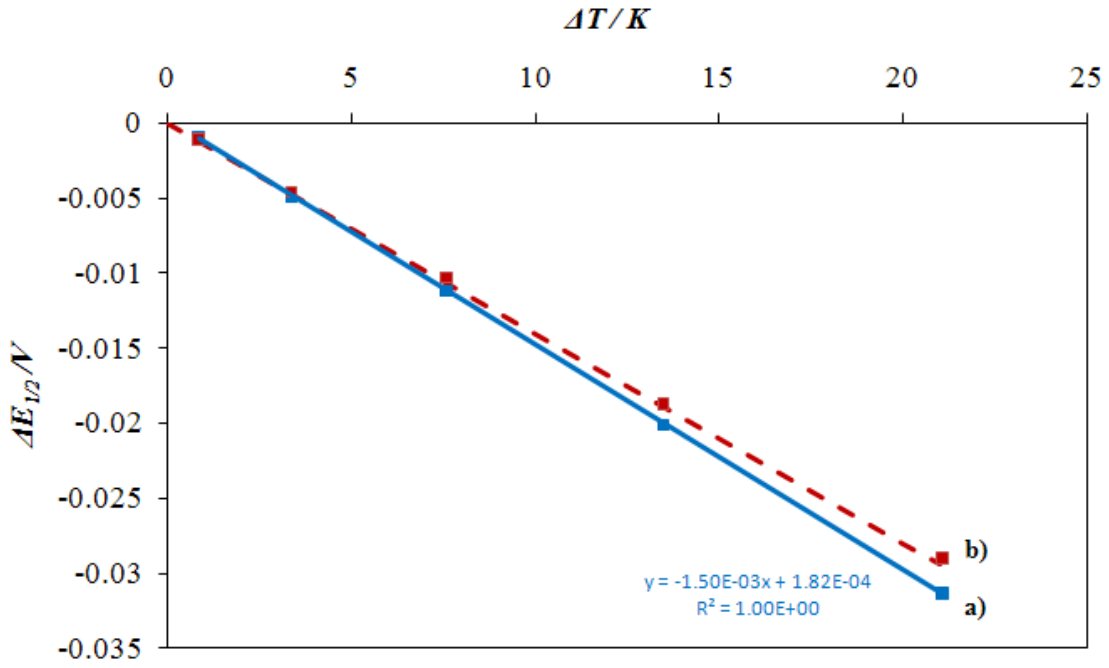

Figure 5.6 Effect of Soret diffusion on the half-wave potential shift. Simulations were done for the oxidation of potassium ferrocyanide in 2 M KCl at a 25 μm ZTC electrode. Values of the difference of Soret coefficients $(\sigma_R - \sigma_{Ox})$, K^{-1}: a) 0; b) $1 \cdot 10^{-2}$. Dashed line corresponds to the results in Figure 5.5.

Interestingly, the results of the simulations of the half-wave potential shift for Pt (Figure 5.7) and Au hot-disk microelectrodes (Figure 5.8) differ substantially from what has been observed in Figure 5.6. In both cases (Pt and Au), the change in the slope of the graphs due to the Soret effect occurs in the opposite direction compared to the results for the zero thermal conductivity electrode. To explain the observed effect of Soret diffusion on the half-wave potential shift in the case of Pt and Au hot microelectrodes, it should be realized that for these electrodes the maximum temperature is reached in solution (Figure 4.4). This means that in the vicinity of the electrode surface the temperature gradient is reversed: the electrode is relatively colder than the solution surrounding it (yet, the temperature of the electrode is still higher than the temperature in the bulk solution).

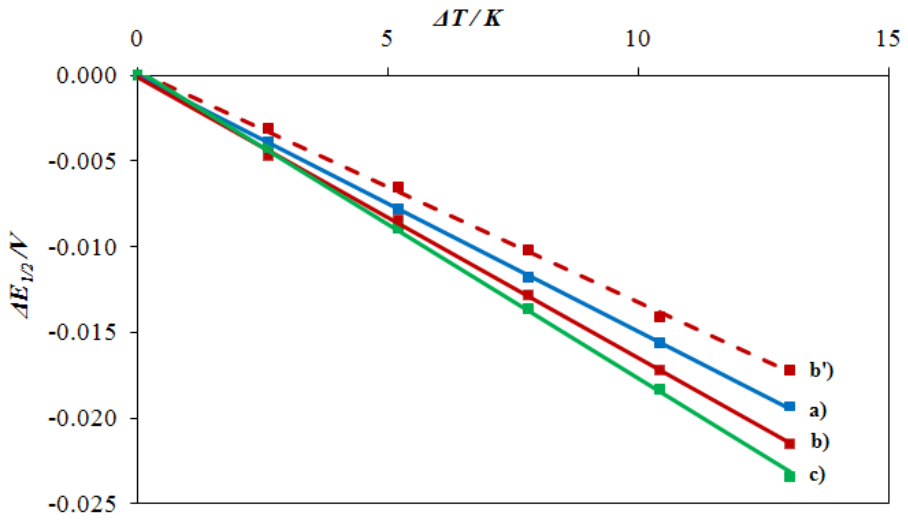

Figure 5.7 Effect of Soret diffusion on the half-wave potential shift. Simulations were done for the oxidation of potassium ferrocyanide in 2 M KCl at a 25 μm Pt hot-disk microelectrode. Values of the Soret coefficients difference $(\sigma_R - \sigma_{Ox})$, K^{-1}: a) 0; b) $5 \cdot 10^{-3}$; b') $-5 \cdot 10^{-3}$; c) $1.0 \cdot 10^{-2}$.

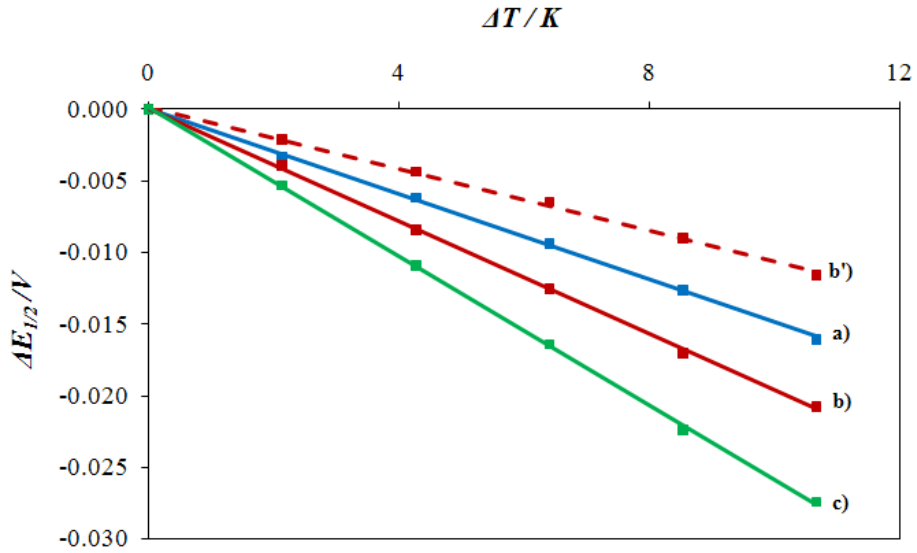

Figure 5.8 Effect of Soret diffusion on the half-wave potential shift. Simulations were done for the oxidation of potassium ferrocyanide in 2 M KCl at a 25 μm Au hot-disk microelectrode. Values of the Soret coefficients difference $(\sigma_R - \sigma_{Ox})$, K^{-1}: a) 0; b) $5 \cdot 10^{-3}$; b') $-5 \cdot 10^{-3}$; c) $1.0 \cdot 10^{-2}$.

If the difference $(\sigma_R - \sigma_{Ox})$ is larger than 0 (this means that the reduced form of the depolarizer is stronger expelled from the hot zone, than the oxidized form), then the surface concentration C_R^s will be larger than C_{Ox}^s. According to equation 5.1 this will lead to the shift of the half-wave potential towards more negative values (negative contribution of the Soret effect to the temperature dependence of the half-wave potential, $E_{1/2} - E^0 < 0$).

For the same value of the electrode surface temperature, the magnitude of the 'reverse' temperature gradient in the vicinity of the electrode surface is larger in the case of Au microelectrode, than Pt. Therefore, the discussed change (due to the Soret effect) in the slope of the half-wave potential temperature dependence is more pronounced for Au microelectrode, and the % difference in the slope of the graphs is roughly four time larger for Au than Pt.

The fact that Soret diffusion of the redox species affects the magnitude of the half-wave shift means that there is an error involved in the determination of the temperature of a hot electrode. Obviously, this error affected the measurements of the electrode temperature in all of the experimental results presented in this thesis. The value of this error depends on the difference of the Soret coefficients for ferro- and ferricyanide ions. According to the simulation results, if the difference of the Soret coefficients $(\sigma_R - \sigma_{Ox})$ is equal to $5 \cdot 10^{-3}$ K^{-1}, then the error in the temperature of a hot microelectrodes determined from the shift of the half-wave potentials is expected to be 8.1% for a platinum microelectrode and 31% for a gold microelectrode.

5.3 EFFECT OF THE SUPPORTING ELECTROLYTE

The nature of the supporting electrolyte can affect mass transport of redox species in nonisothermal systems. This effect manifests itself through the phenomenon of the thermoelectric migration. As has been stated in Section 1.2.1.2, the contribution from the thermoelectric effect to the rate of mass transfer of redox species can be included into the species' "pure" Soret diffusion coefficient. Thus, one can talk only about so-called "effective" Soret coefficients of the species D_i'. To understand this idea better, it should be realized that once a temperature gradient is created in solution around a

microelectrode, then both the redox species and the supporting electrolyte ions are experiencing the Soret effect. However, since the concentration of the supporting electrolyte is much higher than that of the redox species, then the behaviour of the supporting electrolyte ions in the temperature gradient can affect the behaviour of the redox species (hence, the effective Soret coefficient of the redox species). This happens due to the appearance of the thermoelectric potential gradient $\frac{\partial \varphi(x)}{\partial x}$ (equation 1.9). The direction of this potential gradient (either towards the electrode or away from it) affects the concentration of the redox species near the electrode. Thus, it may seem as if the species has either higher or lower Soret coefficient than its "pure" value (without any supporting electrolyte present).

To investigate the effect of the supporting electrolyte, a set of experiments was done, in which the response of a hot recessed microelectrode was monitored by recording fast scan (10 V s^{-1}) cyclic voltammograms one after another. These voltammograms corresponded to the oxidation of $Fe(CN)_6^{4-}$ ions in 2 M aqueous solutions of the three electrolytes: potassium chloride (Figure 5.9, a), lithium chloride (Figure 5.9, b) and tetraethylammonium chloride (Figure 5.9, c).

a)

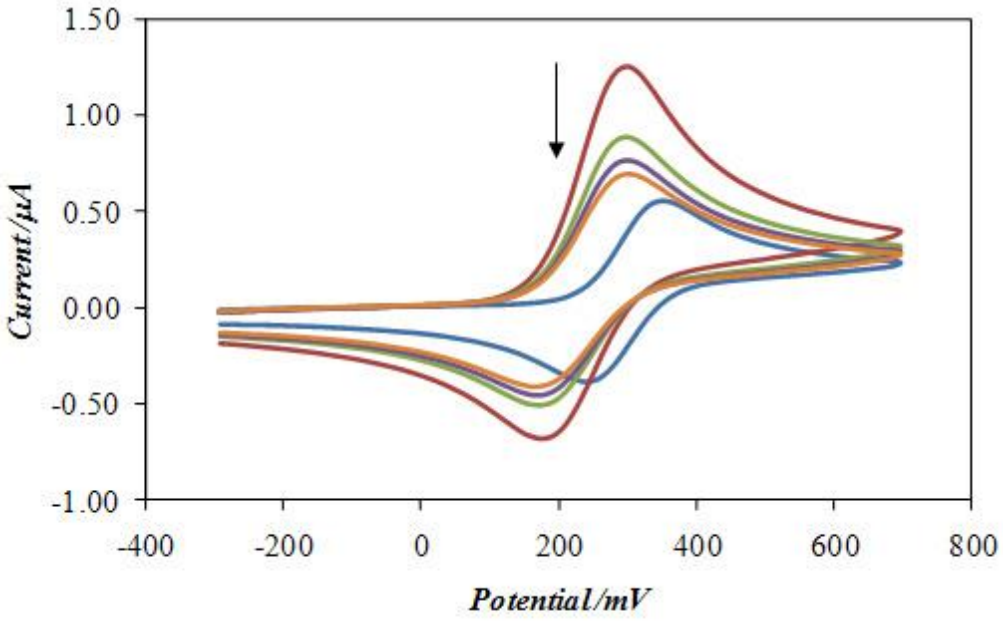

b)

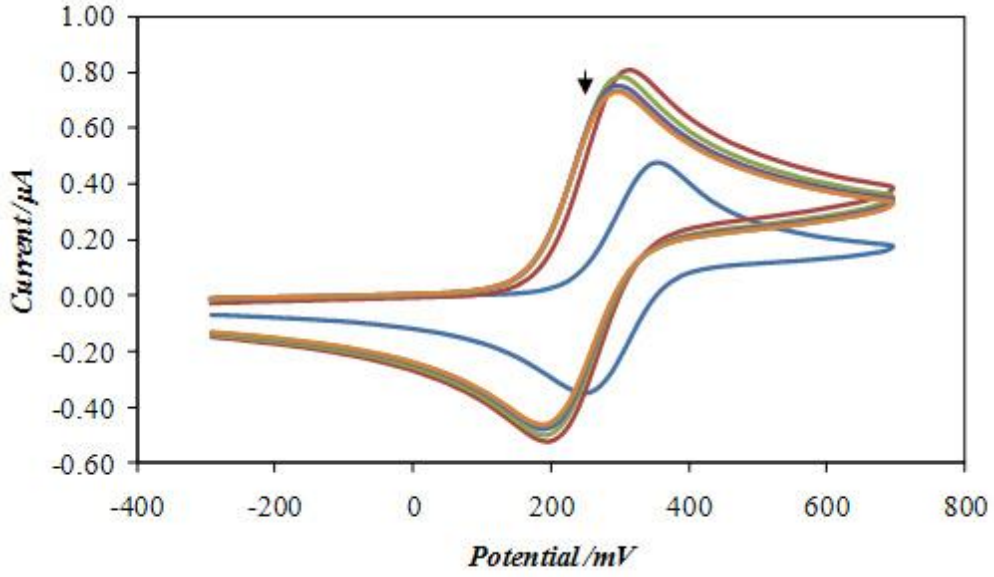

c)

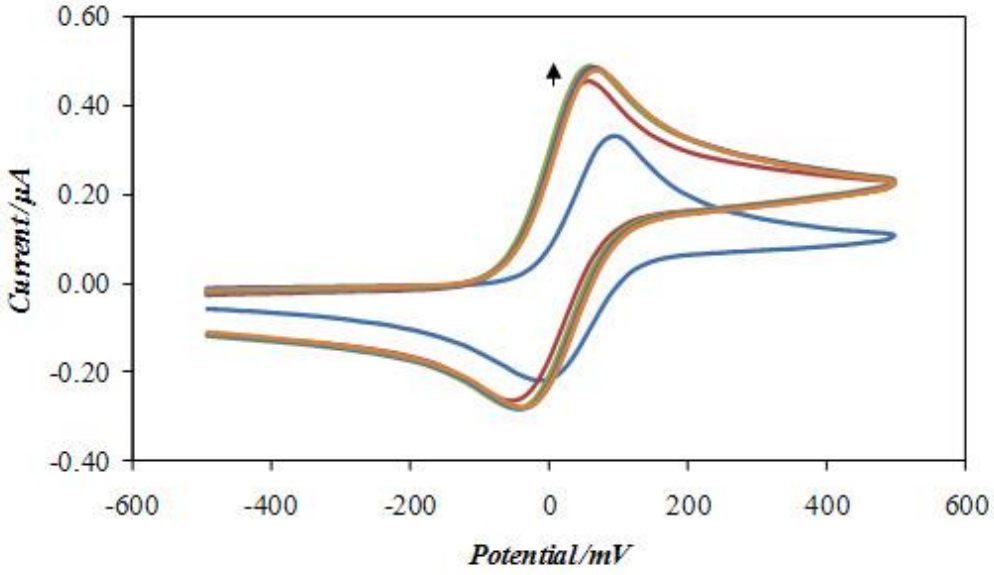

Figure 5.9 Cyclic voltammograms obtained for 0.050 M $K_4Fe(CN)_6$ in 2 M aqueous solutions of KCl (**a**), LiCl (**b**) and Et_4NCl (**c**). Blue CVs were recorded at room temperature; the other CVs were recorded with applied ac heating (205 MHz, 2.40 V_{rms}) in the following order: red, green, violet and orange. Direction of change in peak current with time is indicated by arrows. Time period between subsequent CVs – 0.1 s (during this time the potential was kept at its initial value). Working electrode used in all experiments: 25 μm Pt recessed (34 μm length of a channel), Ag|AgCl|KCl (sat.) – Ref., 0.3 mm Pt – Aux.

Since the heating of the microelectrodes occurs very quickly (see Figure 4.5), it is expected that already the first (red) CVs in Figure 5.9 (a) – (c) are recorded with the temperature having its nearly steady-state distribution. Therefore, the differences in the subsequent voltammograms for the three systems are most likely caused by the thermoelectric potential effect of the supporting electrolyte.

The magnitude of the thermoelectric potential gradient is expected to be proportional to the temperature gradient, the value of the Soret coefficient of the supporting electrolyte salt and the difference of the transference number for the cations and anions of the supporting electrolyte according to the following equation:

$$grad\,\varphi = (t_+ - t_-)\frac{RT}{F}\sigma\, grad\, T \qquad (5.3)$$

where t_+ is the transference number for the cations of the supporting electrolyte, t_- is the transference number for anions and σ is the Soret coefficient of the supporting electrolyte salt and other symbols have their usual meanings. This equation is derived from the expression for the liquid junction potential (for 1:1 electrolytes)[17] and equation 1.12 (section 1.2.1.2)

If potassium chloride is used as a supporting electrolyte, then the magnitude of the thermoelectric potential gradient is not expected to be high, since the transference numbers for potassium and chloride ions are essentially identical ($t_{K^+} = 0.491$ and $t_{Cl^-} = 0.509$ based on the values of the mobility of ions at infinite dilution in aqueous solution at room temperature[95]). Therefore, the contribution of the thermoelectric migration to mass transfer of ferrocyanide ions will be negligible and, consequently, the difference in the subsequent CVs (red to orange) in Figure 5.9 (a) could be explained exclusively by the Soret diffusion of the $Fe(CN)_6^{4-}$ ions ("pure" Soret effect, almost no supporting electrolyte contribution). However, if tetraethylammonium chloride is used as a supporting electrolyte, then the magnitude of the thermoelectric potential gradient is expected to be substantial due to a large difference of the transference numbers for Et_4N^+ and Cl^- ions ($t_{Et_4N^+} = 0.299$ and $t_{Cl^-} = 0.701$). Therefore, the thermoelectric field strength vector will be directed away from a hot microelectrode (since $t_{Et_4N^+} < t_{Cl^-}$) and it

will affect the distribution of $Fe(CN)_6^{4-}$ ions. An increase in the value of the peak currents in the subsequent (red to orange) cyclic voltammograms in Figure 5.9 (c) could be explained by the migration of ferrocyanide ions towards the microelectrode due to the presence of the thermoelectric potential field. Thus, the redox species behaves as if it has a negative Soret coefficient (the change in peak currents is the opposite to the results in Figure 5.3). When the oxidation of ferrocyanide ions occurs in LiCl solution, then one would also expect to observe the changes in the CVs similar to the results for tetraethylammonium chloride, since $t_{Li^+} = 0.336$ and $t_{Cl^-} = 0.664$. However, the voltammograms in Figure 5.9 (b) indicate that the values of the peak currents decrease with time similarly to the results in KCl. This could be explained by the fact that the Soret coefficient for LiCl is much lower than the one for tetraethylammonium chloride (according to the results of Snowdon and Turner,[26] $\sigma_{LiCl} = 0.02 \cdot 10^{-3}$ K^{-1}, $\sigma_{Et_4NCl} = 8.41 \cdot 10^{-3}$ K^{-1} and $\sigma_{KCl} = 1.41 \cdot 10^{-3}$ K^{-1} for their 0.01 M aqueous solutions). Therefore, the strength of the thermoelectric field in lithium chloride solution might not be strong enough to cause an appreciable change in the ferrocyanide concentration distribution.

5.4 ESTIMATE OF THE DIFFERENCE OF SORET COEFFICIENTS FOR FERRI- AND FERROCYANIDE IONS

Using the developed simulation program it is possible to estimate the difference of the Soret coefficients for $Fe(CN)_6^{3-}$ and $Fe(CN)_6^{4-}$ ions. This can be done by fitting the simulated data into the experimental results, as shown in Figure 5.10.

The normalized limiting current difference was calculated based on the following formula:

$$\frac{\Delta i}{i_0} = \frac{\left| i_{\lim}^{reduction} \right| - i_{\lim}^{oxidation}}{i_0} \qquad (5.4)$$

where $i_{\lim}^{reduction}$ is the limiting current for the reduction of $Fe(CN)_6^{3-}$ ions and $i_{\lim}^{oxidation}$ is the limiting current for the oxidation of $Fe(CN)_6^{4-}$; i_0 is the absolute value of the limiting current (either oxidation or reduction) at room temperature without ac heating.

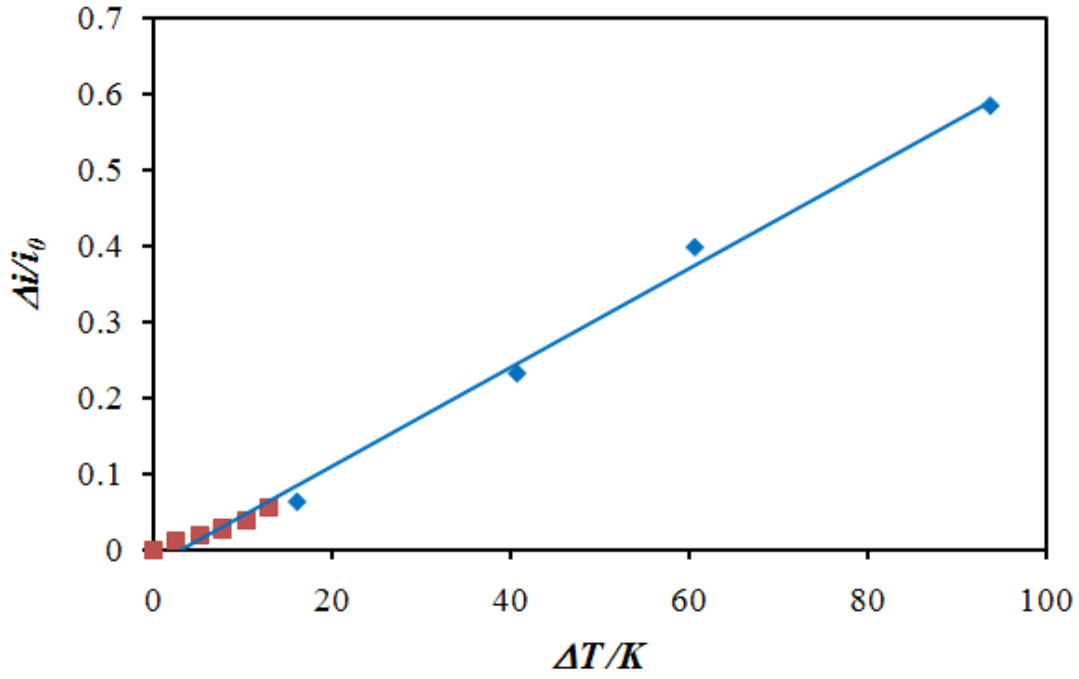

Figure 5.10 Experimental (blue data points) and simulated (red data points) results for the normalized limiting current difference (given by equation 5.4) as a function of the change in the electrode temperature. Simulated data were obtained for the Soret coefficient difference $\sigma_{Fe(CN)_6^{4-}} - \sigma_{Fe(CN)_6^{3-}} = 2 \cdot 10^{-3}$ K^{-1}. Experimental results are based on SS–CVs recorded in 50 mM $K_4Fe(CN)_6$, 50 mM $K_3Fe(CN)_6$ and 2 M KCl with a 25 μm Pt disk microelectrode.

The results shown in Figure 5.10 indicate that the difference of the effective Soret coefficients for ferro- and ferricyanide ions is about $2 \cdot 10^{-3}$ K^{-1} in 2 M KCl solution. At this point, it is hard to say if the absolute value of this difference is correct. However, qualitatively it agrees well with the experimental results shown previously in this Chapter (Figure 5.1). Based on the above value of the difference of Soret coefficients it may be estimated that the error in the electrode temperature determined from $E_{1/2}$ shift is only about 3 – 4%, if a Pt microelectrode is used.

CHAPTER 6: SCANNING ELECTROCHEMICAL MICROSCOPY WITH HOT MICROELECTRODES

This Chapter contains the results of the studies, in which hot microelectrodes were used in the arrangement for the Scanning Electrochemical Microscopy (SECM). Such a novel technique is referred to as Hot-Tip SECM or HT-SECM. Experimental results presented here are preliminary, extensive studies were not done. The research in this area was intended to constitute the main part of this thesis before the electrothermal and dielectrophoretic effects at hot microelectrodes had been discovered. However, currently, the main purpose of including the results of HT-SECM studies is to show that this kind of measurements is technically possible and that the HT-SECM technique has important advantages compared to the conventional SECM.

6.1 APPROACH CURVE EXPERIMENTS

SECM is an electrochemical probe technique, in which the current measured with a microelectrode (tip) is caused by an electrochemical reaction taking place at the electrode surface. There are two types of SECM measurements: approach curve and mapping (or imaging) experiments.[17]

In approach curve experiments, a microelectrode tip is positioned at some distance away from the substrate under investigation and the faradaic current corresponding to the oxidation or reduction of redox species in solution is recorded. The tip is then brought closer to the substrate and, as a result, a so-called approach curve is obtained. Depending on the type of a substrate (electrically conductive or non-conductive), two kinds of approach curves can be recorded at room temperature (Figure 6.1). In the case of a non-conductive (insulating) substrate, a decrease in the current is observed when the tip is few electrode radii away from the substrate surface. This is because the insulating substrate blocks the mass transfer of the redox species to the microelectrode surface.

However, if the substrate is conductive, then an increase in the current is observed, because the substrate can regenerate the product of the electrode reaction (positive feedback).

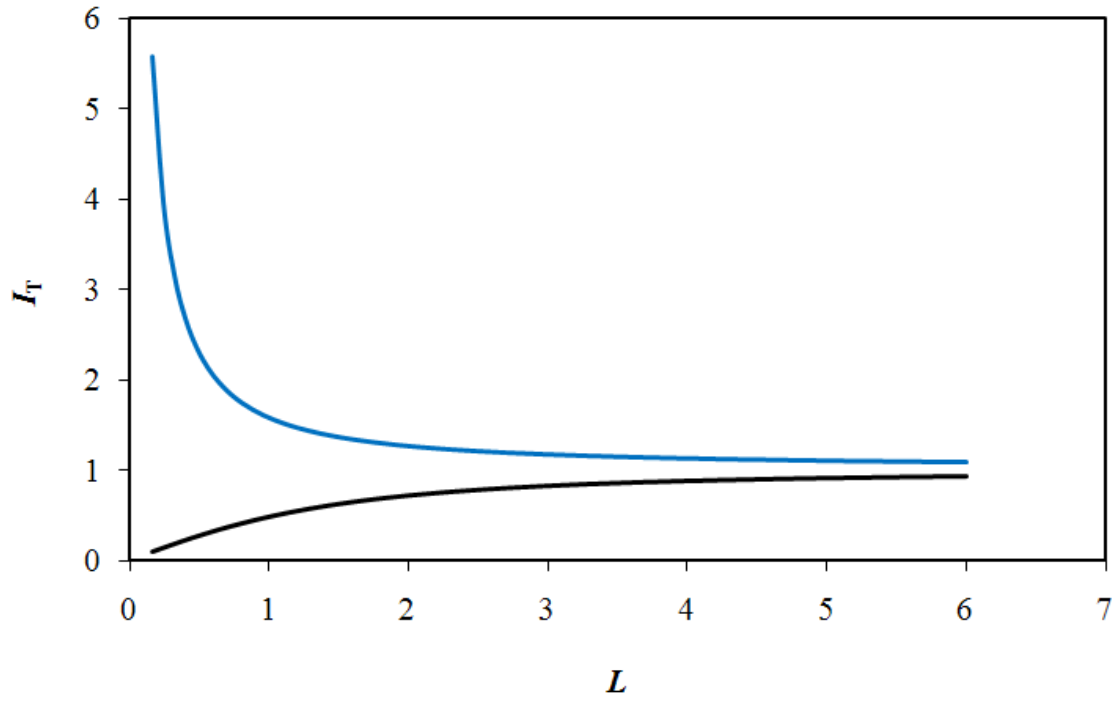

Figure 6.1 Theoretical approach curves over a conductive (blue) and insulating (black) surfaces for a disk microelectrode with R_g factor equal 10. Details in the text.

In Figure 6.1, L is a normalized tip-to-substrate distance ($L = d/a$, where d is the separation distance between the electrode and substrate, a is the radius of the metal disk). I_T is the normalized current calculated from the ratio of $i_{T,L}$ (tip current at a distance L) to $i_{T,\infty}$ (current at infinite separation):[100]

$$I_T^C(L) = \frac{i_{T,L}}{i_{T,\infty}} = 0.78377/L + 0.3315\exp[-1.0672/L] + 0.68 \qquad (6.1)$$

and

$$I_T^{ins}(L) = \frac{i_{T,L}}{i_{T,\infty}} = \frac{1}{A + B/L + C\exp[D/L]} + \frac{EL}{F + L} \qquad (6.2)$$

where I_T^C is the tip current over a conductive surface and I_T^{ins} is the tip current over an insulating surface. Coefficients *A*, *B*, *C*, *D*, *E* and *F* are equal to 0.4571825, 1.4604238, 0.4312735, –2.350667, –0.145437 and 5.5768952, respectively. It should also be noticed that the above equations 6.1 and 6.2 are applicable to tips having R_g factor equal to 10 and to diffusion-controlled heterogeneous electrode reactions. Equation 6.1 is accurate within 0.7% for *L* interval from 0.05 to 20 and equation 6.2 is accurate to about 1%.

When the ac heating of an electrolyte solution near a microelectrode tip occurs, one would expect to observe an increase in the measured current due to more intensive mass transfer of redox species. This is exactly what is observed at large separations between the tip and the substrate. However, once the electrode tip is brought closer to the substrate, the effectiveness of heating is expected to decrease, since the solution resistance increases according to the following equation:[101]

$$\frac{R_{T,\infty}}{R_{T,L}} = \frac{i_{T,L}}{i_{T,\infty}} \qquad (6.3)$$

where $R_{T,L}$ is the solution resistance at a normalized tip-to-substrate separation *L* and $R_{T,\infty}$ is the solution resistance at a very large separation between the substrate and the microelectrode tip.

Approach curves over insulating (alumina, polystyrene) and conductive (glassy carbon) substrates were recorded using hot microelectrodes (Figures 6.2 – 6.4). Without heating, the approach curves over insulating substrates look very similar, since the same microelectrode was used in both experiments under identical conditions. However, when the heating was applied, approach curves became different. This can be seen most easily from the ratio i_h/i_c, where i_h is the faradaic current recorded with a hot microelectrode and i_c is the current at room temperature (cold). While approaching a polystyrene substrate, a characteristic increase in the i_h/i_c current ratio is observed at the distance about 20 μm above the substrate surface. This fact could be explained if the heat transfer from the hot zone in solution (near the tip) to the substrate is considered. Since the thermal conductivity of the considered substrates is substantially different (thermal conductivity of alumina is equal to 40 W m^{-1} K^{-1} and 0.08 W m^{-1} K^{-1} for polystyrene), then the temperature of a hot microelectrode should be higher when it is positioned 20

μm above the polystyrene substrate, than alumina. In addition, the distance at which the increase in the current ratio is observed (Figure 6.3) is comparable with the size of the hot zone in solution (which is proportional to the size of the microelectrode disk, 25 μm). These considerations clearly suggest that the observed phenomenon is related to the substrate heating by the hot tip.

At room temperature, the approach curve over glassy carbon (Figure 6.4, blue curve) also follows an expected shape for conductive substrates. Yet, when the ac heating is turned on, a rather unusual increase in the current is observed at about 20 – 30 μm between the tip and the substrate surface (red curve). This increase also manifests itself through a larger ratio i_h/i_c for the same separation distance, similarly to the results in Figure 6.3. Therefore, it can be suggested that this increase in the faradaic current is also due to the presence of the hot zone in solution, which results in more intensive mass transfer of the redox species back to the hot microelectrode (positive feedback). Further movement of the tip towards the substrate leads to the expected decrease in the heating efficiency according to equation 6.3, and i_h/i_c approaches 1.

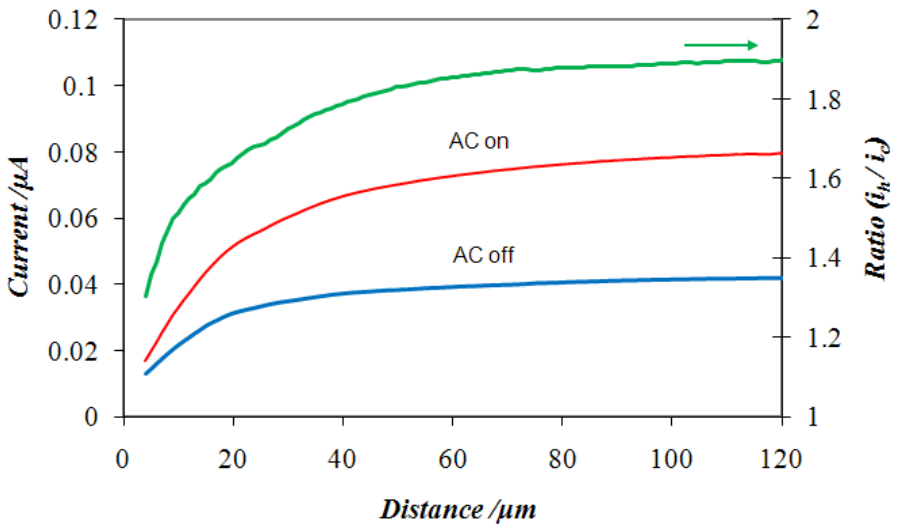

Figure 6.2 Approach curves over alumina. AC on – the curve was recorded with a hot tip; AC off – the curve was recorded at room temperature. Ratio of the currents (i_h/i_c) is represented by the green curve. Experimental conditions: 25 μm Pt disk electrode in 0.01M $K_4Fe(CN)_6$, 0.5 M K_2CO_3, 0.02 M KCN. Reference and counter electrodes: 0.25 mm W wire. AC signal: 145 MHz, 0.56 V_{rms}.

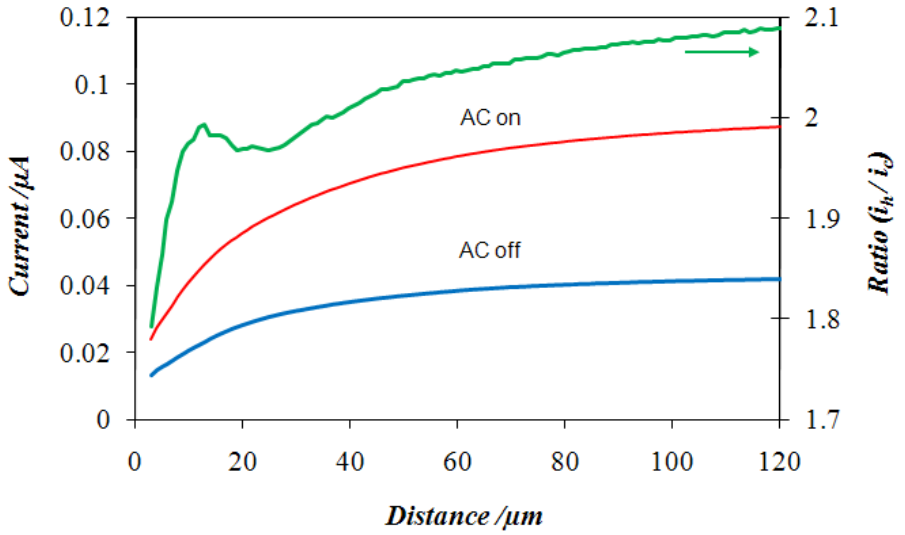

Figure 6.3 Approach curves over polystyrene. AC on – the curve was recorded with a hot tip; AC off – the curve was recorded at room temperature. Ratio of the currents (i_h/i_c) is represented by the green curve. Experimental conditions: 25 μm Pt disk electrode in 0.01M $K_4Fe(CN)_6$, 0.5 M K_2CO_3, 0.02 M KCN. Reference and counter electrodes: 0.25 mm W wire. AC signal: 145 MHz, 0.56 V_{rms}.

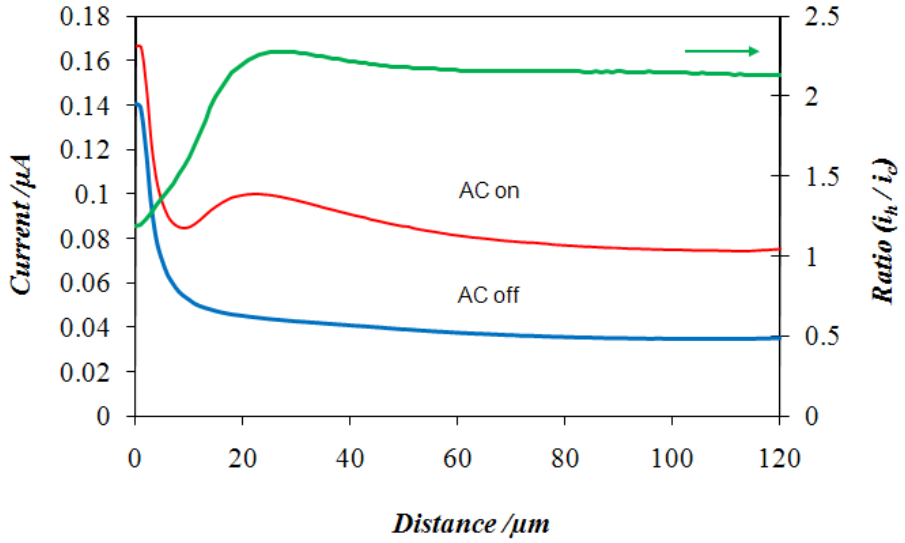

Figure 6.4 Approach curves over glassy carbon. AC on – the curve was recorded with a hot tip; AC off – the curve was recorded at room temperature. Ratio of the currents (i_h/i_c) is represented by the green curve. Experimental conditions: 25 μm Pt disk electrode in 0.01M $K_4Fe(CN)_6$, 0.5 M K_2CO_3, 0.02 M KCN. Reference and counter electrodes: 0.25 mm W wire. AC signal: 145 MHz, 0.56 V_{rms}.

A video showing the approach of a hot microelectrode towards a paraffin wax film on a glass slide has been also recorded (Video 6.1). In this video one can see that, once the hot tip is very close to the substrate, melting of the paraffin film occurs (paraffin film becomes more transparent).

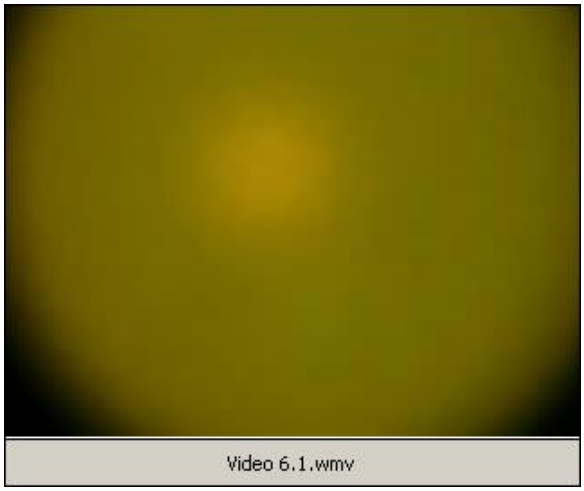

Video 6.1 Boiling above a paraffin film. Conditions: 25 μm Pt disk electrode in 0.01M $FeSO_4$, 1M M H_2SO_4. AC signal: 140 MHz, 2.8 V_{rms} (see Appendix E2 for individual frames).

The results of this simple experiment indicate that, indeed, the heating of the solution takes place during ac modulation (typical melting point of the paraffin wax is between 47 °C and 64 °C).

6.2 MAPPING EXPERIMENTS

In this type of SECM experiments, a microelectrode tip is scanned in the $x - y$ plane above the substrate. As a result, an image of the substrate surface is obtained, since the change in the measured current (at constant temperature) is related either to the change of the substrate topography (distance between the tip and the surface) or its reactivity (electrically conductive or non-conductive, for example).

HT-SECM has been also used to image the surface of a silicon elastomer imprint of a vinyl record. The results are shown below:

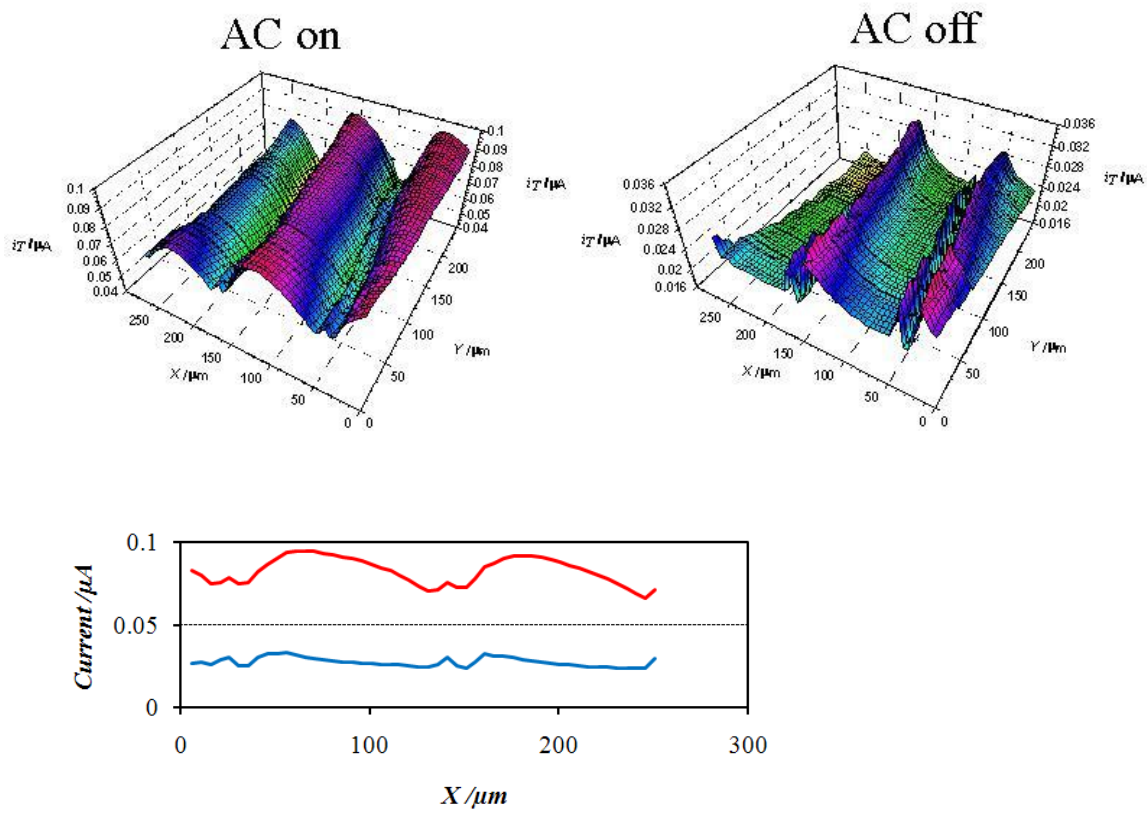

Figure 6.5 *Top:* SECM images of the surface of a silicon elastomer imprint of a vinyl record with (AC on) and without (AC off) ac heating. *Bottom:* Faradaic current profile obtained with a hot tip (red curve) and at room temperature (blue curve). Experimental onditions: 25 μm Pt disk electrode in 0.01M $K_4Fe(CN)_6$, 0.5 M K_2CO_3, 0.02 M KCN. Reference and counter electrodes: 0.25 mm W wire. AC signal: 145 MHz, 0.56 V_{rms}.

Images shown in Figure 6.5 (*Top*) were obtained for the same separation distance between the electrode tip and the substrate. As one can see, application of the ac heating results in larger faradaic currents and, consequently, in a better resolved image of the substrate. This example illustrates an immediate benefit of using HT-SECM: the scan over the substrate surface can be done at a larger separation between the tip and the sample without any loss in the resolution of the imaging. This could be especially helpful in eliminating such situations, when the electrode tip is crashed by the sample during the scan due to a very short tip-to-sample separation (in the case of room temperature SECM measurements). More details and suggestions for future research in the area of HT-SECM will be given in the next Chapter of this thesis.

CHAPTER 7: CONCLUSIONS AND FUTURE RESEARCH

7.1 CONCLUSIONS

Both the experimental data and the results of numerical simulations indicate that convection at ac polarized microelectrodes is caused primarily by the electrothermal flow of an electrolyte solution. The electrothermal force responsible for the solution flow is comprised of two forces: the Coulomb force acting on an unbalanced charge and the dielectric force acting on water molecules. The Coulomb force dominates the dielectric force at frequencies below the cross-over frequency. The unbalanced charge is formed when both the temperature and ac potential gradients are present in solution. As a result, the magnitude of the electrothermal force depends on the magnitude of both the temperature gradient and the potential gradient; it is proportional to $\Delta V_{R_s}^4$, the fourth power of the voltage drop across the solution resistance. In addition, the rate of the electrothermal convection is proportional to the specific resistance of the electrolyte solution and inversely proportional to the electrode radius.

Another phenomenon observed at ac polarized microelectrodes, which does not require the presence of the temperature gradient, is called ac dielectrophoresis. It is directly related to the fact that a strong non-uniform electric field exists near the surface of a disk microelectrode polarized by a high frequency ac waveform. As has been shown in one of the videos (Video 3.1), gold microparticles present in solution are polarized by the electric field and, since the field at the electrode surface is much stronger, the particles are getting attached to the microelectrode surface. The theory of dielectrophoresis can also explain the fact that the vapor bubbles forming during the extreme ac heating of a microelectrode are dislodged momentarily into the bulk solution (Video 3.3).

Much of the understanding of the electrothermal convection and how it affects mass transport of redox species at hot microelectrodes has come after the simulation program has been developed. With this program it is possible to determine the distribution of temperature, calculate the electrothermal force and predict the rate and direction of the solution flow. Even though the program is based on a number of simplifications and approximations, its results qualitatively agree well with all the experimental findings. Thus, it has been confirmed that the electrothermal convection rate increases with the decrease in the concentration of the supporting electrolyte and that the limiting current enhancement ratio is independent of the microelectrode radius. In addition, using the simulation program it has been predicted that the direction of the solution flow (with respect to the electrode surface) changes depending on the thermal conductivity of the electrode material. It has been determined and later confirmed experimentally that the flow of an electrolyte solution is directed towards the electrode surface for a Bi microelectrode, and away from it, if a Pt microelectrode is used (Videos 4.1 and 4.2).

The experimental results obtained during this work indicate that Soret diffusion affects the rate of mass transfer of redox species and, therefore, the faradaic current measured at hot microelectrodes. The magnitude of the Soret diffusion effect on the limiting current depends on the rate of the electrothermal convection: the higher the convection, the smaller the Soret contribution to the current is. This has been observed experimentally by monitoring the difference in the limiting currents for the reduction of ferricyanide and oxidation of ferrocyanide ions and later confirmed by the numerical simulations. In addition, the simulations indicate that Soret diffusion of redox species leads to the shift in the half-wave potential. This introduces an error into the determination of the electrode surface temperature. The magnitude of this error is expected to depend on the nature of the electrode material, with larger errors for Au electrodes than for Pt (for a Pt electrode, the estimated error in the temperature determination due to the Soret effect is about 3 – 4%). Obtained experimental results also indicate that the nature of the supporting electrolyte affects the mass transfer of the redox species. This can be explained by the thermoelectric migration effect due to the fact that ions of the supporting electrolyte also experience the Soret effect. In general, the magnitude of the Soret effect on the mass transfer of the redox species is smaller

than the effect of the electrothermal convection. However, its presence cannot be neglected when working with hot microelectrodes.

Hot microelectrodes can be successfully used in the arrangement for the Scanning Electrochemical Microscopy. This novel technique, which is termed Hot-tip SECM, is expected to be very useful in a number of applications. However, more developments in this direction of research are yet to come.

7.2 FUTURE WORK

The following topics of future research could be proposed:

a) enhancement of sensitivity of electrochemical sensors by dielectrophoretic and electrothermal effects, and
b) Scanning Electrochemical Microscopy with hot microelectrodes (HT-SECM).

AC heated microelectrodes can be used for electrochemical detection of a large number of analytes. This idea is not new; Gruendler *et al.* have reported many successful applications of hot electrodes to the electrochemical sensing (Section 1.3.1). However, operation of their sensors has been improved only due to one positive effect – the effect of the increased temperature. I believe that by heating electrodes with a high frequency ac waveform, the effect of the increased temperature can be complemented by the dielectrophoretic and electrothermal effects. This direction of research is very novel, since the examples of the combined use of the electrochemical detection and the dielectrophoretic separation / preconcentration are extremely rare. As the only example known to me, Gomez-Sjoberg and co-workers have reported about a new technique called "Impedance microbiology-on-a-chip". In this method, dielectrophoresis is used to concentrate bacterial cells into a very small volume, while the growth of the cells was monitored by the impedance measurements.[102,103]

Dielectrophoretic and electrothermal effects observed due to high frequency ac polarization of microelectrodes can be used to increase the sensitivity of electrochemical biosensors. As a starting experiment, a similar approach to DNA hybridization detection could be used as described by Flechsig *et al*.[66] The procedure will involve the preparation of the DNA-SAM modified gold electrode layer and the hybridization will be evaluated based on the ACV response from the ferrocene-labeled complementary strand (target). However, instead of a single disk microelectrode, the use of a

microelectrode array will be required. The magnitude of the dielectrophoretic force acting on bioparticles depends on their size and the electric field gradient, which for disk microelectrodes is inversely proportional to the electrode radius. Hughes and Morgan report successful dielectrophoretic separation of latex particles, 216 nm in diameter, using a microelectrode array of "castellated" design (with square dimensions of 10 μm along all faces).[104] Obviously, in order to successfully manipulate even smaller particles (like oligonucleotides) using dielectrophoresis, microelectrodes with smaller radii will be required. Thus, to provide sufficient sensitivity to the hybridization detection, microelectrode arrays will be employed.

In the next step, hybridization detection will be done using the prepared DNA-SAM modified microelectrode array heated by high frequency ac waveform. According to Flechsig, temperature rise increases analytical signal; however, the decrease is observed if the melting temperature is exceeded. Therefore, the amplitude of the excitation waveform will need to be controlled precisely. To investigate if the dielectrophoresis of the target strand takes place and affects the analytical signal, ACV response of the array will be measured in a wide range of ac heating frequencies (perhaps, 1 – 100 MHz). It is expected that at frequencies corresponding to the positive dielectrophoresis of the target strand, the response of the sensor will be enhanced substantially. In a control experiment, target strands will be fluorescently labeled and their motion will be monitored while frequency of the ac signal is varied.

Electrothermal flow of solution is also expected to improve the sensitivity of the target strand detection due to the mixing effect. Liu *et al.* report a micromixing technique based on cavitation microstreaming principle in order to accelerate the hybridization. As a result, a 5-fold increase in the hybridization signal has been obtained.[105]

Successful implementation of the proposed method for the enhancement of the sensitivity of hybridization detection by the dielectrophoretic and electrothermal effects is contingent upon a number of factors. First of all, it should be realized that it is not applicable for short oligonucleotides. Dielectrophoretic manipulation will require such strong electric fields that the heating of the solution will most likely result in temperatures exceeding the melting temperature of the biomolecules. Therefore, the use

of longer DNA strands having higher melting temperatures will be required. One should also recognize that the effectiveness of the heating will vary with frequency. In the high frequency limit approaching 100 MHz, most of the ac signal will appear as a voltage drop across the solution resistance. Thus, the heating will be the most effective. However, at low frequencies, the heating will be less effective due to the ac power attenuation by the double layer. Therefore, the amplitude of the ac waveform will need to be adjusted accordingly.

Dielectrophoretic and electrothermal effects can improve the performance and the detection limits of the electrochemical aptasensors, which are attracting considerable attention recently.[106] Provided that an increase in temperature does not disrupt the recognition event, aptasensors polarized by a high frequency ac waveform could be used to detect larger substrates, such as viruses, bacteria and proteins. This is especially interesting, since the dielectrophoretic behavior of many of these potential analytes is well known.[107,108]

To the best of my knowledge, there are no examples in the current literature describing application of heated microelectrodes in the arrangement for SECM. This can be explained by the difficulties of implementing such technology using heating methods other than the method proposed by Baranski.[7] However, HT-SECM can have many very interesting applications. Some of these applications are related to the fact that hot-disk microelectrodes can provide localized heating of the substrates. Thus, by using nanometer-sized electrodes one can investigate the effect of both high temperature and high frequency electric fields on various processes outside and inside biological cells. HT- SECM can be also used to study the electron transfer through self-assembled monolayers, membranes and thin films at elevated temperatures. It is believed that an instrument allowing combined HT-SECM – AFM measurements will be very useful in biological and chemical research. Another interesting direction of research with ac polarized microelectrodes is related to the observed electrothermal and dielectrophoretic phenomena. One can envision that the electrothermal flow could be very useful for the pumping of electrolyte solutions, especially if a micropipet electrode is used (for an example of a micropipet probe, see works by Bard *et al.*[109,110]). In the arrangement for HT-SECM such micropipet electrodes could be used as delivery systems or miniaturized

syringes. Similarly, positive and negative dielectrophoretic phenomena observed at hot microelectrodes could be used to manipulate nanoparticles. The results in Chapter 6 indicate that with HT-SECM technique it should be also possible to evaluate the thermal conductivity of various substrates. Although a similar technique for this purpose has been already proposed[111] (Scanning Thermal Microscopy), HT-SECM is based on a different principle of operation and it is not limited with respect to the size of the probe. However, to progress further in this direction of research, it will be necessary to do numerical simulations of the ac heating of substrates. The results of the simulations could provide better understanding of the relationship between the faradaic current, tip-to-substrate separation and the thermal conductivity of the substrate. From experimental viewpoint, it is obvious that the separation between the electrode tip and the surface must be controlled precisely. This could be achieved quite easily, if HT-SECM is combined with AFM. Many of such hybrid SECM-AFM setups have been described in the literature.[112]

To summarize, it should be emphasized that the heating of microelectrodes by a high frequency ac waveform is advantageous compared to other methods. This approach does not have any limitations with respect to the size or the construction of the electrodes. AC polarization of the microelectrodes results not only in the heating of the surrounding solution, but also in the appearance of the ac dielectrophoresis and the electrothermal flow. These effects can improve the electrochemical detection of many important analytes and can lead to numerous applications in chemistry and biology.

APPENDIX A

A1. CALCULATION OF SOLUTION RESISTANCE

Hemispherical microelectrode

The geometry of a hemispherical microelectrode is shown in Figure A1.1. This electrode could be, for example, a hemisphere of mercury electrodeposited on a gold disk surface.

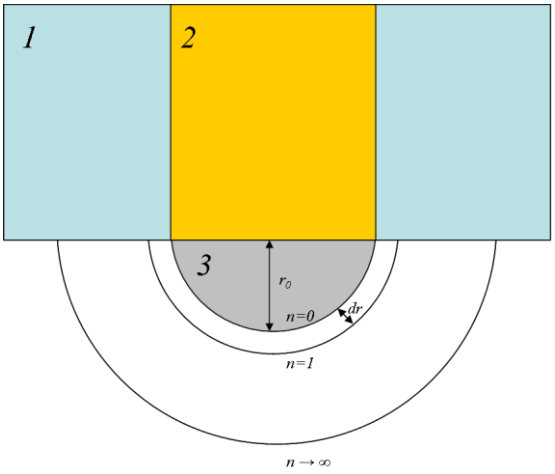

Figure A1.1. Hemispherical microelectrode. *1* – glass; *2* – gold microwire; *3* – mercury hemisphere.

Solution around such an electrode can be divided into an infinite number (n) of hemispherical layers, each having a thickness dr. The resistance of one layer is then given by the following formula:

$$dR = \frac{\rho\, dr}{2\pi r^2} \qquad \text{(A1.1)}$$

where ρ is the specific solution resistance and r is the radius of a corresponding hemisphere.

To calculate the total resistance of the solution around a hemispherical microelectrode (R_{hs}), the following integral needs to be evaluated:

$$R_{hs} = \int_{r_0}^{\infty} \frac{\rho\, dr}{2\pi r^2} = \frac{\rho}{2\pi r_0} \qquad \text{(A1.2)}$$

where r_0 is the radius of a hemispherical electrode.

Spherical microelectrode

Analogously to the case of the hemispherical electrode geometry, the solution resistance around a spherical microelectrode can be evaluated from the following integral:

$$R_s = \int_{r_0}^{\infty} \frac{\rho\, dr}{4\pi r^2} = \frac{\rho}{4\pi r_0} \qquad \text{(A1.3)}$$

where r_0 is now the radius of the electrode microsphere.

Disk microelectrode

This case is more complicated than the others, because the current density is not uniform across the surface of a disk. This is so due to the presence of the 'edge effect' and, as a result, the current density is higher at the edge of a microdisk than at its centre. Rigorous calculation of the solution resistance for disk microelectrodes can be found in a paper by Newman.[92] Here only the final formula is given:

$$R_d = \frac{\rho}{4 r_0} \qquad \text{(A1.4)}$$

where r_0 is the radius of the metal disk.

A2. CALCULATION OF SOLUTION CAPACITANCE

Capacitance of a parallel-plate capacitor is given by the formula:

$$C = \varepsilon \frac{A}{d} \tag{A2.1}$$

where ε is the dielectric permittivity of a medium, A is the surface area of a plate and d is the distance between the plates.

Based on this formula one can derive equations for the capacitance of the solution surrounding microelectrodes of various geometries. This is done similarly to the derivations of the solution resistance and the same Figure A1.1 may be referred to for clarifications.

Solution capacitance in the case of a hemispherical electrode

Capacitance of each of the solution layers can be calculated according to the formula:

$$C = \varepsilon \frac{2\pi r^2}{dr} \tag{A2.2}$$

The total solution capacitance is then comprised of the capacitances of all of n layers (where $n \rightarrow \infty$):

$$\frac{1}{C_{hs}} = \frac{1}{C_1} + \frac{1}{C_2} + ... + \frac{1}{C_n} = \sum_r \frac{dr}{2\pi r^2 \varepsilon} = \int_{r_0}^{\infty} \frac{dr}{2\pi r^2 \varepsilon} = \frac{1}{2\pi r_0 \varepsilon} \tag{A2.3}$$

or

$$C_{hs} = 2\pi r_0 \varepsilon \tag{A2.4}$$

Solution capacitance in the case of a spherical microelectrode

Similarly to the above derivations (equations A2.1 – A2.4) the capacitance of the solution surrounding a spherical microelectrode can be shown to be:

$$C_s = 4\pi \varepsilon r_0 \tag{A2.5}$$

where r_0 is the radius of a metal microsphere.

Solution capacitance in the case of a disk microelectrode

By analogy with the calculations of the solution resistance (for all three electrode geometries) and solution capacitance (hemispherical and spherical microelectrodes), it can be written that the solution capacitance in the case of microdisk electrode geometry is given by the formula:

$$C_d = 4\varepsilon r_0 \qquad \text{(A2.6)}$$

Frequency dependence of the solution permittivity

Frequency dependence of the permittivity can be taken into account using the Debye equation:[113]

$$\varepsilon = \varepsilon_\infty + \frac{\varepsilon_s - \varepsilon_\infty}{1+\omega^2\tau^2} - j\omega\tau\frac{\varepsilon_s - \varepsilon_\infty}{1+\omega^2\tau^2} \qquad \text{(A2.7)}$$

where ε_s is the static permittivity, ε_∞ is the permittivity in the high frequency limit, τ is the relaxation time for molecular orientation and ω is the angular frequency.

A3. CALCULATION OF STRAY CAPACITANCE

Stray capacitance may be regarded as a parasitic capacitance causing nonideal responses in electrochemical measurements. Within the electrochemical system it may arise from the electrode itself, the leads or electrical connections, and is particularly apparent during the high-frequency measurements and if micrometer or submicrometer electrodes (nanodes) are used.[114]

In the high-frequency ac heating experiments the electrode body, which is usually made of glass, behaves as a capacitor when dipped into an electrolyte solution. In addition to the parameters listed above this is the main cause of appearance of the stray capacitance in the electronic diagram in Figure 3.2 (Section 3.2.1).

In order to estimate the magnitude of the stray capacitance, a simple calculation can be done based on a model for a cylindrical capacitor.

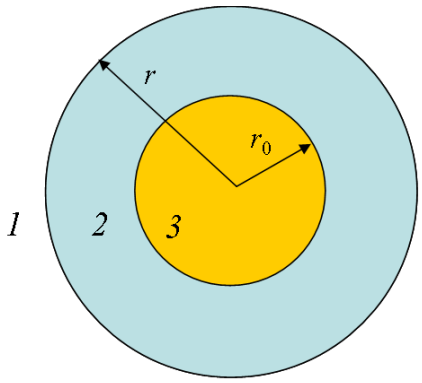

Figure A3.1. Origin of stray capacitance. 1 – electrolyte solution; 2 – glass insulation; 3 – electrode disk.

The fact that an electrolyte solution surrounding a microelectrode can be treated as a conductor allows us to use a formula for the capacitance of a cylindrical capacitor in order to estimate stray capacitance:

$$C = \frac{2\pi \varepsilon_r \varepsilon_0 L}{\ln\left(r / r_0\right)} \qquad \text{(A3.1)}$$

where L is the length of the part of the electrode immersed into an electrolyte solution, r is the radius of the electrode body and r_0 is the radius of the metal disk.

As it can be seen from equation A3.1, the value of the stray capacitance is going to be affected by the depth of immersion of the electrode tip into the solution and by the parameters such as the dielectric constant (ε_r) of the insulation material and the R_g factor of the electrode. Taking $\varepsilon_0 = 8.854 \cdot 10^{-12}$ F/m, ε_r (glass) = 5, L = 1 cm and $R_g = r/r_0$ = =10 one can calculate the stray capacitance to be about 1.21 pF. This is very close to the value C_{st} = 0.913 pF used in the analysis of the electronic circuit for a hot microelectrode (Figure 3.2) and estimated from the resonance frequency.

APPENDIX B

B1. CALCULATION OF VOLTAGE DROP ACROSS THE SOLUTION RESISTANCE

In this appendix a detailed calculation of the ratio of the voltage drop across the solution resistance (ΔV_{R_s}) to the output voltage of the signal generator (ΔV_A) is provided. For clarity, Figure 3.2 (Section 3.2.1) is reproduced here.

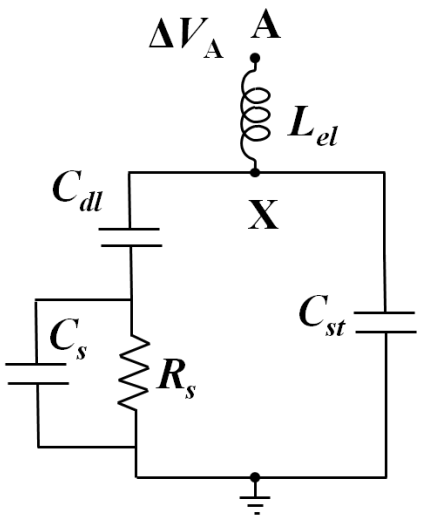

Figure B1.1. Equivalent circuit of a hot microelectrode. L_{el} – inductance of wires, C_{dl} – double layer capacitance, C_s – solution capacitance, C_{st} – stray capacitance, R_s – solution resistance, ΔV_A – output voltage of a signal generator.

In order to calculate the ratio $\Delta V_{R_s} / \Delta V_A$ the circuit shown above needs to be analyzed as follows.

Firstly, the impedance Z_p of the left part of the circuit (to the left from point X and the ground) is calculated:

$$Z_p = \frac{Z_{C_s} Z_{R_s}}{Z_{C_s} + Z_{R_s}} + Z_{C_{dl}} \tag{B1.1}$$

where Z stands for the impedance of the circuit element indicated by the corresponding subscript.

Then the total impedance Z_t of the circuit is calculated according to the formula:

$$Z_t = \frac{Z_{C_{st}} Z_p}{Z_{C_{st}} + Z_p} + Z_{L_{el}} \tag{B1.2}$$

By knowing Z_t it is now possible to determine the voltage at point X:

$$V_X = V_A - \frac{V_A}{Z_t} Z_{L_{el}} \tag{B1.3}$$

and, as a result,

$$V_{R_s} = V_X - \frac{V_X}{Z_p} Z_{C_{dl}} \tag{B1.4}$$

which is the voltage drop across the solution resistance.

Finally, the ratio of the voltage drop across the solution resistance to the voltage at point A can be obtained according to the following equation:

$$\frac{V_{R_s}}{V_A} = \frac{V_X \left(1 - \frac{Z_{C_{dl}}}{Z_p}\right)}{V_A} = \frac{V_A \left(1 - \frac{Z_{L_{el}}}{Z_t}\right)\left(1 - \frac{Z_{C_{dl}}}{Z_p}\right)}{V_A} = \left(1 - \frac{Z_{L_{el}}}{Z_t}\right)\left(1 - \frac{Z_{C_{dl}}}{Z_p}\right) \tag{B1.5}$$

B2. CALCULATION OF VOLTAGE DROP ACROSS THE DOUBLE LAYER

In this appendix a calculation of the ratio of the voltage drop across the double layer ($\Delta V_{C_{dl}}$) to the output voltage of the signal generator (ΔV_A) is provided.

Considering the same equivalent circuit (Figure B1.1) the ratio $\Delta V_{C_{dl}} / \Delta V_A$ can be calculated as

$$\frac{V_{C_{dl}}}{V_A} = \frac{V_B \dfrac{Z_{C_{dl}}}{Z_p}}{V_A} \tag{B2.1}$$

and, by substituting equation B1.3 into equation B2.1, one obtains that

$$\frac{V_{C_{dl}}}{V_A} = \left(1 - \frac{Z_{L_{el}}}{Z_t}\right) \frac{Z_{C_{dl}}}{Z_p} \tag{B2.2}$$

APPENDIX C

C1. OPEN-CIRCUIT POTENTIOMETRIC METHOD OF TEMPERATURE DETERMINATION

To understand how the open-circuit potentiometric method works let us consider the following thermogalvanic cell: Pt| $K_4Fe(CN)_6$, $K_3Fe(CN)_6$, KCl || $K_4Fe(CN)_6$, $K_3Fe(CN)_6$, KCl | Pt. Concentrations of all components in both half cells are exactly the same. However, the left-hand half cell is kept at 0 °C, whereas the temperature of the right-hand half cell is varied from 0 to 85 °C. Consequently, the redox process of interest is the following:

$$Fe(CN)_6^{3-} + e \rightleftarrows Fe(CN)_6^{4-}$$

Nernst potential for each of the half cells is then given by the following equation:

$$E = E^0 + \frac{RT}{F} \ln\left(\frac{\gamma_{Fe(CN)_6^{3-}}}{\gamma_{Fe(CN)_6^{4-}}}\right) \qquad \text{(C1.1)}$$

since the concentration of both redox species is taken to be identical in each half cell. In this equation γ stands for the activity coefficient of the species, E^o is the standard potential and other symbols have their usual meanings.

Next, the cell potential due to the temperature difference between the half cells can be written as follows:

$$E_{cell} = E_{T_2} - E_{T_1} \qquad \text{(C1.2)}$$

where E_{T_2} is the potential of the half cell at temperature T_2 and E_{T_1} is the potential at temperature T_1.

By substituting for half cell potentials from equation C1.1 into equation C1.2 one obtains that:

$$E_{cell} = E^0(T_2) - E^0(T_1) + \frac{R}{F}\left[(T_1 + \Delta T)\ln\left(\frac{\gamma^{T_2}_{Fe(CN)^{3-}_6}}{\gamma^{T_2}_{Fe(CN)^{4-}_6}}\right) - T_1 \ln\left(\frac{\gamma^{T_1}_{Fe(CN)^{3-}_6}}{\gamma^{T_1}_{Fe(CN)^{4-}_6}}\right)\right] \qquad \text{(C1.3)}$$

where ΔT is the temperature difference between the two half cells.

Analysis of this equation indicates that the change in the cell potential as a function of the temperature difference will be primarily determined by the change in the standard electrode potential. The term in brackets may be disregarded as it is not expected to be large. Therefore, by keeping the temperature of one of the half cells constant and varying the temperature of the other, a temperature dependence of the cell potential can be obtained. From the slope of the graph E_{cell} vs. ΔT the temperature coefficient of the electrode reaction standard potential can be determined ($\Delta E^0 / \Delta T$). This coefficient is then used to calculate the change in the temperature of a hot microelectrode from the shift of the half-wave potential. The change in the half-wave potentials is determined from the voltammograms recorded at room temperature and at a hot microelectrode.

C2. DETERMINATION OF TEMPERATURE FROM THE SLOPE OF A STEADY-STATE VOLTAMMOGRAM

The value of the temperature of a hot microelectrode can be determined by the logarithmic analysis of a steady-state voltammogram according to equation 1.3 (Chapter 1). However, this method is somewhat inconvenient since it requires that the graph *E vs.* $\ln\left(\frac{i}{i_{\lim}-i}\right)$ is plotted. Instead, temperature can be determined directly from the slope of the voltammogram. An equation can be derived in the following way.

From equation 1.3 one can obtain the relationship for the faradaic current:

$$i=\frac{i_{\lim}\cdot\exp\left[\left(E-E_{1/2}\right)\frac{nF}{RT}\right]}{1+\exp\left[\left(E-E_{1/2}\right)\frac{nF}{RT}\right]} \qquad \text{(C2.1)}$$

Differentiation of the current with respect to the potential gives:

$$\frac{di}{dE}=\frac{nF}{RT}\cdot i_{\lim}\cdot\frac{\exp\left[\left(E-E_{1/2}\right)\frac{nF}{RT}\right]}{\left(1+\exp\left[\left(E-E_{1/2}\right)\frac{nF}{RT}\right]\right)^2} \qquad \text{(C2.2)}$$

Therefore, the value of the slope at the half-wave potential is given by the formula:

$$\left(\frac{di}{dE}\right)_{i=\frac{i_{\lim}}{2}}=\frac{nF}{4RT_s}\cdot i_{\lim} \qquad \text{(C2.3)}$$

which is the same as the equation 3.6 in Section 3.2.4.

APPENDIX D

D1. SIMULATION OF STEADY-STATE VOLTAMMOGRAMS AT A SPHERICAL ELECTRODE IN THE PRESENCE OF SORET DIFFUSION

The description presented below is strictly applicable to a spherical hot microelectrode. In these considerations the effects of convection and migration on mass transport are neglected. Hence, the flux of the reduced form of the depolarizer to the electrode can be described by the following equation:

$$J_R = -D_R\left(\frac{\partial C_R}{\partial r}\right) - D_R^T C_R\left(\frac{\partial T}{\partial r}\right) \qquad \text{(D1.1)}$$

where D_R is the (isothermal) diffusion coefficient, D_R^T is the thermal diffusion coefficient.

At the steady state, the number of moles of the reduced form passing through an imaginary surface surrounding the electrode must be independent of distance, and it should be related to the steady-state current (i_{ss}) via Faraday's law. In addition, since the variables are no longer dependent on time, partial derivatives in equation D1.1 can be replaced with normal derivatives:

$$\frac{i_{ss}}{nF} = -4\pi r^2 J_R(r) = 4\pi r^2\left(D_R\frac{dC_R}{dr} + D_R^T C_R\frac{dT}{dr}\right) \qquad \text{(D1.2)}$$

This equation can be further rearranged as:

$$\frac{i_{ss}}{4\pi nFD_R^0 r_0 C_R^0} = \frac{D_R(r)}{D_R^0}\frac{r^2}{r_0 C_R^0}\left(\frac{dC_R}{dr} + \sigma_R C_R\frac{dT}{dr}\right) \qquad \text{(D1.3)}$$

where C_R^0 is the bulk concentration of the reduced form, r_0 is the electrode radius, D_R^0 is the bulk diffusion coefficient of the reduced form (D_R depends on temperature, therefore depends on *r*) and $\sigma_R = \frac{D_R^T}{D_R}$ is the Soret coefficient (it is customary to assume that σ_R is temperature independent).

Let us define new dimensionless variables: $x = \frac{r_0}{r}$, $\tilde{I} = \frac{i_{ss}}{4\pi nFD_R^0 r_0 C_R^0}$, $\tilde{D}(x) = \frac{D_R(x)}{D_R^0}$ and $\tilde{C}_R(x) = \frac{C_R(x)}{C_R^0}$.

With these new variables equation D1.3 can be written as:

$$\tilde{I} = -\tilde{D}(x)\left[\frac{d\tilde{C}_R(x)}{dx} + \sigma_R \tilde{C}_R(x)\frac{dT}{dx}\right] \qquad \text{(D1.4)}$$

or

$$\frac{d\tilde{C}_R(x)}{dx} = -\frac{1}{\tilde{D}(x)}\tilde{I} - \sigma_R \tilde{C}_R(x)\frac{dT}{dx} \qquad \text{(D1.5)}$$

By analogy, a similar equation can be written for the oxidized form of the depolarizer. In this case, however, a negative flux (towards the electrode) corresponds to a negative current, therefore:

$$\frac{d\tilde{C}_{Ox}(x)}{dx} = \frac{1}{\tilde{D}(x)}\tilde{I} - \sigma_{Ox} \tilde{C}_{Ox}(x)\frac{dT}{dx} \qquad \text{(D1.6)}$$

For simplicity it is assumed that $C_{Ox}^0 = C_R^0$ and $D_{Ox}(x) = D_R(x)$.

In equations D1.5 and D1.6 $x = 0$ corresponds to the bulk of the solution ($r \to \infty$) and $x = 1$ corresponds to the surface of the electrode ($r = r_0$). These equations can be solved numerically if the temperature profile, $T(x)$, is known.

Based on the previously derived[7] equation 1.7 (Chapter 1) one obtains:

$$T(x) = T_b + \Delta T(2 - x)x \qquad \text{(D1.7)}$$

where T_b is the bulk solution temperature, ΔT is the temperature difference between the electrode surface and the bulk solution and $x = r_0 / r$. This equation was derived assuming that electrical and thermal conductivity of the solution is independent of temperature.

Based on equation D1.7, $\frac{dT}{dx} = 2\Delta T(1-x)$ and equations D1.5 and D1.6 can be written as follows:

$$\frac{d\tilde{C}_R(x)}{dx} = -\frac{1}{\tilde{D}(x)}\tilde{I} - 2\Delta T\sigma_R(1-x)\tilde{C}_R(x) \qquad \text{(D1.8)}$$

and

$$\frac{d\tilde{C}_{Ox}(x)}{dx} = \frac{1}{\tilde{D}(x)}\tilde{I} - 2\Delta T\sigma_{Ox}(1-x)\tilde{C}_{Ox}(x) \qquad \text{(D1.9)}$$

These equations can be converted to the finite difference equations and solved numerically using Excel spreadsheet.

$$\tilde{C}_R(x+\Delta x) = \tilde{C}_R(x) - \left[\frac{1}{\tilde{D}(x)}\tilde{I} + 2\Delta T\sigma_R(1-x)\tilde{C}_R(x)\right]\cdot\Delta x \qquad \text{(D1.10)}$$

$$\tilde{C}_{Ox}(x+\Delta x) = \tilde{C}_{Ox}(x) + \left[\frac{1}{\tilde{D}(x)}\tilde{I} - 2\Delta T\sigma_{Ox}(1-x)\tilde{C}_{Ox}(x)\right]\cdot\Delta x \qquad \text{(D1.11)}$$

In calculations, the following values were used: Δx = 0.0025, $\tilde{C}_{Ox}(0) = \tilde{C}_R(0) = 1$, σ_R = 1×10^{-2} K^{-1} and σ_{Ox} = 0 K^{-1}. For a given value of ΔT the temperature profile was calculated using equation D1.7. Then $\tilde{D}(x)$ was calculated using equation 1.57 (Chapter 1). Concentration profiles $\tilde{C}_{Ox}(x)$ and $\tilde{C}_R(x)$ were calculated first for $\tilde{I} = 0$. Then $\tilde{I}$ was incremented in small steps until $\tilde{C}_R(x=1)$ reached zero to give the limiting current for the oxidation process and, subsequently, $\tilde{I}$ was decremented in small steps until $\tilde{C}_{Ox}(x=1)$ reached zero to give the limiting current for the reduction. As the result, it was possible to obtain the limiting current enhancement factors and numerical relationships between the current and surface concentrations of the reduced and oxidized

forms of the depolarizer. Obtained values of the surface concentration of the redox species are used to estimate the effect of Soret diffusion on the half-wave potential shift according to equation 5.1 (Section 5.2.2).

APPENDIX E

E1. SIMULATION PROGRAM

Shown below is the general overview of the simulation program developed during this PhD work.

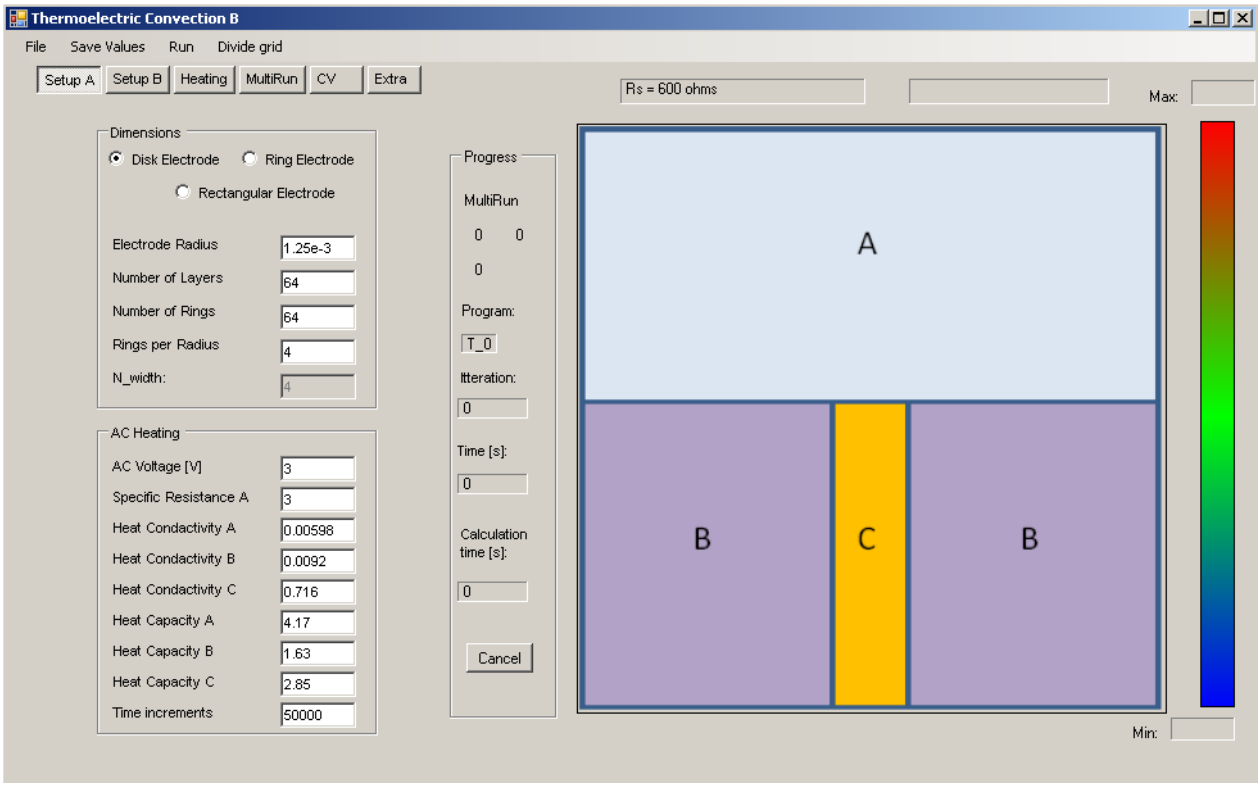

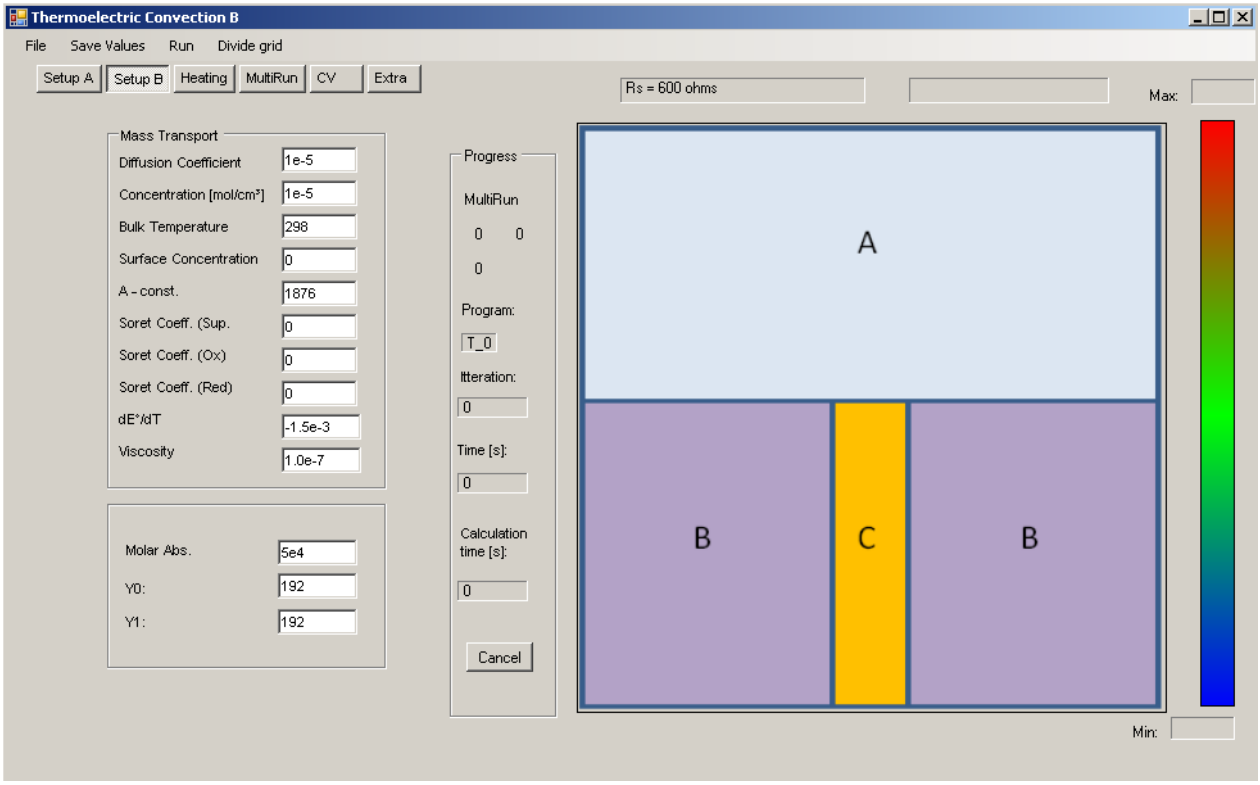
Thermoelectric Convection B
File
Save Values
Run
Divide grid
Setup A
Setup B
Heating
MultiRun
CV
Extra
Rs = 600 ohms
Max:
Mass Transport
Diffusion Coefficient
1e-5
Concentration [mol/cm³]
1e-5
Bulk Temperature
298
Surface Concentration
0
A - const.
1876
Soret Coeff. (Sup.
0
Soret Coeff. (Ox)
0
Soret Coeff. (Red)
0
dE°/dT
-1.5e-3
Viscosity
1.0e-7
Molar Abs.
5e4
Y0:
192
Y1:
192
Progress
MultiRun
0 0
0
Program:
T_0
Itteration:
0
Time [s]:
0
Calculation time [s]:
0
Cancel
A
B
C
B
Min:

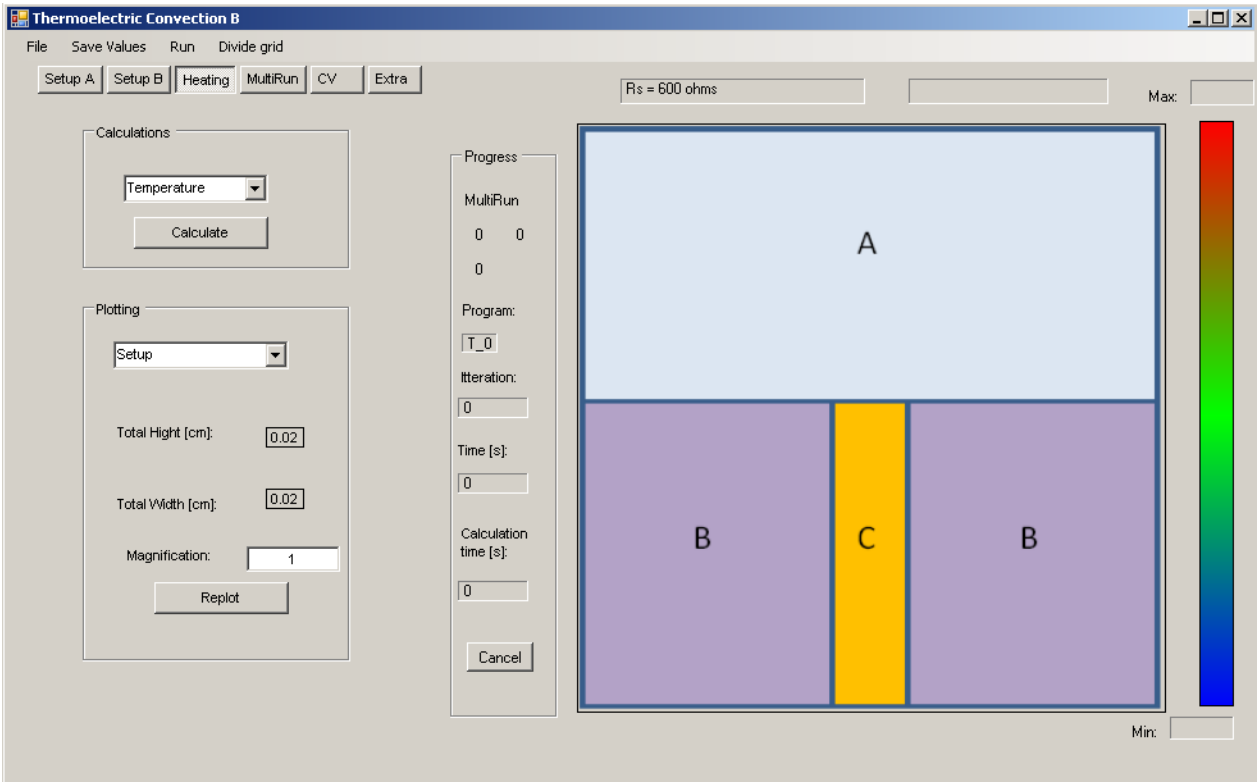
Thermoelectric Convection B
File
Save Values
Run
Divide grid
Setup A
Setup B
Heating
MultiRun
CV
Extra
Rs = 600 ohms
Max:
Calculations
Temperature
Calculate
Plotting
Setup
Total Hight [cm]:
0.02
Total Width [cm]:
0.02
Magnification:
1
Replot
Progress
MultiRun
0 0
0
Program:
T_0
Itteration:
0
Time [s]:
0
Calculation time [s]:
0
Cancel
A
B
C
B
Min:

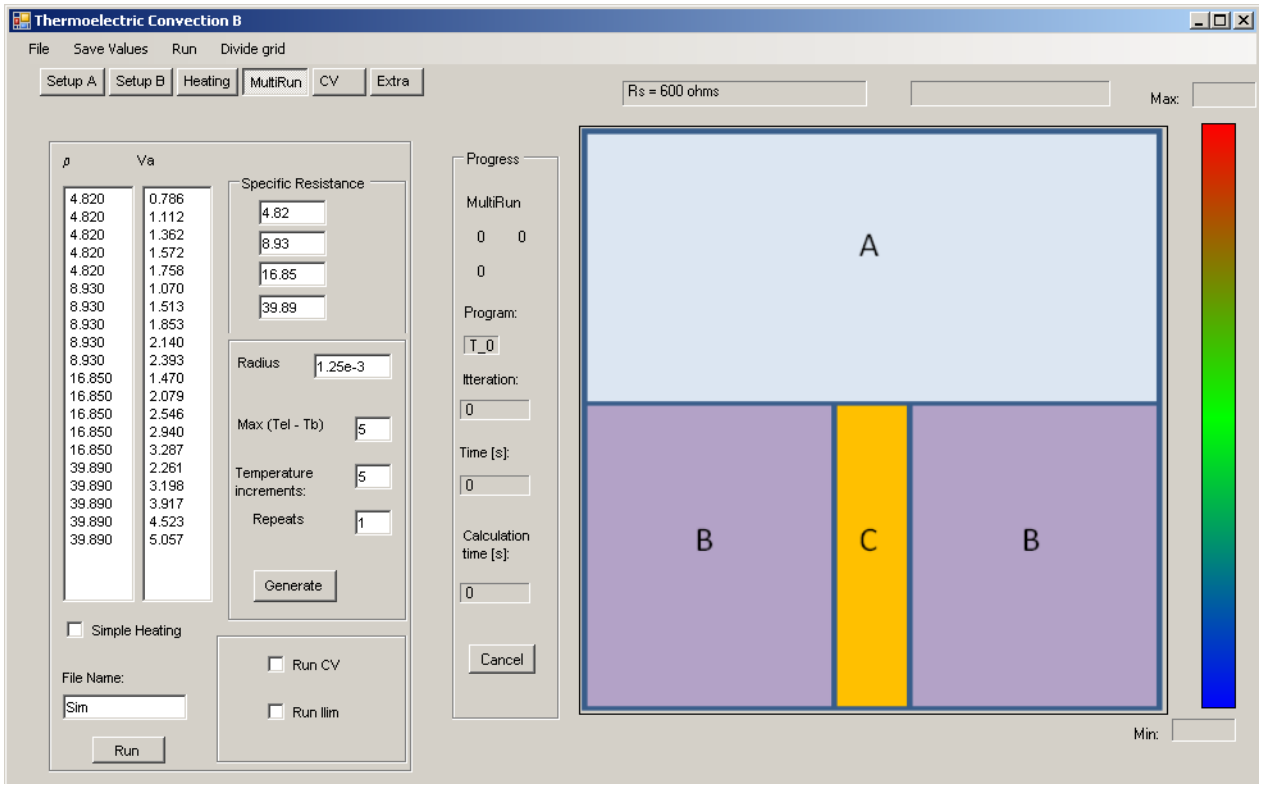
Thermoelectric Convection B
File
Save Values
Run
Divide grid
Setup A
Setup B
Heating
MultiRun
CV
Extra
Rs = 600 ohms
Max:
ρ
Va
4.820 0.786
4.820 1.112
4.820 1.362
4.820 1.572
4.820 1.758
8.930 1.070
8.930 1.513
8.930 1.853
8.930 2.140
8.930 2.393
16.850 1.470
16.850 2.079
16.850 2.546
16.850 2.940
16.850 3.287
39.890 2.261
39.890 3.198
39.890 3.917
39.890 4.523
39.890 5.057
Specific Resistance
4.82
8.93
16.85
39.89
Radius
1.25e-3
Max (Tel - Tb)
5
Temperature increments:
5
Repeats
1
Generate
Simple Heating
File Name:
Sim
Run
Run CV
Run Ilim
Progress
MultiRun
0 0
0
Program:
T_0
Itteration:
0
Time [s]:
0
Calculation time [s]:
0
Cancel
A
B
C
B
Min:

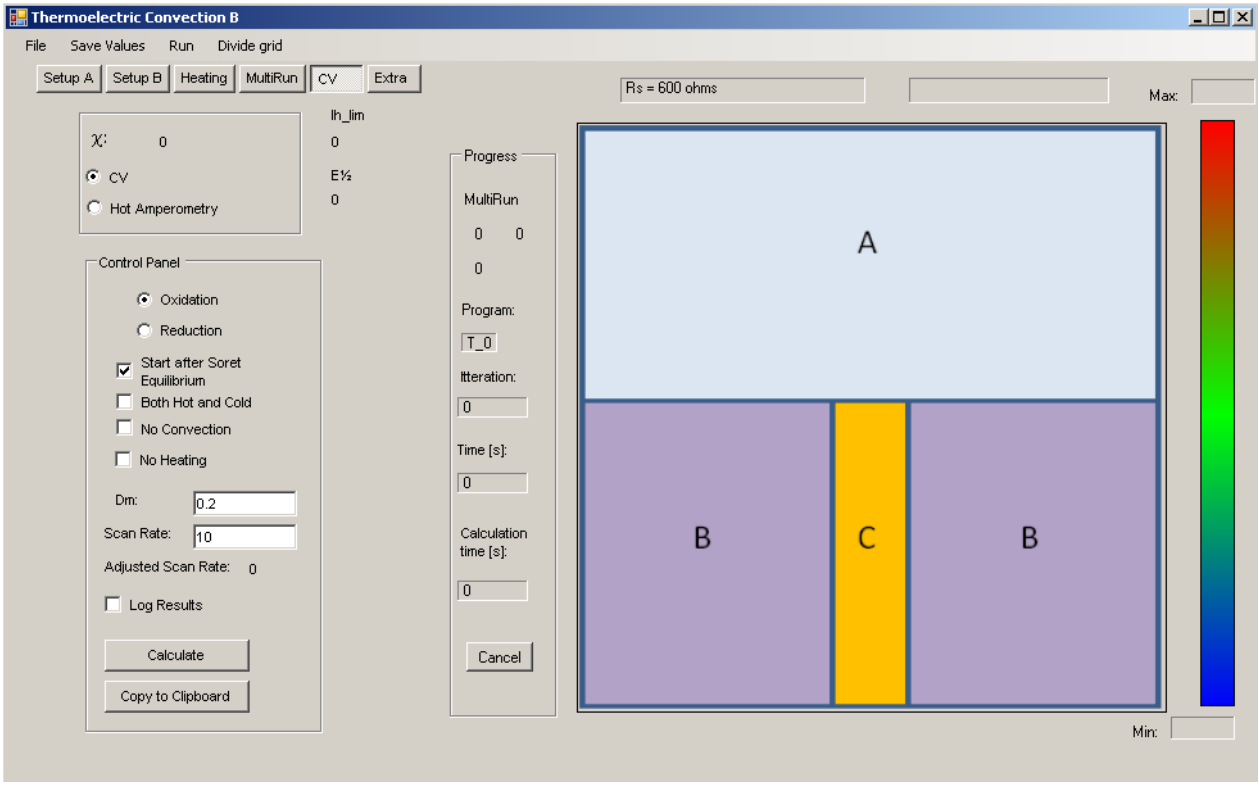
Thermoelectric Convection B
File
Save Values
Run
Divide grid
Setup A
Setup B
Heating
MultiRun
CV
Extra
Rs = 600 ohms
Max:
χ:
0
CV
Hot Amperometry
Ih_lim
0
E½
0
Control Panel
Oxidation
Reduction
Start after Soret Equilibrium
Both Hot and Cold
No Convection
No Heating
Dm:
0.2
Scan Rate:
10
Adjusted Scan Rate:
0
Log Results
Calculate
Copy to Clipboard
Progress
MultiRun
0 0
0
Program:
T_0
Itteration:
0
Time [s]:
0
Calculation time [s]:
0
Cancel
A
B
C
B
Min:

E2. RESULTS OF VIDEO OBSERVATIONS

Shown below are representative snapshots obtained from the recorded video files. Full-length videos can be found on a CD enclosed with this thesis.

a) **b)**

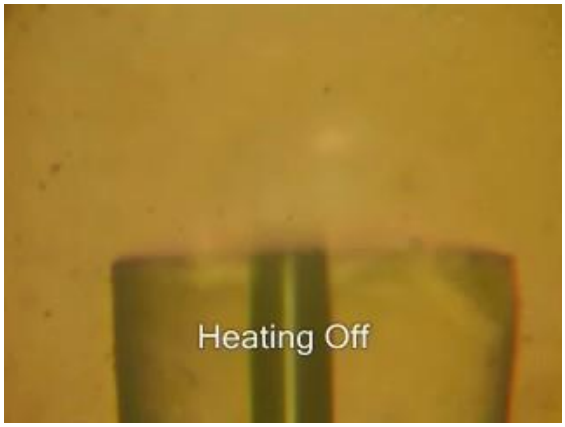

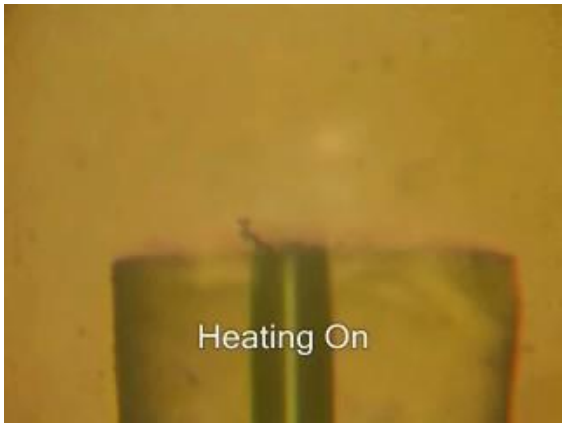

Video 3.1 Microscopic observations of convection at a 25 μm Pt disk electrode heated by an ac waveform of 2.0 V_{rms} at 160 MHz. The solution contained gold microparticles (0.4 to 0.8 μm in diameter) suspended in 0.6 M H_2SO_4. **a)** before heating; **b)** after heating (note accumulation of particles into a microwire).

a) **b)**

Video 3.2 Effect of ac heating on the diffusion layer formed during the reduction of 50 mM methyl viologen in 0.5 M NaCl at a 25 μm Pt electrode. The electrode was heated with an alternating voltage of 2.8 V_{rms} at 160 MHz; the dc potential of the working electrode was –0.5 V vs. Ag | AgCl(s) | 2 M KCl. **a)** before heating; **b)** during ac heating.

a) **b)**

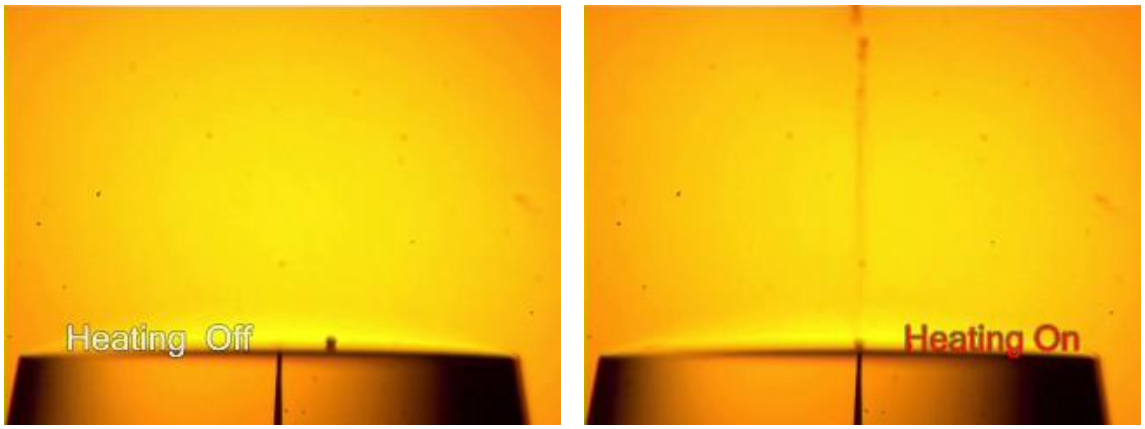

Video 3.3 Jet boiling at an overheated 3.6 μm Pt electrode in 2.0 M KCl containing 50 mM methyl viologen. The electrode was heated with an alternating voltage of 2.8 V_{rms} at 165 MHz; the dc potential of the working electrode was –0.5 V vs. Ag | AgCl(s) | 2 M KCl. The electrode axis and the direction of the jet was perpendicular to the gravitational field. **a)** before heating; **b)** during ac heating (note appearance of a jet).

a) **b)**

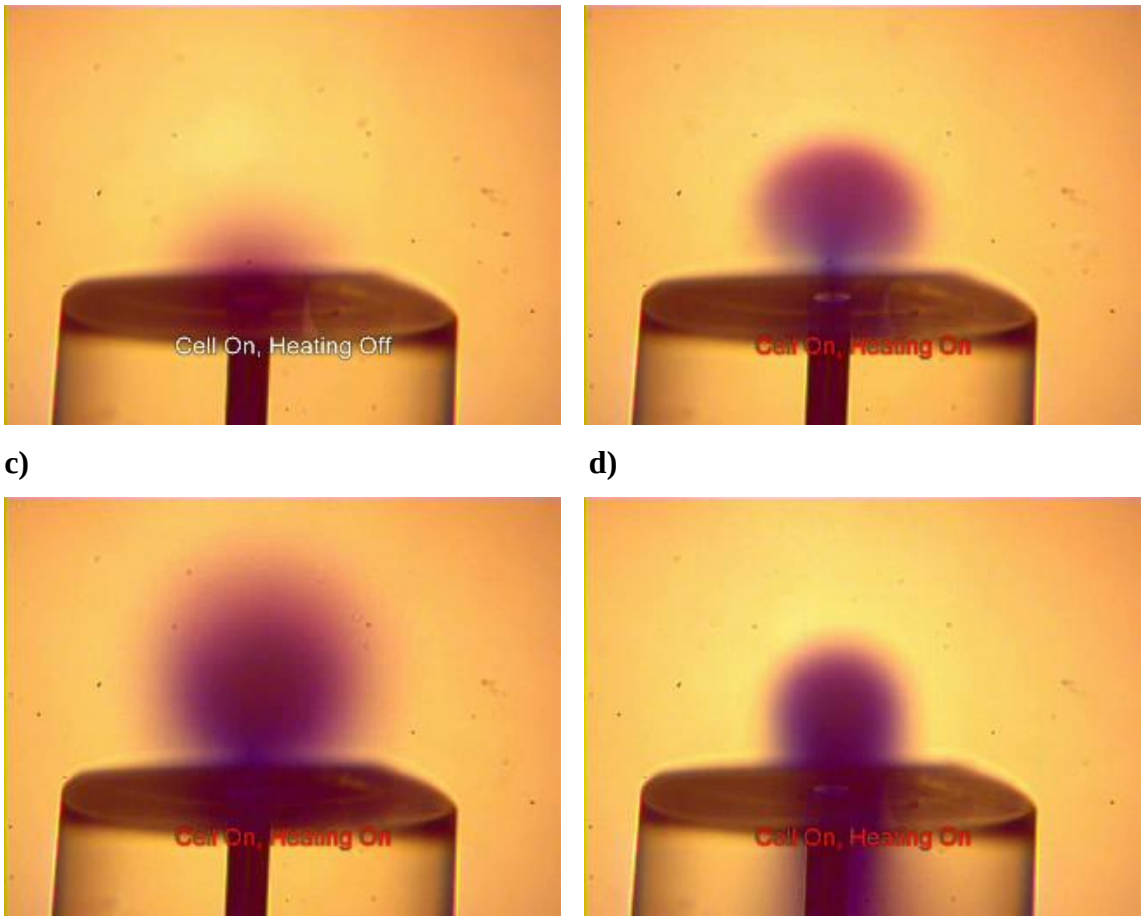

c) **d)**

Video 4.1 Solution flow around a hot Pt microelectrode during the reduction of 50 mM methyl viologen in 0.2 M KCl. The electrode was heated with an alternating voltage of 13.4V_{rms} at 20 MHz. **a)** before heating; **b) – d)** during ac heating.

a) **b)**

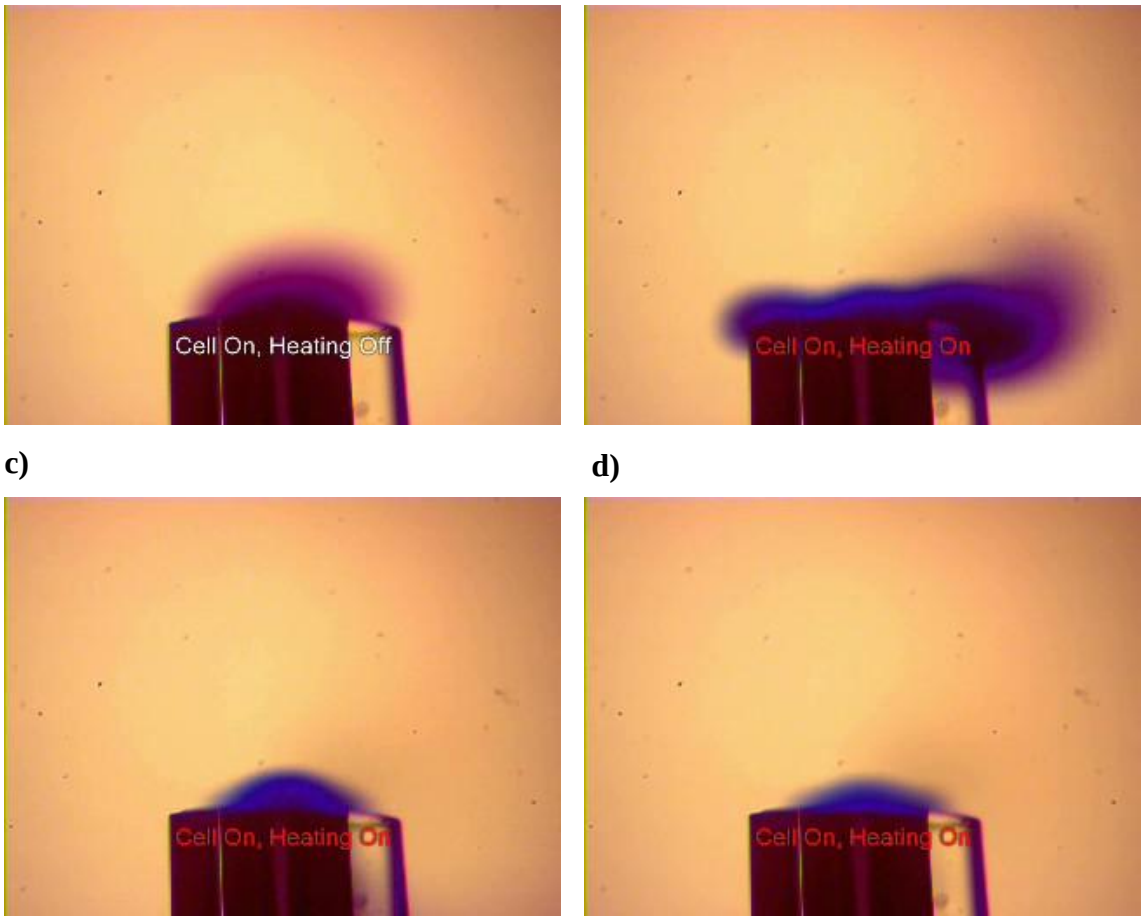

c) **d)**

Video 4.2 Solution flow around a hot Bi microelectrode during the reduction of 50 mM methyl viologen in 0.2 M KCl. The electrode was heated with an alternating voltage of 13.4V_{rms} at 20 MHz. **a)** before heating; **b) – d)** during ac heating.

a) **b)**

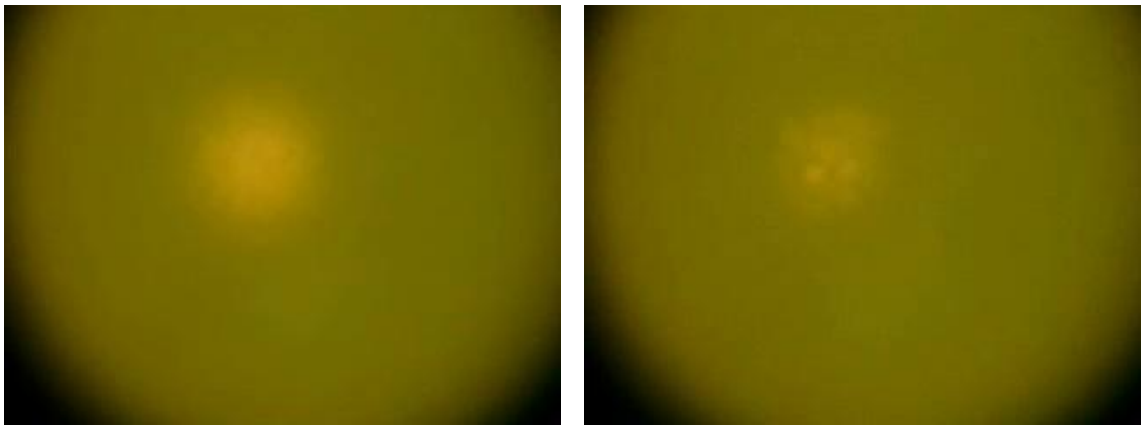

Video 6.1 Boiling above a paraffin film. Conditions: 25 μm Pt disk electrode in 0.01M $FeSO_4$, 1M M H_2SO_4. AC signal: 140 MHz, 2.8 V_{rms}. **a)** before heating; **b)** after ac heating

REFERENCES

(1) Heinze, J. *Angewandte Chemie* **1993**, *105*, 1327-49 (See also Angew Chem , Int Ed Engl , 1993, 32(9), 1268-88).
(2) Zoski, C. G. *Electroanalysis* **2002**, *14*, 1041-1051.
(3) Miller, B. *Journal of the Electrochemical Society* **1983**, *130*, 1639-40.
(4) Gruendler, P.; Zerihun, T.; Moeller, A.; Kirbs, A. *Journal of Electroanalytical Chemistry* **1993**, *360*, 309-14.
(5) Compton, R. G.; Coles, B. A.; Marken, F. *Chemical Communications (Cambridge)* **1998**, 2595-2596.
(6) Moorcroft, M. J.; Lawrence, N. S.; Coles, B. A.; Compton, R. G.; Trevani, L. N. *Journal of Electroanalytical Chemistry* **2001**, *506*, 28-33.
(7) Baranski, A. S. *Analytical Chemistry* **2002**, *74*, 1294-1301.
(8) Gruendler, P.; Zerihun, T.; Kirbs, A.; Grabow, H. *Analytica Chimica Acta* **1995**, *305*, 232-40.
(9) Gruendler, P. *Fresenius' Journal of Analytical Chemistry* **1998**, *362*, 180-183.
(10) Gruendler, P.; Degenring, D. *Electroanalysis* **2001**, *13*, 755-759.
(11) Gruendler, P. *Fresenius' Journal of Analytical Chemistry* **2000**, *367*, 324-328.
(12) Sur, U. K.; Marken, F.; Coles, B. A.; Compton, R. G.; Dupont, J. *Chemical Communications (Cambridge, United Kingdom)* **2004**, 2816-2817.
(13) Gruendler, P.; Kirbs, A.; Zerihun, T. *Analyst (Cambridge, United Kingdom)* **1996**, *121*, 1805-1810.
(14) Gruendler, P.; Flechsig, G.-U. *Microchimica Acta* **2006**, *154*, 175-189.
(15) Valdes, J. L.; Miller, B. *Journal of Physical Chemistry* **1988**, *92*, 525-32.
(16) Zerihun, T.; Gruendler, P. *Journal of Electroanalytical Chemistry* **1996**, *404*, 243-248.
(17) Bard, A. J.; Faulkner, L. R. *Electrochemical methods : fundamentals and applications*; 2nd ed.; John Wiley: New York ; Chichester [England], 2001.
(18) Morris, A. S. *Measurement and instrumentation principles*; Butterworth-Heinemann: Oxford [England] ; Boston, 2001.
(19) Schneider, A.; Flechsig, G.-U.; Gruendler, P. *Journal of the Electrochemical Society* **2000**, *147*, 3768-3770.
(20) Beckmann, A.; Coles, B. A.; Compton, R. G.; Gruendler, P.; Marken, F.; Neudeck, A. *Journal of Physical Chemistry B* **2000**, *104*, 764-769.
(21) Marken, F.; Tsai, Y.-C.; Coles, B. A.; Matthews, S. L.; Compton, R. G. *New Journal of Chemistry* **2000**, *24*, 653-658.
(22) Platten, J. K.; Costeseque, P. *European Physical Journal E: Soft Matter* **2004**, *15*, 235-239.
(23) Tyrrell, H. J. V. *Diffusion and heat flow in liquids*; Butterworths: London, 1961.
(24) Tanner, C. C. *Transactions of the Faraday Society* **1927**, *23*, 75-95.

(25) Agar, J. N.; Turner, J. C. R. *Proceedings of the Royal Society of London. Series A, Mathematical and Physical Sciences* **1960**, *255*, 307-330.
(26) Snowdon, P. N.; Turner, J. C. R. *Transactions of the Faraday Society* **1960**, *56*, 1409-1418.
(27) Riehl, N. *Zeitschrift Fur Elektrochemie Und Angewandte Physikalische Chemie* **1943**, *49*, 306-308.
(28) Morin, M. G.; Saylor, J. H.; Gross, P. M. *Journal of the American Chemical Society* **1951**, *73*, 3977-81.
(29) Alexander, K. F. *Z. physik. Chem.* **1951**, *197*, 233-8.
(30) Thomaes, G. *Journal de Chimie Physique et de Physico-Chimie Biologique* **1956**, *53*, 407-11.
(31) Chang, C.-C.; Yang, R.-J. *Microfluidics and Nanofluidics* **2007**, *3*, 501-525.
(32) Morgan, H.; Green, N. G. *AC electrokinetics : colloids and nanoparticles*; Research Studies Press: Baldock, Eng. ; Philadelphia, Pa., 2003.
(33) Ramos, A.; Morgan, H.; Green, N. G.; Castellanos, A. *Journal of Physics D: Applied Physics* **1998**, *31*, 2338-2353.
(34) Pohl, H. A. *Cambridge Monographs on Physics. Dielectrophoresis: The Behavior of Neutral Matter in Nonuniform Electric Fields*, 1978.
(35) Green, N. G.; Ramos, A.; Morgan, H. *Journal of Physics D-Applied Physics* **2000**, *33*, 632-641.
(36) Holzel, R.; Calander, N.; Chiragwandi, Z.; Willander, M.; Bier, F. F. *Physical Review Letters* **2005**, *95*.
(37) Durr, M.; Kentsch, J.; Muller, T.; Schnelle, T.; Stelzle, M. *Electrophoresis* **2003**, *24*, 722-731.
(38) Chen, D. F.; Du, H.; Li, W. H. *Journal of Micromechanics and Microengineering* **2006**, *16*, 1162-1169.
(39) Park, J.; Kim, B.; Choi, S. K.; Hong, S.; Lee, S. H.; Lee, K.-I. *Lab on a Chip* **2005**, *5*, 1264-1270.
(40) Demierre, N.; Braschler, T.; Muller, R.; Renaud, P. *Sensors and Actuators, B: Chemical* **2008**, *B132*, 388-396.
(41) Voldman, J.; Gray, M. L.; Toner, M.; Schmidt, M. A. *Analytical Chemistry* **2002**, *74*, 3984-3990.
(42) Park, B. Y.; Madou, M. J. *Electrophoresis* **2005**, *26*, 3745-3757.
(43) Lapizco-Encinas, B. H.; Davalos, R. V.; Simmons, B. A.; Cummings, E. B.; Fintschenko, Y. *Journal of Microbiological Methods* **2005**, *62*, 317-326.
(44) Ozuna-Chacon, S.; Lapizco-Encinas, B. H.; Rito-Palomares, M.; Martinez-Chapa, S. O.; Reyes-Betanzo, C. *Electrophoresis* **2008**, *29*, 3115-3122.
(45) Barrett, L. M.; Skulan, A. J.; Singh, A. K.; Cummings, E. B.; Fiechtner, G. J. *Analytical Chemistry* **2005**, *77*, 6798-6804.
(46) Zhang, C.; Khoshmanesh, K.; Mitchell, A.; Kalantar-zadeh, K. *Analytical and Bioanalytical Chemistry* **2009**, No pp yet given.
(47) Kang, Y.; Li, D. *Microfluidics and Nanofluidics* **2009**, *6*, 431-460.
(48) Holzel, R. *Iet Nanobiotechnology* **2009**, *3*, 28-45.
(49) Flechsig, G.-U.; Korbout, O.; Hocevar, S. B.; Thongngamdee, S.; Ogorevc, B.; Gruendler, P.; Wang, J. *Electroanalysis* **2002**, *14*, 192-196.
(50) Marken, F.; Matthews, S. L.; Compton, R. G.; Coles, B. A. *Electroanalysis* **2000**, *12*, 267-273.

(51) Tsai, Y.-C.; Coles, B. A.; Compton, R. G.; Marken, F. *Electroanalysis* **2001**, *13*, 639-645.
(52) Jasinski, M.; Kirbs, A.; Schmehl, M.; Gruendler, P. *Electrochemistry Communications* **1999**, *1*, 26-28.
(53) Jasinski, M.; Gruendler, P.; Flechsig, G.-U.; Wang, J. *Electroanalysis* **2001**, *13*, 34-36.
(54) Marken, F.; Tsai, Y.-C.; Saterlay, A. J.; Coles, B. A.; Tibbetts, D.; Holt, K.; Goeting, C. H.; Foord, J. S.; Compton, R. G. *Journal of Solid State Electrochemistry* **2001**, *5*, 313-318.
(55) Tsai, Y.-C.; Coles, B. A.; Holt, K.; Foord, J. S.; Marken, F.; Compton, R. G. *Electroanalysis* **2001**, *13*, 831-835.
(56) Gruendler, P.; Flechsig, G.-U. *Electrochimica Acta* **1998**, *43*, 3451-3458.
(57) Flechsig, G.-U.; Korbut, O.; Gruendler, P. *Electroanalysis* **2001**, *13*, 786-788.
(58) Wang, J.; Gruendler, P.; Flechsig, G.-U.; Jasinski, M.; Lu, J.; Wang, J.; Zhao, Z.; Tian, B. *Analytica Chimica Acta* **1999**, *396*, 33-37.
(59) Ghanem, M. A.; Hanson, H.; Compton, R. G.; Coles, B. A.; Marken, F. *Talanta* **2007**, *72*, 66-71.
(60) Wang, J.; Gruendler, P.; Flechsig, G.-U.; Jasinski, M.; Rivas, G.; Sahlin, E.; Lopez Paz, J. L. *Analytical Chemistry* **2000**, *72*, 3752-3756.
(61) Rassaei, L.; French, R. W.; Compton, R. G.; Marken, F. *Analyst (Cambridge, United Kingdom)* **2009**, *134*, 887-892.
(62) Lau, C.; Reiter, S.; Schuhmann, W.; Gruendler, P. *Analytical and Bioanalytical Chemistry* **2004**, *379*, 255-260.
(63) Lau, C.; Borgmann, S.; Maciejewska, M.; Ngounou, B.; Gruendler, P.; Schuhmann, W. *Biosensors & Bioelectronics* **2007**, *22*, 3014-3020.
(64) Tseng, T.-F.; Yang, Y.-L.; Chuang, M.-C.; Lou, S.-L.; Galik, M.; Flechsig, G.-U.; Wang, J. *Electrochemistry Communications* **2009**, *11*, 1819-1822.
(65) Wang, J.; Flechsig, G.-U.; Erdem, A.; Korbut, O.; Gruendler, P. *Electroanalysis* **2004**, *16*, 928-931.
(66) Flechsig, G.-U.; Peter, J.; Hartwich, G.; Wang, J.; Gruendler, P. *Langmuir* **2005**, *21*, 7848-7853.
(67) Peter, J.; Reske, T.; Flechsig, G.-U. *Electroanalysis* **2007**, *19*, 1356-1361.
(68) Surkus, A.-E.; Flechsig, G.-U. *Electroanalysis* **2009**, *21*, 1119-1123.
(69) Lau, C.; Flechsig, G.-U.; Gruendler, P.; Wang, J. *Analytica Chimica Acta* **2005**, *554*, 74-78.
(70) Duwensee, H.; Vazquez-Alvarez, T.; Flechsig, G.-U.; Wang, J. *Talanta* **2009**, *77*, 1757-1760.
(71) Climent, V.; Coles, B. A.; Compton, R. G. *Journal of Physical Chemistry B* **2001**, *105*, 10669-10673.
(72) Climent, V.; Coles, B. A.; Compton, R. G. *Journal of Physical Chemistry B* **2002**, *106*, 5988-5996.
(73) Climent, V.; Coles, B. A.; Compton, R. G. *Journal of Physical Chemistry B* **2002**, *106*, 5258-5265.
(74) Climent, V.; Coles, B. A.; Compton, R. G.; Feliu, J. M. *Journal of Electroanalytical Chemistry* **2004**, *561*, 157-165.
(75) Climent, V.; Garcia-Araez, N.; Compton, R. G.; Feliu, J. M. *Journal of Physical Chemistry B* **2006**, *110*, 21092-21100.

(76) Garcia-Araez, N.; Climent, V.; Feliu, J. M. *Journal of the American Chemical Society* **2008**, *130*, 3824-3833.
(77) Garcia-Araez, N.; Climent, V.; Feliu, J. *Journal of Physical Chemistry C* **2009**, *113*, 9290-9304.
(78) Wildgoose, G. G.; Giovanelli, D.; Lawrence, N. S.; Compton, R. G. *Electroanalysis* **2004**, *16*, 421-433.
(79) Sur, U. K.; Marken, F.; Rees, N.; Coles, B. A.; Compton, R. G.; Seager, R. *Journal of Electroanalytical Chemistry* **2004**, *573*, 175-182.
(80) Rassaei, L.; Compton, R. G.; Marken, F. *J. Phys. Chem. C* **2009**, *113*, 3046-3049.
(81) Qiu, F.; Compton, R. G.; Coles, B. A.; Marken, F. *Journal of Electroanalytical Chemistry* **2000**, *492*, 150-155.
(82) Ghanem, M. A.; Thompson, M.; Compton, R. G.; Coles, B. A.; Harvey, S.; Parker, K. H.; O'Hare, D.; Marken, F. *Journal of Physical Chemistry B* **2006**, *110*, 17589-17594.
(83) Cutress, I. J.; Marken, F.; Compton, R. G. *Electroanalysis* **2009**, *21*, 113-123.
(84) Zhang, B.; Zhang, Y.; White, H. S. *Analytical Chemistry* **2004**, *76*, 6229-6238.
(85) Zhang, B.; Galusha, J.; Shiozawa, P. G.; Wang, G.; Bergren, A. J.; Jones, R. M.; White, R. J.; Ervin, E. N.; Cauley, C. C.; White, H. S. *Analytical Chemistry* **2007**, *79*, 4778-4787.
(86) Baranski, A. S.; Boika, A. *unpublished results*.
(87) Zhang, B.; Zhang, Y.; White, H. S. *Analytical Chemistry* **2006**, *78*, 477-483.
(88) Boika, A.; Baranski, A. S. *Analytical Chemistry* **2008**, *80*, 7392-7400.
(89) Huang, W.; McCreery, R. *Journal of Electroanalytical Chemistry* **1992**, *326*, 1-12.
(90) Baranski, A. S.; Diakowski, P. M. *Journal of Physical Chemistry B* **2006**, *110*, 6776-6784.
(91) Baranski, A. S.; Boika, A. *Analytical Chemistry* **2010**, submitted.
(92) Newman, J. *Journal of the Electrochemical Society* **1966**, *113*, 501-502.
(93) Newman, J. *Journal of the Electrochemical Society* **1970**, *117*, 198-203.
(94) Muneer, T.; Jorge, K.; Thomas, G. *Heat transfer : a problem solving approach*; Taylor & Francis: London, 2003.
(95) CRC Press. *CRC handbook of chemistry and physics*; CRC Press, 1992-1993; Vol. 73rd ed.
(96) Batchelor, G. K. *An introduction to fluid dynamics*; 1st paperback ed.; Cambridge University Press: London, 1973.
(97) Mitchell, A. R.; Griffiths, D. F. *The finite difference method in partial differential equations*; Wiley: Chichester [Eng.] ; New York, 1980.
(98) Lyklema, J.; van Leeuwen, H. P.; Minor, M. *Advances in Colloid and Interface Science* **1999**, *83*, 33-69.
(99) Valdes, J. L.; Miller, B. *Journal of Physical Chemistry* **1988**, *92*, 4483-4490.
(100) Sun, P.; Laforge, F. O.; Mirkin, M. V. *Physical Chemistry Chemical Physics* **2007**, *9*, 802-823.
(101) Horrocks, B. R.; Schmidtke, D.; Heller, A.; Bard, A. J. *Analytical Chemistry* **1993**, *65*, 3605-3614.
(102) Gomez-Sjoberg, R.; Morisette, D. T.; Bashir, R. *Journal of Microelectromechanical Systems* **2005**, *14*, 829-838.
(103) Yang, L.; Bashir, R. *Biotechnology Advances* **2008**, *26*, 135-150.
(104) Hughes, M. P.; Morgan, H. *Analytical Chemistry* **1999**, *71*, 3441-3445.

(105) Liu, R. H.; Lenigk, R.; Druyor-Sanchez, R. L.; Yang, J.; Grodzinski, P. *Analytical Chemistry* **2003**, *75*, 1911-1917.
(106) Sassolas, A.; Blum, L. J.; Leca-Bouvier, B. D. *Electroanalysis* **2009**, *21*, 1237-1250.
(107) Lapizco-Encinas, B. H.; Rito-Palomares, M. *Electrophoresis* **2007**, *28*, 4521-4538.
(108) Meighan, M. M.; Staton, S. J. R.; Hayes, M. A. *Electrophoresis* **2009**, *30*, 852-865.
(109) Walsh, D. A.; Fernandez, J. L.; Mauzeroll, J.; Bard, A. J. *Analytical Chemistry* **2005**, *77*, 5182-5188.
(110) Lin, C.-L.; Rodriguez-Lopez, J.; Bard, A. J. *Analytical Chemistry* **2009**, *81*, 8868-8877.
(111) Brown, E.; Hao, L.; Cox, D. C.; Gallop, J. C. *Journal of Physics: Conference Series* **2008**, *100*, No pp given.
(112) Macpherson, J. V.; Unwin, P. R. *Analytical Chemistry* **2000**, *72*, 276-285.
(113) Fawcett, W. R. *Liquids, solutions, and interfaces : from classical macroscopic descriptions to modern microscopic details*; Oxford University Press: Oxford ; New York, 2004.
(114) Bard, A. J.; Stratmann, M. *Encyclopedia of Electrochemistry*; Wiley-VCH: Weinheim, 2002; Vol. 3.
(115) Diakowski, P. M. Alternating Current - Scanning Electrochemical Microscopy. Ph.D. Dissertation, University of Saskatchewan, Saskatoon, SK, 2006.